

Assessment of Drug-loaded
Nanoparticles in a 3D *in vitro*
Brain Tumour Model

DELYAN PAVLOV IVANOV, MPharm

**Thesis submitted to the University of Nottingham
for the degree of Doctor of Philosophy**

September 2014

Abstract

This work describes the creation of a three-dimensional model of the children's brain tumour medulloblastoma using primarily human cells. This *in vitro* cell culture model was created as a platform for testing novel drug delivery systems for local delivery in the brain. The aim of the local delivery strategy was to reduce radiotherapy through the use of nanoparticle-based chemotherapy. The nanoparticles would be delivered after surgery in the cavity left by the excised tumour tissue. The model was intended to evaluate the selective cytotoxicity of advanced drug delivery systems towards tumour tissue and the benefit of nanoparticle therapy compared to free drug.

Normal tissue was modelled using human foetal brain tissue and tumour tissue was represented by a variety of medulloblastoma cell lines. Both were cultured as three-dimensional spheroids free of artificial matrix in ultra-low attachment plates. The tumour and normal cells could be cultured either separately or together and the viability for each cell population determined using a battery of methods. Co-cultures of both cell types had the additional benefit of mimicking the interaction between normal and tumour tissue.

The use of physiologically relevant single and co-culture *in vitro* models could provide information on the relative safety and efficacy of novel brain tumour treatments. The high-throughput platforms used, the algorithms and the validation of a battery of tests in 3D may be extrapolated to other cancer models as well. Moreover the universal marking procedure employed can be employed to label, culture and analyse any two cell types, while preserving tissue heterogeneity and viability.

The key benefit from this thesis is the framework for designing *in vitro* models of tumours that include normal tissue as an internal control. This is an important contribution that can substantiate IC50 values by putting them in the context of drug safety and efficacy. It also highlights the minimum checks and feasibility experiments that need to be done before an *in vitro* assay is accepted for 3D spheroids.

Acknowledgements

Nothing is ever accomplished alone. When I first started this project I knew little about cell culture and nanoparticle formulation. Medulloblastoma was a foggy concept from my undergraduate classes and etoposide was merely a topoisomerase inhibitor.

It was through the careful guidance of Dr Terry Parker that I grew as an expert and became proficient in cell culture. Terry's lessons were not only scientific but also had a philosophic meaning. The notion that you learn more from failure than you gain from easy success and the importance of meeting adversity with optimism are the most important lessons from my doctorate. Although he is no longer with us his legacy still lives in the hearts of everyone he has touched.

I am grateful to Dr Martin Garnett for guiding me through this project with constructive advice and stimulating conversations. The long discussions in the lab, or getting advice on-the-fly in the corridors have made the difference in more than one experiment. Martin's quick reactions, inexhaustible enthusiasm and broad knowledge have shown me what it means to be a scientist.

Dr Cameron Alexander has been invaluable with his advice on polymer chemistry, nanoparticles as well as career guidance and networking support. Sometimes just being submerged in those biweekly group meetings was enough to stimulate me to explore a different software package, a novel method or re-evaluate my experiments in a new way.

As far as different perspectives are concerned, the clinician's view of Dr David Walker has shown me how doctors perceive the things we do and write in research. His counsel has stimulated me to reach diverse audiences. David has encouraged me to go out of my comfort zone, to build collaborations with experts from different fields and has taught me how to cooperate more effectively with a diverse set of people.

In that regard, the industry advice and assistance I have received from Dr Paul Gellert and Dr Marianne Ashford from AstraZeneca has really pulled this project from some of its deepest troughs. The discussions with them and the facilitated consultations with experts throughout AstraZeneca regarding spheroid culture (Eric Tang), GPC (Elizabeth Meehan), nanoparticles (Zahid Nazir) and drug release (Clive Washington) were key in the progression of the project. I also thank them for travelling from Macclesfield to Nottingham for our three-monthly meetings and sharing my woes and triumphs.

Everybody who has been to university knows that nothing gets done without the help of the lab and technical support staff. Whether it was finding a reagent or locating and getting training for a key instrument Christine Grainger-Boulby has always been there for me and I thank her for that. Paul Cooling has also saved me with useful tips, guidance and hands-on help in particle sizing and especially in my first steps in HPLC. The detection of teniposide was a breeze thanks to his know-how and

training. From the medical side it was Sue Willington who saw after me, had the answers to my questions and knew where everything and everybody was. Her advice was still going through my head even after her retirement and helped me keep the stem cells happy. Kudos to Claudia Matz, who has been great at taking care of us in the CDT. I thank Amy Nairn for her assistance in sourcing chemicals and catalysing the University's tortuous procurement procedures.

The experts from the flow cytometry facility have been essential for this project. The inspiring discussions with Adrian Robins, Nina Lane and later with David Onion and Nicola Croxall have stimulated me to learn and embrace flow cytometry and have facilitated the creation of the co-culture model. None of the co-culture work would have been possible without their help. Similarly, I am grateful to Tim Self for his counsel and support with the multiphoton experiments.

I would also like to thank my colleagues in the lab. Anita Sukmawati, Yasmin Abo-Zeid and Robbie Mackenzie for their help with the initial studies on poly(glycerol adipate). Weina Meng and Sanyogitta Puri for the discussions on nanoparticle production and assessment. Karen Beech, Jamie Patient and Adam Taylor for organising the initial ImageJ workshop that got me started on the platform. Vanessa Loczenski Rose, Nora Francini, Fabio Simoes and the postdocs in B15 for helping me with interpreting NMRs and polymer synthesis. Kuldeep Bansal and Lee Moir for lending me their polymers to test in my nanoparticle screen. Everyone in D16 and B15 who has helped me in my quests for reagents, labware and chemistry insight.

My appreciation goes to the researchers from the Children's Brain Tumour Research Centre for motivating me to continue the project, supporting me to go to ISPNO in Singapore and advising me on the molecular and clinical aspects of medulloblastoma. Special thanks to Lisethe Meijer, Lisa Storer, Ruman Rahman, Ramadhan Othman, Durga Sabnis, Aishah Nazir, Toby Gould and Beth Coyle.

I grateful to my friends, back home and here, as well as my family for helping me keep my sanity over those hectic years. Notably, Davide for our escapist tastings with the wine society, Rosanna for the best tiramisu in the world and both of them for the love of art, nature and all that is good in life. I thank my parents for igniting my initial spark of curiosity and the encouragement to go after science. My mother-in-law for her support and coping with her daughter being so far away.

Most importantly, I am grateful to my wife Nelly for believing in me, inspiring me for life and emboldening me to pursue a career in cancer research abroad. I thank her for the sacrifices she has made, for waiting for me to return from the lab after late experiments and nurturing me through the write-up. Last but not least, I thank her for her smile, which makes me meet every sunrise galvanised and ready for adventures.

List of publications

1. Papers

D. P. Ivanov, T. L. Parker, D. A. Walker, C. Alexander, M. B. Ashford, P. R. Gellert, and M. C. Garnett, "Multiplexing Spheroid Volume, Resazurin and Acid Phosphatase Viability Assays for High-Throughput Screening of Tumour Spheroids and Stem Cell Neurospheres," *PLoS One*, vol. 9, no. 8, p. e103817, Aug. 2014

D. P. Ivanov, T. L. Parker, D. A. Walker, C. Alexander, M. B. Ashford, P. R. Gellert, and M. C. Garnett, "In vitro co-culture model of medulloblastoma and human neural stem cells for drug delivery assessment", *Journal of Biotechnology*, Jan. 2015

2. Conference abstracts – oral presentations

3D Cell Culture 2014 - Freiburg, Germany. Multiplexing resazurin reduction, spheroid volume and acid phosphatase activity for spheroid viability in high-throughput

3. Posters

European Society of Toxicology *In Vitro*, The Netherlands, 2014. Co-culture model of human neural stem cells and brain tumour cells for *in vitro* assessment of therapeutic safety and efficacy

International Symposium on Paediatric Neuro-Oncology (ISPNO), Singapore, 2014. 3D co-culture model of medulloblastoma and human foetal neural stem cells for preclinical assessment in drug delivery

9th World Congress on Alternatives and Animal Use in the Life Sciences, Prague, 2014. Offbeat to mainstream: high-throughput, user-friendly three-dimensional cell culture models of brain tumours

Table of Contents

Abstract	ii
Acknowledgements	iii
List of publications	v
List of Figures:	xi
List of tables:	xvii
Abbreviations:	xix
Chapter 1. Introduction	1
Section 1.1 Medulloblastoma	1
1.1.1 Medulloblastoma overview	1
1.1.2 Biological basis of medulloblastoma subtypes	6
1.1.3 Treatment modalities	10
Section 1.2 Local therapy	24
1.2.1 The rationale for local therapy	24
1.2.2 Types of local therapy	24
Section 1.3 Project overview and aims	31
1.3.1 Postsurgical NP delivery- project aim	31
1.3.2 Project rationale	32
1.3.3 <i>In vitro</i> model requirements	36
1.3.4 Project plan- objectives	42
Chapter 2. Experimental materials and methods	44
Section 2.1 Materials	44
2.1.1 Cell culture	44
2.1.2 Polymer synthesis and nanoparticle studies	44
Section 2.2 Cell culture	45
2.2.1 Human neurospheres (neural stem/progenitor) cells	45
2.2.2 Neurosphere propagation	45
2.2.3 Culture of human medulloblastoma cell lines	46
2.2.4 Mycoplasma testing	46

2.2.5	Cell line authentication	46
Section 2.3	Methods for spheroid production	47
2.3.1	Non-adherent cell culture flasks.....	47
2.3.2	3D Biomatrix hanging drop plates	47
2.3.3	3D microtissues agar moulds.....	48
2.3.4	Ultra-low attachment plates	49
Section 2.4	Tissue processing	49
Section 2.5	Spheroid viability assessment	50
2.5.1	Spheroid volume determination – microscopy and image- analysis	50
2.5.2	Resazurin (Alamar Blue) assay	50
2.5.3	Acid phosphatase assay	51
2.5.4	Cell number determination	51
Section 2.6	Marking cells with tracer dyes	52
Section 2.7	Co-culture of human foetal neurospheres and tumours ..	53
Section 2.8	Poly (glycerol adipate) synthesis and substitution.....	54
2.8.1	Backbone synthesis.....	54
2.8.2	Polymer characterisation.....	55
2.8.3	Acylation with C8 and C18	56
Section 2.9	Nanoparticle preparation and characterisation.....	57
2.9.1	Nanoprecipitation.....	57
2.9.2	Emulsification-solvent evaporation	58
2.9.3	Separation of free drug from nanoparticles.....	58
2.9.4	DLS and Zeta potential	59
Section 2.10	Flow cytometry	61
Section 2.11	Confocal and multiphoton microscopy	67
Chapter 3.	3-D monocultures of foetal neurospheres and medulloblastoma cell lines	69
Section 3.1	Introduction.....	69

Section 3.2	Materials and methods.....	71
3.2.1	Cell lines and culture.....	71
3.2.2	Doubling time determination for UW228-3 cells in monolayer	72
3.2.3	Monolayer sensitivity to etoposide	72
3.2.4	Spheroid production using the 3D Biomatrix platform.....	72
3.2.5	Production of spheroids using 3D Microtissues® agar moulds.	73
3.2.6	Tissue processing for histology and Haematoxylin and eosin staining	73
3.2.7	Spheroid production in ultra-low attachment plates.....	73
3.2.8	Phase microscopy and image analysis	73
3.2.9	Growth kinetics	73
3.2.10	Cytotoxicity experiments.....	73
3.2.11	Resazurin, Acid phosphatase and Cell counting	74
3.2.12	Assay Validation	74
3.2.13	Data analysis.....	75
Section 3.3	Monolayer experiments in UW228-3	76
Section 3.4	Initial search for a suitable 3D cell culture growth platform	77
3.4.1	Non-adherent cell culture flasks.....	77
3.4.1	3D Microtissues® agar moulds:	77
3.4.2	3D Biomatrix hanging drop plates	79
3.4.3	Ultra-low attachment plates	82
Section 3.5	Assay validation in healthy spheroids.....	85
Section 3.6	Assay validation in spheroids treated with etoposide.....	91
Section 3.7	Conclusions	104
Chapter 4.	Co-culture model of medulloblastoma	108
Section 4.1	Introduction	108
Section 4.2	Materials and methods.....	111
4.2.1	Materials:	111

4.2.2	Cell lines and culture	111
4.2.3	Cell label optimisation experiments	111
4.2.4	Co-culture formation	111
4.2.5	Spheroid viability monitoring	112
4.2.6	Multiphoton confocal microscopy.....	112
4.2.7	Cytotoxicity screen.....	112
4.2.8	Flow-cytometry	112
4.2.9	Imaging flow cytometry	115
4.2.10	Data analysis and statistics:	115
Section 4.3	Stain selection considerations and experiments.....	115
Section 4.4	Preliminary experiments with etoposide	126
Section 4.5	Marking normal brain cells and UW-228-3 with CDCFDASE and CellTrace Violet	128
Section 4.6	Analysing the effects of etoposide	132
Section 4.7	Discussion and conclusions.....	142
Chapter 5.	Etoposide loaded Poly (glycerol adipate) nanoparticles ..	145
Section 5.1	Introduction.....	145
Section 5.2	Chapter methods.....	146
5.2.1	Synthesis of poly(glycerol adipate) PGA:.....	146
5.2.2	Analysis of polymer.....	146
5.2.3	Acylation of poly(glycerol adipate):	146
5.2.4	Production of nanoparticles via nanoprecipitation	146
5.2.5	Imaging the interaction of fluorescent nanoparticles and medulloblastoma cells	147
5.2.6	Etoposide-loaded nanoparticles: drug loading determination	148
Section 5.3	Polymer synthesis and characterisation	148
5.3.1	Synthesis of polymer backbone	148
5.3.2	Substitution	150
Section 5.4	Nanoparticle preparation and optimisation.....	154

5.4.1	RBITC loaded nanoparticles- size, zeta potential, confocal with spheroids.....	154
5.4.2	Etoposide loaded nanoparticles- size, zeta potential, loading, stability	159
Chapter 6.	Screening and evaluation of a nanoparticle library.....	162
Section 6.1	Review of etoposide and teniposide submicron delivery systems	162
Section 6.2	Nanoparticle screening strategy	175
Section 6.3	Materials and methods.....	178
6.3.1	Materials.....	178
6.3.2	Polymer characterisation.....	179
6.3.3	Nanoparticle preparation	179
6.3.4	Separation of nanoparticles and free drug.....	180
6.3.5	Size and zeta potential characterisation	180
6.3.6	Drug loading	181
6.3.7	Drug release	181
6.3.8	Cell culture	184
6.3.9	Data analysis	184
Section 6.4	Polymer characteristics:	185
Section 6.5	Drug loading results	186
Section 6.6	Release experiments.....	196
Section 6.7	Nanoparticles in single spheroid cultures of foetal neurospheres and UW medulloblastoma	206
Chapter 7.	Summary, conclusions and future work.....	215
	Supporting information.....	222
	References.....	224

List of Figures:

Figure 1-1. Mid-sagittal (side) view of the human brain	2
Figure 1-2. MRI Image showing medulloblastoma with CSF flow obstruction	3
Figure 1-3. Histopathological types of medulloblastoma.....	5
Figure 1-4. The four molecular subgroups of medulloblastoma	7
Figure 1-5. Incidence and most common mutations in patients with SHH medulloblastoma	8
Figure 1-6 Energy dissipation of protons and photon radiation in tissues	14
Figure 1-7 Isodose distribution in the sagittal projection along the spinal column for (a) X-rays, (b) IMRT, and (c) protons. Adapted from [60] with permission from Elsevier.	15
Figure 1-8. Metabolism and activation of cyclophosphamide.....	20
Figure 1-9. Postsurgical local nanoparticle delivery	31
Figure 2-1. Schematic representation of the 3D Biomatrix system.	47
Figure 2-2 Dispensing cell suspension in order to form hanging drops	48
Figure 2-3 The 3-D petri dish plastic mould.....	48
Figure 2-4 Cell labelling strategy for tumour monolayers and foetal neurospheres	52
Figure 2-5 The synthesis of poly(glycerol adipate)	54
Figure 2-6. Substitution of the pendant hydroxyl groups in poly(glycerol adipate).....	56
Figure 2-7. The nanoprecipitation method for nanoparticle production	57
Figure 2-8 Solvent-emulsification method for nanoparticle production. ...	58
Figure 2-9. Schematic representation of gel-permeation chromatography	59
Figure 2-10. Histogram plots of fluorescence intensity for two cell samples	62
Figure 2-11. Overlaid histograms of non-marked cells and marked cells in the same plot.....	63
Figure 2-12. Dot plots in flow cytometry	64
Figure 2-13. Regions and Gating in flow cytometry	65
Figure 2-14. Compensation in flow cytometry	66
Figure 2-15. Jablonski diagrams comparing one-photon fluorescence and two-photon fluorescence	68

Figure 3-1. Etoposide dose-response curve for exponentially growing UW228-3 medulloblastoma cells in monolayer.....	76
Figure 3-2 Phase microscope image of normal neurospheres cultured in serum-free media in non-adherent flasks. Foetal	77
Figure 3-3. Spheroids in the 3D microtissues micromoulds.	78
Figure 3-4. Phase-contrast images of the spheroids produced by VCR cells using two sizes of the 3D Petri Dish-	78
Figure 3-5 Phase-contrast images of DAOY spheroids formed in hanging drops after 48h of culturing in hanging drops at different seeding cell densities.	79
Figure 3-6 Microscope phase-contrast images of spheroids formed in hanging drops by the VCR cell line at two different concentrations.....	79
Figure 3-7 H&E stained sections of spheroids formed by VCR cells after 4 days of culture in hanging drop plates.....	80
Figure 3-8 Phase-contrast microscope photo of foetal neurospheres seeded in the hanging drop plate.	81
Figure 3-9. Growth curves for spheroids.....	84
Figure 3-10. Volume, resazurin and acid phosphatase as methods to determine viability in NSC and UW228-3 spheroids.....	86
Figure 3-11 Assay characterisation using Z-factors, Signal Window (SW) and Coefficient of variation (CV) for UW228-3 cells.....	89
Figure 3-12. Assay characterisation using Z-factors, Signal Window (SW) and Coefficient of variation (CV) for NSCs.....	90
Figure 3-13 Plate uniformity assessment for volume and diameter of spheroids before and after outlier removal.....	91
Figure 3-14 . Dose-response curves for UW228-3 (5000cells/well) and NSCs (10000cells/well) spheroids exposed to increasing concentrations of etoposide.	93
Figure 3-15 Phase-contrast image of a representative plate of UW spheroids treated with etoposide. Each column represents 6 replicate spheroids at the same condition. Left to right untreated control, and half-decimal-log concentrations of etoposide 0.03-300µM.	94
Figure 3-16. Phase-contrast microscope image of UW228-3 spheroids exposed to increasing concentrations of etoposide.....	95
Figure 3-17 Phase-contrast image of a representative plate of NSC spheroids treated with etoposide. Each column includes 6 replicate	

spheroids at the same condition. Left to right untreated control, and half-decimal-log concentrations of etoposide 0.03-300 μ M.	96
Figure 3-18 Confidence intervals for etoposide IC50 determinations for different assays in UW228-3 cells.	98
Figure 3-19. Methods of combining different IC50 determinations between experiments for UW228-3 cells.....	99
Figure 3-20. Confidence intervals for etoposide IC50 determinations for resazurin and Volume in neural stem cells.	100
Figure 3-21. Z-factors in cytotoxicity tests for Volume.....	101
Figure 3-22 Coefficient of variation for different assays of etoposide treated plates.....	102
Figure 3-23. Phase-contrast microscope images of NSC exposed to increasing concentrations of etoposide.	103
Figure 4-1. MoFlo laser and filter setup	114
Figure 4-2. Histogram plots of control (blue) and CDCFDA SE (5 μ M) stained normal brain cells NSCs (red) before and after 35% software compensation in the CM-DiI channel.	119
Figure 4-3 Dot plots and histograms of control and CM-DiI (5 μ M) dyed samples of tumour VCR cells	120
Figure 4-4. Flow cytometry dot plots of VCR cells stained with CDCFDASE or CellTrace Violet	123
Figure 4-5. Flow cytometry dot plots showing the compatibility of cell labelling and health status determination for VCR cells	124
Figure 4-6. Dot plots showing the analysis of a mixture containing VCR cells marked with CDCFDASE and CellTrace Violet	125
Figure 4-7 Flow cytometry analysis of monolayers and spheroids of non-stained VCR cells exposed to etoposide for 24h	126
Figure 4-8. Histograms of the frequency distributions of long-term fluorescent labelling for UW and NSC cells labelled with CellTrace Violet and CDCFDASE	129
Figure 4-9. Two dimensional dot plots showing single and mixed populations of UW and NSC cells marked with both dyes	131
Figure 4-10. Volume and metabolic activity of spheroids marked with the supravital dyes compared to unstained controls	132
Figure 4-11. Medulloblastoma in vitro model experimental setup.	133
Figure 4-12. Medulloblastoma co-culture model analysis.....	135

Figure 4-13 . Dot plots showing compatibility of cell labelling and determination of health status	136
Figure 4-14 Co-cultures exposed to different levels of etoposide.....	137
Figure 4-15. Dot plots showing the change of viability after etoposide treatment.....	139
Figure 4-16 Percentage of apoptotic and dead cells in the UW228-3 tumour and neural progenitor populations after treatment with etoposide.....	140
Figure 4-17 Dose-response data for co-cultures of neural stem cells and UW medulloblastoma cells exposed to etoposide	141
Figure 4-18 Imaging flow cytometry- representative examples of the different cell populations	141
Figure 5-1. GPC chromatogram of PGA polymer synthesized in house ...	149
Figure 5-2. NMR spectrum for non-functionalised poly (glycerol) adipate.	151
Figure 5-3 NMR spectrum for the C8 substituted PGA.....	152
Figure 5-4. NMR spectrum for C18-substituted polymer.....	153
Figure 5-5 Control images(x40) of a tumour VCR spheroid attached to a coated cover slip	156
Figure 5-6 Control image(x40) of a VCR monolayer without nanoparticles showing the cells which support the spheroids' attachment to the cover slip. Scale bar 50µm.	156
Figure 5-7. Confocal images(x40) of a VCR spheroid after 24h exposure to RBITC loaded nanoparticles	157
Figure 5-8 Confocal image(x63) of the monolayer of cells supporting the tumour spheroid after 24h nanoparticle exposure	157
Figure 5-9. Highlights from the confocal images of nanoparticles interacting with medulloblastoma spheroids and monolayers	158
Figure 5-10. Standard curve for etoposide determination using fluorescence spectrophotometry	160
Figure 5-11. Etoposide drug loading for nanoparticles made with C8 and C18-PGA	160
Figure 6-1. Chemical formulas of the parent drug podophyllotoxin and its semi-synthetic epipodophyllotoxin derivatives etoposide and teniposide.	163
Figure 6-2. Comparison of the two most common methods for nanoparticle preparation.....	176

Figure 6-3. Chemical structures of polymers used in the nanoparticle screen.....	185
Figure 6-4 Standard curves for teniposide and etoposide and spread of fluorescence values for encapsulated drug samples made using nanoprecipitation.....	187
Figure 6-5 Drug loading percentages for nanoparticles made using nanoprecipitation.....	188
Figure 6-6 Concentration of drug passing through a Sephadex GH25 column (PD-10) after the solvent emulsification method.....	190
Figure 6-7 Drug loading results for nanoparticles made with the solvent-emulsification method.....	191
Figure 6-8. Radii of empty and teniposide-loaded nanoparticles determined by DLS.....	193
Figure 6-9 TEM image of PLA-PEGMA nanoparticles.....	194
Figure 6-10. PLA-PEGMA nanoparticle size distribution after image analysis using TEM.....	195
Figure 6-11 TEM pictures of teniposide-loaded PLA-PEGMA nanoparticles	196
Figure 6-12 Teniposide stability in PBS immediately after dilution from DMSO stock and after 24h	197
Figure 6-13 Standard curves for teniposide in PBS and PBS with 1% cholate.....	198
Figure 6-14. Linearity of Teniposide determination using HPLC.....	199
Figure 6-15 Representative chromatograms of blank release media solution and teniposide standards.....	200
Figure 6-16 Teniposide HPLC assay robustness: Recovery of teniposide after freeze-thawing	201
Figure 6-17 Recovery of teniposide after passage through centrifugal ultrafiltrators.....	202
Figure 6-18 Quantitation of amount of PEG-PCL nanoparticles passing through the Nanosep 300kDa ultrafiltration device.....	202
Figure 6-19 Release from teniposide-loaded nanoparticles of PEG-PCL and PLA-PEGMA.....	205
Figure 6-20 Confidence intervals for the release half-time and time constant.....	205
Figure 6-21 In vitro toxicity of empty nanoparticle carrier formulations.....	207

Figure 6-22. Preliminary screen of teniposide-loaded nanoparticles using spheroid Volume reduction as surrogate measure of viability.	208
Figure 6-23. Preliminary screen of teniposide-loaded nanoparticles using resazurin reduction as surrogate measure of viability.	209
Figure 6-24 Dose-response comparison of teniposide versus teniposide-loaded PEG-PCL NPs	212
Figure 6-25 Dose-response comparison of teniposide versus teniposide-loaded PLA-PEGMA NPs	213

List of tables:

Table 1-1 Staging system for medulloblastoma	4
Table 1-2. Clinically used patient risk stratification for medulloblastoma .	10
Table 1-3. Proposed further patient risk stratification within medulloblastoma subgroups.....	10
Table 1-4. Summary of clinically relevant systemic and local chemotherapeutics used in medulloblastoma.....	23
Table 4-1. Excitation and emission maxima of the fluorescent labels employed in the experiments	114
Table 4-2. Dye combination and detection configuration used in the Flowsight imaging flow cytometer.....	115
Table 4-3. Optimisation of cell staining for VCR cells labelled as monolayer and cultured as spheroid in non-treated flasks	116
Table 4-4. Optimisation of cell staining for foetal neurospheres dyed as a single cell suspension and cultured as spheroids in non-treated flasks...	117
Table 4-5. Combination of dyes chosen for further development in labelling and analysing co-culture spheroids.	121
Table 4-6. Table summarising cell counts of VCR cells exposed to increasing concentrations of etoposide	127
Table 4-7. Marking UW-228 and NSC cells with supravital dyes CDCFDASE and CellTrace Violet	130
Table 5-1. Mean molecular weight determinations for five different batches of poly (glycerol adipate) determined by GPC.....	150
Table 5-2. Characterisation of RBITC-loaded fluorescent nanoparticles ..	154
Table 5-3 Fluorescent dyes used in confocal imaging experiments.	155
Table 5-4. Recovery of known amount of etoposide in nanoparticle samples	160
Table 5-5. Comparison of etoposide-loaded nanoparticles made with the 100%C8-PGA from the present study with historical data from Puri[180].	161
Table 6-1 Literature review of nanoparticle delivery systems using etoposide.	170
Table 6-2. Characteristics of polymers used in the screening program. Molecular weight was determined by NMR and is given in kilodaltons, kDa. Glass transition temperatures (T _g) and melting temperatures (T _m) were	

measure using DSC. The Lower critical solution temperature for the thermoresponsive (LCST) was only investigated in the PEGMA-based polymers.	186
Table 6-3 Concentrations used to form nanoemulsions and reported critical micelle concentration for the excipients used	190
Table 6-4 Median sizes of empty and drug-loaded nanoparticles.....	193
Table 6-5. Kinetic solubility of teniposide in different release media.	197
Table 6-6. Linear regression fit parameters for the standard curves from Figure 6.8.....	198
Table 6-7. Inter-assay precision for 6 levels of teniposide measured in six independent experiments	200
Table 6-8 Presence of nanoparticles in the filtrate of nanoparticle release samples after passing through Amicon 10 KDa filtration devices.....	203
Table 6-9. Teniposide release from PEG-PCL micelles as measured by Amicon 10kDa ultrafiltration devices 1h after start of experiment.	203
Table 6-10 Teniposide release from PEG-PCI micelles after correction for teniposide recovery	204

Abbreviations:

3D-CRT	Three-dimensional conformal radiation therapy
7-AAD	7-aminoactinomycin D
ALL	Acute lymphoblastic leukaemia
AMPK	5' adenosine monophosphate-activated protein kinase
Annexin-V-APC	Annexin V Allophycocyanin
APH	Acid phosphatase
ara-C	Cytosine arabinoside (cytarabine)
ATP	Adenosine triphosphate
BBB	Blood-brain barrier
BCG	Bacillus Calmette–Guérin
bFGF	Basic fibroblast growth factor
BMQC	2,3,6,7-tetrahydro-9-bromomethyl-1H,5H-quinolizino(9,1-gh)coumarin
C18	Stearoyl substituted
C8	Octanoyl substituted
CCG	Children with Cancer Group
CDCFDASE	5-(and-6)-carboxy-2'7'-dichlorofluorescein diacetate succinimidyl ester
CED	Convection enhanced delivery
CI	Confidence interval
CLSM	Confocal laser scanning microscopy
CM-DiI	Chloromethyl-1,1'-diiododecyl-3,3,3' tetramethylindocarbocyanine
CNS	Central Nervous System
CRT	Conformal radiation therapy
CSF	Cerebrospinal fluid
CSI	Craniospinal irradiation
CT	Computer tomography
CTNBB1	Beta catenin 1
CTV	CellTracker Violet
CV	Coefficient of variation
CYP2B	Cytochrome P450 2B
DAPI	4',6-diamidino-2-phenylindole
DCM	Dichloromethane
DEPG	Demethylepipodophyllotoxin benzylideneglucoside
DLS	Dynamic light scattering
DMEM	Dulbecco's Modified Eagle's Medium
DMSO	Dimethyl sulfoxide
DNA	Deoxyribonucleic acid
DVA	Divinyl adipate
ECM	Extracellular matrix
EGF	Epidermal growth factor
EMA	European Medicines Agency
EPR	Enhanced permeability and retention
EU	European Union
FBS	Foetal Bovine Serum
FCM	Full culture medium
FDA	Food and Drug Administration
GDC-0449	Vismodegib- Smoothened Inhibitor
GLI	Glioma-Associated Oncogene Homolog 1 (Zinc Finger Protein)
GLOBOCAN	Global Burden of Cancer Study
GPC	Gel permeation chromatography
Gy	Gray [J.kg ⁻¹]
HBSS	Hank's Balanced Salt Solution
HEPES	4-(2-hydroxyethyl)-1-piperazineethanesulfonic acid
HPLC	High performance liquid chromatography
IC50	50% Inhibitory concentration
ICH	International Conference on Harmonisation
IMRT	Intensity modulated radiation therapy
IQ	Intelligence quotient
LCA	Large cell/anaplastic medulloblastoma
LOD	Limit of detection
LOQ	Limit of quantitation
MBEN	Medulloblastoma with extensive nodularity
MGMT	06-methylguanine-methyltransferase
MRI	Magnetic resonance imaging
MRP	Multi drug-resistant protein
Mw	Molecular weight
MYC	Avian Myelocytomatosis Viral Oncogene
MYCN	Avian Myelocytomatosis Viral Oncogene Neuroblastoma Derived
NMR	Nuclear magnetic resonance
NP	Nanoparticle
NSC	Neural stem cell

PBS	Phosphate Buffered Saline
PCL-PEG	Poly(caprolactone)-PEG
PCL-PEGMA	Poly(caprolactone)-co-poly(ethyleneglycolmethacrylate)
PDL-PEG	Poly(decylactone)-PEG
PDMS	Polydimethylsiloxane
PEG	Polyethylene glycol
PEG-PGA	PEG-poly(glycerol adipate)
PFA	Paraformaldehyde,
PGA	Poly(glycerol adipate)
P-gp	P-glycoprotein pump
PI	Propidium iodide
PLA-PEGMA	Poly(lactic acid)-co-poly(ethyleneglycolmethacrylate)
PNPP	p-nitrophenylphosphate
PTCH1	Patched 1
PTFE	Poly(tetrafluoroethylene)
PVA	Poly(vinyl alcohol)
PVC	Poly(vinyl chloride)
RBITC	Rhodamine B isothiocyanate
RFU	Relative units of fluorescence
SHH	Sonic hedgehog
SIOP	International Society of Paediatric Oncology
SMO	Smoothed, Seven Transmembrane Spanning Receptor
SOBP	Spread-out Bragg Peak Profile
SPG	Benzaldehyde adduct of the non-purified extract of P.emodi
STR	Short tandem repeats
SUFU	Suppressor Of Fused protein
SVZ	Subventricular zone
SW	Signal window
TACE	Transcatheter arterial chemoembolization
THF	Tetrahydrofuran
TIT	Triple intrathecal therapy
TopoII	Topoisomerase II
TP53	Tumour protein 53
TPGS	Tocopherol polyethylene glycol 1000 succinate
UK	United Kingdom
ULA	Ultra-low attachment
US	United States
WHO	World Health Organisation
WNT	Wingless signalling pathway

Chapter 1. Introduction

Cancer is one of the leading causes of morbidity and mortality in children. The 2012 World Health Organisation (WHO) GLOBOCAN report estimates that each year 160, 000 children are diagnosed with cancer worldwide[1]. Of these approximately 30% are comprised of acute lymphoblastic leukaemia, closely followed by central nervous system (CNS) malignancies (25%)[1], [2]. The most common paediatric malignant brain tumour is medulloblastoma and the number of new cases totals more than 5000 children around the globe, with 500 in the US, 500 in the EU and 80-90 new patients per year in the UK[1]-[4].

Section 1.1 Medulloblastoma

1.1.1 Medulloblastoma overview

Medulloblastoma is an embryonal tumour of the cerebellum that has two peaks in incidence around the age of 4 and the age of 7, followed by a rapid decline in patients aged 20-30 years. It is referred to as a posterior fossa tumour since it occurs in the cerebellum which is situated in the posterior fossa of the brain (Figure 1-1). The posterior fossa is an intracranial cavity formed by the tentorium cerebelli and the foramen magnum which hosts the cerebellum, the brain stem and the fourth ventricle of the brain. The tentorium cerebelli is a fold of the dura matter which covers the cerebellum and divides it from the cerebrum. Tumours located below the tentorium, like medulloblastoma, are called infratentorial and are more common in childhood. In contrast, tumours located above the tentorium are supratentorial and are more prevalent in adults[5].

Patients usually present with a combination of headache, vomiting, nystagmus often accompanied with posture and balance abnormalities (broad stand, unsteady gait and tendency to fall backward). In advanced cases the tumour could obstruct normal CSF flow from the apertures of the fourth ventricle. The flow impediment usually leads to increased

intracranial pressure and hydrocephalus. The increase of pressure in the brain can cause neural damage and requires surgical intervention to redirect the flow of CSF via catheters (shunting). Upon MRI scan, medulloblastoma is seen as a posterior fossa mass in the cerebellum and the fourth ventricle (Figure 1-2).

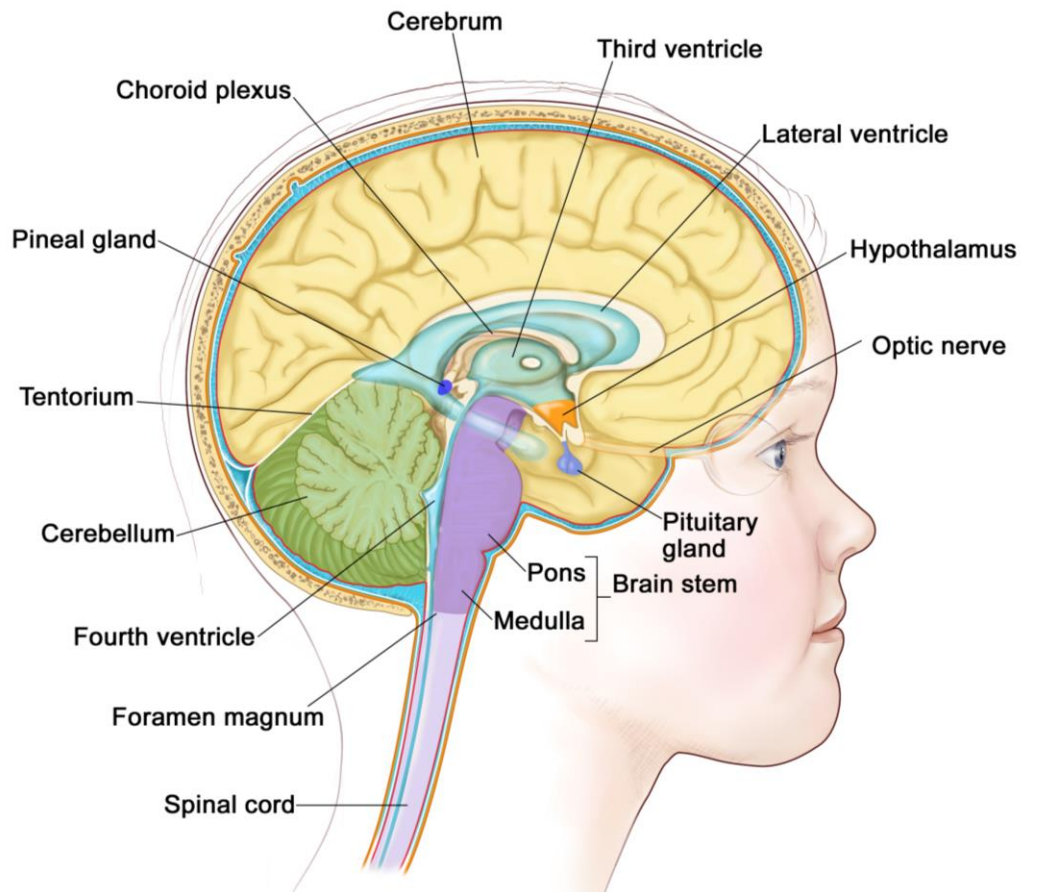


Figure 1-1. Mid-sagittal (side) view of the human brain. The tentorium cerebelli is a fold in the dura matter that splits the brain into a supra- and infratentorial part, above and below the tentorium respectively. Medulloblastoma arises infratentorially in the posterior fossa, usually affecting the cerebellum and the roof of the fourth ventricle. CSF flows from the lateral and third ventricle into the fourth ventricle through the cerebral aqueduct. From there the CSF bathes the subarachnoid space in the brain through the median and lateral apertures, it also drains into the central canal of the spinal cord. Image for the National Cancer Institute © (2010) Terese Winslow, U.S. Govt. has certain rights.

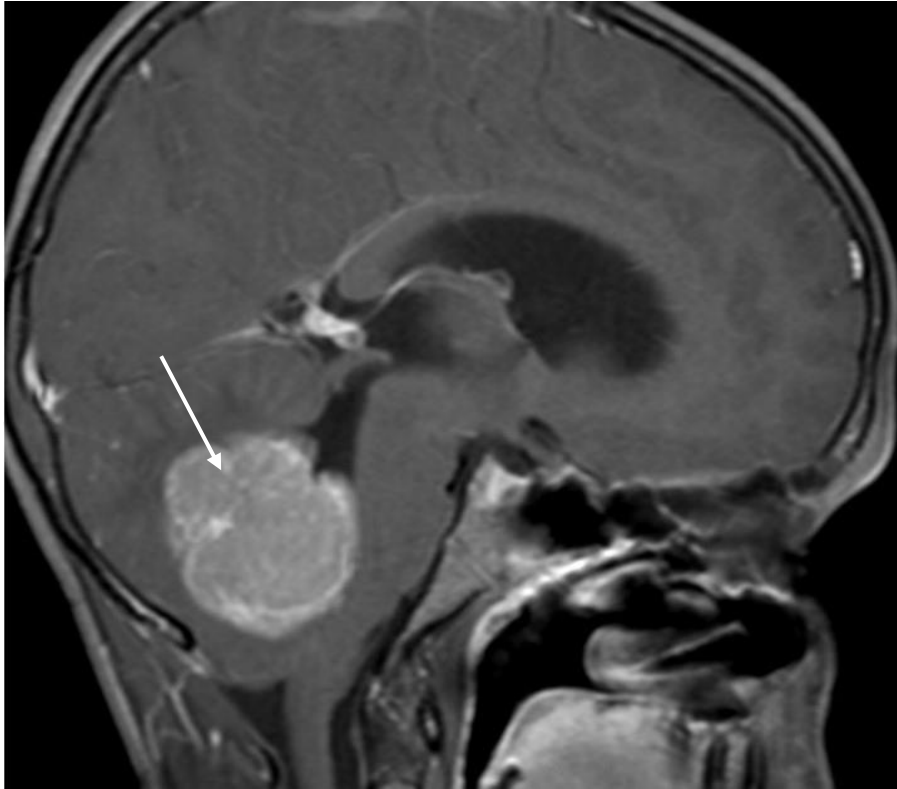


Figure 1-2. MRI Image showing medulloblastoma with CSF flow obstruction. A Gadolinium-based MRI contrast agent has been used to identify the tumour (white arrow). The blood vessels of tumours often have an incomplete basement membrane, permeable to the contrast agent[6]. Image from Radiopaedia.org, Dr Paresh K. Desai

The WHO classifies medulloblastoma as a grade IV tumour. It has been given the highest ranking based on its rapid division, propensity to invade the adjacent tissues and metastasize in over 30% of cases[7]. Medulloblastoma tumours most frequently develop in the median part of the cerebellum (vermis) or the roof of the fourth ventricle and proceed to invade the adjacent tissues. Nevertheless, a small percentage of medulloblastoma cases occur in adults, in whom tumours may develop in one of the cerebellar hemispheres. Chang et al[8] established a staging system based on tumour size, invasion of the neighbouring tissues and metastasis in 1969 (Table 1-1). The Chang staging system has been successfully applied for patient risk stratification and low T and M stages were found to be good prognostic factors for disease outcome[9]. The risk stratification system is later used to determine the intensity of therapy.

Stage	Definition
Tumour	
T ₁	Tumour ≤ 3cm in diameter and limited to the midline position in the vermis, roof of the fourth ventricle and (less frequently) to the cerebellar hemispheres
T ₂	Tumour ≥ 3cm in diameter, further invading one adjacent structure or partially filling the fourth ventricle
T ₃	Divided in to 3a and 3b
T _{3a}	Filling the fourth ventricle with extension into the aqueduct of Sylvius, foramen of Magendie or foramen of Luschka, thus producing marked internal hydrocephalus
T _{3b}	Tumour arising from the flow of the fourth ventricle of brain stem and filling the fourth ventricle
T ₄	Tumour further spreading through the aqueduct of Sylvius to involve third ventricle of midbrain or tumour extending to the upper cervical cord
Metastasis	
M ₀	No evidence of gross subarachnoid or haematogenous metastasis
M ₁	Microscopic tumour cells found in CSF
M ₂	Gross nodular seedlings demonstrated in cerebella, cerebral, subarachnoid space of ventricles
M ₃	Gross nodular seeding in the spinal subarachnoid space
M ₄	Extraneural metastasis

Table 1-1 Staging system for medulloblastoma proposed by Chang et al[8].

In current clinical practice full brain and spine MRIs are used to pinpoint tumour staging, while a CSF biopsy can be utilised to distinguish between M₀ and M₁ stage even before surgery, provided there is no CSF flow obstruction.

A definitive medulloblastoma diagnosis can be obtained upon histological examination of the tumour after surgery. Medulloblastoma is characterised by small, densely packed cells with prominent nuclei and a high number of mitotic and apoptotic cells in the tissue. According to the latest 2007 WHO classification[7] medulloblastoma is divided in four groups dependent on its histopathological features (Figure 1-3). Classical medulloblastoma (Figure 1-3A and A') accounts for three-quarters of cases and is characterised by sheets of poorly differentiated overlapping cells with big nuclei and small cytoplasmic fraction which can often arrange in rosettes or palisading structures[10].

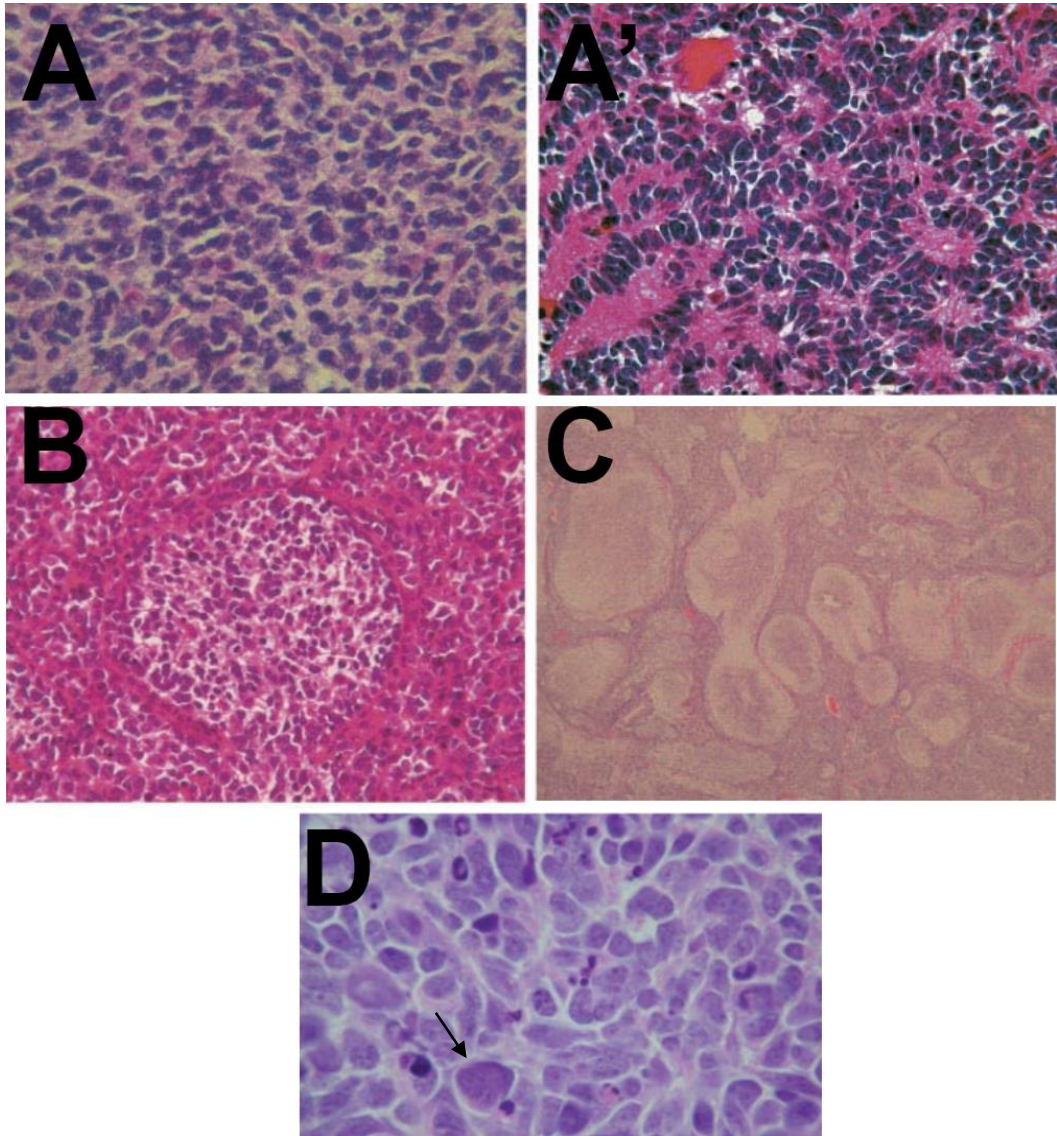


Figure 1-3. Histopathological types of medulloblastoma according to the 2007 WHO classification. A-classical medulloblastoma with sheets of undifferentiated small cells with high nuclear:cytoplasmic ratio; A'-classical medulloblastoma with characteristic Homer-Wright (neuroblastic) rosettes; B-desmoplastic medulloblastoma with nodules; C-medulloblastoma with extensive nodularity; D-large-cell anaplastic medulloblastoma with big nuclei and "cell wrapping" (black arrow). Images adapted from Ellison[11] with permission by Wiley.

Desmoplastic (nodular) medulloblastoma (Figure 1-3B) is found in 7% of cases and is characterised by a biphasic distribution of cells in nodules and nodule-free regions, differentiated by reticulin staining. Desmoplastic medulloblastoma can exhibit different degrees of nodularity and is often associated with neural lineage differentiation in the nodules and more rarely, astrocytic differentiation in the internodular regions. The MBEN (Figure 1-3C- medulloblastoma with extensive nodularity) type is considered to be an extreme form of the nodular medulloblastoma, it is

relatively rare (3% of cases) and is associated with infants in whom it usually carries a good prognosis. In contrast, the combined category of large cell/anaplastic medulloblastoma (Figure 1-3D) is more common (10-22%) and indicates high risk patients independent of metastatic status[12]. It is characterised with abundance of larger cells, polymorphic nuclei and high mitotic index.

Despite offering some predictive potential in cases of large-cell/anaplastic and MBEN disease, the histopathological classification fails to stratify more than 70% of patients who present with classical medulloblastoma. In this regard, novel insights into the molecular biology of medulloblastoma allow for more precise patient risk stratification and provide important clues for improved treatment.

1.1.2 Biological basis of medulloblastoma subtypes

The extensive studies on the medulloblastoma genome in the first decade of the 21st century and broad international collaboration led to the publication of a scientific consensus paper in 2012 indicating that medulloblastoma is comprised of at least four main molecularly distinct subgroups[13]. The subgroups differ in the activation of core biological pathways, their clinical presentation and the therapy outcome (Figure 1-4).

The WNT subgroup is found in 10% of medulloblastoma cases and currently has the best prognosis with over 95% progression-free survival[14]. It is named after the disturbed canonical WNT pathway and is associated with classical histology, mutations in exon 3 of CTNBB1, nuclear expression of β -catenin and monosomy 6 (loss of chromosome 6). Recent studies have reported that patients with WNT driven medulloblastoma have leaky blood vessels lacking the markers associated with an intact blood-brain barrier[15]. This could possibly explain the increased chemosensitivity of those tumours and the favourable prognosis for patients.

Introduction

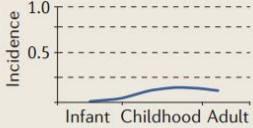
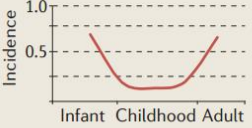
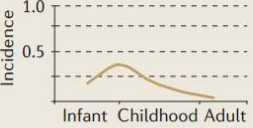
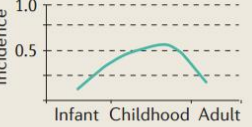
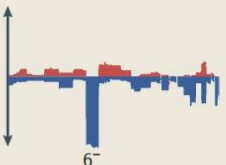
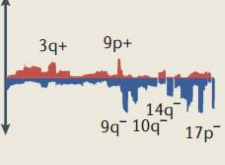
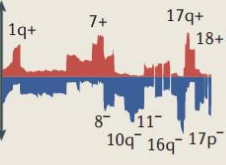
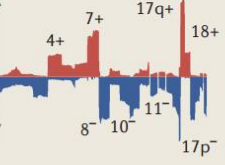
	WNT (~10%)	SHH (~30%)	Group 3 (~25%)	Group 4 (~35%)
Gender ratio (M/F)	~1/1	~1.5/1	~2/1	~3/1
Age distribution				
Histology	Classic; very rare LCA	Classic > desmoplastic/nodular > LCA > MBEN	Classic > LCA	Classic; rarely LCA
Metastasis at diagnosis	~5–10%	~15–20%	~40–45%	~35–40%
Overall survival (5 years)	~95%	~75%	~50%	~75%
Proposed cell of origin	Lower rhombic lip progenitor cells	CGNPs of the EGL and cochlear nucleus; neural stem cells of the SVZ	Prominin 1 ⁺ , lineage ⁻ neural stem cells; CGNPs of the EGL	Unknown
Genomic features				
Cytogenetics				
Driver genes [†]	<ul style="list-style-type: none"> • CTNNB1 (90.6%) • DDX3X (50%) • SMARCA4 (26.3%) • MLL2 (12.5%) • TP53 (12.5%) 	<ul style="list-style-type: none"> • PTCH1 (28%) • TP53 (13.6%) • MLL2 (12.9%) • DDX3X (11.7%) • MYCN (8.2%) • BCOR (8%) • LDB1 (6.9%) • TCF4 (5.5%) • GLI2 (5.2%) 	<ul style="list-style-type: none"> • MYC (16.7%) • PVT1 (11.9%) • SMARCA4 (10.5%) • OTX2 (7.7%) • CTDNEP1 (4.6%) • LRP1B (4.6%) • MLL2 (4%) 	<ul style="list-style-type: none"> • KDM6A (13%) • SNCAIP (10.4%) • MYCN (6.3%) • MLL3 (5.3%) • CDK6 (4.7%) • ZMYM3 (3.7%)
Expression signature	WNT signalling	SHH signalling	<ul style="list-style-type: none"> • MYC signature • Retinal signature 	Neuronal signature

Figure 1-4. The four molecular subgroups of medulloblastoma- cytogenetic profile, demographic and clinical features summary. CDK6, cyclin-dependent kinase 6; CGNPs, cerebellar granule neuron precursors; CTDNEP1, CTD nuclear envelope phosphatase 1; CTNNB1, β -catenin; EGL, external granule cell layer; GLI2, GLI family zinc finger 2; KDM6A, lysine-specific demethylase 6A; LCA, large cell and anaplastic; LDB1, LIM domain binding 1; LRP1B, low density lipoprotein receptor-related protein 1B; MBEN, medulloblastoma with extensive nodularity; MLL, mixed lineage leukaemia; OTX2, orthodenticle homeobox 2; PTCH1, patched 1; SCNA, somatic copy number aberration; SHH, sonic hedgehog; SNCAIP, α -synuclein interacting protein; SPTB, spectrin- β erythrocytic; SVZ, subventricular zone; TCF4, transcription factor 4; TNXB, tenascin XB. Adapted from [16] with permission by Macmillan publishers.

The SHH (sonic hedgehog) pathway is disturbed in 30% of patients and the group combines a very heterogeneous set of patients. Sonic hedgehog binds to Patched (PTCH1) receptors on the cell membrane which activates the signal mediator Smoothed (SMO). In turn SMO activates glioma associated oncogene (GLI) transcription factors which translocate to the nucleus and activate gene expression. GLI factors can be transported out of the nucleus by Suppressor of fused (SUFU) which inhibits the SHH pathway. The SHH pathway is essential in neurogenesis and the formation of many organs during development. Patients with medulloblastoma can have mutations in PTCH1, SMO, SUFU, GLI1, GLI2 leading to the heterogeneity of disease presentation, response to therapy and outcome for patients[17].

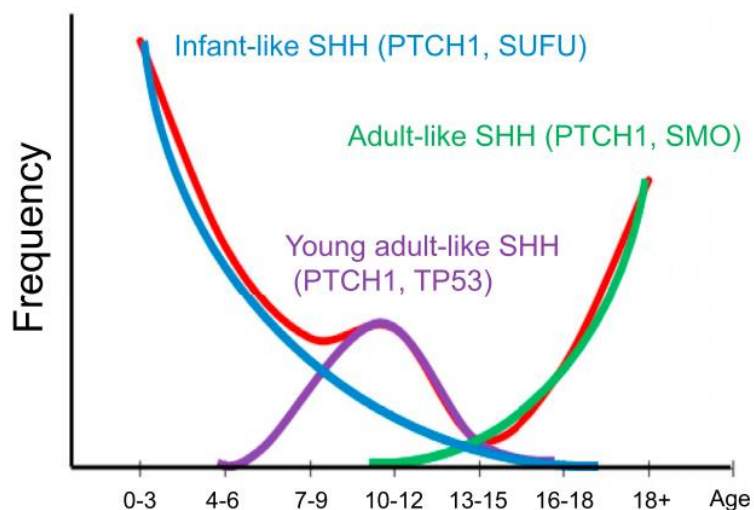


Figure 1-5. Incidence and most common mutations in patients with SHH medulloblastoma dependent on age. Red line shows the distribution for all cases. Infants with PTCH1 and SUFU mutations are shown by the blue line; children with PTCH1 and TP53 mutations are plotted with the purple line and adult cases with PTCH1 and SMO mutations (green line). Adapted from [17] with permission by Elsevier.

Initial studies with SMO inhibitors have highlighted the limitations of targeting a single player in the SHH pathway. The drug GDC-0449 (Vismodegib) was used to block SMO in patients with constantly activated PTCH1. Despite the initial rapid and significant response, the tumours returned within months[18]. This shortcoming combined with the possible effects on bone growth[19] may limit the usefulness of SMO inhibitors in patients with mutations downstream of the target.

Treatment of children (4-15 years old) with SHH mutations poses additional difficulties because patients often exhibit mutations in TP53 (Li-Fraumeni syndrome)[20]. Since TP53 is responsible for DNA repair and initiation of apoptosis upon identification of DNA damage, those patients are especially susceptible to secondary malignancies and should be spared from radiotherapy and alkylating chemotherapy[21].

Other factors that may place patients from the SHH group into a high-risk category include GLI2 amplification and 14q chromosome loss[22]. The advances made in the molecular biology of the SHH group are bound to bear fruit and careful patient characterisation along with multimodal therapies would be the key in improving survival for this group of patients. For example, the tumours in this group have been shown to recur mostly locally making them candidates for local therapy approaches, increased tumour bed irradiation and aggressive surgery[23].

Group 3 encompasses around 25% of medulloblastoma patients, it is often driven by MYC amplifications and carries the worst outcome for patients with around 50% survival. The presence of large cell anaplastic morphology, isochromosome 17 or MYC amplifications are all thought to confer a higher risk to patients. The tumours in this group often recur in the pia and arachnoid mater leading to leptomeningeal metastasis. In this regard, CSF prophylaxis in the form of intra-CSF chemotherapy may be a promising treatment to reduce mortality.

Group 4 is the most common group (35% patients) with classical histological features, frequent incidence of isochromosome 17q and intermediate survival. Chromosome 11 loss or chromosome 17 gain were found to carry a good prognosis within this Group, while M_1 status was found to determine high-risk patients. Apart from these considerations and the characteristic MYCN amplifications this continues to be the least biologically understood group of medulloblastoma.

The utility of the biological classification of medulloblastoma lies in the improvement of patient stratification and the possibility to tailor

treatment based on subgroup, risk of relapse and signal transduction mechanisms (Table 1-2 and Table 1-3).

	Low risk	Standard risk	High-risk (any trait)
Age	>7	3-7	<3
M-status	M ₀	M ₀	M ₁₋₄
Resection degree	<1.5cm ²	<1.5cm ²	>1.5cm ²
Histopathology	β-catenin nuclear staining	Classic <3years and MBEN	Large-cell/anaplastic
Subgroup	WNT- CTNNB1(exon 3)		MYC/MYCN, amplification GLI2 amplification
Therapy	Reduced	Standard	Aggressive/ Novel treatments
Survival	>90%	70-80%	30-60%

Table 1-2. Clinically used patient risk stratification for medulloblastoma. Adapted from [6]. M-status is determined from cytological examination of the CSF and preoperative MRI. MBEN-medulloblastoma with extensive nodularity. WNT-signalling pathways is most reliably diagnosed through direct sequencing of β-catenin 1 (CTNNB1). MYC v-myc avian myelocytomatosis viral oncogene homolog, MYCN is the neuroblastoma derived homolog of MYC. Any single feature of the high risk group is enough to stratify a patient as high-risk

	Low Risk	Standard Risk	High-risk
WNT	M ₀ , Non LC/A	M+, LC/A	N/A
SHH	M ₀ , non GLI2 Non Chr14q loss	M ₀ and either GLI2 ampl Or 14 loss	M+ TP53- GLI2 amplification 14q loss
Group 3	N/A	M ₀ , non LC/A non-MYC/MYCN non iso17q	M+ LC/A Iso17q
Group 4	Either Chr11 loss Chr17 gain M ₀	Neither Chr 11 loss ,nor Chr 17 gain ;M ₀	M+

Table 1-3. Proposed further patient risk stratification within medulloblastoma subgroups as reported by [22] and [21]. LC/A-large cell anaplastic; GLI- glioma associate oncogene, TP53-tumour protein 53 (Li-Fraumeni syndrome)

1.1.3 Treatment modalities

In the beginning of the 20th century, when medulloblastoma was first described by Wright [24] and later classified and treated by Cushing and Bailey [25], the disease carried a poor prognosis with survival measured in months and high percentage of operative mortality. The combination of surgery and radiotherapy in the middle of the century led to five-year survival rates of 40% [26]. The currently reported five year survival figures are between 50% (for high risk patients) up to 90% (low risk patients) and have been achieved through a combination of surgery, radiotherapy and chemotherapy [6]. While each modality is essential for prolonging patient survival, cure often comes at the expense of a multitude of side effects.

1.1.3.1 Surgery

Surgical removal of the tumour has been the mainstay of treatment since the initial work of Bailey and Cushing[25]. It serves to provide tissue for diagnosis, relieve the blocked CSF flow (through shunting) and reduce tumour burden to numbers low enough for radio- and chemotherapy to control[6]. Complete surgical resection along with the patient's metastatic index have been the most robust predictors of disease outcome[27]. The goal has been set to less than 1.5cm² of residual tumour burden as determined by a postoperative MRI[9]. Despite the good prognosis associated with radical resections, nearly a quarter of patients are at risk of developing cerebellar mutism[28]. Cerebellar mutism, also known as "posterior fossa syndrome", appears within a few days of surgery and manifests with transient mutism, ataxia, hypotonia and emotional lability. While most symptoms subside within 4 weeks, speech impediments may persist for over a year and cognitive development may be impaired in the long term[29]. Damage to the dentato-thalamo-cortical pathway has been implicated to result in posterior fossa syndrome and surgical techniques which avoid splitting the cerebellar vermis have been suggested to minimize cerebellar mutism[30].

1.1.3.2 Radiotherapy

The second pillar of medulloblastoma treatment is radiotherapy and improvements in the delivery of radiation have been instrumental in increasing patient survival throughout the last century[31]. The essential role of radiotherapy is attributable to the radiosensitivity of medulloblastoma and its tendency to metastasize within the CNS. While patients in the 1940s received mostly local radiotherapy and survival rates were below 5%, the introduction of full craniospinal irradiation(CSI) in the 50s and 60s brought survival up to 40%[26], [32]. The general strategy in medulloblastoma radiotherapy has remained unchanged since then and includes full craniospinal irradiation supplemented with a local boost dose to the location of the tumour[33]. What has evolved is the greater appreciation of the adverse effects of radiotherapy and the

strategies to maximise the benefits of this treatment modality while keeping the risks low.

As soon as patients started surviving from medulloblastoma longer than a few months it became apparent that their cognitive development[34], growth[35] and endocrine functioning[36] were impaired and that survivors were developing secondary malignancies[37]. The initial optimism of the 1960s[26] was toned down by the end of the 20th century when the reduction of the quality of life of medulloblastoma survivors became widely recognised[38]–[43]. Progressive reduction of the patient's intelligence quotient (IQ) and deterioration in fine motor skills were set on a background of radiation related morbidity[44] and social isolation[45].

The serious late side effects of radiotherapy (sequelae) necessitated the development of strategies aimed at reducing the impact of CSI on the normal tissue by utilising increasingly smaller doses of radiation and minimising normal tissue damage. Radiotherapy is not recommended for children under 3 years due to unacceptable toxicity[46]. For older children reductions of the craniospinal dose from 36 Gy, to 24 Gy and eventually to 18 Gy are being explored as well as confining the traditional posterior fossa boost (total dose 50-55Gy) to the tumour bed only[47]. Regardless of CSI dose reduction a study by Gajjar et al[48] found 3-4 IQ points/year decrease in various domains for patients aged 3-7 years and 2 IQ points/year decrease for older patients. On the other hand, a recent study utilising reduced CSI (23.4Gy) comparing irradiation of the whole posterior fossa to focusing the boost solely on the tumour bed has shown less neurocognitive damage in the group receiving radiation to the tumour bed only[49].

Apart from radiotherapy dose reduction, refinements to the amount of radiation delivered to the normal tissue have been crucial in controlling adverse effects for patients. For instance, the introduction of conformal radiation allowed oncologists to use multiple beam paths to focus radiation at the posterior fossa thus limiting the exposure of vital tissues[6]. Three-dimensional conformal radiation (3D-CRT) requires

brain imaging from CT or MRI to build a three-dimensional model of the patient's brain. Afterwards multiple high energy x-ray beams are arranged so that they intersect at the tumour bed and posterior fossa while limiting exposure to the cochlea and hypothalamus[50]. An even more advanced modality is intensity modulated radiation therapy (IMRT) which uses more beams, achieves a more conformal dose and allows for sophisticated radiation dose shaping[51]. Nevertheless IMRT delivers a higher integral dose of radiation compared to 3D-CRT and while it can be set up to spare certain areas (the cochlea and optical nerves) it exposes others (like the temporal lobes) to additional radiation which may potentially contribute to cognitive decline[52]–[55].

Radiation exposure of a growing number of brain areas is increasingly recognised to significantly contribute to quality of life decrease. For this reason, specific dosing strategies are developed to minimize normal tissue exposure. For example, sparing the hippocampus is now thought to be essential in order to minimize IQ decline and memory impairments in patients[56]. The list of sites at risk from brain irradiation includes the eyes, SVZ (subventricular zone), cochlea, pituitary gland, parotids, optic nerves, brainstem, and the cerebrum. The organs at risk from irradiating the spine include the heart, lungs, liver, kidneys and gonads. Clearly the list is going to expand as more information on cognitive decline and secondary malignancies becomes available for survivors.

A promising strategy to decrease normal tissue exposure to ionising radiation is substituting x-ray photons with proton radiation (Figure 1-6). When high energy x-ray photons enter the tissue they deposit energy throughout their path. In reality the maximum energy release depth for 6 MV photons is 1.5cm. After the maximum, the energy of photons starts to decrease gradually as the x-rays pass through the tumour and exit the body. In contrast, protons, which have a positive charge and a defined mass, travel through the body depositing a small amount of radiation and release most of their energy at a defined position in a sharp peak, called the Bragg peak. When multiple proton beams are combined a spread-out Bragg peak profile (SOBP) is constructed. The advantage of protons is that

the dose can be focused on the tumour and unlike photons there is no exit dose through the normal tissues.

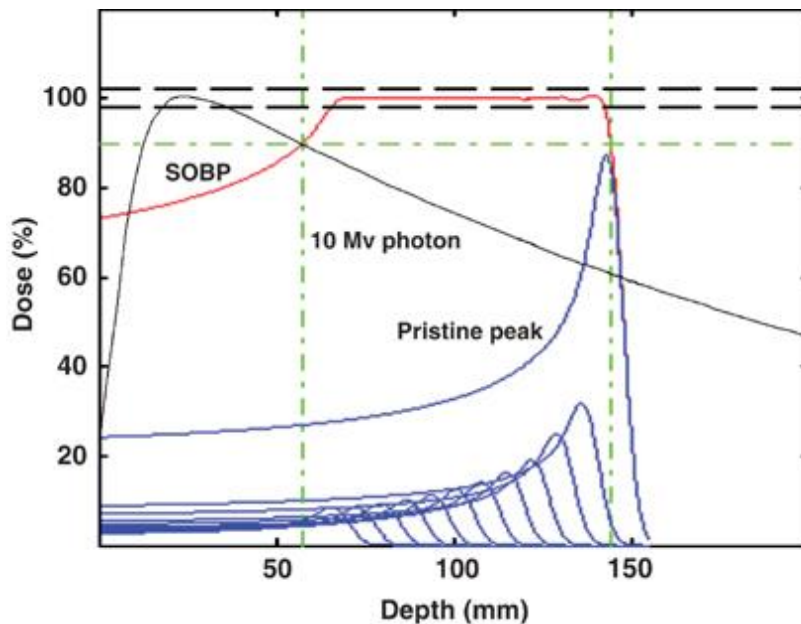


Figure 1-6 Energy dissipation of protons and photon radiation in tissues. The spread-out Bragg peak (SOBP, red), is made up of the sum of individual (pristine) proton Bragg peaks (blue). A conventional 10 MV photon beam is depicted in black. The dashed lines (black) indicate the clinical acceptable variation in the plateau dose of $\pm 2\%$. The dot-dashed lines (green) indicate the 90% dose and spatial, range and modulation width, intervals. The SOBP dose distribution of even a single field can provide complete target volume coverage in depth and lateral dimensions, in sharp contrast to a single photon dose distribution; only a composite set of photon fields can deliver a clinical target dose distribution. Note the absence of dose beyond the distal fall-off edge of the SOBP. Adapted from [57] with permission by Macmillan publishers.

The utility of protons in radiotherapy was initially recognised in 1946 by Robert Wilson[58] and despite the fact that the first patients were treated in 1954, the procedure only gained FDA approval in 1988. The theoretical benefit of using protons in medulloblastoma stems from the lack of exit dose, especially in preserving the cochlea and hippocampus of patients[56][59]–[61]. The argument for utilising protons for irradiating the spine is even stronger since that will potentially limit exposure of the lung, heart, kidneys and gonads of patients (Figure 1-7).

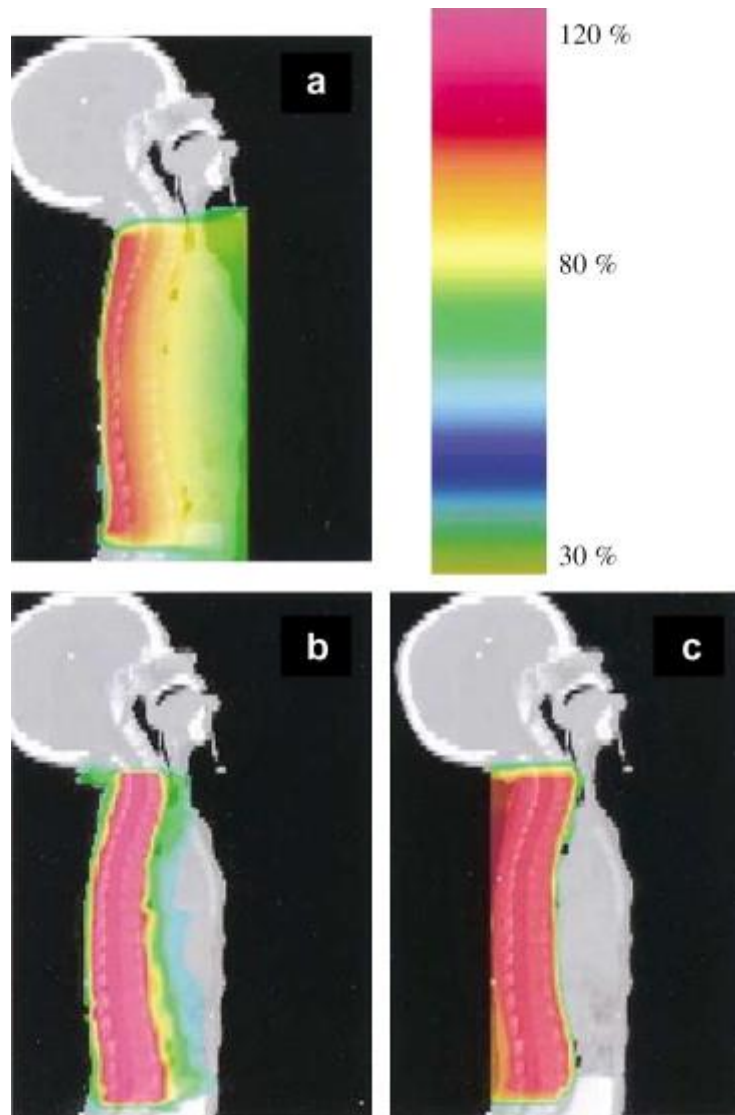


Figure 1-7 Isodose distribution in the sagittal projection along the spinal column for (a) X-rays, (b) IMRT, and (c) protons. Adapted from [60] with permission from Elsevier.

Although the hopes for proton therapy are still high[62], recent data has indicated increased risks of brain stem necrosis[63], [64] and 4-6 point/year IQ neurocognitive decline in patients treated with proton radiation[65]. The debate for the practical benefit of proton therapy is still ongoing[66], [67] and concerns have been raised regarding the risks of secondary malignancies due to neutron scattering[68], [69]. While the dose to distal structures is minimized with protons, the tumour bed and the neighbouring tissue still have to receive a substantial radiation dose. This is because the nature of craniospinal radiation postulates a certain dose (18-24 Gy, up to 36 Gy in high-risk patients) to the whole neuraxis in order to prevent recurrences. In this respect protons are merely a step forward in decreasing certain side effects but will largely exhibit the

plethora of off-target toxicity problems characterising ionising radiation in general.

Regardless of the type of radiation, irradiating the brain shows a dose-dependent decrease in cognitive functioning and academic achievement. The age of the patient and the distribution of radiation to the adjacent normal tissue are equally important to predict declines in the quality of survivorship[70]. In addition to efforts on refining radiotherapy, strategies to reduce the total dose of radiation should be actively pursued in order to improve the quality of life for patients.

1.1.3.3 Chemotherapy

In this regard, chemotherapy is the main modality that has the capability of reducing and partially replacing radiotherapy. Initial chemotherapy regimens struggled to achieve statistically significant benefit in patient survival compared to radiotherapy alone[71], [72]. In those first large studies improvement was only detected for high-risk patients with brain stem involvement, subtotal resection and metastasis. As a turning point, the premature termination of a study aiming to reduce radiotherapy and omit chemotherapy gave some clues that chemotherapy was indeed an essential modality[73].

Later, the SIOP III trial[74], employing etoposide among other chemotherapeutics, showed an improvement in progression free survival with combination therapy over radiotherapy alone. At the same time the CCG-9892[75] and CCG 921[9] studies reported 5-year survival rates above 80% and showed the feasibility of reducing craniospinal radiotherapy to 23.4 Gy for standard risk patients when cisplatin, vincristine and either lomustine or cyclophosphamide were combined. The following SIOP IV trail confirmed the high survival rates for average-risk patients but did not find any advantage of hyper-fractionating radiotherapy[76]. Despite the reassuring survival figures from the combination of chemotherapy and radiation, patients were experiencing increased risks of secondary malignancies[44] and decline in intellectual abilities and academic achievement[77]. The latest trials are building on the experience from the previous studies and will be exploring options to

further decrease radiotherapy (18Gy CSI dose) for standard-risk patients with the help of intensified chemotherapy combinations (ClinicalTrials.gov/NCT00085735).

In contrast to standard and low risk patients, who have a relatively good prognosis, survival for high-risk patients ranges from 30 to 60%[78]–[80]. The protocols for high-risk patients usually use high dose radiotherapy and aggressive chemotherapy regimens with stem cell rescue. The dose and schedule of the chemotherapeutics are usually determined by the extent of side effects and bring patients to the very limit of their endurance.

Another challenging group of patients is comprised of children under 3-4 years in whom radiotherapy is contraindicated due to severe neurocognitive impairment. Apart from a small subgroup of patients with medulloblastoma with extensive nodularity, most patients have a poor prognosis and 5-year survival rates generally vary around 50% depending on confounding factors[81].

Systemic chemotherapy exposes the whole body to the drug and produces a variety of adverse effects that limit dosing, disrupt chemotherapy schedule and can sometimes have a lethal outcome. There are a variety of factors that play a role in the adverse effects of chemotherapy. The most important are the distribution of drugs in the body, metabolism to toxic metabolites, pharmacodynamic interactions with targets in normal cells and the variability in dose needed to eliminate the tumours. All of these factors are interdependent and they interact with indicators such as the age, health, genetic profile of the patient as well as previous and concomitant therapy. The border between treatment success and failure is often very thin.

The most commonly used drugs in medulloblastoma therapy are vincristine, platinum compounds (cisplatin and carboplatin), alkylating agents (nitrosoureas, procarbazine, cyclophosphamide) and topoisomerase inhibitors (mainly etoposide). None of these drugs is used as a single agent, they are most commonly combined in various protocols.

Chemotherapy is normally administered either orally or by injection and the drugs distribute throughout the whole body before they reach their target: leftover tumour tissue and single tumour cells in the central nervous system. In this regard the blood-brain barrier (BBB) poses the greatest obstacle to chemotherapy as drug penetration is often limited due to the tight junctions of the blood vessels of the brain. The BBB limits the transport of drugs with Mw higher than 400 Da and normally excludes hydrophilic, charged and highly protein-bound drugs[82]. Moreover, specialised transporter molecules in the endothelial cells actively transport most cytotoxics out of the brain as soon as they try to diffuse through the barrier. This efflux is accomplished through the superfamily of ATP-binding cassette (ABC) transporters like the P-glycoprotein pump (P-gp, ABCB1), the multi drug-resistant protein family (MRPs, ABCC) and the breast cancer resistance protein (BCRP, ABCG2) [83]. On the other hand, brain tumours are thought to have leakier blood vessels and an incomplete blood-brain barrier[84]. While the extent of the permeability has been reported to vary both between and within tumours[85], the extent of drug distribution within the tumour may be diminished due to increased interstitial pressure[86]. Furthermore, tumour clusters below 250µm in diameter may lack blood vessels and will be shielded by the intact normal BBB[87]. All of these pharmacokinetic limitations have necessitated the use of high systemic doses so that the fraction reaching the tumour can exhibit some meaningful pharmacological action. This in turn leads to large amounts of drugs distributing throughout the body and exerting a series of side effects.

Dividing tissues like the bone marrow receive the primary assault and myelosuppression with leukopenia, neutropenia, thrombocytopenia and anaemia are the primary dose-limiting toxicities of most chemotherapeutics used in medulloblastoma. The specific side effects for the most common drugs used in medulloblastoma chemotherapy will be given below as an illustration of the multitude of organs affected by systemic protocols.

The alkylating nitrosoureas, carmustine and lomustine, are particularly notorious for causing prolonged myelosuppression. Lomustine can be

administered orally and is the drug of choice in medulloblastoma. The main strength of the nitrosoureas stems from their lipophilicity and ability to cross the BBB thereby exerting control over macroscopic vascularised cerebral lesions[88]–[90]. The nitrosoureas are alkylating cytotoxics, which are related to the nitrogen mustards. The alkylating antineoplastic drugs were the first modern anticancer class introduced through the work of Goodman and Gilman in 1942-1946[91]. The nitrosoureas release a reactive 2-chloroethyldiazonium ion which reacts with DNA mainly alkylating guanine residues and crosslinking DNA strands through the 2-chloroethyl moiety[92]. The alkylated DNA can be repaired by O⁶-methylguanine-methyltransferase (MGMT) which is often expressed in medulloblastoma and is one of the mechanisms contributing to resistance to chemotherapy[93]. Apart from myelosuppression, additional side effects like gastrointestinal disturbances, liver toxicity and lung fibrosis may limit treatment. Furthermore, alkylating agents increase the risk of secondary malignancies and may affect fertility in boys and girls[94], [95].

Cyclophosphamide is another example of an alkylating drug used in medulloblastoma. It requires hepatic activation to 4-hydroxycyclophosphamide which is later metabolised in tumour cells to phosphoramidate mustard (Figure 1-8). The last step is hypothesized to confer some degree of selectivity of cyclophosphamide towards normal cells which are believed to express higher levels of the detoxifying enzymes aldehyde dehydrogenase and glutathione transferase[96]. Initial studies using radiolabelled cyclophosphamide indicated penetration into brain tumours[97], but this statement has been questioned lately as detection of inactive metabolites may have given rise to false-positive results[98]. The argument for the use of cyclophosphamide comes from a large study where over 300 patients were given either Regimen A (vincristine, cisplatin and lomustine) or Regimen B (vincristine, cisplatin and cyclophosphamide)[44], [99]. Despite the proven CNS distribution of lomustine and the doubtful results for cyclophosphamide, patient survival and secondary malignancies were the same in both groups. In addition to the similar efficacy to the nitrosoureas, cyclophosphamide has

comparable toxicity and adverse effects. The only notable difference being increased risk of haemorrhagic cystitis due to acrolein release during metabolism (Figure 1-8).

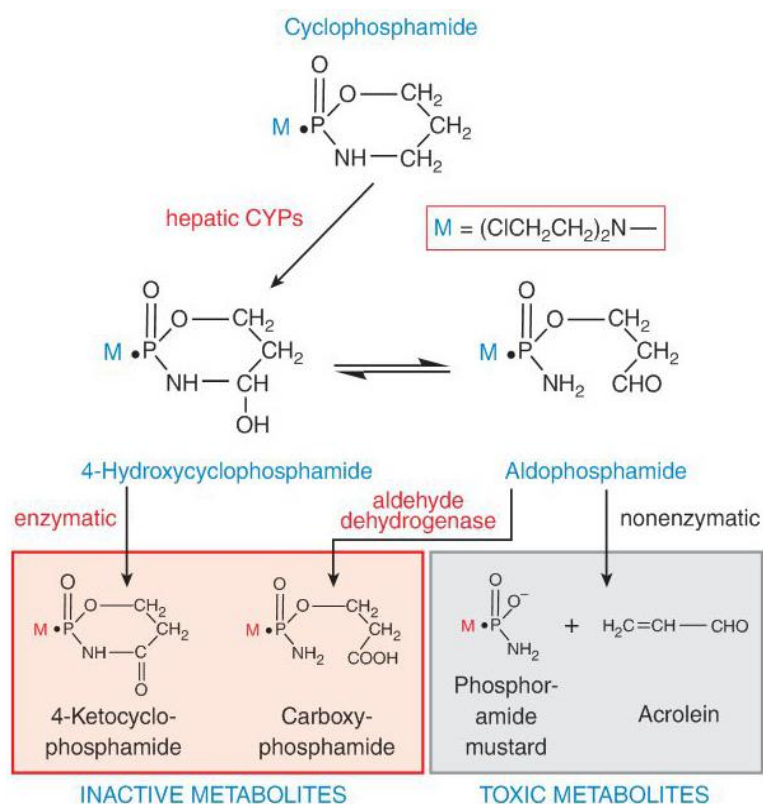


Figure 1-8. Metabolism and activation of cyclophosphamide. Cyclophosphamide requires activation by hepatic CYP2B enzymes. The 4-hydroxy derivative can be degraded to inactive metabolites in normal cells by the enzymes aldehyde dehydrogenase, glutathione transferase and others. The active metabolite phosphoramidate mustard is thought to confer cytotoxic action, while acrolein has been implicated in causing haemorrhagic cystitis in patients. Figure adapted from [96]

In contrast, vincristine behaves very differently to the alkylating drugs and is the medulloblastoma chemotherapeutic exhibiting the least amount of myelosuppression. The low toxicity towards the bone marrow allows vincristine to be administered during radiotherapy. The dose limiting toxicity is severe peripheral neurotoxicity manifesting with foot drop, muscle weakness, constipation, ileus and neuropathy. Vincristine blocks the polymerization of tubulin and arrests mitotic cells in metaphase. The heightened toxicity to neurons may be explained by inhibition of tubulin polymerization in postmitotic neurons resulting in axoplasmic transport inhibition in the axons [100], [101]. The effects of vincristine are confined to the peripheral nervous system because vincristine does not cross the intact BBB [102]. Still, if the drug is injected

in the CSF it is almost 100% lethal to patients[103]. The propensity of some medulloblastoma cells to differentiate towards the neural lineage[11] and the heightened toxicity of vincristine to both dividing and neuronal cells serves to explain the central role of vincristine use in medulloblastoma chemotherapy. Nevertheless, the utilisation of vincristine in brain tumours relies on the hypothesis that the latter have a leaky BBB. The intratumoral distribution of vincristine would be potentially augmented if the blood-tumour barrier were to be disrupted by radiation[104]. Many researchers have tried to determine the distribution of vincristine in brain tumours by using rodent glioma models and have reached conflicting conclusions[105], [106]. A study in humans using the related drug vinblastine has found detectable levels in intracerebral tumours[107] and has illustrated the poor utility of using CSF concentrations[108] to infer intracerebral or intratumoural levels of drugs. It goes without question that any drug, and especially vincristine, cannot be expected to eliminate medulloblastoma tumours as a single therapeutic. It appears more likely that unprotected peripheral neurons will be severely damaged before vincristine has chance to cross the heterogeneous blood-tumour barrier and circumvent the increased interstitial pressure in brain tumours.

The third class of essential chemotherapeutics in medulloblastoma therapy is the platinum compounds. Most conventional medulloblastoma protocols include cisplatin and the drug's distribution in brain tumours has been documented[84], [109]. Cisplatin needs to be activated by displacement of the chloride ligands with water. The active metabolite forms DNA adducts with purine bases and crosslinks DNA which starts a cascade of stress signalling, induction of apoptosis and cell death[110]. During treatment cisplatin may lead to dose-limiting myelosuppression, neurotoxicity, renal impairment and has a high emetogenic potential. Most importantly, the combined insult from cisplatin and radiotherapy to the cochlear nerves very often results in hearing loss in patients necessitating treatment de-escalation[111]. The ototoxicity is persistent and most medulloblastoma survivors require a hearing aid. The toxic

effects of cisplatin require mandatory monitoring of renal function and hearing as well as the standard blood counts[112].

Systemic etoposide is also employed in some regimens, like the SIOP-PNET-III protocol[74] and extensively in high-risk medulloblastoma patients[113] and infants[114]. The use of etoposide along with its most pronounced side effects of myelosuppression and increased risk of secondary malignancies will be more extensively reviewed in Section 6.1.

As the biological understanding of medulloblastoma develops further, novel targeted agents emerge in prospective treatment strategies[115]. While these new drugs hold great promise, the location of the tumours behind the blood-brain barrier, the frailty of the paediatric population and the relative rarity of the different subtypes may severely delay targeted agent introduction into therapy. This is exemplified by the case of SHH inhibitors, where development of resistance and suppression of bone growth were the main barriers to introduction[18].

This summary of the most important chemotherapeutics used in medulloblastoma outlines their grave systemic side effects. On one hand, conventional chemotherapy drugs do not discriminate sufficiently between normal and tumour cells and on the other systemic administration requires large doses. That is why many clinicians and researchers have turned to local delivery in the hope of using less drug and delivering drugs closer to their target (Table 1-4).

Systemic chemotherapy					
Drug Class	Main drugs	Mechanism of action	Blood-brain barrier penetration	Dose-limiting toxicity	Long-term effects
Alkylating agents	Carmustine, Lomustine, Cyclophosphamide	Alkylating DNA	Carmustine, Lomustine +++ Cyclophosphamide -	Myelosuppression	Secondary malignancies Infertility
Vinca alkaloids	Vincristine	Blocks tubulin polymerisation	-	Peripheral neurotoxicity	Neuropathy
Platinum compounds	Cisplatin Carboplatin	DNA adducts	+	Myelosuppression Ototoxicity Nephrotoxicity	Hearing loss
Podophyllotoxins	Etoposide	Topoisomerase II poison	-	Myelosuppression	Secondary malignancies
Local chemotherapy					
Drug Class	Main drugs	Mechanism of action	Evidence in medulloblastoma	Dose-limiting toxicity	Long-term effects
Antifolate	Methotrexate	Dihydrofolate reductase inhibition	Infants [81]	Chemical arachnoiditis	Progressive demyelinating encephalopathy
Antimetabolite	Cytarabine; Depocyte-liposomal formulation	Antimetabolite – DNA damage	Leptomeningeal metastasis [116], [117]	Chemical arachnoiditis, cauda equina [118]	Leukoencephalopathy
Podophyllotoxins	Etoposide	Topoisomerase II poison	Feasibility studies [119]–[121] and alternating with cytarabine [122]	Headache, seizures [120]	Remain to be established
Alkylating agents	Mafosfamide*	Alkylating DNA	No effect on survival [123]	Headache, vomiting, irritability [121]	Remain to be established

* no longer on the market

Table 1-4. Summary of clinically relevant systemic and local chemotherapeutics used in medulloblastoma.

Section 1.2 Local therapy

1.2.1 The rationale for local therapy

Local drug delivery has emerged because of the problems outlined above with poor BBB penetration, blood-tumour barrier heterogeneity, increased tumour interstitial pressure and the poor access to tumour micrometastases. The idea of delivering treatment where it is needed is not new and some of the first antitumour treatments were local. Surgical removal of the tumour can be regarded as the ultimate local treatment for tumours. The implantation of radioactive elements within tumours is known as brachytherapy and was utilised[124] shortly after the discovery of radiation by Becquerel in 1896. Brachytherapy is still in use today, mostly in localised prostate cancer[125], but has also been tested in cases of recurrent medulloblastoma[126] and glioblastoma multiforme[127]. As far as local chemotherapy is concerned, one of the first chemotherapeutic delivery strategies to be tested in medulloblastoma was the administration of intrathecal methotrexate in 1967[128]. A short overview of the different strategies for local chemotherapy will be given below.

1.2.2 Types of local therapy

The main types of local chemotherapy depending on the route and place of delivery are intrathecal/intra-CSF, intratumoral/interstitial and intracavitary chemotherapy.

1.2.2.1 Intra-cerebrospinal fluid (intra-CSF) therapy

Intra-cerebrospinal fluid administration can be accomplished by injecting a drug either into the cerebrospinal canal (intrathecal) or into the ventricles of the brain (intraventricular) administration. Intra-CSF delivery is used in the management of pain, spasticity and leptomeningeal metastases. Pain and spasticity are thought to be controlled by pain signalling in the dorsal horn neurons of the spinal cord. That is why opioids[129], the marine snail peptide zoconotide[130] and baclofen[131] are delivered intrathecally. In contrast leptomeningeal metastasis often involves the whole neuraxis and bolus injections or

infusions of antineoplastic drugs are done both intrathecally and intraventricularly.

Since the purpose of antitumoural intra-CSF therapy is to eradicate tumour cells in the CSF and CNS, this mode of drug delivery can be likened to craniospinal irradiation to a certain extent. The difference being that instead of radiation, an anti-cancer drug is used to eradicate the tumours. Yet, the effects of chemotherapy can be milder or similar to those of radiotherapy depending on the drug exposure, distribution in the CSF, meninges and the brain. In addition, the safety and efficacy of intra-CSF chemotherapy will also depend on the mechanism of drug action and its capacity to kill tumour cells without affecting the normal tissues. In this respect the main merit of intra-CSF chemotherapy lies in the opportunity to concentrate high cytotoxic concentrations in the CSF and target floating tumour cells and leptomeningeal micrometastases. These small (<500µm) clusters of tumour cells would not have developed their own imperfect blood vessels and would normally be shielded from systemic chemotherapy. Furthermore, the doses required to reach therapeutic levels in the CSF would be much lower than the ones required to reach the same level via systemic dosing. Finally, drugs administered in the CSF would only penetrate a few millimetres into the brain limiting their side effects to the pial and arachnoid cells as well as the small blood vessels of the subarachnoid space and potentially sparing most of the brain.

A full review of intrathecal therapy is beyond the scope of this work and the interested reader is referred to the excellent work by Conroy et al[132]. However a few examples of currently employed intra-CSF chemotherapeutics will be given below in order to illustrate the clinical use of this mode of local therapy and examine the effects of the direct interaction of drugs and the brain.

Methotrexate was one of the first agents to be used intrathecally in cases of leptomeningeal metastasis in leukaemia in the 1950s[133]. It was later trialled in medulloblastoma[128], although its use in medulloblastoma today is reserved for patients <3 years in whom

radiotherapy is contraindicated[81][47]. The side effects of intra-CSF methotrexate are divided into acute, sub-acute and chronic depending on their time of onset and persistence. The acute side effects start in the first 24 hours of administration and present with chemical arachnoiditis-seizures, headache, nausea, vomiting and fever. Those symptoms are very common and are usually managed with steroids like dexamethasone. The sub-acute side effects include speech paralysis and paraplegias. Later, patients often develop chronic leukoencephalopathy, which may lead to progressive demyelinating encephalopathy and affect cognitive functioning[134]–[136]. The neurotoxic side effects of methotrexate could be potentiated by previous craniospinal irradiation, which limits its utility in medulloblastoma patients.

Cytarabine (cytosine arabinoside, ara-C) is another drug commonly used in intrathecal therapy, with a long history in leukaemia starting in the 1960s[137]. Compared to intrathecal methotrexate, cytarabine is associated with fewer systemic side effects, but the dose-limiting toxicity of ara-C is chemically induced arachnoiditis. Cytarabine's neurotoxic side effects are further potentiated in the slow release liposomal formulation and require concomitant steroid administration[118]. In haematological malignancies intrathecal cytarabine is most commonly included in a "triple intrathecal therapy" (TIT) regime alongside intrathecal methotrexate and hydrocortisone[138]. The exact benefit of the TIT regimen is somewhat controversial with some studies seeing improvement in CNS disease status without impact on survival[139]. In contrast, others have combined intensified TIT with high dose systemic chemotherapy to completely eliminate radiation from ALL treatment[140]. The reservations regarding long-term methotrexate toxicity in previously irradiated patients have discouraged the adoption of TIT in medulloblastoma and have stimulated the use of alternative drugs for intrathecal administration.

Etoposide is a promising chemotherapeutic for intra-CSF delivery with numerous feasibility studies showing lack of neurotoxicity[119]–[121]. Intra-CSF etoposide delivery achieves cytotoxic etoposide concentrations in the cerebrospinal fluid with doses as small as 0.5mg, while systemic

etoposide requires three hundred times higher doses and fails to reach measurable CSF levels[120]. Recent studies in recurrent embryonal tumours have explored alternating administration of intrathecal etoposide and liposomal cytarabine to control leptomeningeal metastasis[122]. Peyrl et al. supplemented a previously described[141], metronomic, low-dose antiangiogenic, systemic, 5-drug regimen with additional intrathecal therapy to achieve an augmented CSF control. The antiangiogenic systemic therapy was used to inhibit tumour vascularisation while the intrathecally delivered etoposide and cytarabine were included to control leptomeningeal metastasis. Interspersing etoposide and cytarabine served to space out cytarabine dosing and minimize arachnoiditis while maintaining cytotoxic protection in the CSF. In contrast to the sustained release profile of liposomal cytarabine, etoposide is quickly eliminated from the CSF via bulk flow and tumour exposure to the drug may often be suboptimal. The limited half-life necessitates either prolonged etoposide infusions or reformulation of the drug in a sustained-release form. As far as this research work is concerned, the lack of neurotoxicity history for etoposide and the clinical sensitivity of medulloblastoma to the drug were the main reasons for selecting it as a model compound in the nanoparticle formulation studies later in the project. For a more in-depth look at etoposide's characteristics and formulation strategies see Chapter 6.

As a therapeutic strategy intra-CSF therapy has a few notable limitations[142], [143]. Unlike the fast equilibration in the bloodstream, drugs in the CSF are not quickly equilibrated and gradients in drug distribution may lead to imperfect tumour control. Moreover drugs delivered in the CSF would only kill floating cells and small clumps of tumour cells because most small molecules would only diffuse through a very limited distance into the tissues. Bigger tumour foci having leaky blood vessels and disseminated tumour cells and metastases not directly in contact with the CSF, may be better controlled by systemic therapy administered alongside intra-CSF delivery. The greatest potential of intra-CSF delivery for medulloblastoma is as an alternative strategy to reduce craniospinal irradiation as shown in ALL[140]. In a similar analogy it can

be hypothesized that posterior fossa boost radiotherapy could be decreased by the use of intratumoral and interstitial drug delivery.

1.2.2.2 Intratumoral, interstitial and intracavitary delivery

These three types of local delivery often use similar strategies but differ in the targeted tissue. Intratumoral delivery involves drug loading directly into the tumour tissue. Interstitial therapy is usually accomplished by delivering the drug in the extracellular (interstitial) compartment of the tissues neighbouring the tumour. In postoperative interstitial administration the drug is delivered after resection of the tumour in the cavity left by the tumour tissue. A very similar strategy is employed in intracavitary therapy where the drug is delivered in a natural body cavity, for example the bladder during intravesical therapy for bladder cancer.

Intratumoral therapy is mostly used in inoperable tumours, or as a strategy to downstage tumours to an operable size. It can be accomplished by injecting a drug directly into the blood supply of a tumour, or directly into the tumour itself. The transcatheter arterial chemoembolization strategy (TACE) in inoperable hepatocellular carcinomas exploits the double blood-supply of the liver (both through the hepatic artery and the portal vein)[144]. TACE is performed by injecting a drug dissolved in oil (lipiodol) into the hepatic artery blood supply of the tumour and later embolising the artery with gelatine sponge microparticles (Gelfoam). Intratumoral injection of ethanol is often combined with TACE in the treatment of hepatocellular carcinoma as a palliative technique with moderate survival benefit [145].

The effectiveness of local administration can be maximized if the drug is entrapped in a delivery vehicle which provides a sustained release thus limiting diffusion into the systemic circulation[146]. Modified intratumoral release has been achieved using polymeric matrices[147], gels[148], liposomes[149] and emulsions[150]–[152]. Additional pros of sustained release local therapy can be expected based on the data from studies which have demonstrated that prolonged exposure to low-dose chemotherapy can be very effective by suppressing angiogenesis in solid tumours[153]. That means that slow release of a relatively small dose of

the drug in the tumour may be enough to suppress growth or even initiate remission.

Intracavitary therapy can be delivered in the cavity left by a tumour after surgical removal or by delivery in natural a body cavity. For example, intravesical therapy for bladder cancer has used chemotherapeutics[154] and immunotherapy with Bacillus Calmette–Guérin(BCG)[155] delivered directly into the bladder as adjuvant treatment prolonging survival[156].

Postsurgical intracavitary therapy is an opportunistic strategy where a drug delivery system is implanted into the postsurgical tumour cavity to destroy the residual cancer tissue there. The first clinically approved postoperative intracavitary drug delivery system in brain tumours was Gliadel[157]. Gliadel wafers are disc shaped biodegradable polymer implants that are impregnated with carmustine. They are instilled into the tumour cavity and slowly release carmustine into the adjacent tissue reaching higher levels than systemically delivered carmustine. Carmustine was chosen based on its lack of neurotoxicity and because it gave the longest prolongation of survival in preclinical mouse models[158]. Despite the encouraging results in animal models, the clinical results in glioblastoma multiforme have been modest with 2-3 months of increased survival[159]. This has been hypothesized to be due to problems with the passive drug diffusion of carmustine penetrating only around 1 mm into the adjacent tissues[160]. Gliadel's main advantage over systemic therapy is the lack of myelosuppression and pulmonary toxicity. Nevertheless, the wafers have a spectrum of local side effects with brain oedema, increased risk of infections and potential for hydrocephalus in cases of wafer dislodgement in the ventricles[161].

An alternative strategy employed in both intratumoral and interstitial drug delivery is to actively inject the drugs through microcatheters directly implanted into the brain interstitium or tumour by using convection enhanced delivery (CED)[162], [163]. CED perfuses the tissues by applying a pressure gradient, resulting in bulk flow and wider drug distribution[164]. It is a relatively new technique[165] but holds great potential in the delivery of targeted toxins, macromolecules[166]

and submicron drug delivery systems[167]. Problems with backflow, catheter positioning and leaks have plagued CED in phase III clinical studies[168], [169]. Future developments in optimising catheter design and placement as well as identifying the best agent for effective convection enhanced delivery will probably yield the first breakthrough in this therapeutic approach.

There appear to be two major blocks to the successful implementation of local therapy. The first one is related to the drug reaching its target and the second one concerns the risk of off-target effects. Even in the most advantageous form of local delivery, when the bulk of the tumour has been removed and the drug delivery systems is only required to kill the remaining residual cancer tissue, drug penetration is a major limitation[170]. Although controlled-released small molecule drugs have the potential to diffuse relatively quickly in the extracellular matrix (ECM), they often remain trapped in the first cell layers or the pores of the extracellular matrix of tumours. Moreover, lipophilic drugs, like carmustine, can distribute in fatty tissues, cell membranes and the myelin sheaths of neurons[171]. The increased interstitial pressure and the fibrotic nature of tumour tissue can pose an additional impediment to the distribution of local therapy to all cells in the tumour[172]. The adverse effects caused by the lack of discrimination between tumour and normal tissue embody the second major problem in local therapy. Most matrix systems release free cytotoxic drug in the interstitium and affect tumour and normal cells alike, potentially causing neurotoxicity, seizures, oedema and chemical meningitis.

The abovementioned limitations can be partially circumvented by using advanced delivery systems like drug loaded submicron particles. These nanomedicines with their larger size would only enter the larger pores of the ECM and could theoretically travel a longer distance in the interstitium[173]. They can be co-administered or coated with various enzymes to digest the ECM of tumours[174], [175] and can be used to exploit biological differences between tumour and normal cells to deliver drugs solely to their target. This line of thought was used to form the basis of the current project.

Section 1.3 Project overview and aims

1.3.1 Postsurgical NP delivery- project aim

The ultimate aim of this project is to provide an alternative strategy for minimizing irradiation to the posterior fossa of medulloblastoma patients. The reduction of radiation will be accomplished by local administration of drug-loaded nanoparticles in the cavity left by the tumour after surgical removal of medulloblastoma. The purpose of the nanoparticle delivery system is to prevent local tumour recurrence by targeting the leftover tumour tissue after surgery. The nanoparticles will be administered directly onto the tumour bed using a gel or foam-based carrier formulation, which will allow the surgeon to close the dural incision before the particles are released from the gel into the surrounding tissues. The use of nanoparticles would allow the exploitation of differential endocytosis rates between tumour and brain tissue thereby minimizing normal tissue drug exposure and side effects (Figure 1-9). Additional discussion regarding the targeting mechanism will follow later in this section and in Chapter 5.

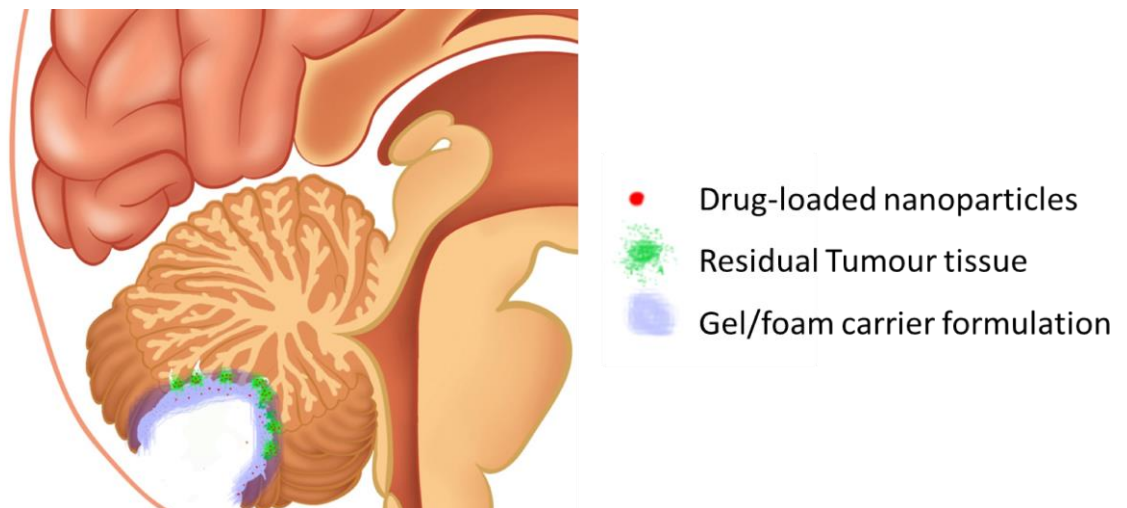


Figure 1-9. Postsurgical local nanoparticle delivery. After surgical removal of the tumour there is always some residual tumour tissue left (green), often leading to tumour recurrence despite irradiation. Drug-loaded nanoparticles (red) can be applied directly onto the tumour bed after surgery to selectively target and kill cancer cells. Targeting can be achieved passively, solely on the basis of differential endocytosis rates between normal brain tissues and actively proliferating tumours. A gel or foam-based carrier formulation (grey) can be used to deliver the nanoparticles and keep them in place for the time necessary to close the incision. Figure adapted from the original image by Janet Fong '09.

As seen by Figure 1-9, the local delivery of nanoparticles onto the tumour bed has several advantages. It circumvents the blood-brain barrier and ensures direct contact between the drug delivery system and its target-leftover tumour tissue. The targeting in this case is passive, exploiting increased endocytosis rates in actively growing tumour cells, compared to normal brain. Since the particles are administered interstitially, they do not need to extravasate and the mechanism of enhanced-permeation and retention (EPR) effect does not play a role.

1.3.2 Project rationale

The reasoning behind this projects comes from previous work in the group which has exploited the behaviour of nanoparticles made from the biodegradable polymer poly(glycerol adipate)[176]. In her doctoral thesis Weina Meng was able to demonstrate that fluorescently labelled poly(glycerol adipate) nanoparticles had a 6-times higher uptake in tumour spheroids compared to normal rat brain[177]. The observed enhanced tumour endocytosis effect was strongly dependent on the dimensionality of culture and was only observed in physiologically relevant three-dimensional tissue models[178], [179]. At the same time, another member of the group, Sanyogitta Puri, was working on the incorporation of cytotoxic drugs into poly(glycerol adipate) nanoparticles and achieved reasonable drug loading with a selection of cytotoxic drugs[180]. These previous findings have stimulated the idea that if poly(glycerol adipate) nanoparticles were to be loaded with cytotoxic drugs, they could be delivered locally to the tumour bed of medulloblastoma patients after surgery. A special foam or gel carrier, partially inspired by the already available haemostatic systems in neurosurgery[181], could be applied directly to the tumour bed and contain the nanoparticles for a limited time until dura matter closure. Before proceeding with the major milestones of the project a few important concepts in nanoparticle delivery will be discussed in order to clarify the place of the proposed system in the overarching theme of nanomedicines.

1.3.2.1 Local nanoparticle delivery overview

Nanomedicines are defined as nanosized tools (1 to 1000nm) for the diagnosis, prevention and treatment of disease[182]. In contrast to the conventional 100nm cut-off for colloid systems the upper border is widened to 1000nm to include submicron systems that are employed for medicinal purposes. The potential of nanomedicines lies in their different behaviour in the body when compared to conventional low molecular weight (Mw) drugs.

The majority of small molecule drugs ($M_w < 500 \text{ Da}^1$, $\log P < 5$ [183]) are designed so that they freely distribute between most cells in the body being sufficiently hydrophilic to dissolve in the bodily fluids and engage with their intracellular targets, while being lipophilic enough to cross phospholipid membranes. Cancer therapeutics achieve a certain level of specificity by interacting with their specific target. However, cytotoxics are largely designed to kill dividing cells on the premise that tumour cells divide more rapidly than normal tissues. The side effects of cancer therapy come as a direct consequence of the interaction of chemotherapeutics with the rapidly dividing cells of the normal hematopoietic tissues, gastrointestinal epithelium or off-target effects in other tissues (cardiac for anthracyclines, neurons for Vinca alkaloids, etc.). The whole-body distribution of small molecule drugs can be likened to the grave effects of whole body radiation often causing severe suffering or patient death. In this respect advanced drug delivery systems exploit certain cancer characteristics to deliver a focused dose of the drug to the tumour tissue, while sparing normal organs, much like conformal radiation.

When a drug is transported within a nanocarrier, the large size of the drug delivery system limits its distribution in the body as it cannot easily transverse most membranes and body barriers. This leads to the distribution of nanomedicines in different compartments of the body and the effect can be exploited to minimize toxicity and optimise efficacy. On the other hand the restricted distribution adds an extra layer of

¹ Cancer therapeutics of natural sources usually have Mw below 1000 Da.

complexity as oral delivery or even extravasation in the case of systemic delivery may be hindered by the size of the carrier[184].

Covering the whole field of nanomedicines with polymer therapeutics, drug conjugates, liposomes, dendrimers, nanocapsules and nanoparticles is beyond the scope of this work and the interested reader is referred to the review by Duncan[185]. This project and the subsequent analysis will focus on local delivery of drug loaded nanoparticles which physically entrap a cytotoxic drug. The main considerations and key concepts in delivering drugs to tumours will be briefly summarized below.

The choice of using nanoparticles as opposed to any of the other form of nanomedicines was driven by the data for selective medulloblastoma tumour uptake of fluorescently labelled nanoparticles[177]. Non-covalent physical entrapment of the drug was similarly decided based on previous experience[180], but also with the intention to preserve drug activity and facilitate unhindered dissociation from the carrier. Likewise the opportunistic strategy for local interstitial drug delivery after surgery was identified as lower risk since it circumvents the blood-brain barrier. Although a number of ways to cross or disrupt the BBB have been proposed including nasal delivery[186], barrier-disruption[187] and nanoparticle coating[188], brain tumour accumulation from these systems is generally below 1%. The often cited enhanced permeability and retention (EPR) effect[189]- nanoparticle retention due to the leaky blood vessels and poor lymphatics in tumours- is not a phenomenon explored in this project. This is due to the fact that local interstitial delivery does not exploit the vasculature and because the target of this drug delivery system is residual cancer tissue which may be microscopic without any vessels of its own. Furthermore, receptor-mediated targeting was not chosen due to the heterogeneity of medulloblastoma lacking a single antigen target, the added complexity of active targeting[190] and the poor reported distribution (0.01% of the injected dose) for antibody-targeted therapeutics[191].

The altered endocytotic activity of actively proliferating tumour cells as opposed to normal tissue is the hypothesized passive targeting strategy

for the drug delivery system developed in the present work[192]. This mechanism was proposed initially in the 1970s by de Duve and Trouet[193], [194]. The fact that the nanoparticles will be delivered locally in the cavity of the cerebellum means that they will be subject to endocytosis by either tumour cells or normal tissues in the brain. In this regard, the studies performed by Meng[177] in three-dimensional culture and by Favretto[195] in monolayers have indicated the relatively high endocytosis activity in two medulloblastoma cell lines.

Mammalian cells can internalise nanoparticles via a number of endocytosis pathways mediated by clathrin coated pits, caveolin, clathrin and caveolin-independent pathways or macropinocytosis[196]. Clathrin-mediated endocytosis is often referred to as the classical endocytosis pathway because it is present in all mammalian cells and is involved in receptor-mediated endocytosis of essential nutrients like low density lipoproteins and transferrin. The second, caveolin-mediated, pathway is interesting because caveolin is not expressed in neurons[197], but SHH medulloblastoma cells express this protein[198] which may potentially make them more susceptible to NP-based therapy[195], [199]. A related strategy that targets caveolin-mediated endocytosis is exploited by the clinically available liposomal doxorubicin (Doxyl)[200] and paclitaxel-carrying albumin nanoparticles (Abraxane)[201]. It can be hypothesized that local NP therapy will be most beneficial in high-risk SHH medulloblastoma tumours which are known to metastasize mainly locally[23] and exhibit abnormal endocytosis activity[195], [197], [198]. Once endocytosed, the nanoparticles will normally be transported to the endosomes and would finally end up in the lysosomal compartment. In this hydrolytic environment the physically entrapped drug will be released from its polymeric carrier after degradation of the polymer.

1.3.2.2 The rationale behind polymer selection

The initial polymer chosen for this project was poly (glycerol adipate) - a predominantly linear polyester of glycerol and adipic acid synthesized under mild conditions via a reversible lipase-catalysed reaction[176]. The polymer has pendant secondary hydroxyl groups in the glycerol

moiety that can be substituted with fatty acids and other functionalities to customise its physicochemical characteristics. Moreover, studies by Meng have indicated that poly(glycerol adipate) nanoparticles are selectively taken up by tumour cells as opposed to normal brain tissues[177]. Poly (glycerol adipate) has been shown to be rapidly hydrolysed in the low pH of the lysosomes by naturally occurring lipases thereby releasing its cargo into the cells[179]. The drug was chosen to be only physically entrapped in order to maintain its biological activity intact and prevent the formation of partially hydrolysed drug derivatives with questionable action.

1.3.2.3 The choice of drug

Etoposide was initially identified as a drug that has shown little neurotoxicity[119]–[121] and has demonstrated efficacy against medulloblastoma in patients[81], [202], [203]. As a secondary option, the chemically related teniposide was identified as demonstrating higher activity in preclinical models but underperforming in the clinic due to its lower solubility and suboptimal formulation. More information regarding etoposide and teniposide and the strategies for improving their delivery will be given in Chapter 6.

1.3.3 *In vitro* model requirements

From the inception of this project it was clear that a suitable 3-D *in vitro* model would need to be used in order to test the safety and toxicity of the drug-loaded nanoparticles and compare these against the non-encapsulated drug. The main purpose of the *in vitro* models was to be able to determine whether a drug delivery system offers selectivity of uptake and cytotoxicity towards medulloblastoma tumours compared to normal brain tissue. Conveniently, Meng et al. had already established some key *in vitro* models culturing medulloblastoma spheroids onto rat brain slices[177], [178]. These initial models, along with complementary research in the group[204]–[206], were instrumental in showing the importance of dimensionality not only in representing actual tissues rather than simple monolayers but also in altering the behaviour of cells and their propensity to take up nanoparticles. However the use of rat

brain slices as a surrogate for normal human brain has a number of drawbacks. Rodent models are increasingly recognised as poor models of human biology[207], [208] and their predictive potential has been severely questioned[209]. That is why the exclusive use of human tissue was added as an overarching requirement for the *in vitro* models necessitating a redesign of the previous *in vitro* systems.

The new model was designed so that it reflects key components of local delivery to the brain. The two main elements of the *in vitro* platform are the tumour cells, representing the small avascular tumour micrometastases, and the neurospheres representing the normal human brain.

It is important to note that the purpose of creating these models was not to study the biological phenomena of hypoxia, change of gene expression and stem cell enrichment in spheroids. The main utility of the disease model was intended to inform whether the formulation of cytotoxic drugs into nanoparticles can improve the selectivity and cytotoxicity of chemotherapy. Therefore, the determination of cytotoxicity was selected as the main endpoint with the possibility to distinguish apoptosis and necrosis as a secondary endpoint for the model. This decision allows for comparing normal and tumour tissue on the same scale. However, it bears the disadvantage that it may miss a possible impairment of functionality in the normal tissue occurring before any evidence of cytotoxicity. This downside is partially offset by the use of foetal neurospheres enriched for neural progenitors which may possibly be more sensitive to cytotoxic insults than fully differentiated cells. A more in-depth look into the various endpoints of the models will be given in Chapters 3 and 4.

1.3.3.1 Tumour tissue

Tumour micrometastases are not composed of cells spreading as a single layer. They grow in clusters with their own extracellular matrix, gradients of nutrients and oxygen driving different levels of cytotoxic assault resistance. Multicellular tumour spheroids, which have been popularised by Sutherland in the 1970s[210], recapitulate those features very well

compared to monolayers. For example, spheroids mimic natural cell-cell and cell-matrix interaction, features not normally found in cells cultured on tissue culture plastic[211], [212]. The inclusion of naturally secreted extracellular matrix is critical as the nanoparticles will have to transverse it to reach all tumour cells and using monolayers will not reflect that physiological trait of tumour foci. Small avascular tumour micrometastases often display a hypoxic core with quiescent cells which are more resistant to radiation and chemotherapy[213]–[215]. In this respect, multicellular tumour spheroids can be cultured to sizes beyond the diffusion distance of oxygen (300-500 μm) and exhibit similar gradients and resistance patterns[216], [217]. In addition, gene expression profiles in spheroids have been reported to be closer to those of parent tumours compared to monolayers[218], [219].

1.3.3.2 Tumour cell line selection

The ideal representation of human tumours *in vitro* would be accomplished by using primary patient derived tissues. However, these are not always readily available and are more suitable for the later stages of model development, when culture conditions and procedures are optimised. That is why the initial experiments used cell lines with the intention to upgrade to patient derived primary tissues upon protocol optimisation in the validation stage of the model. Accordingly, a selection of medulloblastoma cell lines was chosen for model development experiments.

The DAOY cell line was derived initially from a desmoplastic medulloblastoma from a 4-year old boy[220]. Although the parent tumour displayed some evidence of glial and neuronal differentiation this was not seen in the cell line when cultured *in vitro*. The DAOY cell line has been reported to be tetraploid with multiple genome alterations and expressing abnormal SHH signalling with defective TP53[221]–[223]. The lack of TP53 probably contributes to the genomic instability of DAOY cells and may indicate a possible connection with the relatively rare Li-Fraumeni syndrome, provided that the change in signalling has not been

acquired *in vitro*. DAOY cells have also been reported to differ from patient tumours in their chromosomal aberrations profile[221].

In view of these concerns the VC312R medulloblastoma cell line was also included in the screening[224], although the latter has not been associated with any of the medulloblastoma subgroups. However, during the first half of the project, it was discovered that the VC312R cell line is listed on the International Cell Line Authentication Committee web site as a misidentified cell line (www.iclac.org), citing the work by Higgins et al[225]. The paper reported that the cell line may have been contaminated with rat DNA and, while that has not been confirmed in house, a decision was made to terminate its use in future experiments. Although, this discovery is very concerning and has revealed a weakness in the initial cell line selection, the work performed on the cell line covers very basic methodology feasibility studies on spheroid formation and spectral dye compatibility and is not intended to be interpreted more widely. The experiments performed with the cell line were later repeated and reproduced with the UW228-3 cell line which was authenticated in-house.

The third cell line employed, UW228-3[226], is reported to be similar to either Sonic hedgehog driven (SHH)[227] or Group 3[228] medulloblastoma. Adding to the controversy is the finding that in contrast to the diploid cells of the parent tumour, UW228-3 cells are aneuploid. While gains in MYC expression and chromosomes 1 and 7[226][221] are common for Group 3 medulloblastoma, it is possible that those mutations were present in a small subgroup of cells within the parent tumour which were selected upon *in vitro* culture. Subgroup affiliation can be used to select for patients that are going to benefit the most from local therapy. For example, interstitial therapy at the tumour bed may be most advantageous in SHH medulloblastoma as it tends to recur mainly locally [23]. In contrast, the dismal prognosis and the frequent leptomeningeal metastases associated with Group 3 may favour the concomitant use of local intra-CSF delivery as well.

Nevertheless, the chosen cell lines were solely used as models serving to establish the methodology of the assays. This compromise was accepted with the vision that subsequent studies would include primary tumour tissue from patients.

1.3.3.3 Normal brain tissue surrogate

Apart from the target tumour cells, the *in vitro* testing strategy was designed to include a normal tissue component representing the non-malignant brain tissue at the site of delivery. This is a vital component of the model serving to establish the safety and selectivity of treatment and put toxicity in perspective.

Since miniaturized models of the human brain are still in their infancy[229], human foetal brain tissue cultured as neurospheres was selected as a surrogate for the developing human brain[230]. This choice was dictated by the desire to model the growing brain in children and aimed at including the mix of pluripotent, differentiated and mature cells forming in neurospheres of human foetal brain tissue [231]. When human foetal brain tissue is cultured in serum-free media containing basic fibroblast growth factor (bFGF), and epidermal growth factor (EGF), the resultant neurospheres become enriched for neural progenitor cells which actively divide. The population of dividing progenitors allows them to multiply at a reasonable rate and be propagated for screening purposes. The terms foetal neurospheres, neural progenitors and neural stem cells are used interchangeably throughout this thesis to identify the normal brain tissue surrogate component of the model. Both human[232] and mouse[233] neural progenitor cells have been used as an *in vitro* models of developmental neurotoxicity and significant interspecies differences have been reported[234], [235]. These findings further strengthen the choice of human tissue for the models.

While the neurospheres have been found to contain a mix of progenitors, glial and neuronal cells, they were not expected to reach the level of specialisation of the tissues *in vivo* during the duration of the assay. There are a number of specialised cells at the site of nanoparticle delivery (cerebellar vermis and roof of fourth ventricle). Depending on tumour

location and size these may include cells of the cerebellar nuclei, cerebellar granular neurons, Purkinje cells, stellate cells, basket cells, astrocytes, oligodendrocytes, microglia, ependymal cells covering the ventricle, cells of the choroid plexus, etc. Although neurospheres are much simpler clumps of progenitors, glial and neuronal cells they have the potential to show integral toxicity to the whole mix of cell types. The progenitor cells in the developing children's brain may be an especially important collateral damage target as insults to structures known to host them have been linked to neurocognitive deficits in medulloblastoma patients[236].

1.3.3.4 The influence of culture method

Although there are a variety of methods to grow cells in three-dimensional cell culture[237]–[239], spheroids were chosen for this *in vitro* model of medulloblastoma due to a number of physiological and practical considerations. For instance, scaffold cultures were excluded because the addition of naturally-derived or synthetic matrix can influence gene expression in a non-physiological way[240], [241]. Moreover, matrix and organ-on-a-chip technologies introduce the possibility of non-specific drug binding to the scaffold, the PDMS chip or tubing[242]. Scaffold-free spheroid culture methods stimulate the cells to secrete their own extracellular matrix and exhibit more of the natural characteristics of the parent tumour[243], [244]. Chapter 3 will discuss the rationale for choosing the right platform for spheroid culture and analysis.

Another important aspect of modelling medulloblastoma is the interaction between normal and tumour tissue. Tumour and neural progenitor cell spheroids can be cultured together in a co-culture model with increased physiological relevance. The interaction between tumour and host tissue has been repeatedly demonstrated to affect chemo[245] and radiosensitivity[246], proliferation[247], angiogenesis[248], cell adhesion[249] and gene expression[250]. In view of these considerations the ultimate model of medulloblastoma was envisaged to be a co-culture model of normal and tumour tissue where the viability of each cell

population can be determined separately. Further considerations about the development of the co-culture model will be given in Chapter 4.

1.3.3.5 Culture media

The necessity of culturing two cell types together brought forward the question of finding a common media composition that can support both cell types. The medulloblastoma tumour cell lines are normally cultured in adherent monolayers in serum containing media. However multiple studies have shown the increased expression of stem cell markers when medulloblastoma cell lines were cultured in serum-free media as spheroids[251]–[253]. That is why the same media that was employed to enrich the neurospheres for progenitor cells was used in the culture of the tumour spheroids.

1.3.4 Project plan- objectives

The overall aim of this project is to create an *in vitro* model of medulloblastoma suitable for ranking novel nanoparticle formulations carrying cytotoxic drugs for local delivery.

A set of milestones was set-up where both cell types were initially cultured separately as spheroids in high-throughput before moving on to the more complex co-culture model of the disease. At the same time a formulation program was established for the synthesis and substitution of the biodegradable polymer and the preparation and characterisation of the drug loaded nanoparticles.

1.3.4.1 Separate 3D cultures of normal and tumour tissue

The first objective was to reliably and reproducibly culture normal and tumour cells in 3D using a format that facilitates the comparison of dose response relationships of cytotoxic compounds for both cell types.

Cell viability was the endpoint and a suite of surrogate measures was used including spheroid volume, metabolism and enzymatic activity.

1.3.4.2 Co-culture model of medulloblastoma

The second landmark was the establishment of a co-culture model of medulloblastoma. The model included both foetal neurospheres and medulloblastoma tumour cells in order to model the interaction between normal and tumour tissue.

The objective was to culture the normal and tumour cells together, expose them to cytotoxic insults and determine the viability for each cell type within the co-culture separately.

Intermediate milestones were ensuring reliable marking for both cell types and developing the methods to analyse the co-cultures. Special emphasis was placed on preserving heterogeneity in view of future application for primary cultures.

1.3.4.3 Loading of nanoparticles with cytotoxic drugs- etoposide or analogues

The nanoparticle formulation work was done in parallel to the cell culture experiments. Preliminary aims were to synthesize poly(glycerol adipate) and substitute it with different fatty acids. The next step was to load the nanoparticles with drugs and characterise the amount of drug loading.

1.3.4.4 In vitro testing of the nanoparticles

The objectives were to establish the drug release profile from the nanoparticles and test them in the in vitro medulloblastoma model.

Chapter 2. Experimental materials and methods

Section 2.1 Materials

2.1.1 Cell culture

Dulbecco's Phosphate Buffered Saline (PBS), Dulbecco's Modified Eagle's Medium - high glucose (DMEM), Ham's nutrient mixture F12, L-Glutamine solution 200 mM, Penicillin/Streptomycin solution (10,000 units penicillin and 10 mg streptomycin/mL), Heparin, Agarose, Sodium pyruvate, Trypsin 10X solution 4-nitrophenyl phosphate disodium salt hexahydrate, Accutase and etoposide were obtained from Sigma-Aldrich (Dorset,UK).

Foetal Bovine Serum (FBS), N2 supplement, B27 supplement serum-free supplement, DMEM without phenol red, basic human Fibroblast Growth Factor (bFGF), human recombinant Epidermal Growth Factor (EGF), Accutase and 0.4% Trypan Blue Stain solution were supplied by Invitrogen (Paisley, UK). Resazurin was sourced from Acros Organics (Loughborough, UK)

Ultra-low attachment (ULA) 96-well round bottom plates were obtained from Corning (Amsterdam, The Netherlands).

3D-Biomatrix hanging drop plates were obtained by 3D Biomatrix,USA.

The 3D Petri Dish micromoulds were obtained from Microtissues, Providence, US with the help of Rob Pineda from the Laboratory of Biophysics and Surface Analysis(LBSA), University of Nottingham.

2.1.2 Polymer synthesis and nanoparticle studies

Divinyl adipate (DVA) was obtained from Fluorochem, Glycerol, Novozyme 435, Stearoyl chloride, Pyridine, Rhodamine B isothiocyanate (RBITC) and etoposide were obtained from Sigma-Aldrich; Tetrahydrofuran (THF), Dichloromethane, Acetone, the Heidolph RZR1 stirrer and all filters and glassware were obtained from Fisher Scientific (Loughborough, UK). All other chemicals used in the preparation of the polymer and nanoparticles were obtained from Sigma-Aldrich.

Section 2.2 Cell culture

All experiments were performed in standard cell culture conditions at 37°C and 5% CO₂.

2.2.1 Human neurospheres (neural stem/progenitor) cells

Foetal human brain tissue was received from the Joint MRC / Wellcome Trust (grant # 099175/Z/12/Z, Ethics committee approval 08/H0906/21+5, Health Research authority NRES Committee North East - Newcastle & North Tyneside 1) Human Developmental Biology Resource. The tissue was rinsed in HBSS and the meninges and any blood vessels removed. The tissue was chopped using two scalpel blades and then mechanically dissociated into a single cell suspension by pipetting with a plastic tip (1 mL) pipette. The resultant suspension was passed through a cellular sieve (30 µm) and cultured in non-treated flasks to form stem cell enriched neurospheres in neural stem cell media[230].

2.2.2 Neurosphere propagation

The Neural stem cell (NSC) defined serum-free media was made using DMEM/F12 (1:1), B27 (1:50), N2 (1:100), L-Glutamine (2 mM), hEGF (20 ng/mL), bFGF (10 ng/mL) and Heparin (5 µg/mL). Penicillin/Streptomycin solution (0.4ml per 100ml of media) was added during the first two passages of the neurospheres and excluded afterwards. Neurospheres were subcultured for less than 15 passages. Briefly, when the neurospheres reached a diameter of 100-300 µm they were rinsed with PBS, resuspended in Accutase (1 mL) and agitated for 5 minutes at 37 °C followed by mechanical dissociation. The suspension was diluted with fresh NSC media and centrifuged at 300g for 5 minutes. The cell pellet was resuspended in Ca²⁺ and Mg²⁺ free PBS and the final single-cell suspension diluted to the desired concentration with NSC media.

2.2.3 Culture of human medulloblastoma cell lines

UW228-3 medulloblastoma cell line [254] was obtained from Prof. Silber (University of Washington, Seattle, USA) with the help of the Children's Brain Tumour Research Centre at the University of Nottingham. UW cells were cultured in DMEM/F12 media supplemented with L-Glutamine (2 mM), sodium pyruvate (1 mM) and FCS (10%). Subculturing was performed using 0.025% Trypsin in Ca²⁺ and Mg²⁺ free PBS solution for 5 minutes.

DAOY cell line was obtained from the ATCC (HTB-186) by Prof. Terry Parker. The VC312R² (VCR) medulloblastoma cells were a gift from Prof. Geoff Pilkington (School of Pharmacy and Biomedical Sciences, University of Portsmouth, UK). Both cell lines were maintained in 75 cm² flasks in DMEM medium supplemented with 10% Foetal Calf Serum and 200 mM glutamine (Full culture medium, FCM) at 37 °C and 5% CO₂.

2.2.4 Mycoplasma testing

Mycoplasma testing was performed independently by a trained technician with a Mycoalert mycoplasma detection kit (Lonza, Rockland, USA) according to the manufacturer's instructions. Cell-free media was collected after incubating for 48h with the cells and mixed with equal volume (100µl) of Mycoalert reagent in 96-well white plates. Luminescence was read on a POLARstar plate reader (BMG Labtech, UK) after 5 minutes incubation, (Reading 1) followed by a further 10 minute incubation with 100µl Mycoalert substrate. A second luminescence reading was then taken (Reading 2) and the ratio of Reading 2/Reading 1 calculated. Ratios higher than 1.0 indicated the presence of mycoplasma contamination. Positive and negative controls were used for validation.

2.2.5 Cell line authentication

The human origin of the UW228-3 cell line was established in the lab by Ramadhan Othman[255] through sequencing of human β-actin using polymerase chain reaction. Moreover the cell line was further

² See Section 1.3.3.2 for the controversies surrounding DAOY and VC312R

characterised as Group 3 based on NPR3 positivity[228]. A limitation of this work is the lack of cell line authentication for the DAOY and VC312R cell lines and the absence of short tandem repeat (STR) analysis.

Section 2.3 Methods for spheroid production

2.3.1 Non-adherent cell culture flasks

Human foetal neural tissue was routinely cultured as neurospheres in non-treated cell culture flasks using neural stem cell media and they formed numerous spheroids with a broad size distribution. When plated at 200-400 kcells/ml they slowly grew to 100-300 μm spheroids before being subcultured after a period of 4-7 days.

UW228-3 and VCR cells also formed heterogeneous neurospheres in those conditions. However they grew much quicker, required frequent media exchanges and reached 300 μm size within 3-4 days.

2.3.2 3D Biomatrix hanging drop plates

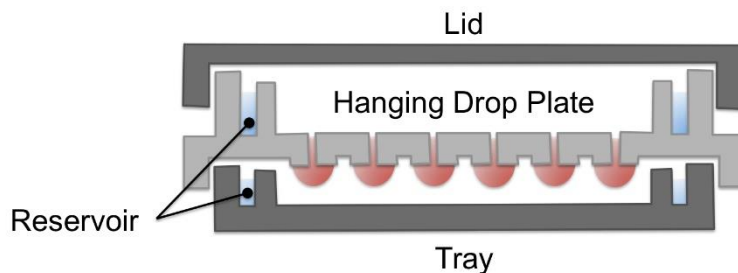


Figure 2-1. Schematic representation of the 3D Biomatrix system. The 3D Biomatrix platform is made up of three plastic plates. The bottom one is called the tray, forms the base and has a channel that acts as a reservoir of water maintaining humidity and protecting the hanging drops from evaporating and causing osmotic shock. The middle plate has 384 holes where the cell suspension is dispensed and the hanging drops are formed. The third plate is a lid that seals the whole system.

Spheroids were formed according to manufacturer's instructions[256] and the work of Tung et al[257]. A cell suspension was prepared to the desired concentration and the reservoirs of the tray and the hanging drop plate were prefilled with either molten agarose solution (1%) or PBS. Cell suspension (20-30 μL) was pipetted into the holes of the hanging drop plates so that the solution would flow and hang to the bottom of the plate as shown in Figure 2-2:

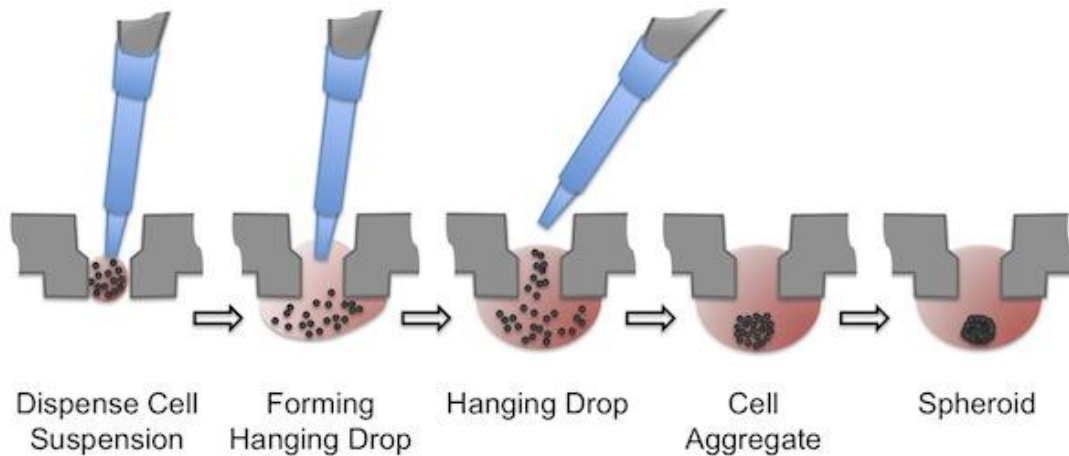


Figure 2-2 Dispensing cell suspension in order to form hanging drops

After forming the hanging drops the lid was closed and the whole system placed in an incubator at 37 °C and 5% CO₂. Gravity brings the cells in close contact at the edge of the drop and they start forming spheroids within 24h by secreting their own extracellular matrix to hold them together. Every other day 7 µL of media were removed and replaced with 10µL of fresh media.

2.3.3 3D microtissues agar moulds

The 3D-petri dish is a system for scaffold-free spheroid production which is composed of a plastic micro-mould that is used to cast agarose gels Figure 2-3

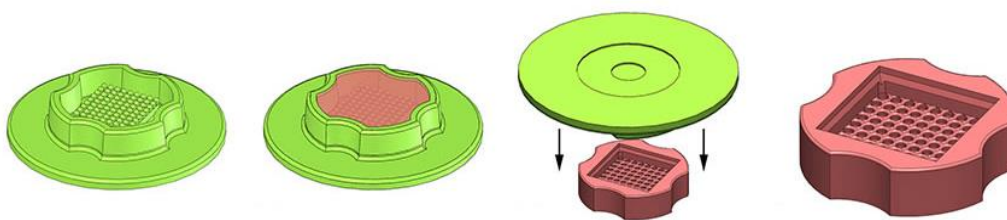


Figure 2-3 The 3-D petri dish plastic mould and the process of casting an agarose gel for culturing spheroids When a cell suspension is dispensed in the rectangular recess (seeding chamber) of the agarose gel, the cells settle down in the numerous wells and form spheroids in liquid overlay culture.

Spheroids were formed according to manufacturer’s protocol[258], [259]. Both the micro-moulds and the agarose were autoclaved before the experiment. The agarose was dissolved in PBS by microwaving until boiling. The molten agarose was allowed to cool down to 70 °C and 500 µL of the solution was pipetted into the micro-mould. The micro-

mould was placed in a 6-well plate in the fridge to cool down and the agarose gel gently removed by flexing the assembly. The agarose 3D Petri Dish™ was then incubated twice with cell culture medium for 15 minutes and excess media removed. The cell suspension was dispensed in the seeding chamber and allowed to settle into the wells for 20 minutes. Afterwards additional medium enough to cover the petri dish was added to the outside of the petri dish. Spheroids were formed in 24-48h.

2.3.4 Ultra-low attachment plates

Ultra-low attachment (ULA) 96-well round bottom plates are commercially available plates pre-coated with a hydrophilic polymer that prevents attachment and triggers the formation of a single spheroid per well. Using these plates, spheroids of different size were formed in NSC media with both cell types using single-cell suspensions with a constant volume of 200 μ L and concentrations ranging from 250 to 200 000 cells per ml. The plates were centrifuged lightly at 100g for 3 minutes after seeding to bring the cells closer together, minimize cell death and encourage the formation of a single spheroid [260], [261]. Old medium was carefully exchanged with fresh (150 μ L) on days 3 and 5, taking care not to disturb the spheroids, and spheroids were cultured for 7 days before final analysis.

Section 2.4 Tissue processing

Prior to processing all tissues were fixed using paraformaldehyde solution (PFA, 4%) in PBS. Incubation time was 15 minutes for cell suspensions and 40 for spheroids followed by a wash with PBS. Spheroids for wax embedding were dispersed in a warm agarose solution (5 %, 500 μ L, Type IA). The agarose was allowed to set and the excess gel that did not contain any spheroids was removed using a scalpel. The tissue was processed using a Leica TP1020 tissue processor on a 16h cycle with xylene. The wax embedded tissue was cut on a Microtome (Slee Cut 4060) at 10 μ m sections. Sections were mounted on Aminopropyltriethoxysilane coated slides with distyrene plasticizer in xylene.

Section 2.5 Spheroid viability assessment

2.5.1 Spheroid volume determination – microscopy and image-analysis

Images of all spheroids were taken daily for growth determination and on day 3, day 5 and day 7 in cytotoxicity experiments using an Olympus CKX41 microscope with a 10X objective and an attached Olympus E330 camera. The scale of images was determined using a calibration slide. Images were analysed using the open-source software ImageJ (Fiji package) and a macro was written to automate the process (Supporting information macro S1). The macro works on whole folders of images, converts them to black and white, and uses the Yen thresholding algorithm [262]. It proceeds to clean any artefacts from the image, fills holes in the spheroid, separates it from debris and determines the area, maximum and minimum Feret diameter of the spheroid. The maximum Feret diameter, also known as calliper diameter, measures the longest distance between any two points of the spheroid boundary. The minimum Feret diameter measures the minimum distance between the boundaries of the spheroid. The macro also saves a copy of the file of each analysed image with a blue outline of the spheroids it has detected and an additional file with the numerical measurements for the whole folder. Variation in the area determination between the algorithm and manual measurement was found to be less than 5%. Data from the macro was analysed in Excel and the measured area (S) of the 2D projection of the spheroids was used to calculate the radius ($R = \sqrt{\frac{S}{\pi}}$) and the volume ($V = \frac{4}{3}\pi R^3$) of an equivalent sphere [263].

2.5.2 Resazurin (Alamar Blue) assay

A stock solution of resazurin (440 μM in PBS), was aliquotted and stored at -18°C . Frozen aliquots were thawed and kept in the fridge before use, protected from light. On the day of analysis a working solution of 60 μM resazurin was prepared in NSC medium. Medium in the wells was partially replaced with working solution (150 μL) and the plates were

placed back in the incubator. Fluorescence was measured with an excitation wavelength of 530 nm and emission 590 nm on a Galaxy Fluostar plate reader at 4h after dye addition.

2.5.3 Acid phosphatase assay

Acid phosphatase (APH) activity was determined using 4-nitrophenyl phosphate as described by Friedrich [264], [265]. The APH assay was performed on the same spheroids after the Resazurin assay. Resazurin was removed using two washes with PBS to leave 100 μ L, APH assay buffer (100 μ L), containing para-nitrophenylphosphate (PNPP, 2 mg/mL), TritonX (0.1 % vol/vol) in Citrate buffer (0.1 M), was added and the plates incubated for 90 minutes at 37 °C. Afterwards NaOH (1 M, 10 μ L,) was added to the wells and the absorbance was read at 405 nm with a reference wavelength of 630 nm on an Asys Expert 96-well plate reader.

2.5.4 Cell number determination

After volume and Resazurin assays, spheroids from the growth kinetics and cytotoxicity experiments were dissociated and counted. Dissociation was carried out after washing the spheroids twice with Ca²⁺ and Mg²⁺ free PBS (150 μ L), removal of PBS, followed by 20 minute incubation with Accutase (50 μ L) at 37 °C. Mechanical dissociation with a multichannel pipette was carried out to form a single cell suspension and all six wells representing the same conditions were pooled in a microcentrifuge tube and centrifuged at 300g for 5 minutes. The supernatant was taken off and the cells were resuspended in PBS (200 μ L). Cell counts were performed using the Orflo Moxi Z automated thin-film sensor cell Coulter counter. The Moxi Z software has an internal curve-fitting algorithm which finds the healthy part of the cell population and expresses overall viability based on cell size reduction and debris content without the use of special reagents.

Section 2.6 Marking cells with tracer dyes

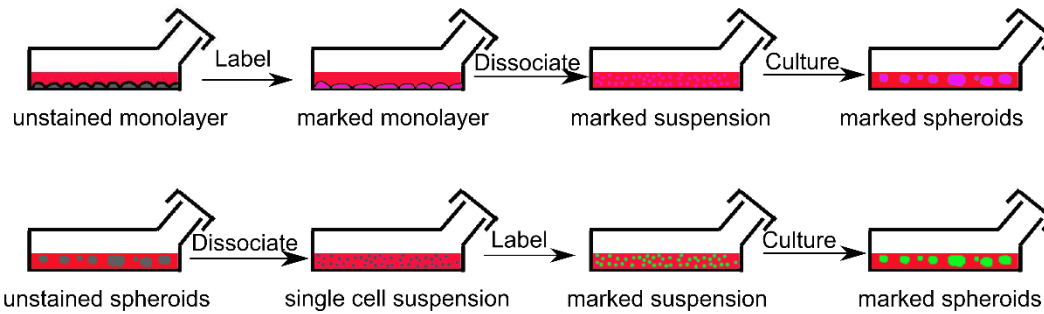


Figure 2-4 Cell labelling strategy for tumour monolayers and foetal neurospheres. VCR and UW228-3 cell were stained in monolayer (top row), while neurospheres had to be dissociated and stained as a single cell suspension (bottom row). In initial experiments cell were cultured in non-adherent flasks forming spheroids of all sizes. Later ultra-low attachment plates were brought to increase reproducibility and facilitate analysis and quantification.

Initial experiments included the VCR cells and were done in non-treated flasks. Varying labelling conditions (HBSS, PBS, media), concentrations (5-40 μM) and dye exposure times (5-30 minutes) were tested in effort to minimize staining toxicity while maintaining high cellular fluorescence.

After the adoption of the ultra-low attachment plates and the substitution of the VCR cell line with UW, cell marking optimisation screening was performed with UW and NSC cells with both CellTrace Violet and CDCFDASE in concentrations ranging from 2.5 to 20 μM .

UW228-3 (UW) cells were labelled in monolayers prior to culturing as spheroids. Cells, grown to 80% confluence in cell culture treated flasks, were washed twice with HBSS (with Ca^{2+} and Mg^{2+}) and incubated with 2.5-20 μM concentrations of CDCFDASE and CellTrace Violet in HBSS (with Ca^{2+} and Mg^{2+}) for 30 minutes at 37 °C. Afterwards they were washed twice with HBSS and incubated for further 3-4 hours in FCM in order to remove any unconjugated dye. The labelled cells were dissociated using 0.025% Trypsin

Human foetal neurospheres (NSC) were dissociated and the cell suspension was incubated with 2.5-20 μM concentrations of CDCFDASE and CellTrace in HBSS for 30 minutes at 37 °C.

Both cell types were seeded in ultra-low attachment plates (200 μ L, 7000 cells per well). The plates were centrifuged lightly at 100g for 3 minutes after seeding and the cells organised into one single spheroid per well within 24h. Controls of unstained cells of each type were included in every plate. Old media were carefully exchanged with fresh media (150 μ L) on days 3 and 5. Spheroids were cultured for 7 days before final analysis.

The effect of both cell marker dyes on spheroid proliferation and metabolic activity were assessed by comparing marked spheroid volume and metabolic activity to unstained controls. Flow cytometry was used to assess dye retention in each condition.

Section 2.7 Co-culture of human foetal neurospheres and tumours

Co-culture spheroids were established by plating a homogenous mix of fluorescently labelled tumour and normal cells (200 μ L, 3500 cells/well from each type) as a single-cell suspension in ULA plates at the same time. Co-culture spheroids formed in 24h and were cultured for 7 days, exchanging with fresh media (150 μ L) on days 3 and 5.

Section 2.8 Poly (glycerol adipate) synthesis and substitution

2.8.1 Backbone synthesis

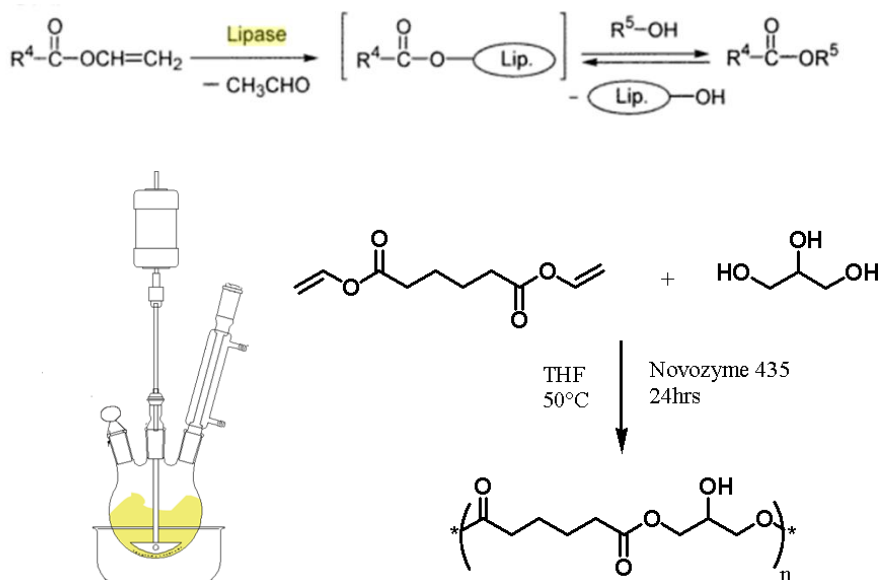


Figure 2-5 The synthesis of poly(glycerol adipate). Lipases are hydrolytic enzymes that can catalyse both hydrolysis and esterification. They can work in organic solvents and the reaction is driven to completion because acetaldehyde is released through the condenser. Their preference for primary hydroxyl groups determines the predominantly linear structure of the product.

Equimolar quantities (0.05 mol) of Divinyl adipate (DVA, 9.91g) and glycerol (4.6 g) were added to a clean, dried three-neck 250 ml round bottom flask, followed by THF (15 ml). The flask was maintained at 50 °C and allowed to equilibrate for 10 minutes. A stirring rod fitted with a Teflon paddle was placed in the flask, with the stirrer paddle held just above the bottom of the flask (approximately 2-3 mm) to limit crushing of the enzyme support. A mechanical overhead stirrer (Heidolph RZRI stirrer) was secured over the water bath with the stirring rod held in place with a Quickfit thermometer adaptor. The system was also fitted with an open top condenser (to enable release of the acetaldehyde produced as a by-product of the reaction) and the free open neck of the flask stoppered. To such a set-up, 1 g of Novozyme 435 was added via the available flask neck and the residual resin washed from the sides of the glassware with an additional 5 ml THF (making the total volume of

THF used 20 ml). Stirring commenced at 2000 rpm and the reaction was allowed to proceed for 24 hours.

Afterwards THF (100 ml) was added to the flask, washing any residual polymer off the stirring paddle. The contents of the flask were then vacuum-filtered by standard Buchner filtration through 2 layers of GF/A (Whatman) filters to remove the residual immobilised enzyme. The filtrate was poured into a round bottomed flask and the solvent removed via rotary evaporation at 80 °C (Laborota 4000, Heidolph Instruments attached to Rotavac plug and pump). The flask was then heated to 100 °C for 30 minutes. The resultant viscous polymer sample was transferred into a jar and stored for 48h in the vacuum oven (60 °C) to remove any traces of solvent, then sealed and stored over silica gel in a desiccator.

2.8.2 Polymer characterisation

All synthesised polymers were analysed by gel permeation chromatography (GPC). Gel Permeation Chromatograph (GPC) results were obtained using a Polymer Labs GPC-120, run with HPLC THF at 40 °C with a flow rate of 1 mL/min, using two PolarGel-M columns and calibrated with polystyrene standards. The polymer samples were prepared at 10 mg/mL in THF in a dry glass vial prior to filtration through a 2 µm syringe filter.

The GPC results from this setup were compared after analysis in Liverpool where the setup included a Viscotek system, TDA Model 300 coupled to a gpcMAX integrated solvent and sample delivery module (degasser, pump and auto-sampler) ran by OmniSEC3 software and two ViscoGEL GMHHR-N columns.

The solutions were mixed for an hour on the roller-mixer (SRT1) to allow the polymers to fully dissolve. The samples were then filtered (0.2 µm PTFE syringe filters, Whatman) into 2.0 mL glass vials. PTFE septa (Sigma) were used in the vial lids to avoid solvent evaporation and clogging up of the injecting needle. Control (THF) samples were run prior

to the other samples. The mean molecular weight M_w of the main peak was taken as the average molecular weight of the polymer batch.

$^1\text{H-NMR}$ analysis of the PGA polymers (2mg) was performed using deuterated acetone ($(\text{CD}_3)_2\text{CO}$, $\delta_{\text{H}}=2.05\text{ppm}$) as solvent (0.7ml) on a 400Mhz Bruker spectrometer. The data was processed using MestReNova 6.0.2 software. The NMR spectra were used to verify polymerisation of PGA and determine degree of substitution in the substituted polymers[266].

2.8.3 Acylation with C8 and C18

Substitution of the secondary hydroxyl group in the backbone polymer was carried out using the relevant acyl chloride in THF with the addition of pyridine as a catalyst and acid scavenger (Figure 2-6)[176].

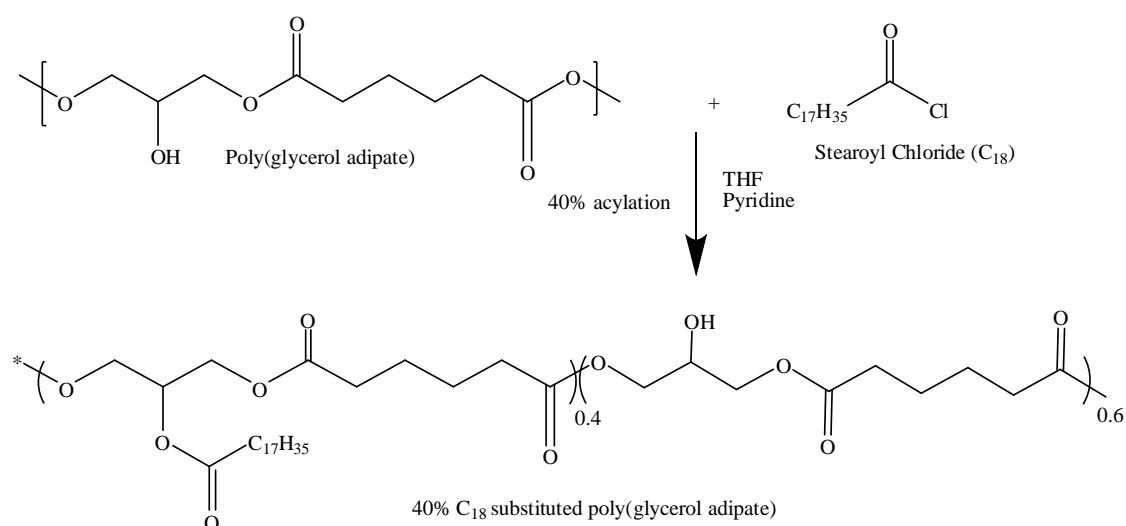


Figure 2-6. Substitution of the pendant hydroxyl groups in poly(glycerol adipate) with 40% Stearic acid as described by Kallinteri[176].

Poly(glycerol adipate) (2.10 g) was dissolved in dry THF (10 mL) and the mixture heated to reflux until the polymer was dissolved followed by the addition of acyl chloride (1.4 mL for stearoyl chloride). Afterwards, pyridine (0.4 mL) was added and the reaction refluxed (2 h) and then poured onto HCl (2 M, 100 mL) and followed by extracting three times using DCM (50 mL). The organic phase was collected and washed then with water (100 mL), dried over magnesium sulphate and the solvent removed by rotary evaporation to a white waxy solid.

Section 2.9 Nanoparticle preparation and characterisation

2.9.1 Nanoprecipitation

Polymer and drug/dye in acetone

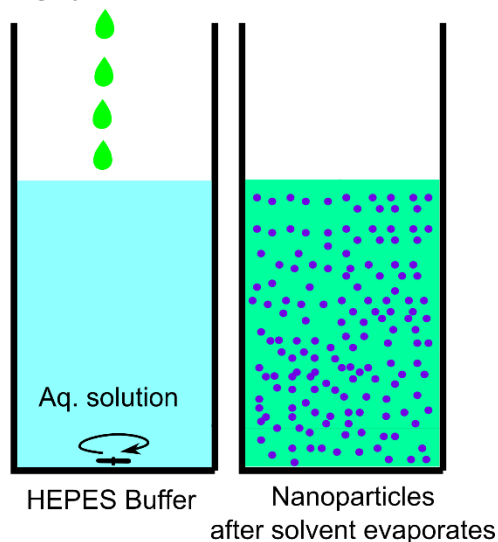


Figure 2-7. The nanoprecipitation method for nanoparticle production. A water-miscible solvent (acetone) is used to dissolve the polymer along with the drug or dye to be encapsulated. The organic phase is added to an aqueous solution (buffer or surfactant) under stirring. Nanoparticles are formed immediately and the solvent is left to evaporate

Fluorescently-labelled nanoparticles were produced as described by Meng[179]. Briefly 100%-C18-substituted PGA (20 mg) were dissolved in acetone (2 mL) containing RBITC (125 μ L, 2 mg/mL in methanol). The solution was added dropwise into HEPES buffer (10 mM, pH=7.4, 7 mL) under stirring.

Etoposide-loaded nanoparticles were produced according to the method described by Puri[180]. Etoposide (2 mg) and 40%C8-PGA (10 mg) were dissolved in acetone (1 mL) and evaporated to dryness by blowing dry N_2 . After an hour the matrix was dissolved in acetone (1 mL) and quickly added to water (5 mL) under stirring.

A different procedure was employed in the polymer library screening experiments in Chapter 6. Etoposide or teniposide (1.5 mg) and polymer (10 mg) dissolved in acetone (1 mL) were mixed with water (2 mL) using a chamber mixer (Pharmacia, 50-60 Hz, 5 MPa).

In all cases the vials were protected from light using aluminium foil and were left under magnetic stirring, in a fume hood overnight to remove residual acetone. The suspensions were filtered through a 0.45 μm syringe filter before separation of the free drug.

2.9.2 Emulsification-solvent evaporation

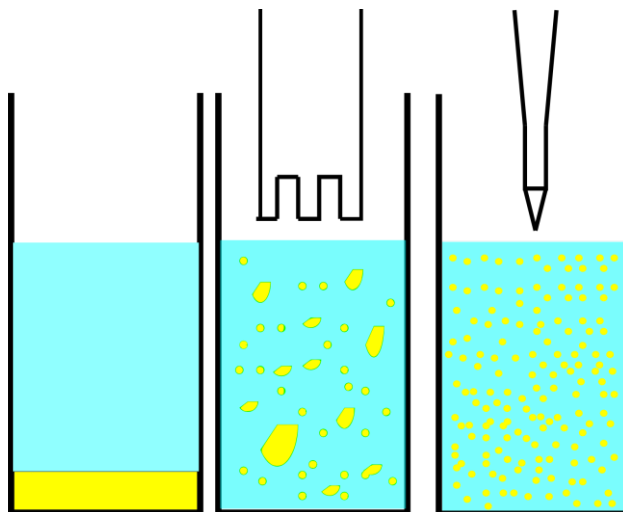


Figure 2-8 Solvent-emulsification method for nanoparticle production. The polymer and drug are dissolved in a solvent with very limited water-miscibility (DCM, CHCl_3 , Ethyl acetate or Benzyl alcohol). The mix is homogenized under high-shear forces to form a coarse emulsion. High-energy techniques such high-pressure homogenizing or ultrasonication are used to form nanoemulsion. The solvent is later removed either by dilution or more often through evaporation at reduced pressure.

Etoposide or teniposide (3 mg) and polymer (17 mg) were dissolved in dichloromethane (DCM, 1 mL) and mixed with water (4 mL) with or without the addition of different surfactants using a high-shear mixer (Ultra-Turrax, IKA T25) for 1 minute at 24000 rpm. The resultant coarse emulsion was immediately sonicated with a probe sonicator (Bandelin UW2070, 60%power, 2 minutes). The Nanoemulsion was evaporated using a rotary evaporator at 30 $^{\circ}\text{C}$. The resultant nanoparticles were filtered through a 0.45 μm syringe filter and rapidly transferred for separation of the free drug.

2.9.3 Separation of free drug from nanoparticles

The loaded nanoparticles were separated from the free dye or drug via Low pressure gel permeation chromatography using a SepharoseCL-4B column (2.5x25 cm, GE Healthcare) [267]. The setup was automated

with a peristaltic pump, a UV detector (280 nm) and autosampler that collected 2 mL fractions. As seen in Figure 2-9, the macromolecular nanoparticles would not enter the cross-linked gel and eluted first while the lower molecular weight drug/dye would enter the pores of the gel and had a longer retention time. Separation was verified using the UV detector by the separation between the nanoparticle and drug/dye peak.

Later for the extensive polymer screening campaign when higher throughput was desired the Sephadex GH25 (PD-10, GE Healthcare) columns were employed. These columns can separate up to 2.5 mL of nanoparticle suspension. A control with a solution of the free drug without any polymer was included to verify separation of nanoparticles from unincorporated free drug.

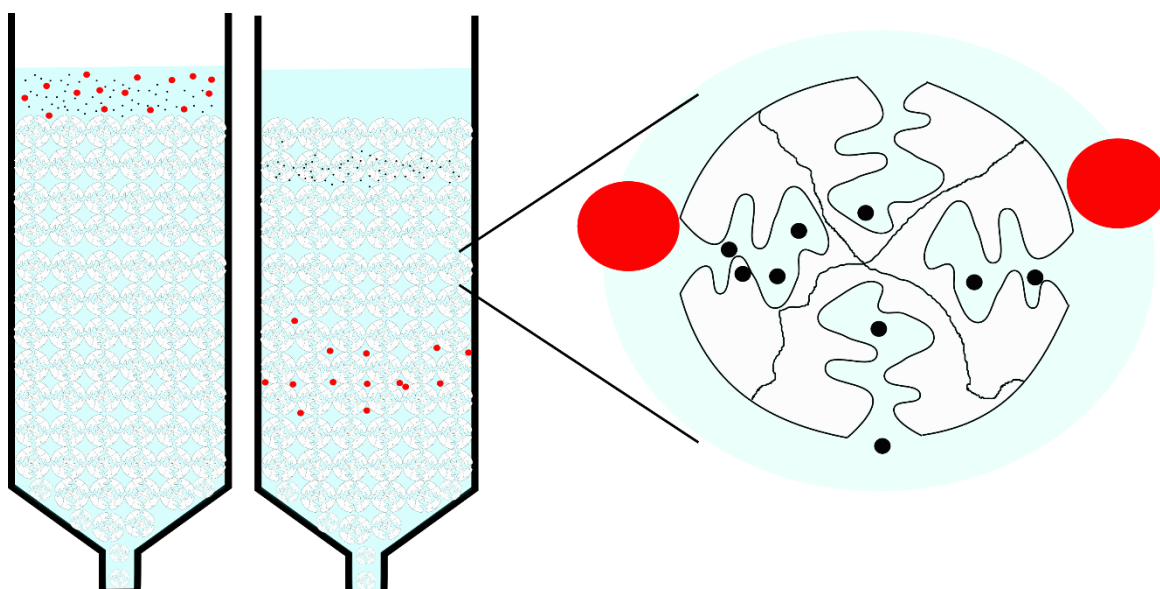


Figure 2-9. Schematic representation of gel-permeation chromatography. The columns are filled with cross-linked polymers comprised of gelled particles with multiple pores. Small molecules (black dots) enter the pores and are retained longer on the column while big particles (red dots) are excluded by the pores and are eluted first. Left panel shows columns with nanoparticles eluting while drug is retained. Right panel shows a magnification of a single gel bead and the size-exclusion mechanism.

2.9.4 DLS and Zeta potential

The main technique used to determine the size of the nanoparticles made in this work was dynamic light scattering (DLS). The term is synonymous with photon correlation spectroscopy (PCS) and quasi-elastic light scattering (QELS). DLS is used to determine sizes for particles dispersed in liquid. It is called dynamic light scattering because it measures the

variations in the intensity of scattered light over time, while static light scattering (SLS) gives a time-averaged value and is used to measure molecular weight and radius of gyration.

In the typical DLS setup, a collimated monochromatic laser light is used to illuminate a dispersion of nanosized (0.5-1000nm) particles in solution. The fluctuations in the intensity of scattered light are measured over time at a set angle (90° for the Viscotek 802). These fluctuations are caused by the random Brownian motion of the submicron particles and depend on their size- smaller particles cause more rapid fluctuations in light intensity while bigger particles cause slower fluctuations. What is really determined in DLS experiments is not the size but the diffusivity of particles in the medium:

$$D = \frac{kT}{6\pi\eta r} \quad \text{Equation 2-1.}$$

D-diffusion coefficient	k-Boltzmann constant
H- viscosity of the media	T-absolute temperature

The radius (r), calculated using this Stokes-Einstein equation is the so-called hydrodynamic radius in the solvent (water). The particle shape is assumed to be spherical and the concentration of particles should be low enough to prevent multiple scattering from different particles.

A limitation of DLS arises when polydisperse mixtures of particles are analysed. The intensity of scattered light using the Rayleigh approximation is proportional to the sixth power of the radius (r⁶) which leads to overestimations in the percentage of large particles by intensity measurements. For Rayleigh scattering, particles with a diameter smaller than the laser wavelength by a factor of 10, mass and number distributions can be calculated by dividing to the d³ and d⁶ respectively. However, these computations are mainly valid for particles with diameters less than 50nm[268].

As a surrogate measure for particle charge, the zeta potential (ζ) of particles dispersed in buffer was determined via Laser Doppler

Electrophoresis. What is actually measured is the electrophoretic mobility of the particles under the influence of an applied electric field.

When a charged particle is dispersed in water, a strongly associated layer of counter-ions attaches to its surface (Stern layer). A more loosely associated diffuse layer surrounds the Stern layer formed under the influence of electrical attraction and thermal motion. When an electrical current is applied, the particle along with the Stern layer and a certain part of the diffuse layer starts moving towards the oppositely charged electrode. The 'slipping plane', where this process occurs, separates the mobile fluid and ions associated with the particle from the fluid associated with the medium. Therefore the zeta potential is a measure of the difference in potential between the particle and medium at the slipping plane in the diffuse layer.

The Zetasizer ZS, uses the shift in phase between a scattered and a reference beam to determine the electrophoretic mobility and the zeta potential of the particles.

Zeta potential in buffered aqueous solutions depends on particle type, buffer concentration and pH. The surface electrical charge is important for colloid particle stability and zeta potential values up to $\pm 30\text{mV}$ are generally expected to confer electrostatic stabilisation of dispersions. Values $\pm 10\text{mV}$ are usually considered approximately neutral.

Section 2.10 Flow cytometry

Flow cytometry is a technique which analyses cells (or micron-sized particles) as they pass through a beam of light. It allows the analysis of multiple cellular parameters within heterogeneous populations with speeds of thousands of cells per second.

In the classical setup a suspension of cells is delivered to the fluidics system of a flow cytometer, which focuses the cells into a thin jet stream. The cells are arranged by the use of hydrodynamic focusing- injecting them in a laminar stream of sheath fluid (buffered saline). The cells are delivered one by one in the fluid stream to one or multiple interrogation points. There is a laser at each interrogation point which illuminates the

cells and the scattered light is collected by detectors in front and to the side of the laser beam. The forward scatter, is the light that is detected in front of the laser beam and is a measure of cell size. The light scattered to the side is detected by the side scatter detector and the recorded signal gives an idea of the granularity and complexity of the cells.

In addition, a carefully arranged optical system of mirrors, filters and detectors splits the scattered light from each laser to a number of different wavelength bands. For example, the scattered light from the most common blue, 488nm, Argon laser can be split into a number of channels spanning green, orange, yellow, and a number of shades of red (Figure 4-1). The information is digitized in the signal processing unit and can be displayed in a variety of ways.

The simplest way of plotting the information is by using a histogram plot. The histogram plot maps the distribution of fluorescence intensity in a single channel for the cell population (Figure 2-10).

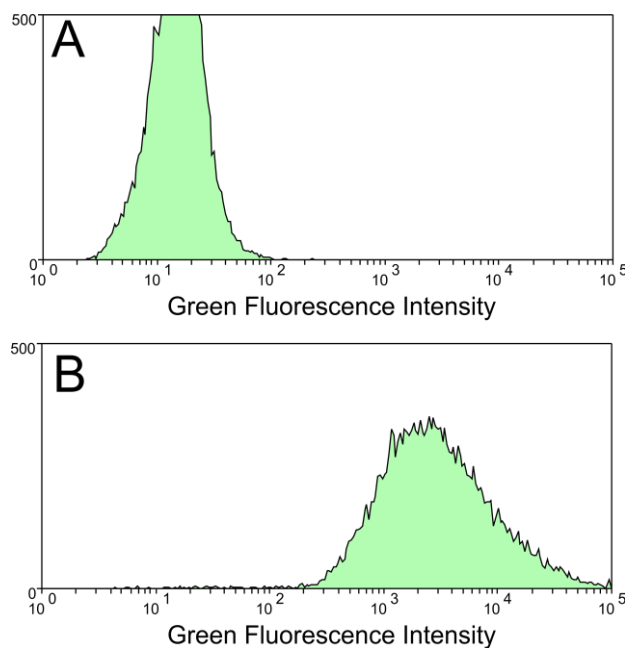


Figure 2-10. Histogram plots of fluorescence intensity for two cell samples. A- control cells without green fluorescent dye. B- cells prestained with green fluorescent dye. X-axis intensity Y-axis number of events.

As seen in Figure 2-10 the control sample has a low fluorescence in the green channel and the whole population is situated to the left of 100

relative units of fluorescence (RFU). In contrast, almost every cell from the stained sample has fluorescence intensity higher than 100 RFU.

Histogram plots can be overlaid so that the control and stained samples are plotted on a single graph (Figure 2-11). This way of plotting the data allows the user to examine whether the intensities of the unstained and stained cells overlap. Here the control and the marked samples are very well separated into two populations.

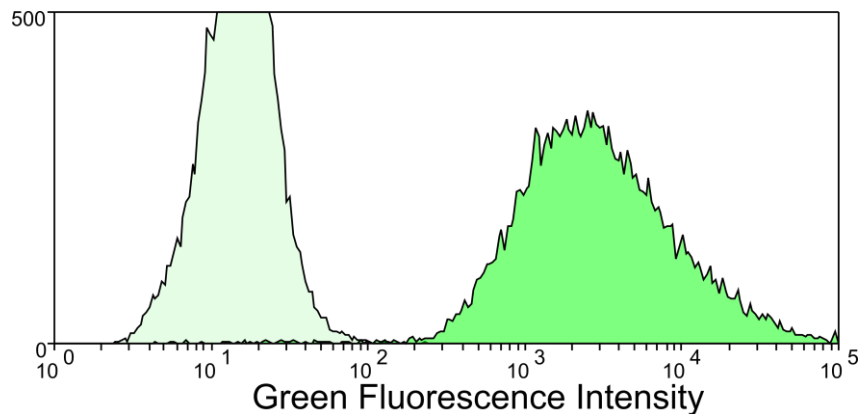


Figure 2-11. Overlaid histograms of non-marked cells and marked cells in the same plot. The lighter-green population to the left is the unstained control. The population to the right is the fluorescently labelled sample.

Another way of presenting flow cytometry data is through the use of dot plots. Dot plots are made by combining two histograms in a single plot and each axis represents fluorescence intensity in the respective channel. Figure 2-12A shows a plot of the intensity in the forward scatter versus side scatter for a sample of unstained cells. In its essence, this is a figure where cell size is plotted on the x-axis and cell complexity is plotted on the y-axis. In the left corner of the plot the particles are very small and simple. Those particles represent the inevitable debris found in the majority of cell suspension samples. Figure 2-12B shows side versus forward scatter for the stained sample. There are no major differences between the two samples because the staining procedure has not affected the size or granularity of the cells. Figure 2-12C shows a plot of the intensity of fluorescence in the green and blue channels for unmarked control cells. As illustrated, the cells have very low fluorescence in each channel. The plot can be subdivided into four quadrant subplots. The lower left quadrant is defined by the unstained control and contains

unstained cells. The lower right quadrant in Figure 2-12C would be reserved for cells which are more fluorescent than the unstained control in the green channel. The upper left quadrant represents cells with blue fluorescence brighter than the control. The upper-right quadrant would be taken by cells brighter than the control in both the green and the blue channels. The utility of this quadrant splitting is seen in Figure 2-12D, where the fluorescence of the stained cells is visualised. It can be seen that around 88.5% of those cells exhibit blue fluorescence brighter than the unstained control. Nevertheless, close to 11% of the stained cells have the same fluorescence as the unmarked control and cannot be distinguished based on this staining procedure.

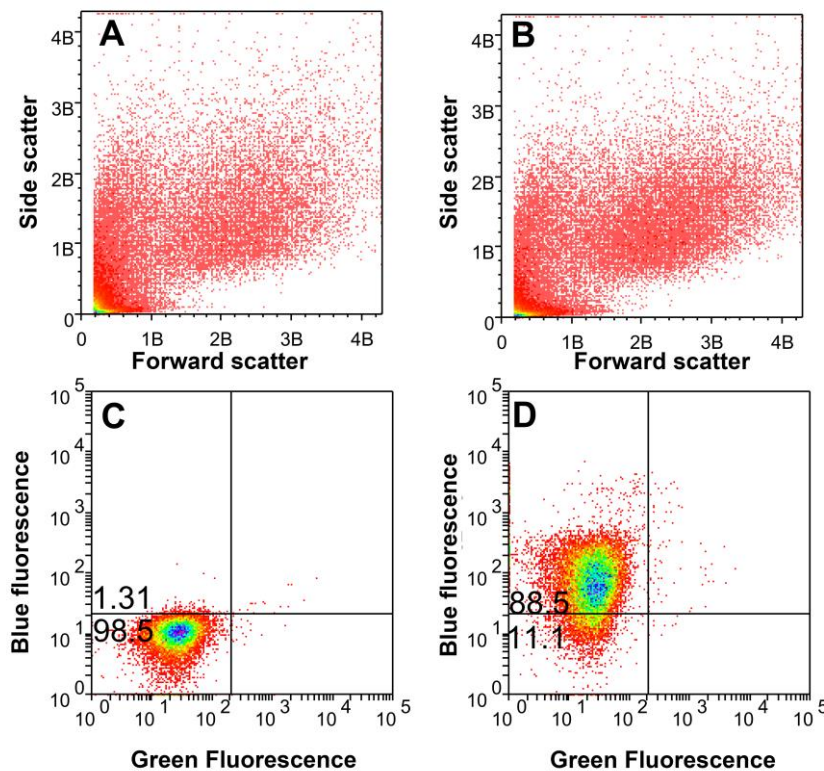


Figure 2-12. Dot plots in flow cytometry. A-side vs forward scatter for unstained control B-side/forward scatter for fluorescently labelled cells; C-dot plot of green vs blue fluorescence in unstained control; D-dot plot of green vs blue fluorescence in cells stained with blue dye.

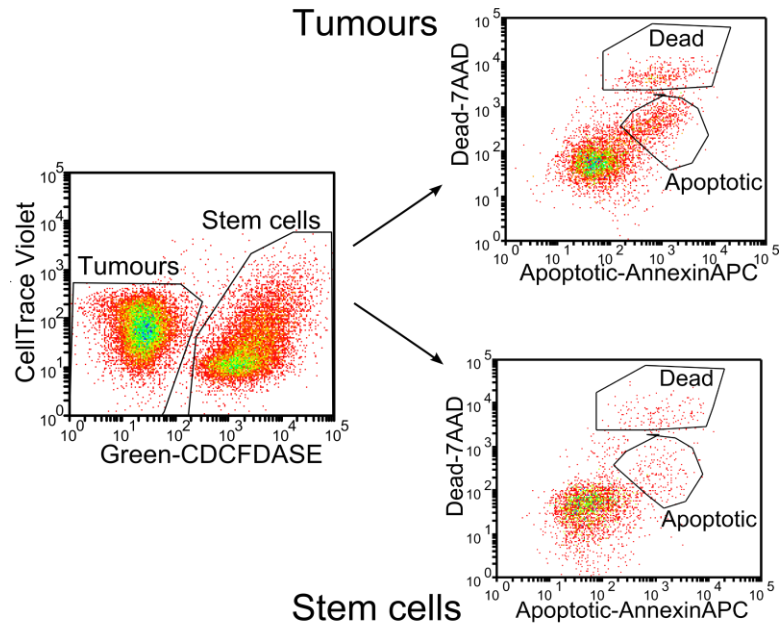


Figure 2-13. Regions and Gating in flow cytometry. The left dot plot plots the intensity in fluorescence in a mixed sample of tumours and normal (stem) cells marked with a violet and green fluorescent dye respectively. Regions of interest are drawn along the green (stem cell) and violet (tumour) populations. When these are applied as gates the top (tumour) and bottom (stem cell) dot plots can be created. In the separate tumour and stem cell dot plots the viability of each cell population is determined separately using viability markers 7-AAD (cell death) and Annexin-V-APC (apoptosis).

A useful technique in flow cytometry is the ability to gate populations of interest by drawing regions which allow analysis of different cell populations in various ways. The single graph in the left part of Figure 2-13 shows a dot plot of the fluorescence intensity in two channels- violet and green. There is a clear separation into two populations- one which is intensely fluorescent in the green channel, and a population that exhibits fluorescence solely in the violet channel. If one applies the prior knowledge that the normal (stem) cell populations have been marked with a green dye and that the tumours have been stained with a violet dye then a region can be drawn around each population. The flow cytometry software can then be used to gate on each population separately and analyse the tumour and neural progenitor cells for their viability status with a combination of viability dyes. More information regarding cell marking and viability dyes will be given in Chapter 4. This figure serves solely to illustrate the utility of gating in flow cytometry.

Another important aspect in flow cytometry and fluorescence is spectral overlap. When a fluorophore is excited it emits light which is centred

around a single wavelength. However, the spectrum of emitted light can be quite broad, gradually tailing off towards the longer wavelengths. For example, when fluorescein is excited by the blue laser, its peak fluorescence is in the green wavelengths but it also spills into the orange and yellow wavelengths. The amount of this spectral overlap will be proportional to the intensity of fluorescence in the main channel and can be accounted for either during acquisition or in the post-processing of data. The process of correcting for the spillover of fluorophores into neighbouring channels is known as compensation. When this is done during data acquisition it is generally referred to as hardware compensation. Compensation can be done using a variety of different software tools as well. The general procedure involves subtracting a certain percentage of the intensity of the fluorophore from the adjacent channels.

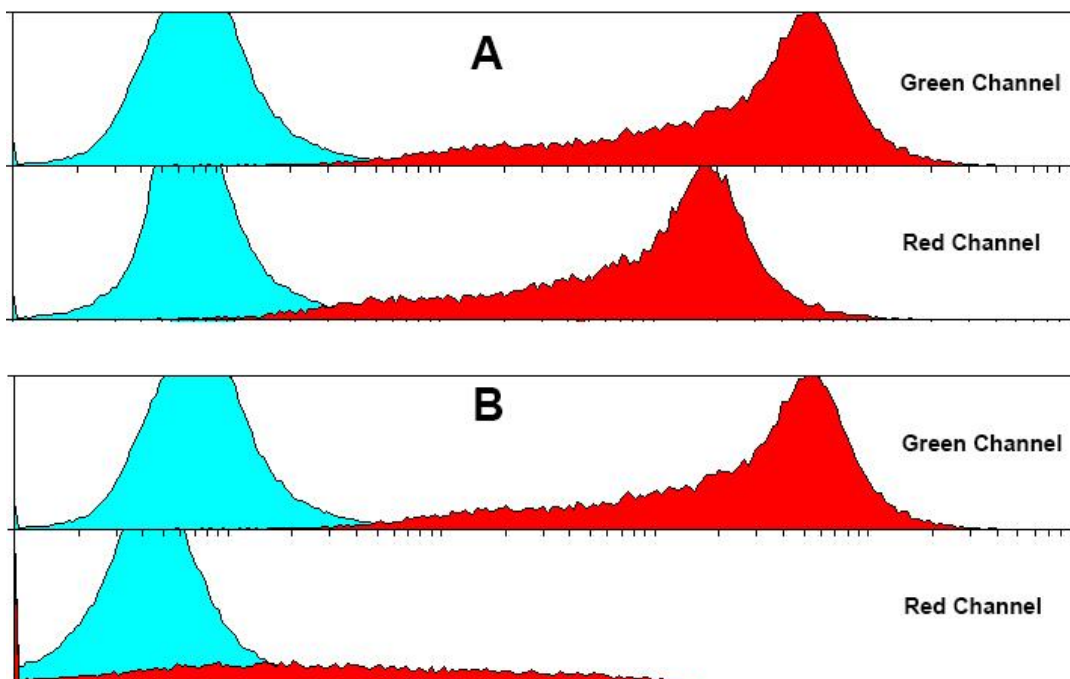


Figure 2-14. Compensation in flow cytometry. Histogram plots in fluorescence intensity in the green channel and the red channel.. Unstained control populations are shown in blue. The stained populations are depicted in red. A shift in fluorescence between the two indicates that the cells are positive for the dye. A-sample stained with CDCFDASE before compensation; B-the sample after applying software compensation.

The utility and limitations of compensation are shown in Figure 2-14. In these experiments cell samples were marked with a dye (CFDA SE) and the fluorescence intensity of the labelled cells (red on the histogram) was plotted against the unstained control (blue population on the histogram).

Figure 2-14A shows the intensity of fluorescence in the desired CFDA SE channel and the spectral overlap in the neighbouring red channel. The stained cells (red) had brighter fluorescence than the control (blue) in both channels. A software compensation algorithm was used to correct for this phenomenon Figure 2-14B. Although the fluorescence in the red channel was minimized, applying compensation did not lead to a simple shift towards the left but had a profound effect in the shape of the histogram of the marked cells. This shows that the spectral overlap was too great to be fixed through simple compensation. The combination of CFDA SE and red dyes was deemed unsuitable for the purposes of this experiment.

Section 2.11 Confocal and multiphoton microscopy

Both confocal and multiphoton microscopy are subtypes of fluorescence microscopy. They use a laser to illuminate a single point in a sample labelled with specific fluorophores and produce an image based on the emitted fluorescence light. What distinguishes them from conventional wide-field fluorescence is the ability to eliminate out-of-focus light and optically section a thick specimen. This means they can produce three-dimensional images in the x,y and z directions. Being able to also image specimens in the vertical axis is especially important for analysing spheroids as they are three-dimensional structures in which the periphery and inner parts of the spheroid often have very different properties.

Confocal laser scanning microscopy[269] focuses laser light through a pinhole aperture to excite a single point in the object of interest. The fluorescence, emitted by the illuminated point, reaches the detector through another, emission pinhole, which serves to eliminate light coming from out-of-focus planes. The object is scanned point by point to produce an image of a single plane. Multiple planes can be sequentially scanned and combined to render a three-dimensional representation of the image. Although the laser light is focused in a single point, the beam illuminates the sample in its entire depth and can cause photobleaching and toxicity[270]. Another limitation of confocal microscopy is that the penetration depth is limited by the opacity of the tissue and the

excitation wavelength of the fluorophore. Spheroids are not transparent and light scattering, especially for the shorter wavelengths (UV, violet, blue) can significantly limit penetration notably in spheroids larger than 100 μm in diameter.

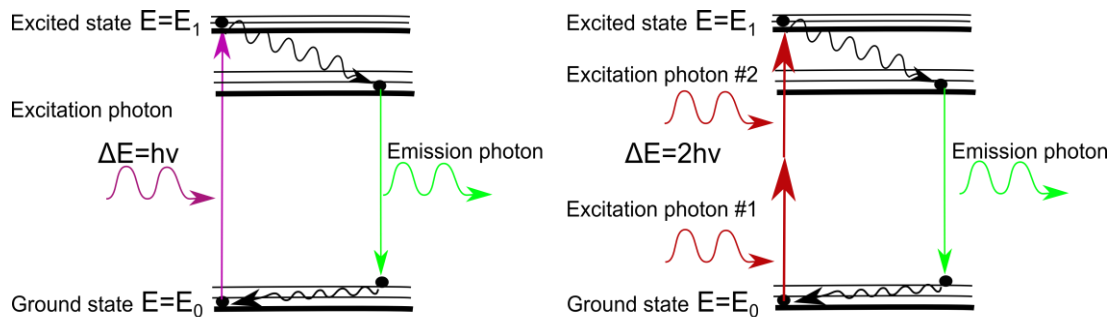


Figure 2-15. Jablonski diagrams comparing one-photon fluorescence and two-photon fluorescence. In one photon fluorescence a fluorophore receives energy from a single photon in order to transition from its ground state to an excited state. After a small non-radiative energy dissipation, the excited fluorophore releases its energy as fluorescent light and returns to the ground state. The emitted photons normally carry less energy than the excitation ones (Stokes shift). In two photon fluorescence, two longer wavelength photons delivered by a femtosecond pulsed laser are used to convert the fluorophore to its excited state.

In contrast to the single photon excitation used in confocal microscopy, multiphoton microscopy excites the fluorophore by delivering two longer wavelength photons in a single point[271]. An infrared pulsed laser is programmed to deliver two photons in a precise focal point in the specimen. This gives multiphoton microscopy a significant advantage over confocal because photobleaching is confined to a smaller area where the two photons coincide. Moreover, the near infrared wavelengths can penetrate deeper into the tissue making the visualisation of spheroids larger than 100 μm possible. Furthermore, since there is no need for a pinhole, more light can reach the detector and brighter images of thick specimens can be achieved[270].

Chapter 3. 3-D monocultures of foetal neurospheres and medulloblastoma cell lines

Section 3.1 Introduction

This chapter shows the development of the prototypical *in vitro* model of medulloblastoma. The purpose was to culture both normal tissue (neural stem cells) and a medulloblastoma cell line separately as spheroids, expose them to different concentrations of etoposide and compare their relative drug sensitivity.

As noted in Section 1.3.3, multicellular spheroids have been reported to match many aspects of the true behaviour of small avascular tumours [243]. Culturing cells in 3D accounts for the complex cell-cell, cell-extracellular matrix interactions, and the formation of nutrient and oxygen gradients which tumours exhibit *in vivo* [237].

Although the advantages of using spheroids in cancer research have been known since the 1970s [210], monolayer cultures are still the primary form of cell-based screening. That is because three-dimensional cultures have been notorious for their slow growth, expensive maintenance and the difficulties associated with viability determination in 3D. In order to match the ease and convenience of 2D assays the ideal 3D screen should be quick, reproducible and amenable to high-throughput using standard methods such as phase and fluorescent microscopy and standard plate readers.

Two methods claim to have all of the above qualities and aim to replace monolayer cultures as the methods of choice for anticancer drug screens: hanging drop plates and overlay cultures. The hanging drop plates developed by InSphero [272] and 3D Biomatrix [257] utilise the 96 and 384 well format and rely on growing the spheroid in a hanging drop. Their main drawback is the need to transfer the spheroid to a normal 96 or a 384-well plate in order to probe viability and proliferation. The liquid overlay method overcomes these challenges and utilises either in-house prepared poly-hydroxyethyl methacrylate [260] and agarose [264] coated

plates or commercially available ultra-low attachment plates [261]. Spheroids grown using the liquid overlay method are scaffold free and the extracellular matrix that keeps them together is naturally secreted by the cells [273]. This is especially advantageous for testing the interaction between submicron delivery systems and tissues. In monolayer assays all cells are exposed to the nanoparticles. In contrast, the presence of extracellular matrix in spheroids mimics the obstacles to nanoparticle penetration in a more physiologically relevant way.

Although both liquid overlay and the hanging drop methods can produce spheroids with diameters of 100 μm to over 1 mm, the preferred size for analysis is 300-500 μm . This ensures that the right pathophysiological gradients of oxygen and nutrients are present along with a core of hypoxic quiescent cells thought to be responsible for the increased chemo- and radioresistance of spheroids and solid tumours [216], [217], [264]. Another reason for choosing this size range was to match the size of avascular small metastases and leftover tumour tissue, which were identified as the primary target of the nanoparticle delivery system as discussed in 1.3.3.1. A preliminary search for the optimal platform to culture the normal foetal neurospheres and medulloblastoma cells was initiated. The priority was to establish a cell-based analytical platform with optimal levels of speed and reproducibility in order to faithfully determine dose-response relationships for a number of formulations.

The replacement of monolayers by 3D cell culture will require validated, cost-effective, high-throughput compatible methods to assay spheroid growth, viability and the effects of treatment. Over 50 years of spheroid research has shown that the growth of cells in three dimensions is only advantageous in a practical sense if analysis is rapid and reliable in high throughput and with standard equipment. Since liquid overlay cultures are stationary and produce a single spheroid in the middle of each well, tracking growth can be easily accomplished with phase-contrast light microscopy. Images of the spheroids in each well can be collected and analysed using specialised equipment like the Celigo cytometer [261] or commercial software programmes [261], [264], [274]. However, the investment in new equipment or image editing software can be seen as a

hindrance to the mainstream implementation of spheroid research. Therefore, it was decided to work with the open-source software ImageJ and develop an in-house automated macro for spheroid analysis to facilitate image analysis within the scientific community.

Apart from volume, cell viability within the spheroid can be assessed using metabolic assays like the reduction of Resazurin [275] or measuring ATP [261]. These assays are convenient and quick, however, they have not been properly validated for use in 3D cultures yet. Friedrich et al [265] have validated and encouraged the use of the acid phosphatase assay to determine viability and claimed that metabolic assays may not be equally suited for the task.

This chapter describes the pathway for development of the simpler, separate culture version, of the two *in vitro* medulloblastoma models. In this instance, the neural stem cells and medulloblastoma tumours were cultured in separate wells apart from one another. The main focus was throughput plus reproducibility, and viability was chosen as the primary endpoint. Spheroid volume, metabolism and acid phosphatase activity were employed as surrogate markers for viability.

The brain tumour medulloblastoma cell lines DAOY and VCR were used in the initial experiments and later UW228-3 was chosen to represent the pharmacological target of treatment. Human foetal brain tissue spheroids cultured in neural stem cell media to enrich for neural progenitors were selected to determine possible off-target effects on the developing brain. Etoposide was used in those experiments as the initial plan was to compare the sensitivity of the cells to free etoposide at this stage and include etoposide-loaded nanoparticles later.

Section 3.2 Materials and methods

3.2.1 Cell lines and culture

All experiments were performed in standard cell culture conditions at 37 °C and 5% CO₂ as described in Section 2.2

3.2.2 Doubling time determination for UW228-3 cells in monolayer

Uw228-3 cells were dissociated, suspended in FCM and 400 000 cells were seeded in 75cm² cell culture treated flasks. Cells were cultured for 60-80 hours, dissociated and counted using a haemocytometer. Initial and final cell counts were fitted to an exponential growth equation using GraphPad Prism 6.0 and the doubling time was determined as an average from three independent experiments.

3.2.3 Monolayer sensitivity to etoposide

Adherent cultures of UW228-3 cells were exposed to etoposide in order to determine their intrinsic sensitivity to etoposide while actively growing in monolayer. UW228-3 were dissociated, suspended in full culture medium and seeded in tissue culture treated flat bottom 96-well plates (150µl, 500cell/well). The initial seeding density was chosen to ensure exponential growth for the duration of the assay, after an optimisation screen with seeding densities from 500-10000 cells/well.

Cells were left to attach for 24h, the old medium was replaced with half-log₁₀ dilutions of etoposide (1nM-100µM) in FCM (150µl) and the cells incubated with the drug for 48h. DMSO levels were kept constant at 0.2% for all wells, the untreated control was used to determine 100% viability and 25%DMSO was used as positive control for complete cell kill. After drug treatment the old medium was replaced with fresh drug-free medium and the cells were incubated for further 48h. On the last day the viability of the cultures was determined using resazurin reduction (2h incubation) after complete medium renewal. There were six replicate wells for each condition and dose-response curves were plotted as the average of three independent experiments.

3.2.4 Spheroid production using the 3D Biomatrix platform

Spheroids were formed in the hanging-drop plates according to the manufacturer's manual and the methods described in section 2.3.2

3.2.5 Production of spheroids using 3D Microtissues® agar moulds

Spheroids were formed according to manufacturer's protocol [258], [259] as described in Section 2.3.3

3.2.6 Tissue processing for histology and Haematoxylin and eosin staining

Tissue processing was done after fixation with 4% polyformaldehyde as per Section 2.4

3.2.7 Spheroid production in ultra-low attachment plates

Ultra-low attachment plates were used as shown in Section 2.3.4

3.2.8 Phase microscopy and image analysis

Image analysis and volume measurements were done with the specialty written ImageJ macro as described in Section 2.5.1.

3.2.9 Growth kinetics

UW228-3 cells were seeded in ULA plates at concentration ranging from 250 cells to 200 000 cells/mL and NSCs were seeded at 1000 to 200 000 cells/mL. They formed spheroids which were photographed daily and analysed for metabolic and acid phosphatase activity on day 7. Spheroid volume growth was calculated by comparing spheroid volume on days 3 and 7 to that of day 1. ($V_{\text{growth}} = 100 \times V_{\text{day7}}/V_{\text{day1}}$).

3.2.10 Cytotoxicity experiments

Single cell suspensions were seeded in ULA plates at concentrations determined by the growth kinetics to produce spheroids between 300-500µm in size on day 3 (2.5×10^4 cells/mL for UW228-3 and 5×10^4 cells/mL for NSCs). Old medium (150µl) was carefully removed on day 3 and replaced with medium containing etoposide ranging from 0.03 µM to 300 µM from a 50 mM etoposide stock solution in DMSO. The drug exposure time was 48h (until day 5) when medium was exchanged twice with fresh etoposide-free medium (150 µL), reducing drug concentrations

to 1/16th of initial levels. Afterwards spheroids were incubated for a further 48h until day 7 when their viability was assessed using spheroid volume, resazurin metabolism and acid phosphatase activity. Negative control spheroids were cultured with 0.2% DMSO as vehicle and used to determine 100% viability while the positive control ones were exposed to 25% DMSO and represented 0% viability. The 300 μ M etoposide concentration contained a higher level of DMSO (0.6%) and was used along with the positive control to elicit complete cell death and represent the bottom of the dose-response curve. A row of wells with media only and no cells was included to exclude contamination and verify that the positive control is functioning properly. Six replicate spheroids per condition were exposed to a total of 9 levels of etoposide in each experiment and the displayed results are the average of at least three independent experiments. In the case of neural stem cells, tissue from three different foetuses was used in the different experiments.

3.2.11 Resazurin, Acid phosphatase and Cell counting

Cell metabolism, enzymatic activity and absolute cell counts after spheroid dissociation were assessed as per the methodology described in Section 2.5

3.2.12 Assay Validation

Resazurin, Acid phosphatase and Volume determination assays were optimised and evaluated based on their Z-factor [276], Signal window [277] and Coefficient of Variation.

Z-factors were calculated using the equation:

$$Z = 1 - \frac{3 * (SD_{sample} + SD_{control})}{Mean_{sample} - Mean_{control}}$$

In growth experiments, the standard deviation and mean of the readings for medium-only wells were used as control. Z'-factors, reported in cytotoxicity assays, have been calculated by substituting the values for

positive and negative control in the above equation. Signal window (SW) was defined as:

$$SW = \frac{Mean_{sample} - Mean_{control} - 3*(SD_{sample} + SD_{control})}{SD_{sample}}$$

Coefficient of variation was calculated as $CV\% = \frac{SD}{Mean} \times 100$

Acceptance criteria [278] were set at Z-factor > 0.4, SW > 2 and CV% < 20%. They were used along with the biological considerations to optimise the cell density needed for the cytotoxicity screens. Plate uniformity was assessed on whole plates seeded with 2.5×10^4 cells/mL UW228-3 and 5×10^4 cells/mL NSCs. Phase contrast photographs were taken on day 3 after seeding and the variation in volume of the resultant spheroids was examined (acceptance criteria CV < 20%). Signal variability validation was carried out on the 7th day of the etoposide exposure experiments. Non-normalised (raw) assay readouts at each etoposide concentration were compared to the 25% DMSO positive control and Z-factor, SW and CV were calculated for each condition.

3.2.13 Data analysis

Results from volume, Resazurin reduction, APH activity and cell number measurements were analysed in MS Excel and GraphPad Prism 6. In assay validation experiments, readings for each assay were normalised so that the highest reading represents 100% and the reading for cell-free media 0%. Data was fitted to a straight line using Prism's least squares algorithm. In cytotoxicity experiments, readings were normalized so that untreated control has 100% viability and the readings for the positive control were taken as 0% viability. Dose response curves were fitted using either the four-parameter logistic equation for monophasic dose response (UW228-3) or the biphasic dose-response equation (NSCs) in Prism. Results are displayed as mean \pm SD. Combined IC50 values from several experiments were derived by pooling the data together and analysing all runs from a single assay as one, using the logIC50 means (geometric means of IC50s) or by employing Prism's extra-sum-of-squares F-test to

fit a curve with a common logIC₅₀ between experimental runs as described in [279]. There were n=6 replicates for each condition in each individual experiment and displayed data represent the mean of at least three independent experiments

Section 3.3 Monolayer experiments in UW228-3

Some preliminary work was done on the UW 228-3 cell line in order to determine doubling time and sensitivity to etoposide. The UW228-3 cell line was found to have a doubling time of 29h (SD=5h, n=3) in monolayer which is similar to the doubling time reported in the original studies on the cell line[226].

When seeded in 96-well plates and cultured for 48h with etoposide, followed by a 48h drug-free period, the exponentially dividing UW228-3 cells were killed by etoposide treatment in a dose-dependent manner. Using resazurin reduction as a surrogate viability measure, the IC₅₀ for etoposide was determined to be 0.36 μ M (Figure 3-1) which is in agreement with the studies by Othman et al [228]. These preliminary data were used to define the range of concentrations to be used in the 3D and confirm the sensitivity of the cell line to the drug.

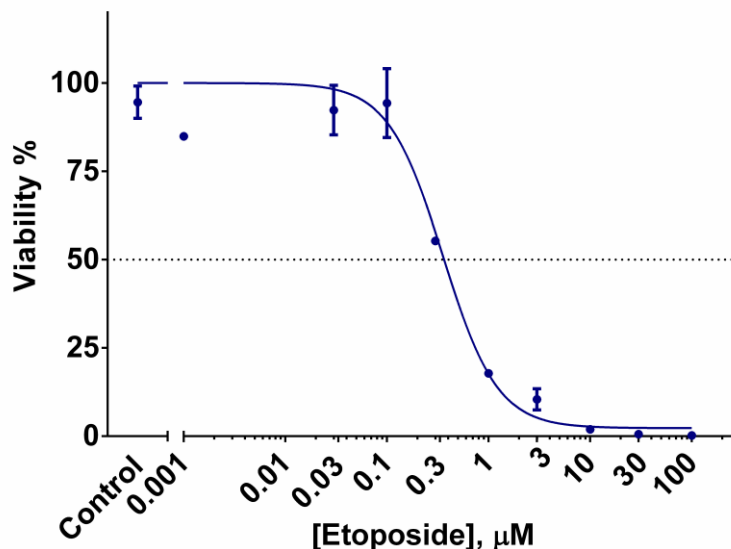


Figure 3-1. Etoposide dose-response curve for exponentially growing UW228-3 medulloblastoma cells in monolayer. IC₅₀ was 0.36 μ M (95%CI=0.29-0.44 μ M, n=3 experiments with 6 replicates for each condition).

Section 3.4 Initial search for a suitable 3D cell culture growth platform

3.4.1 Non-adherent cell culture flasks

Neural stem cell enriched neurospheres were routinely cultured as neurospheres in non-treated flasks as described in 3.2.2.

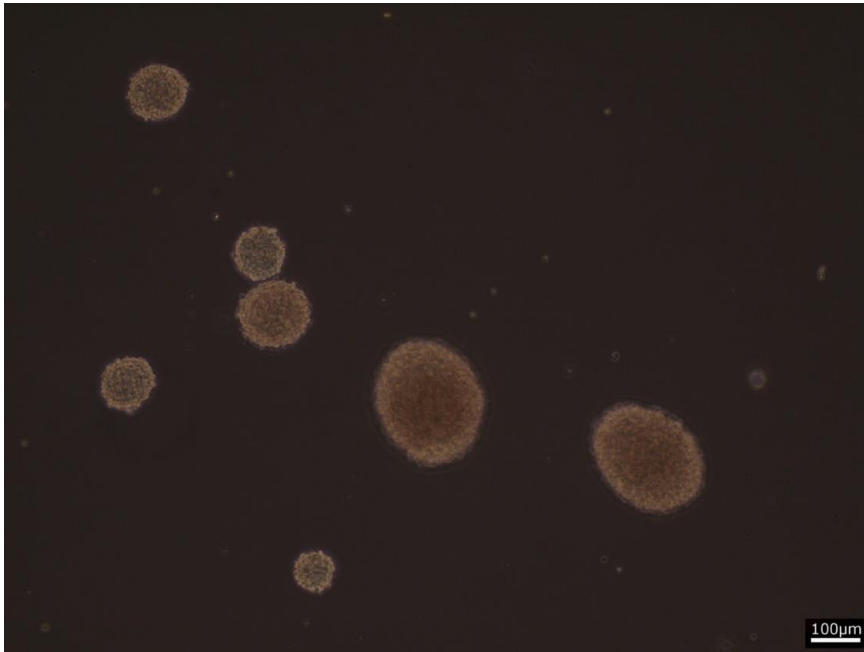


Figure 3-2 Phase microscope image of normal neurospheres cultured in serum-free media in non-adherent flasks. Foetal neurospheres were cultured for 6 days in non-adherent flasks. Spheroids with diameter ranging from 80 μm to 250 μm are visible. Scale bar 100 μm

Figure 3-2 shows the broad distribution of sizes that is characteristic for spheroids cultured using this simple method. Although this technique was suitable for neurosphere expansion, the poor reproducibility and the variety of spheroid sizes makes it unfit for medium and high-throughput analysis. Some researchers have relied on manual sorting[204] while others have opted for large particle sorters like the COPAS system[280].

3.4.1 3D Microtissues[®] agar moulds:

The 3D Petri Dish[™] micromoulds are filled with molten agarose solution, which is allowed to set in the fridge and afterwards separate from the plastic. The numerous micro-wells in the agarose 3D Petri dish[®] are used

as a non-adherent hydrogel growth surface and spheroids are grown in overlay culture (Figure 3-3)[259].

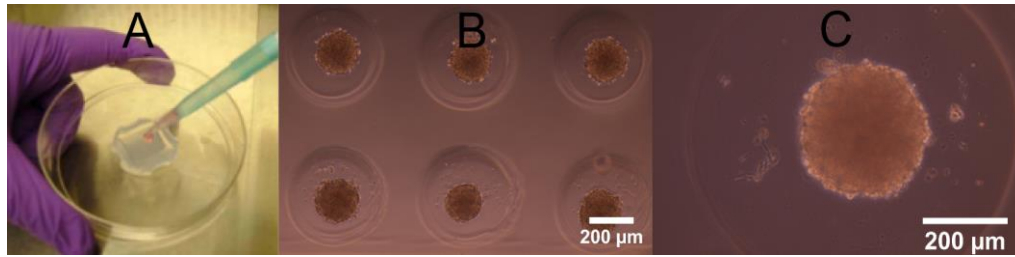


Figure 3-3. Spheroids in the 3D microtissues micromoulds. A-loading the agarose micromould (image taken from the 3D Petri Dish™ manual); B-VCR spheroids 48h after seeding; C-VCR spheroid 72h after seeding

	Small /Day 1	Small /Day 4	Large /Day 1	Large /Day 4
400 X10 ³ cells				
Size(µm)/ Growth(%)	190 µm	210 µm/10%	290 µm	280 µm /-4%
300 X10 ³ cells				
Size(µm)/ Growth(%)	180 µm	200 µm/11%	220 µm	250 µm/14%
200 X10 ³ cells				
Size(µm)/ Growth(%)	150 µm	190 µm/26%	200 µm	240 µm/20%

Figure 3-4. Phase-contrast images of the spheroids produced by VCR cells using two sizes of the 3D Petri Dish-small with 256 wells and large with 81 wells. Cells were seeded with 190µl of medium at three different concentrations. The spheroids formed in the first 24h had a higher number of single cells in the periphery without a well-defined border. By day 4 most spheroids had a dense well-pronounced border. Most spheroids grew to roughly the same diameter which was probably determined by the size of the wells

The VCR cells formed spheroids within 24h using the 3D Petri dish. The spheroids were initially loosely packed with many single cells in the periphery. Although with prolonged culturing time the border of the spheroids became denser, they did not grow much in diameter (Figure 3-4).

The main advantage of the micromoulds is that a large number of spheroids with a narrow size distribution could be formed in a single

seeding step. However, those spheroids would later need to be sorted and transferred to a standard 96- or 384-well plate if the spheroids are to be assayed in a larger set of experiments. Alternatively, each agarose mould can represent one condition, with as many as 256 replicate measures in the mould, but the limiting factor here will be the number of moulds that can be produced at one go. Moreover the plastic used to mould the agarose loses its flexibility with multiple autoclave cycles which may increase costs in big screens.

3.4.2 3D Biomatrix hanging drop plates

The hanging-drop plates have been hailed as the state-of-the-art in matrix-free spheroid technology. In theory they offer high-throughput formats, reproducible sizes and promise compatibility with standard assays and plate readers. The most popular manufacturers are InSphero [272] and 3D Biomatrix [257].

Both DAOY and VCR cells formed spheroids when seeded at various cell densities and the size of the spheroid was controlled by the number of cells seeded Figure 3-5 and Figure 3-6.

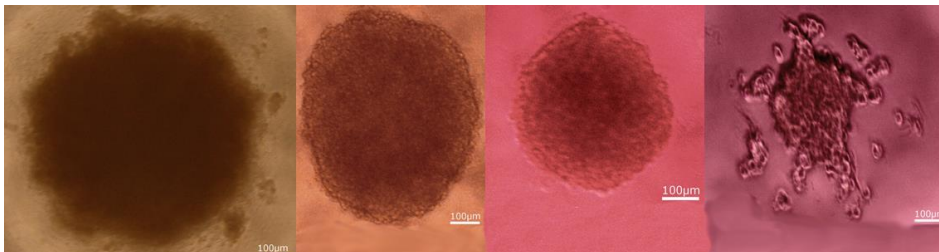


Figure 3-5 Phase-contrast images of DAOY spheroids formed in hanging drops after 48h of culturing in hanging drops at different seeding cell densities. Left to right- 60 000 cells (800 µm); 30 000 cells (700 µm); 7 500 cells (400 µm), 3 750 cells (300 µm); Scale bar 100 µm

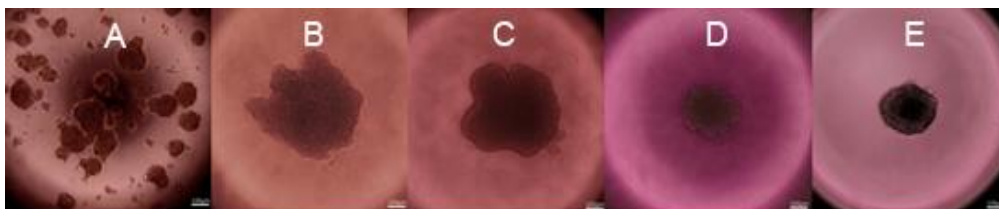


Figure 3-6 Microscope phase-contrast images of spheroids formed in hanging drops by the VCR cell line at two different concentrations. A-C (7 500 cells per well), D,E (3 750 cells per well). A- after 24h-numerous small spheroids, B- after 48h the spheroids are coming together and forming a 500 µm aggregate, C- After 72h the aggregate is becoming more compact with well-defined edges; D- after 48h the cells have formed a single 240 µm

spheroid, E- after 72h the spheroid is compacting but size has remained the same; scale bars 100 μ m

The number of cells needed to form a spheroid with a diameter of about 300-500 μ m that has been reported to exhibit a hypoxic core deprived from nutrients was 3750 to 7500 cells per well [264]. In the first 24 hours cells formed multiple smaller spheroids (VCR) or loose aggregates (DAOY) which gradually rounded and united in a single spheroid by the second day. Further compaction of the spheroids and the formation of a well-defined border were observed by 72h. The spheroids were harvested by purging the hanging drops with additional HBSS from the top of the plate, fixed, embedded in paraffin, sectioned and stained with haematoxylin and eosin H&E

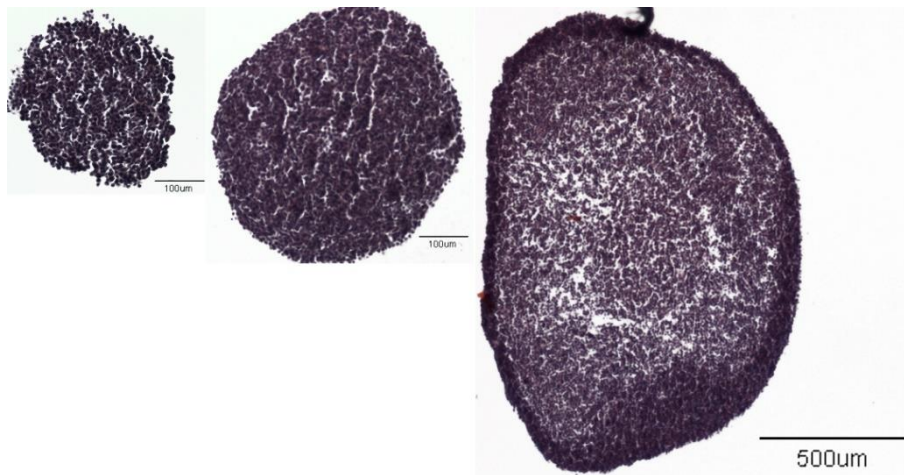


Figure 3-7 H&E stained sections of spheroids formed by VCR cells after 4 days of culture in hanging drop plates. A- Spheroid 300 μ m with lots of loosely packed cells in the periphery, scale bar 100 μ m. B- Spheroid (500 μ m) with a well-formed border and uniform packing throughout, scale bar 100 μ m. C- Spheroid (1500 μ m) with a very dense border and loosely packed core, scale bar 500 μ m.

The H&E staining reveals that smaller spheroids (300 μ m) in the initial 48h of culture have a higher number of loose cells in the periphery. These “free cells” could play an important part in metastasis by invading neighbouring tissues. With longer culturing periods the cells pack in a tighter formation and eventually develop a dense border which is an indication of a vital mechanism explaining the higher chemoresistance of cells in the core of the spheroid. That could be an additional mechanism of tumour cell survival apart from the resting phase hypothesis[257], [281].

The encouraging results for the tumour cell lines led to attempts to culture the foetal neurospheres in the hanging drop plates as well. The normal cells did not merge together to form a single spheroid but produced a number of small spheroids instead. Although at higher concentrations some of the smaller spheroids united in a big one in the centre of the drop, there was still a number of small ones floating around the main spheroid.

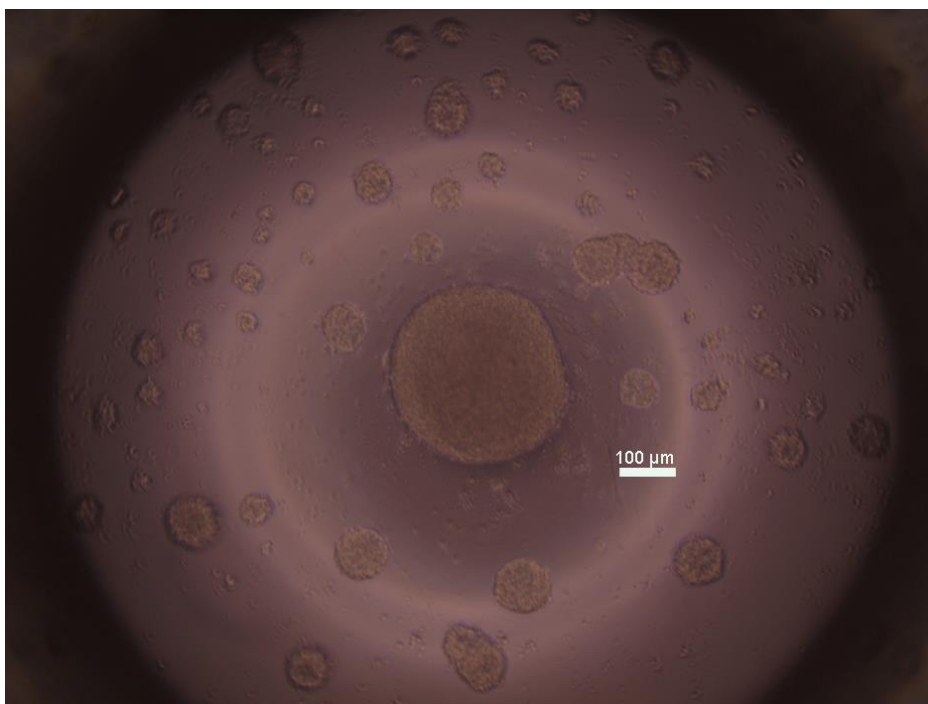


Figure 3-8 Phase-contrast microscope photo of foetal neurospheres seeded in the hanging drop plate. Despite the formation of a single (300 μ m) spheroid there were still a number of smaller spheroids within the same drop that did not merge with the main one.

The mechanism of spheroid formation for the tumour and the normal cells appears to be different. The tumours form spheroids when their cells are close to each other by flocculating and secreting their own extracellular matrix. In contrast, the foetal brain cells form spheroids derived from a single mother cell and do not flocculate as readily. Even though neurospheres can merge, as exemplified by the big spheroid formed in the hanging drop, this happens much slower than it does in medulloblastoma cell lines.

The failure of normal brain cells to form a single spheroid per well combined with the need for spheroid transfer to a normal plate-reader-

compatible 96 or 384-well plate precluded to use of the hanging drop platforms for this project.

3.4.3 Ultra-low attachment plates

The landmark paper by Vinci et al[261] recommended the use of ultra-low attachment plates to grow spheroids in a reproducible medium- to high-throughput manner.

At the time of receiving the plates the VCR medulloblastoma cell line was deemed unsuitable for further development due to issues with etoposide sensitivity (see Sections 1.3.3.2 & 4.4) and doubts about origin raised in the literature[225]. The DAOY cell line was excluded because of its tetraploidy and number of genetic aberrations falling outside that of *in vivo* medulloblastoma[221]. The UW228-3 cell line was confirmed to be human and sensitive to etoposide[228] and was therefore taken forward in the next experiments. It was used as a model of the parent tumour in order to establish assay methodology and proof of principle.

Both normal brain progenitor cells and UW-228-3 tumour cell lines formed one centrally positioned spheroid in each well of the round bottom 96-well plates. Single spheroid formation and cell survival were encouraged with a light centrifugation which brought the cells together. Centrifugation reduced cell loss and yielded viable spheroids within 24h with as few as 50 and up to 40000 cells. Centrifugation is reported to encourage paracrine signalling and suppress apoptosis in the early stages of spheroid formation [282]. The spheroids were cultured for 72h before the first media change to allow for the formation of extracellular matrix and spheroid compaction.

UW 228-3 medulloblastoma cells formed spheroids ranging from 92 μm (50 cells) to 840 μm (40×10^3 cells) in diameter and coefficient of variation $CV_{\text{diameter}} \leq 5\%$ ($n=6$). The spheroids formed by NSCs were 150 μm (200 cells) to 730 μm (40×10^3 cells) in diameter and $CV_{\text{diameter}} \leq 4\%$ ($n=6$). The culture in ULA plates was quick and reproducible and did not differ much from a regular monolayer screen except for the fact that the spheroids were left for 3 days before drug addition.

Brain progenitor cells and tumours exhibited different size increases over the 7 day duration of the experiment (Figure 3-9Error! Reference source not found.A and B). Both cell types showed a similar relationship between seeding concentration and proliferation capacity. Very low seeding densities (50-100 cells/well) resulted in little growth, intermediate ones (1000 and 5000 cells/well for NSCs and UWs respectively) proliferated the most, while seeding high cell numbers yielded big spheroids whose growth was hindered by the constant volume of media and the geometry of the well. Similar findings have been reported by Mori et al. [282], who argued that paracrine enhancement of Notch signalling in intermediate sized spheroids is one of the reasons for their enhanced growth.

The neural progenitors had grown faster at the conditions of the assay (Figure 3-9A). This can be explained by the composition of the NSC media containing EGF and bFGF, which stimulate the division of stem cells. The decreased proliferation of the tumour cell line can be a consequence of having a lower percentage of stem-like cells responsive to EGF and FGF within the tumour spheroids and lack of interactions with normal tissue, which could enhance tumour growth [248]. Nevertheless, tumour spheroids increased their volume to 270% of the spheroid volume at day 1, showing a slow and steady growth pattern similar to the behaviour of tumours in-vivo which grow slowly rather than exponentially.

Seeding densities of 10000 cells per well for the NSCs and 5000 cells per well for the UW228-3 cell line were seen as a good compromise in order to minimize the difference in growth rate (Figure 3-9C) between the two cell types, and yield similar spheroid size at day 3 (Figure 3-9D).

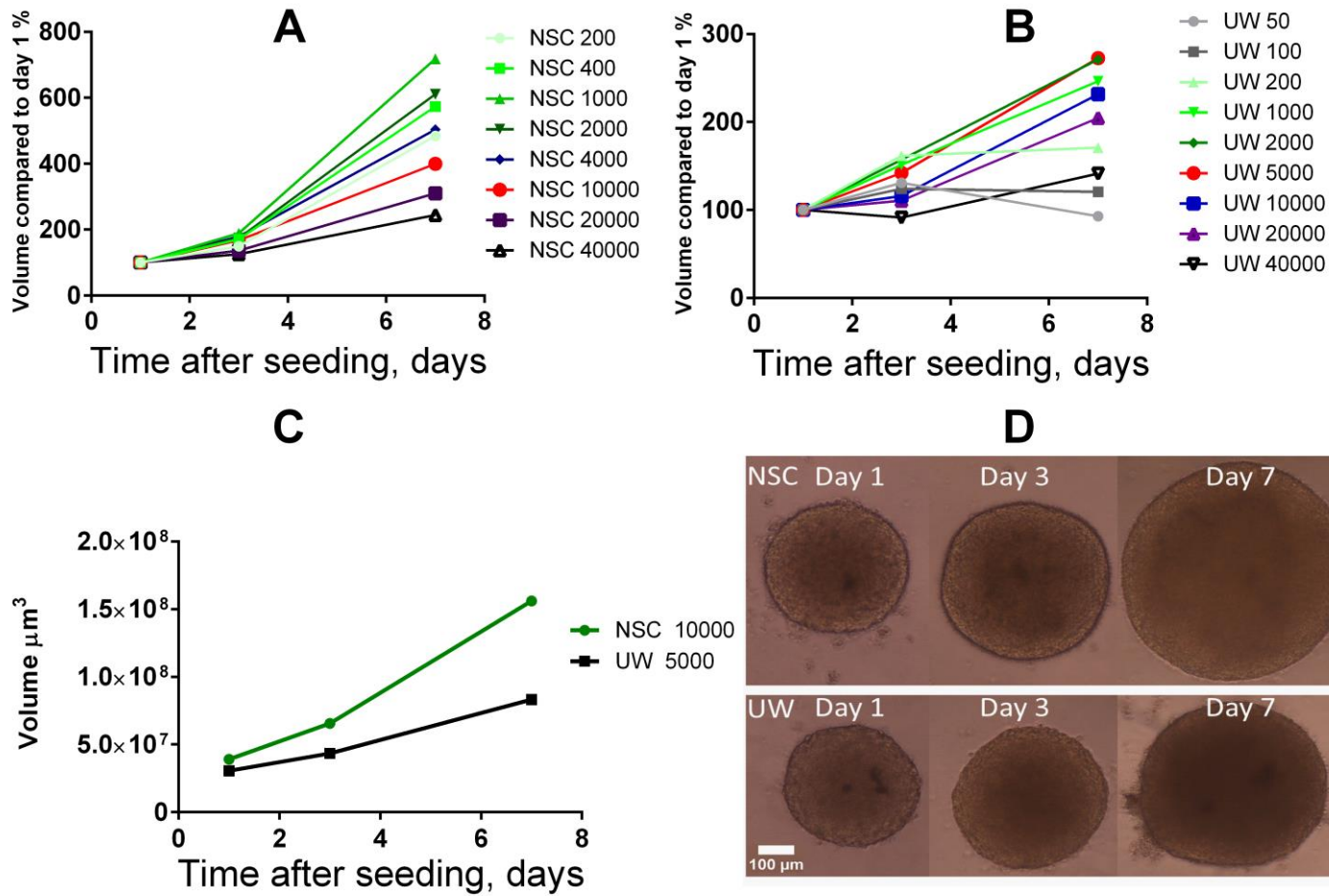


Figure 3-9. Growth curves for spheroids of normal progenitor and UW228-3 medulloblastoma cells. A and B- Spheroid volumes compared to day 1 in % for NSCs (A) and UW228-3 (B) seeded at different cell densities per well. C-Increase in volume of NSC and UW spheroids seeded at 10 and 5 thousand cells per well respectively. C-representative light microscopy images of the spheroids formed by each cell type. Scale bar 100µm

Section 3.5 Assay validation in healthy spheroids

Apart from investigating growth patterns, these initial experiments were used to probe the suitability of spheroid volume, metabolic activity and acid phosphatase activity to predict numbers of viable cells within spheroids of various sizes of both cell types. Spheroids were grown for 7 days and their ability to reduce resazurin, acid phosphatase activity (performed on a second twin plate) and volume were determined as described above. Spheroids were dissociated and the resultant cell counts were plotted against assay response (Figure 3-10).

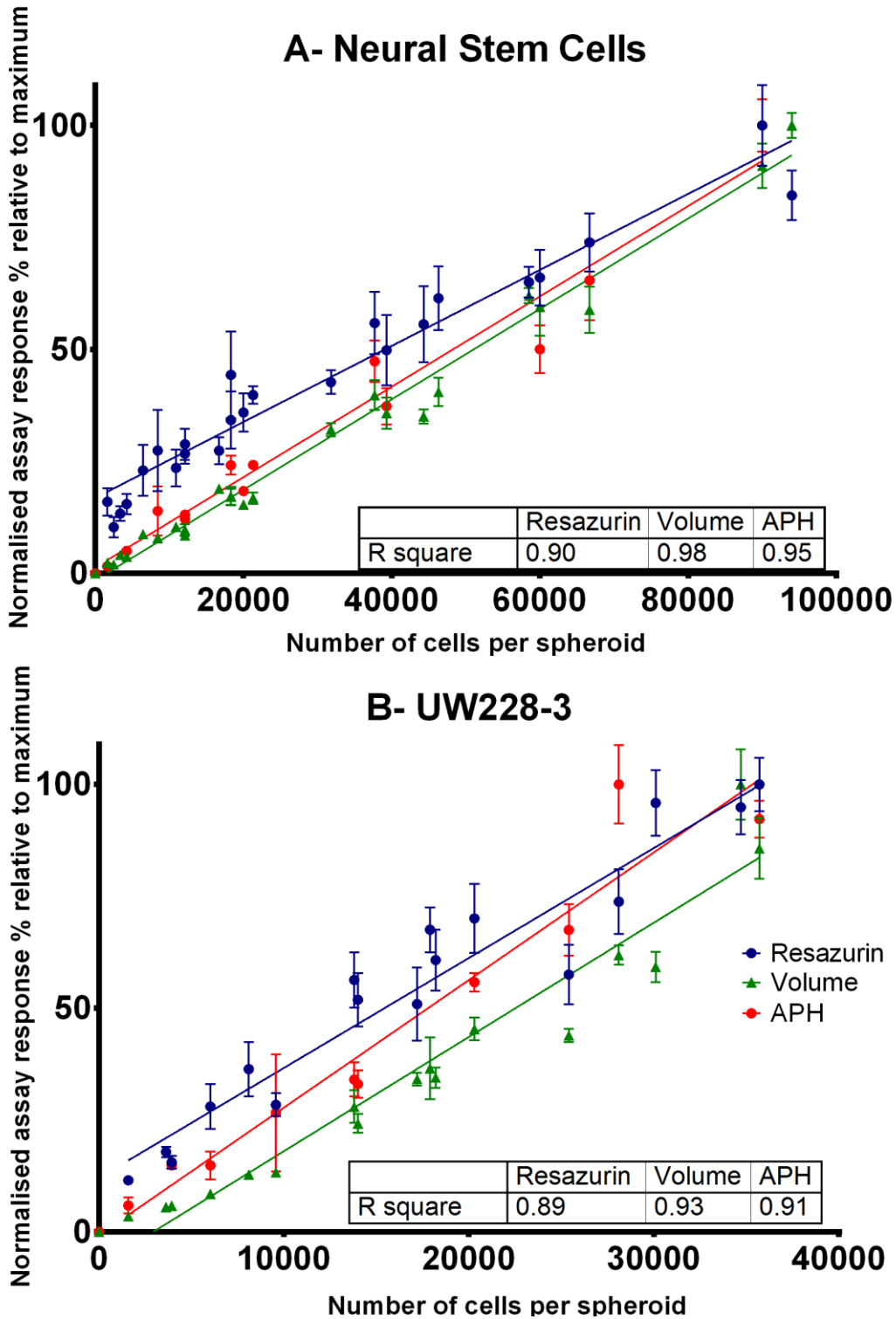


Figure 3-10. Volume, resazurin and acid phosphatase as methods to determine viability in NSC and UW228-3 spheroids. A. NSCs spheroids, diameter 200-800µm. B. UW228-3 tumour spheroids, diameter of 160-700µm. Both cell types were grown as spheroids for a week and then probed for volume, metabolic and acid phosphatase activity. Spheroids were enzymatically dissociated and normalised assay response plotted against the number of cells per spheroid in order to compare the three assays. Normalised assay responses from three independent experiments were pooled together, plotted and the linearity of each method was examined

The graphs clearly show that for healthy spheroids, over the range of 160-800 μm in diameter, volume correlates best with the number of healthy cells within a spheroid. As spheroids grow in size the cells in the core have less access to nutrients and oxygen, become firstly hypoxic and afterwards necrotic. Although the core of the spheroid becomes less populated the opposite is true for the periphery where a layer of densely packed cells is established [265], [283], [284]. This phenomenon can explain the relatively constant relationship between volume and cell number of the spheroids in this experiment. However this relationship will need to be confirmed and validated for every new cell type used and the relevant spheroid size as spheroids of $>500 \mu\text{m}$ in diameter will have a more pronounced necrotic core and deviate from linearity [274], [285]. With the use of our specially written ImageJ macro (Supporting information macro S1) we were able to increase greatly the speed of image processing and facilitate the use of spheroid volume in rapid automated screens. The algorithm estimates spheroid volume using the area of the spheroid and fits the radius to that of an equivalent sphere. The spheroids do not need to be perfect spheres as the estimation is roughly valid for ellipsoids of width/length ratio up to 1.5 [263]. Moreover initial studies utilising the maximum and minimum Feret diameter and estimating the volume of an ellipsoid (data not shown) exhibited greater variation due to thresholding artefacts affecting automatic measurements. The macro is optimised for phase-contrast images and requires manual magnification calibration at line 6. However the code can be easily adapted to suit applications like fluorescence imaging by altering the thresholding mechanism and using additional macros distributed with the free Fiji version of ImageJ [286], [287].

Acid phosphatase activity correlated almost linearly with cell number and volume for UW228-3 and NSCs. As evident from Figure 3-10A, in healthy NSC cells volume and acid phosphatase can be used interchangeably as markers of viability. Moreover, the correlation coefficient was above 0.9 for spheroids of both cell types indicating an excellent linear relationship. Although the APH method is faster and easier than photographing and

computing spheroid volume it requires lysing the cells and has to be the final assay in a high-content analysis program.

The reduction of Resazurin, also known as Alamar Blue, by metabolically active cells was the final method for viability determination. Resazurin reduction was proportional to the number of cells within NSC and UW spheroids. However this method had a higher variability than volume and APH activity and the r^2 values for Resazurin were the lowest of the three methods tested. Nevertheless, the Resazurin assay has the advantages of being non-toxic to the cells at the concentrations and time of exposure, can be used many times on the same cells and can also be multiplexed with other assays. Our initial concern with using Resazurin was that it may only detect metabolically active cells and miss hypoxic quiescent cells in the core of the spheroid. Cells in the periphery of the spheroid have good access to oxygen and nutrients and are actively dividing. Therefore their metabolism is much more rapid than the cells in the core of the spheroid where ATP levels have dropped to the minimum and metabolism is much slower [213], [288], [289]. In this way smaller spheroids were expected to be more metabolically active and appear more 'alive' than bigger spheroids which have a significant quiescent population [265]. This effect was observed in the NSC population (Figure 3-10A) and led to minor overestimation of viability for smaller spheroids.

Apart from viability validation the growth studies were also used to select the seeding concentration for both cell types that resulted in spheroid diameter at day 3 of around 400-500 μm , namely 5000 and 10000 cells/well for UW228-3 and NSCs respectively. The size was chosen because it fits the requirements for gradients of oxygen, nutrients and proliferation rate that are essential for a biorelevant spheroid screen [264].

Additionally, Z-factor, Signal window and Coefficient of variation were compared for the assays in both cell types at each seeding cell density after 7 days of culture in order to determine their suitability for high throughput screening. Both the Z-factor and Signal window take into account the variability of empty (media-only) control wells as well as the

sample wells and provide a useful benchmark for hit-detection fitness in high-throughput screening (HTS). The coefficient of variation provides information on assay variability and can uncover pipetting problems especially at low seeding densities.

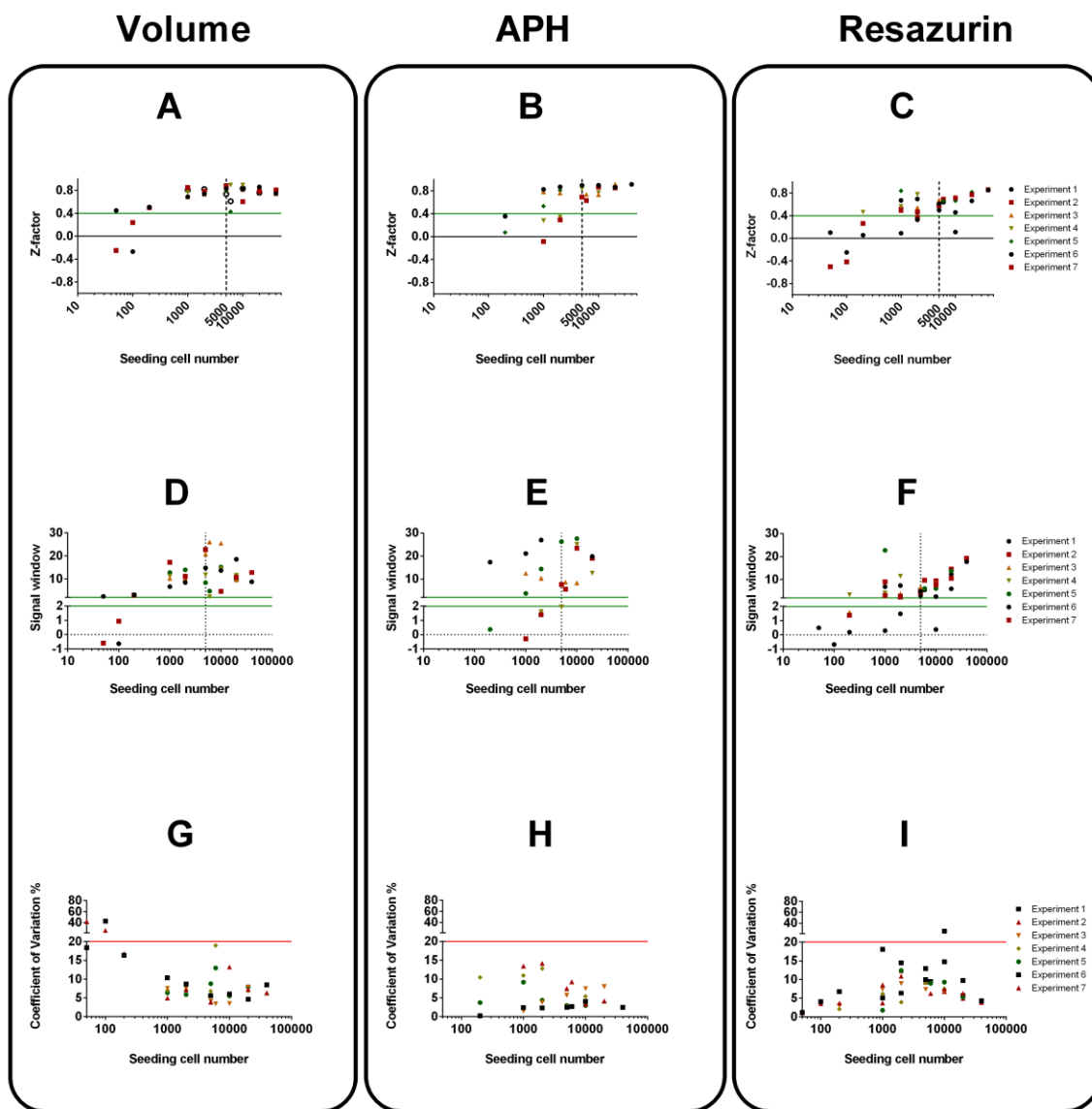


Figure 3-11 Assay characterisation using Z-factors, Signal Window (SW) and Coefficient of variation (CV) for UW228-3 cells. Z-factors (A-C), Signal window (D-F) and Coefficient of variation (G-I). Acceptance criteria $Z\text{-factor} > 0.4$, $SW > 2$ and $CV < 20\%$ were colour coded so that values above the green lines meet quality criteria whereas values above the red line fail. Dotted line at 5000 cells represents chosen seeding density for spheroid cytotoxicity screening

In UW228-3 cells (Figure 3-11) spheroid volume determination provided a sufficient working range for HTS when spheroids were seeded at density higher than 1000 cells/well. This high sensitivity is due to the ability of the thresholding macro algorithm to recognise empty wells and report them as

such. Although the APH and Resazurin assays were also able to detect spheroids at the 1000cells/well, they excelled in all indicators at seeding concentration of more than 5000 UW228-3 cells/well. This along with the biorelevance arguments discussed above showed that seeding density of 5000 cells/well or more is optimal for cytotoxicity screening.

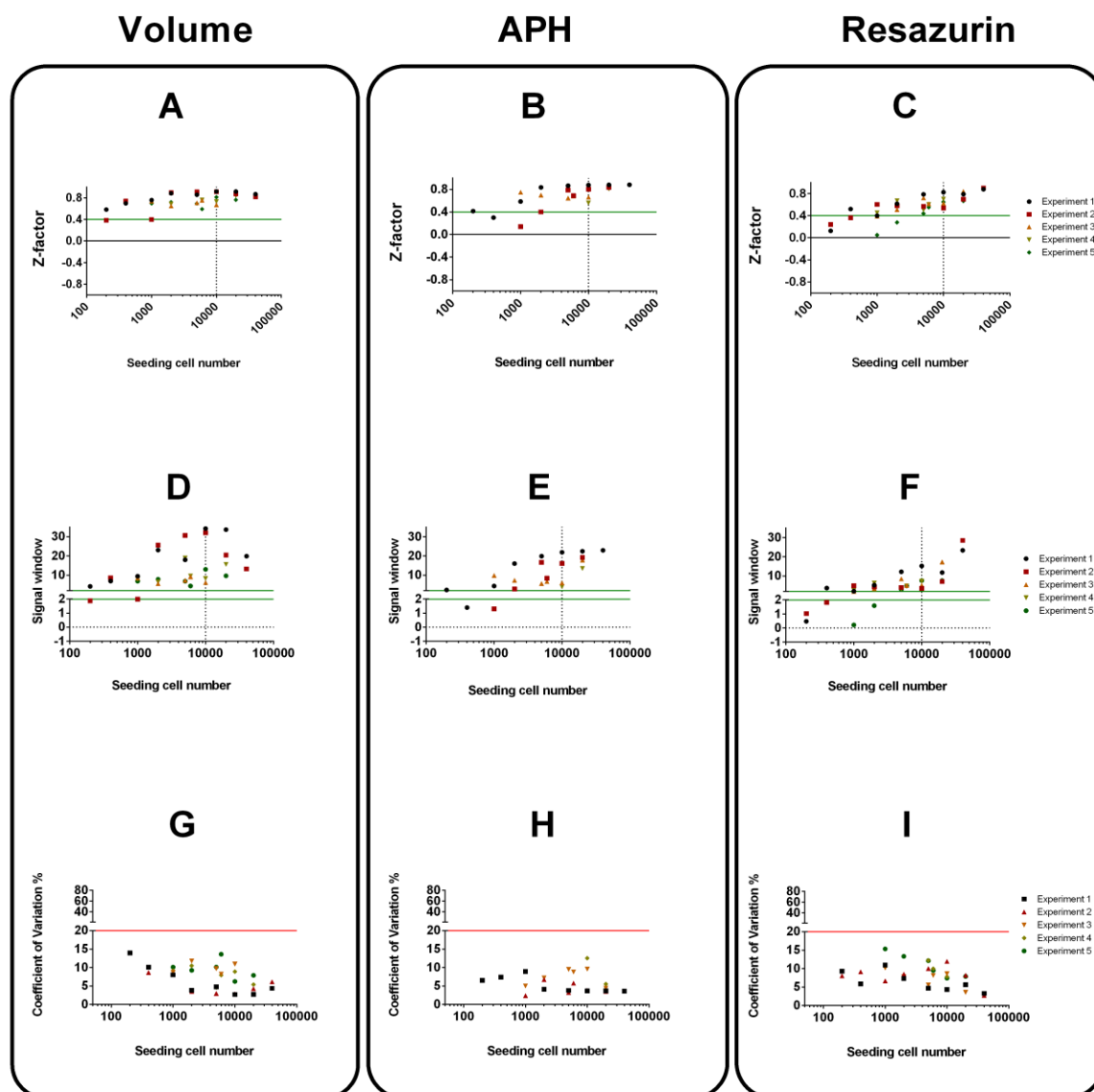


Figure 3-12. Assay characterisation using Z-factors, Signal Window (SW) and Coefficient of variation (CV) for NSCs. Z-factors (A-C), Signal window (D-F) and Coefficient of variation (G-I). Acceptance criteria $Z\text{-factor} > 0.4$, $SW > 2$ and $CV < 20\%$ were colour coded so that values above the green lines meet quality criteria whereas values above the red line fail. Dotted line at 10000 cells represents chosen seeding density for spheroid cytotoxicity screening

Neural stem cells produced spheroids with narrower size distribution and could be used in screens at even lower seeding densities (Figure 3-12). Volume and APH had generally higher Z-factor and SW than Resazurin as

their signals had lower variability. All parameters were within specification for spheroids initially made up of more than 2000 cells. Nevertheless a seeding density of 10000 cells/well was chosen as it produced neurospheres of similar size to the tumour spheroids at the day of drug application.

Section 3.6 Assay validation in spheroids treated with etoposide

Plate uniformity was assessed prior to etoposide addition at day 3. Spheroid uniformity was evaluated by the variability of spheroid diameter and volume along the whole plate in at least three plates on different dates (Figure 3-13).

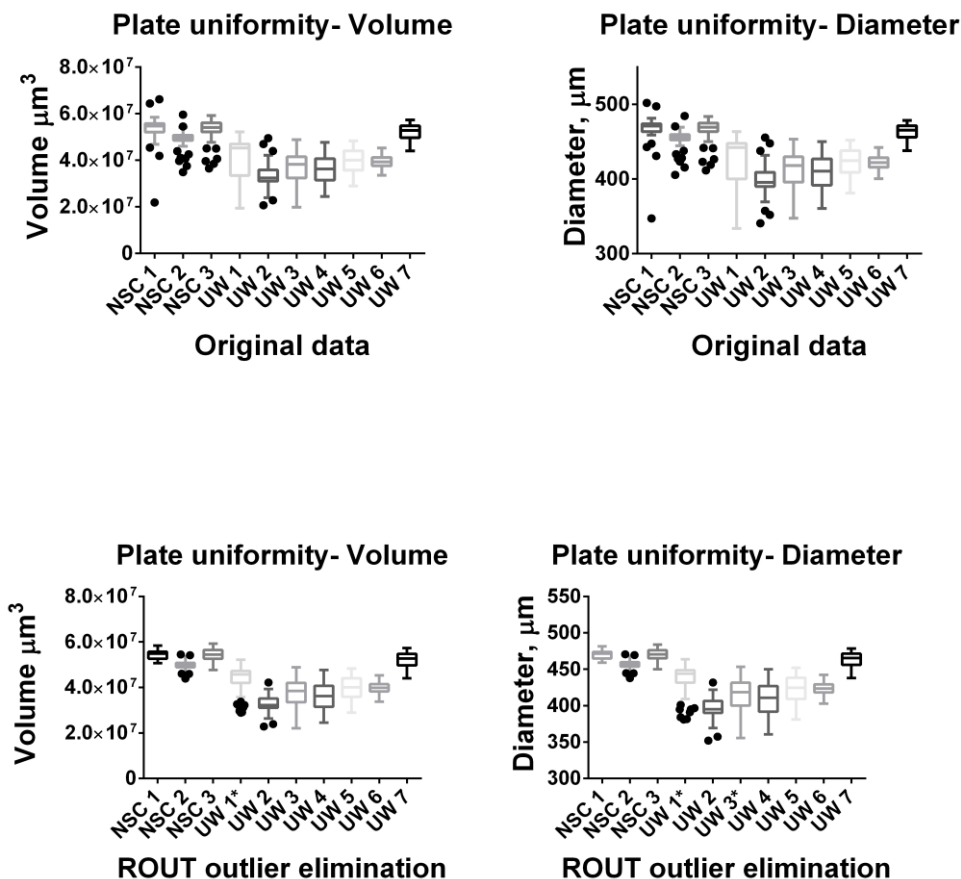


Figure 3-13 Plate uniformity assessment for volume and diameter of spheroids before and after outlier removal. NSC and UW populations are marked according to experiment number. All populations, with the exception of UW1, had a normal distribution according to the D’Agostino-Pearson omnibus K2 test after outlier elimination using Prism’s ROUT algorithm.

The mean diameter for UW spheroids was 422 μm with a coefficient of variation of 4-7% between 7 plates of 33 to 66 spheroids each. NSC spheroids had a mean diameter of 463 μm and CV of 3% between 3 plates containing 66 spheroids each. The coefficient of variation for volume measurements was around 9% for NSC and ranged from 6 to 22% for UW228-3 cells with only one plate exceeding the 20% limit. Several outliers were identified and were attributed to deficiencies in pipetting technique and equipment. Therefore the GraphPad Prism ROUT method was used to eliminate outliers before testing for normality of volume distribution. The D'Agostino-Pearson omnibus K2 test showed a normal distribution of the cleaned volume data in all but one case. Even without outlier elimination a one-tailed t-test, for a sample of 6 replicates from the plate population, with $\alpha=0.05$ will have $1-\beta=74\%$ power to detect a 20% viability drop in UW228-3 cells (CV 15%) and 99% power to detect the same viability drop in NSC cells (CV 9%) [290].

After the plate uniformity assessment, the tissues were exposed to etoposide for 48h, followed by a 48h period in plain media for the drug effects to fully manifest. The dosing scheme was chosen with the intention to model the delivery of a single dose of nanoparticles after surgery. Since the incision is closed after surgery, redosing of nanoparticles would not be possible in the absence of additional surgical interventions. Moreover, submicron drug delivery systems have high surface-to-volume ratio and often exhibit rapid drug release. That is why drug exposure was limited to 48h to model the predicted optimal timeframe for drug release from the nanoparticles. Additionally, other researchers have determined the stability of etoposide in cell culture media to be 48h, maintaining levels above 90% of the nominal etoposide concentration[291]. The second 48h drug-free period was chosen because the toxic effects of topoisomerase inhibitors do not normally manifest immediately. The affected cells need to accumulate a critical number of single and double strand breaks before they go into apoptosis and die. The total duration time of the screen was 7 days and spheroid viability was determined using volume, acid phosphatase, metabolic activity and dissociated spheroid cell counts (Figure 3-14).

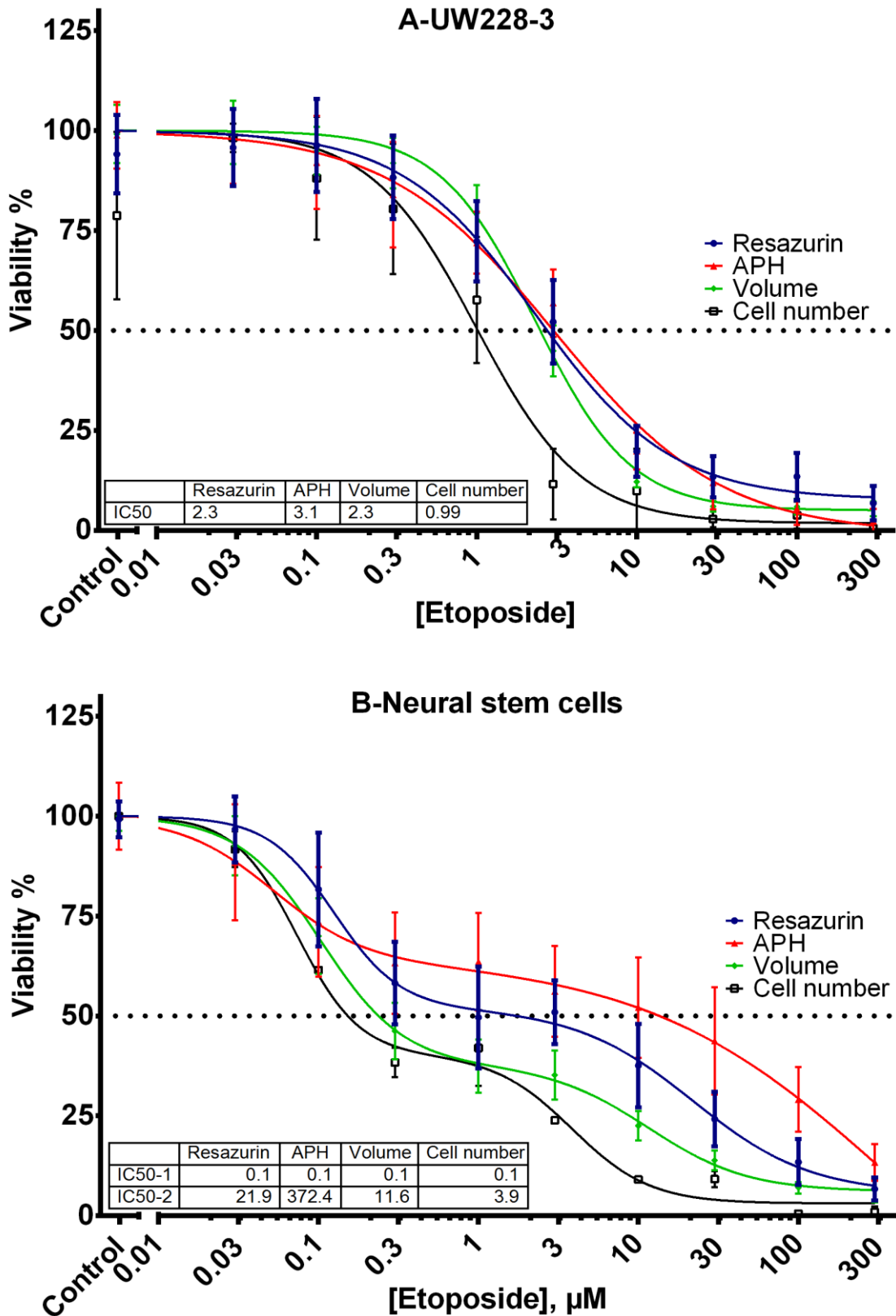


Figure 3-14 . Dose-response curves for UW228-3 (5000cells/well) and NSCs (10000cells/well) spheroids exposed to increasing concentrations of etoposide. Normalized viability is expressed as volume, resazurin reduction, acid phosphatase activity and cell number. Data is pooled from at least three separate experiments.

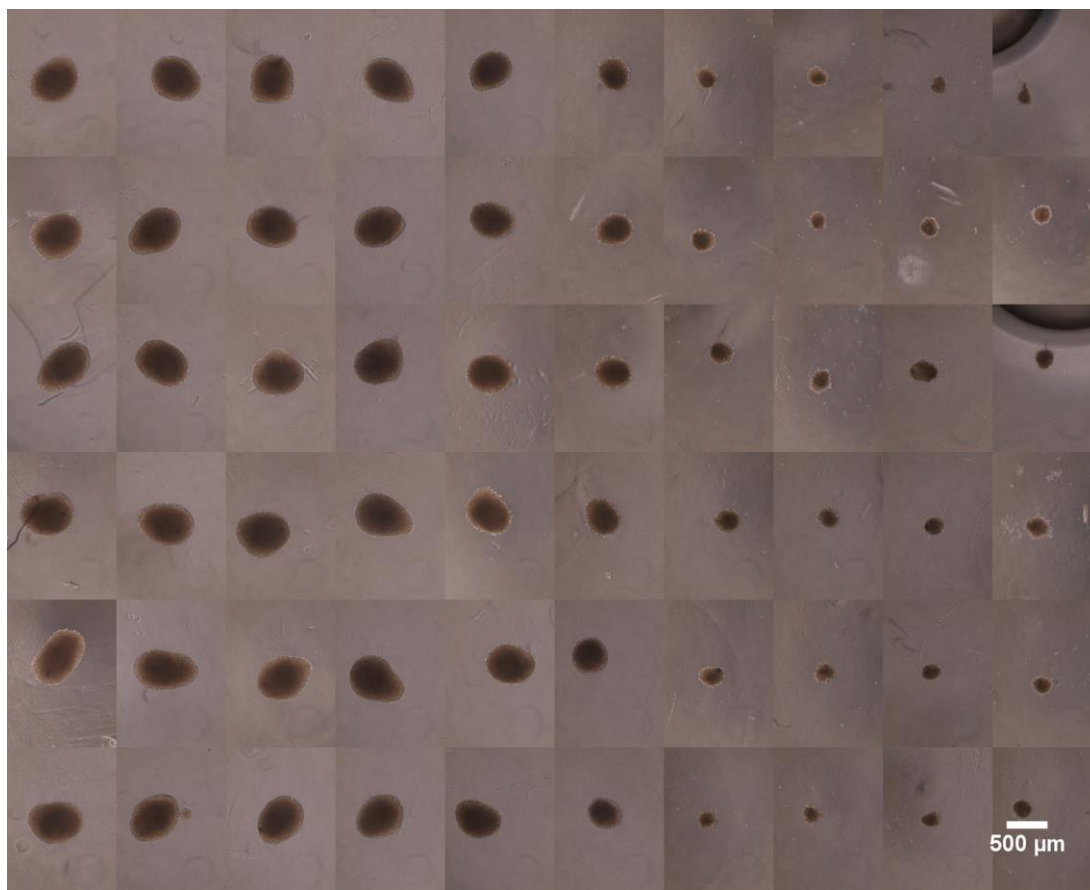


Figure 3-15 Phase-contrast image of a representative plate of UW spheroids treated with etoposide. Each column represents 6 replicate spheroids at the same condition. Left to right untreated control, and half-decimal-log concentrations of etoposide 0.03-300µM.

The dose-response curves for UW228-3 (Figure 3-14A) spheroids produced by reduction in volume (Figure 3-15), metabolism or acid phosphatase activity were very similar and the three assays appeared to be equally suited for a spheroid screen in this cell line. Viability determined by cell counts for dissociated spheroids was comparable to that calculated using the other assays up to drug concentrations affecting spheroid health. At pharmacologically active concentrations there appears to be an overestimation of cell death after subjecting the spheroids to enzymatic and mechanical dissociation. Apoptotic and stressed cells may be more sensitive to the dissociation process and that could be the reason behind the fast drop in viability estimated using cell numbers. Regarding phosphatase activity it is worth noting that at high drug concentrations the APH assay fails to detect any enzymatic activity in UW228-3 cells, whereas there was still some signal present from the Resazurin assay.

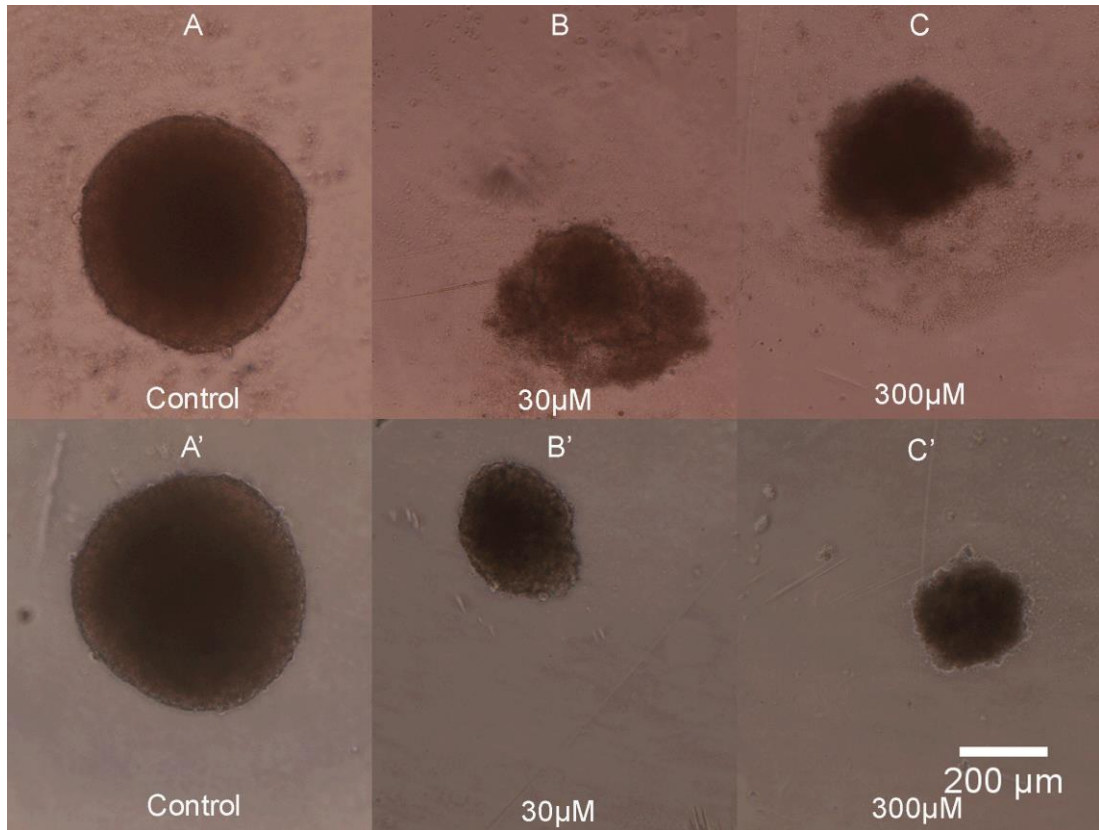


Figure 3-16. Phase-contrast microscope image of UW228-3 spheroids exposed to increasing concentrations of etoposide. Panels A-C show intact UW228-3 spheroids with a halo of debris and dead cells at high drug doses impeding image analysis. Panels A'-C' capture the same UW228-3 spheroids after PBS rinse. Controls were cultured in plain media, concentration of etoposide is given in μM and scale bar applies for all images.

Initially the volume measurements for the tumour cell line at high drug doses were thought to be less reliable because the spheroids were surrounded by a cloud of debris and dying cells and it was not possible to distinguish the dead cells from the living ones without bias (Figure 3-16, panels A-C). Similar observations about the difficulties in volume measurements have also been reported by Friedrich [265]. However it was soon apparent that the debris and apoptotic cells can easily be washed out by exchanging the media twice with PBS (Figure 3-16, panels A'-C'). This greatly facilitated automated image analysis by improving the speed and accuracy of spheroid size measurements.

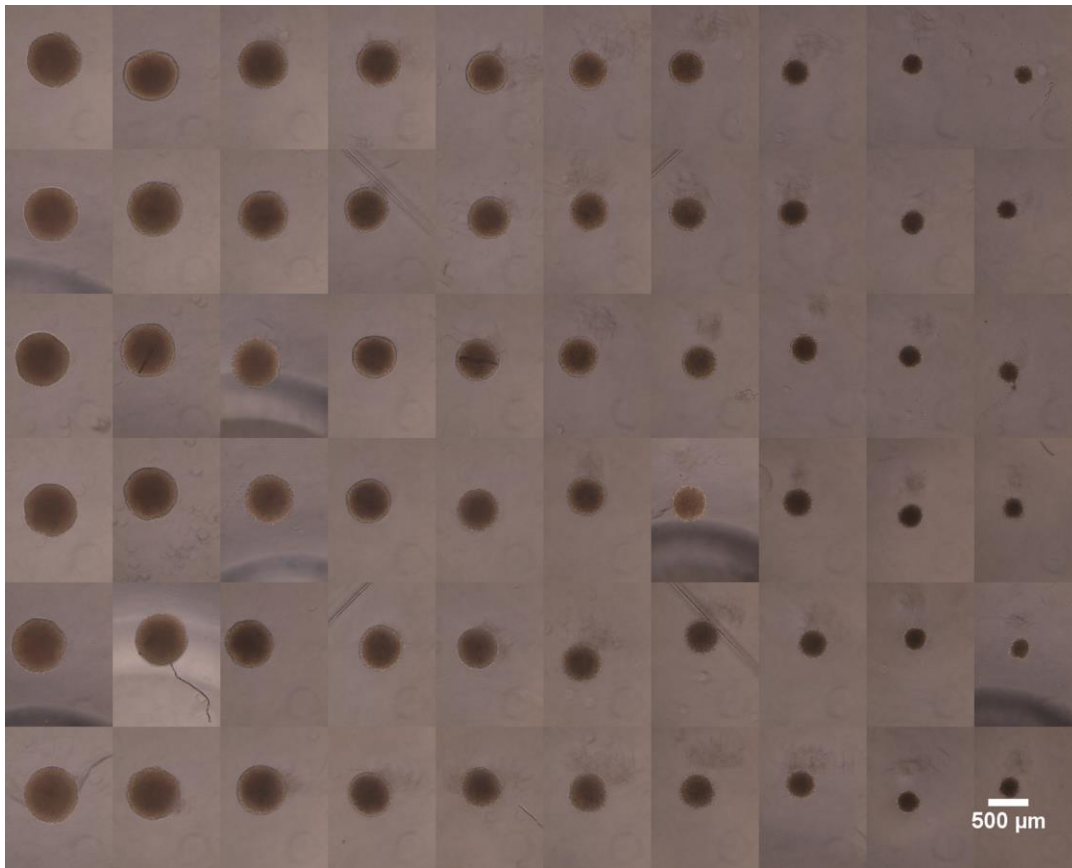


Figure 3-17 Phase-contrast image of a representative plate of NSC spheroids treated with etoposide. Each column includes 6 replicate spheroids at the same condition. Left to right untreated control, and half-decimal-log concentrations of etoposide 0.03-300µM.

Contrary to the UW228-3 monophasic response, foetal brain tissue-derived NSCs (Figure 3-14B, Figure 3-17) had a biphasic etoposide dose-response curve. Initially there was a very sharp decrease in viability down to 50% at concentrations approaching 0.3 µM. Beyond this concentration point the viable cell fraction decreased only slightly when etoposide concentrations were increased from 0.3 to 3 µM. This was followed by a moderate decrease in viability down to around 5% at the highest drug concentrations. The biphasic behaviour of the NSC spheroids is a sign that there are at least two distinct cell populations within the microtissues. The gradients of nutrients and oxygen can trigger differentiation into glia and neurons which would have a different sensitivity to the parent stem cells. Moreover, there could be an indigenous population of partially-differentiated progenitor cells in the foetal brain tissue which have a

limited division potential and differ from the true stem cell phenotype [231], [284].

Viability estimates for NSC spheroids using the suite of four methods varied more than those for the UW228-3 cell line. That was probably due to the heterogeneous character of the tissue derived from foetal brains. Viability estimates using cell number and volume were of similar magnitude and were both generally lower compared to the values determined by resazurin and APH. Despite the fast drop in spheroid volume and cell counts, the metabolic activity as determined by resazurin reduction, dropped more slowly. The innate features of apoptosis, which starts with cell shrinkage while metabolic activity is not impaired, can give a possible explanation to these differences. Treatment with increasing concentrations of etoposide would push some of the cells in the spheroid towards apoptosis, leading to cell shrinkage and reduction in spheroid volume. It could also make the affected cells more sensitive to enzymatic digestion and the effects of mechanical agitation, leading to cell loss upon spheroid dissociation. However the apoptotic cells within intact spheroids would remain metabolically active, continue to reduce Resazurin and register as alive in the assay. Similarly to our findings, Chan et al [292] noted a difference in viability estimation between various cytotoxicity assays being developed for high throughput screening in 2-D assays. In some experiments using etoposide they showed that ATP and metabolism-based assays underestimated cytotoxicity compared to cell number. They have attributed this to increase in cell volume and mitochondrial mass relative to cell number. Other studies have also demonstrated increased ATP content and mitochondrial activity during etoposide treatment and have linked this with apoptosis [293], autophagy [294] or AMPK activation [295]. The viability measurements using acid phosphatase enzymatic activity against PNPP were the highest of all four assays. That was most pronounced for high etoposide concentrations between 10 and 100 μ M where the fraction of apoptotic cells was the highest. Acid phosphatase is a digestive enzyme and has a role in cell death, apoptosis and autophagy [296]. The extensive cell kill induced at high etoposide concentrations could be triggering an increase of specific and non-specific phosphatase

activity in stem cells. The biphasic curve also hints at the possibility that there are two cell populations with different drug sensitivity and enzymatic activity. The first population which is very sensitive to etoposide has a relatively low phosphatase expression and a more resistant second population which expresses higher APH activity.

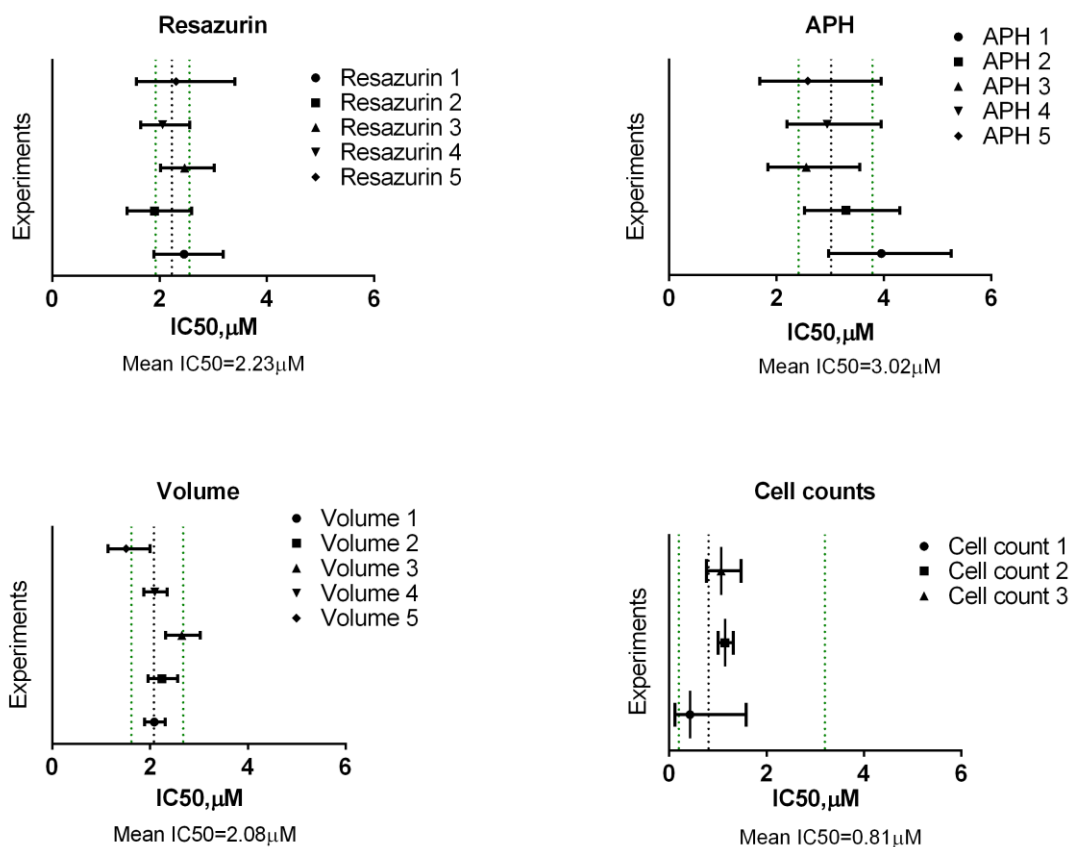


Figure 3-18 Confidence intervals for etoposide IC50 determinations for different assays in UW228-3 cells. The 95% confidence intervals (CI) for each experiment were plotted against the geometric mean (black dotted line) and 95% CIs (green dotted lines) for all individual experiments for each assay.

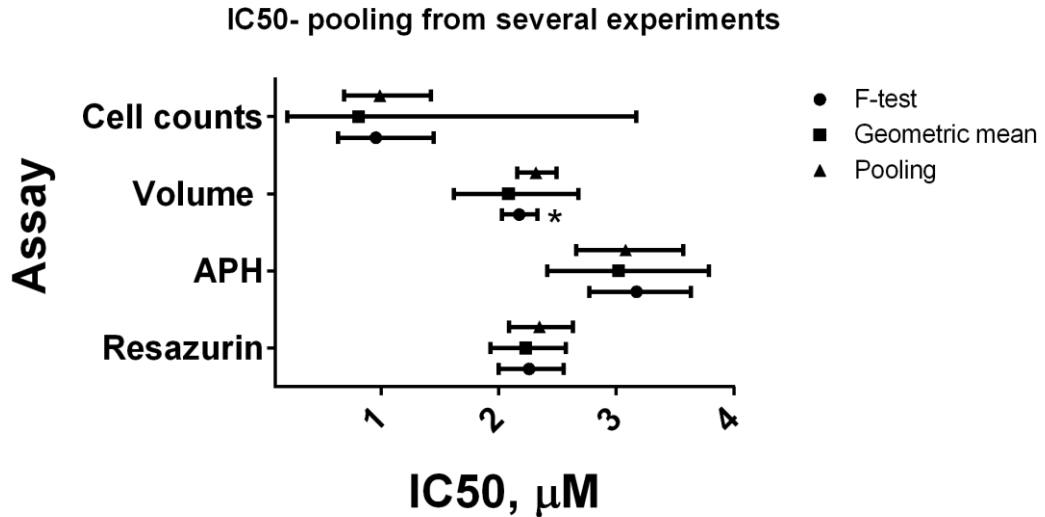


Figure 3-19. Methods of combining different IC₅₀ determinations between experiments for UW228-3 cells. Data was subjected to an F-test to find a common curve that described all runs (Prism's F-test); The mean of logIC₅₀ values was used in the geometric mean method and combining all normalised readings from different runs together was employed in the pooling method. Error bars are 95% Confidence intervals. The * in Volume F-testing means that the calculated IC₅₀ values were statistically different between runs according to the extra-sum-of-squares F-test.

The precision of the four assays for UW228-3 cells (Figure 3-18) was assessed by comparing the 95% confidence intervals (CIs) for each experimental IC₅₀ determination to the geometric mean values for all IC₅₀ determinations along with the associated 95% confidence interval of the mean. The geometric mean of all experiments was calculated using the logIC₅₀ values which have a distribution closer to normal as opposed to IC₅₀ results which tend to be skewed [297]. This approach was chosen after comparing it to the methods of pooling the data into one or using Prism's extra-sum-of-squares F-test to compare IC₅₀ values of dose-response curve fits [279] (Figure 3-19). It was deemed useful as a graphical aid to assess between-run variability and gave slightly broader CIs as seen in the case for Cell counting for example. Overall, resazurin and volume assays were superior to APH and direct cell counting. Although estimating viability using volume exhibited the smallest confidence intervals for the individual measurements, the IC₅₀ values between runs varied more than those for resazurin. Moreover resazurin had the narrowest 95% confidence interval for the mean of the five separate runs.

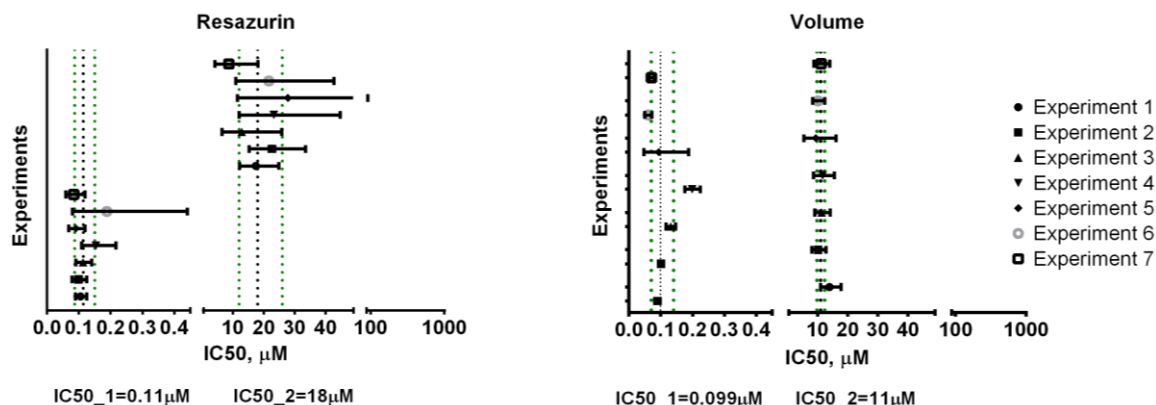


Figure 3-20. Confidence intervals for etoposide IC₅₀ determinations for resazurin and Volume in neural stem cells. The 95% confidence intervals (CI) for each experiment were plotted against the geometric mean (black dotted line) and 95% CIs (green dotted lines) for all individual experiments for resazurin and Volume determinations.

For assay precision in neurospheres, only Resazurin and Volume gave IC₅₀ values that were reproducible and had reasonable 95% confidence intervals varying less than one order of magnitude (Figure 3-20). Volume determinations yielded the tightest CIs with the highest level of precision out of the four assays. The determinations of IC_{50_1} and IC_{50_2} from APH and Cell counting varied over two orders of magnitude and were not included in the graph. The high level of variability in cell number estimation is due to the extra number of steps required to dissociate the spheroids and the possibility for cell loss during the process of mechanical and enzymatic cell separation. The APH assay, on the other hand, may have been affected by non-specific substrate cleavage at high etoposide concentrations leading to overestimation of viability and poor non-linear regression fits.

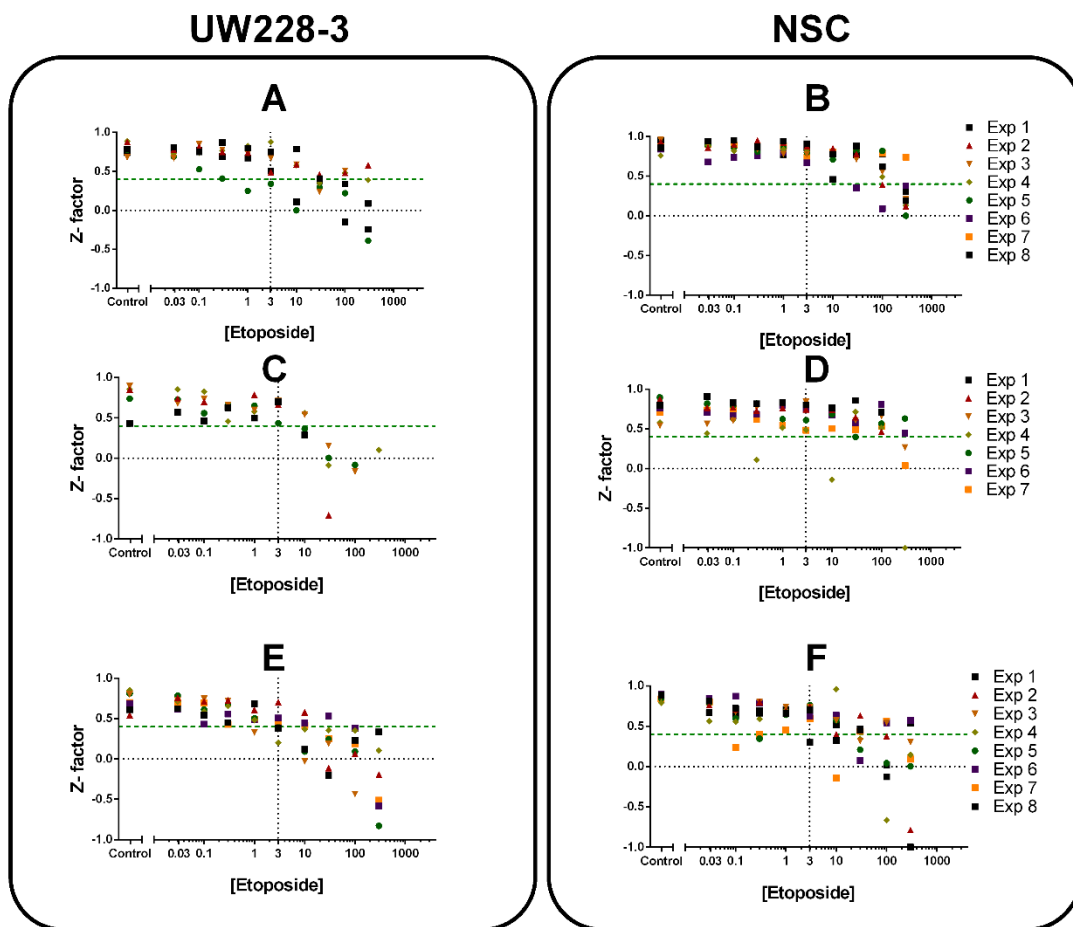


Figure 3-21. Z-factors in cytotoxicity tests for Volume- A and B; Acid phosphatase- C and D; and Resazurin- E and F.

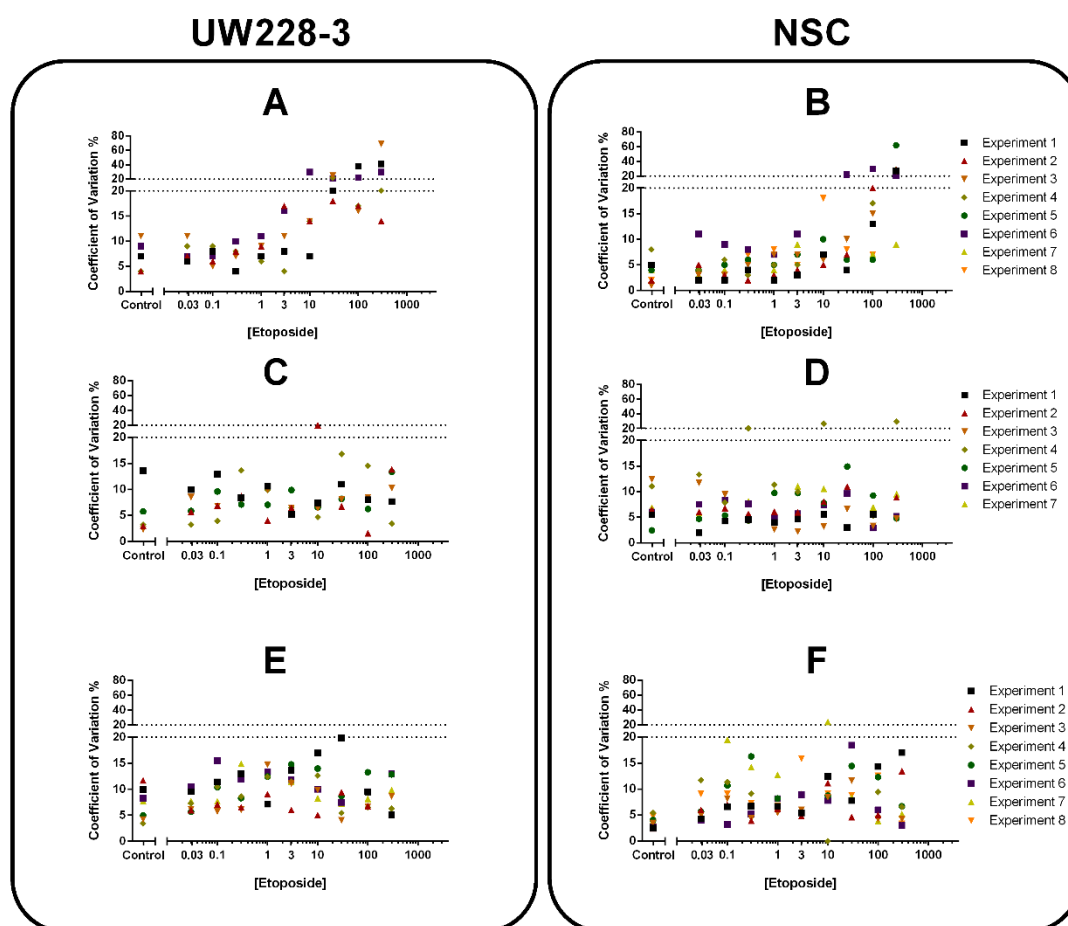


Figure 3-22 Coefficient of variation for different assays of etoposide treated plates. A and B- Volume; C and D-APH; E and F-Resazurin.

Additionally, signal uniformity assessment was performed on all etoposide treated plates to determine variability at each concentration. This test is similar to the signal variability assessment in the NCAT's Assay guidance manual [278] but instead of only using high, medium and low signal points we have used the whole dose-response curve to determine Z-factors (Figure 3-21) and Coefficient of Variation (Figure 3-22). The Z'-factors of all three assays were higher than 0.5 for the medium-only control wells and remained above the threshold of 0.4 even up to the IC₅₀ concentration of 3 μ M. This shows that the assays are well within their optimal working range for high-throughput screening at viabilities down to 50%. Although normalising the data did not affect the results of non-linear regression as described by Motulsky and Christopoulos [279], it was found to change the CV of the measurements and therefore CV calculations were done on the raw data before normalisation. CV was below 15% for most of the spheroids on the dose-response curve for APH and Resazurin assays.

Volume had the lowest variability at low concentrations of etoposide, closely followed by the APH assay. However, the variability of volume measurements increased significantly in the wells where cell death was predominant (30-300 μM) making volume measurements less reliable at high etoposide concentrations despite the washing procedure. It is worth noting that despite the low CV% of the APH assay compared to Volume determinations and Resazurin, the precision of the APH IC₅₀ fits was generally lower.

Overall, volume measurements were the best method to study etoposide activity in foetal brain tissue closely followed by Resazurin reduction. Volume measurement sensitivity was greatly improved by washing off debris and dead cells with PBS similarly to the UW228-3 cells (Figure 3-23).

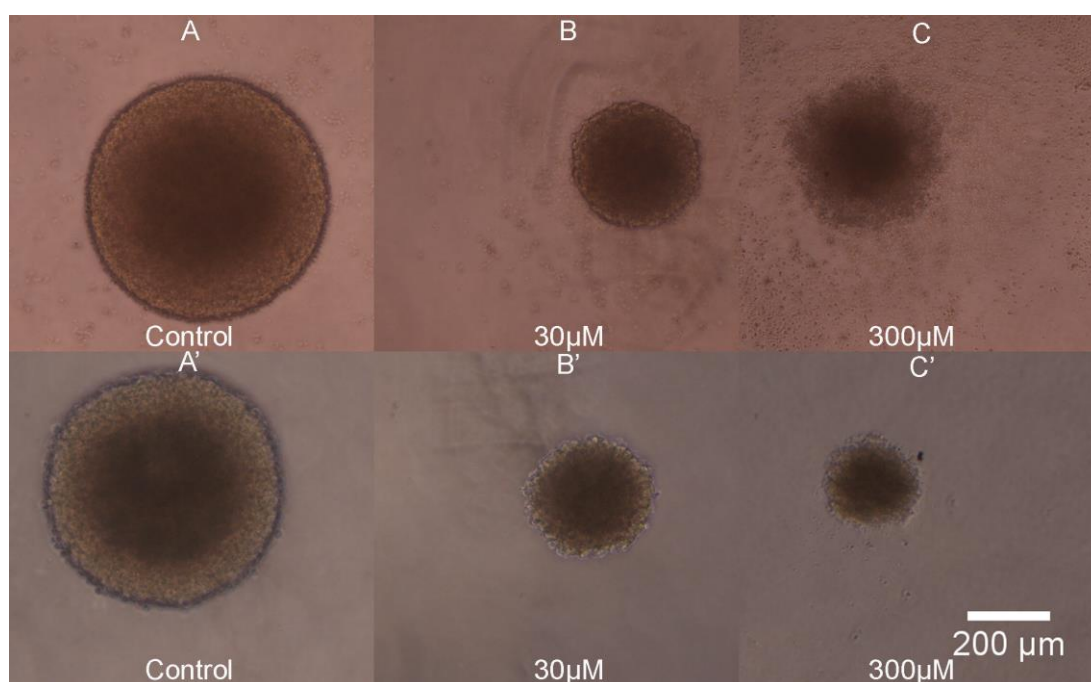


Figure 3-23. Phase-contrast microscope images of NSC exposed to increasing concentrations of etoposide. A-C spheroids before PBS wash. A'-C'- the same spheroids after PBS wash. Control is grown in plain media, concentrations of etoposide on drug treated spheroids shown in μM , scale bar applies to all panels.

Spheroid size reduction and metabolic activity determination complement each other as they use different mechanisms to estimate viability and can paint a fuller picture of spheroid health. When the rate of volume decrease is slower than the change in metabolic activity it would suggest that the proportion of dead cells, within the spheroid, is influencing the volume

reading or that cells increase their volume due to treatment. However, a faster rate of volume decrease compared to resazurin reduction would indicate stress-induced cell shrinkage without loss of metabolic activity. This is even more important in the context of impaired functionality of normal tissue. Often changes in cell volume will precede any other marker of viability indicating a nonspecific insult to baseline cell performance.

On the other hand, a proportion of larger cells with increased metabolic activity at intermediate levels of etoposide, as described by Chan et al [292] may be present in our neurospheres assay causing an underestimation of cytotoxicity in the case of volume and resazurin. Nevertheless viability estimates for volume and cell numbers were not statistically different for the most part of the dose-response curve. While some cells in the spheroids could increase in volume, others may shrink due to apoptosis and yet another group would detach from the spheroid bringing volume estimates for viability closer to cell numbers.

Although live cell counts can be viewed as the “gold standard” for viability determinations in 2D, the extensive procedure for spheroid dissociation introduces variability outweighing the benefits of accuracy. Therefore, based on the lower variability of IC50 measurements and the similarities with actual cell numbers, in cases dealing with a new drug delivery strategy for a particular drug, volume would be a superior assay able to distinguish smaller differences in IC50s.

Section 3.7 Conclusions

Three-dimensional human cell culture is a useful tool that can help narrow the gap between preliminary *in vitro* studies and *in vivo* experiments required for drug development. Spheroids were cultured just as easily as monolayers in 96-well ultra-low attachment plates and a suite of assays was employed to probe their viability.

The open source ImageJ macro can automatically measure whole batches of spheroids and record the results both numerically and as an image. Spheroid volume was shown to be an excellent predictor for the number of viable cells in healthy spheroids. It can also be used as a reference

method for cytotoxicity assays where the normalized volume readings are compared to other ways of estimating cell health.

In this respect, the acid phosphatase assay was tested and its linear response to cell number in medulloblastoma spheroids of 160-700 μ m validated. It is a simple, quick method for viability determination that does not require any expensive ingredients and is high-throughput compatible. However, it relies on lysing the cells in question and needs to be the final assay in a high-content screening chain.

The third assay tested, resazurin reduction, does not have these shortcomings because it is not toxic to the cells in the concentrations and exposure times used. Additionally, it can be performed multiple times and coupled with other studies. The difference in metabolic rate between the cells in the periphery and the middle of the spheroid can account for the lower r squared values of resazurin data fit compared to the other two methods. Although it appears inferior to volume determination and APH, we have demonstrated that metabolic activity can reliably be used in cytotoxicity screens despite its perceived limitations. An interesting recent study has shown some of the constraints of resazurin diffusion into colon cancer spheroids forming tight junctions[298]. While Walzl et al. have concluded that the resazurin assay is unsuitable for viability determinations in these cases, they have found an easy way to circumvent that problem by incubating the spheroids with ethylene glycol tetraacetic acid. Intriguingly, the authors have reported that cytostatic compounds could be distinguished from cytotoxics in colon cancer models using resazurin. This differentiation was accomplished by combining spheroid morphology and resorufin fluorescence in the absence of tight junction disruption.

The optimal seeding densities for both cell types were determined by biological considerations for spheroid size and gradients and were also benchmarked for Z -factor >0.4 , Signal window >2 and Coefficients of variation $<20\%$. The suite of assays was performed on the same spheroids and the results compared and validated against the number of cells in a spheroid using both healthy tissue and spheroids exposed to a cytotoxic

drug. Plate uniformity was examined for spheroid volume at day 3 and signal variability was assessed for volume, resazurin and APH assays during the cytotoxicity screen. After comparing the precision of IC50 determinations for all assays, cell volume and resazurin were found to perform better than APH and cell counts for both cell types. As volume, metabolism and acid phosphatase activity can all be influenced by cytotoxic drugs in a different manner, multiplexing those assays is the best way to get the true picture of cellular response.

Etoposide sensitivity of the UW228-3 medulloblastoma cell line was carried out in parallel with human foetal brain tissue derived stem cells (NSC) in order to have a comparison with cells representing human brain tissue. While the tumours exhibited a normal four parameter logistic dose-response curve, the NSCs had a biphasic response. The most likely explanation for this data is the presence of two sub-populations of cells within the neurospheres with a different sensitivity towards etoposide. The first sub-population had a low acid phosphatase activity and was more susceptible towards cytotoxic action, whereas the second one had a higher APH activity and was more resistant to topoisomerase inhibitors. The foetal NSC cells would be expected to have a relatively high proportion of stem cells[204]. Under 3D culture conditions and the associated gradients of oxygen and nutrients the population of early progenitor cells can differentiate into late progenitors, neurons and glia which would have different rates of division and different sensitivity to etoposide. The faster dividing and more sensitive cell population is probably the less-differentiated one. Those undifferentiated cells are responsible for the growth, development and repair in vivo. While they make up a higher proportion of the brain in childhood when the brain is still growing and developing, they are confined to specific locations in the adult brain and have a supportive role. Establishing the proportions of stem-like, neural and glial cells that make up the neurospheres and how those change during etoposide exposure would bring greater insight into the off-target effects of topoisomerase II inhibitors. Furthermore, the relative cell type proportions in the neurospheres could be influenced by changes in the media, such as EGF and FGF withdrawal that would promote progenitor

differentiation into neurons and glia. Nevertheless, foetal brain tissue as a whole was more sensitive to etoposide up to concentrations of 5-10 μM when the neurospheres' slow decrease in viability was surpassed by the sharp decline in tumour cell survival. This is a biorelevant concentration that has been established to be tolerable in humans thereby inferring some limited selectivity of free etoposide [299].

Although etoposide is not generally regarded as a neurotoxic drug [121] there are reports which have demonstrated neurotoxicity in mice after blood-brain barrier disruption [300]–[302]. The heightened sensitivity of a sub-population of the neurosphere cells to etoposide can be explained by the presence of growth factors in the media which limit differentiation and stimulate division. In the normal human brain *in vivo*, only a small percentage of the available neural stem cells proliferate whereas the others are quiescent and may be spared from the effects of the cytotoxic drugs [303], [304]. Nevertheless this study suggests that free etoposide is not discriminating between actively dividing tumour and normal cells.

This Chapter has established a quick and reliable way to culture and analyse neural progenitors and tumour cells in 3D allowing to probe their relative sensitivity to chemotherapy. The next step was to bring both tissues together in a single co-culture model of medulloblastoma and analyse the viability of each cell type separately.

Chapter 4. Co-culture model of medulloblastoma

Section 4.1 Introduction

This chapter presents the development of an advanced co-culture model of medulloblastoma. Employing cultures of both normal and tumour tissue provides information for the relative safety and efficacy of treatment and can be used to rank formulations according to their therapeutic safety ratio.

It builds on the model from the previous chapter by including the interaction between normal and tumour cells. This tumour-host interaction has been reported to influence tumour gene expression, growth, enhance vascularisation and modulate tumour sensitivity to chemotherapy[246]–[248]. Including a normal tissue component was proven to be vital in the successful development of a lung cancer model[305]. Moreover, spheroid co-cultures have been used to demonstrate differential response to local intravesical treatment in bladder cancer [306], [307]. The medulloblastoma model described here was created with the intention to evaluate the relative uptake and cytotoxicity of drug-loaded nanoparticles compared to free drug in future experiments. In order to accomplish this aim, a reliable method to tell apart and quantify each population separately had to be established.

There are a number of methods that can be used to distinguish between different populations of cells cultured together in co-cultures. Specific antigens can be employed [307], [308], cells can be genetically modified to express fluorescent proteins [309], [310] and fluorescent dyes can be utilised for medium-term cell monitoring [311]. This method was developed with primary tissues in mind where the increased heterogeneity is thought to better reflect the true nature of tumours. However, the diversity can also hinder the discrimination between the normal and tumour population.

Medulloblastoma is an embryonal tumour that shares many antigens with developing neural progenitor cells [251], [312]–[315]. Moreover,

medulloblastoma is made up of least four clinically and molecularly distinct types of tumours [13]. There appear to be further differences within subgroups [17], [22] as well as intratumoral heterogeneity especially after treatment with radiation and chemotherapy [23]. The combination of common antigen presentation and disease heterogeneity precluded the use of specific antibodies to distinguish between developing brain tissue and the tumour cells

Another option was to use genetic manipulation to stably express a fluorescent protein into each of the cell populations[309], [310]. This usually involves introducing foreign genetic material into the cells and then selecting for the clones with favourable expression of the product of interest. A possible complication could arise if certain viruses (e.g. lentivirus) were to insert their sequence next to important genes and change cell behaviour. However, the main concern was that by artificially selecting the most highly fluorescent clones, the heterogeneity of primary tissues would be lost.

Therefore, a procedure of temporarily marking the cells with fluorescent dyes, which would not affect their viability was chosen as the most suitable method. Supravital dyes are compatible with primary tissues and can be used to stain heterogeneous populations of cells. They employ a simple, universally applicable marking procedure and have no requirement for the presence of specific cellular antigens. The most common strategies for long-term supravital fluorescent cell labelling involve either marking the cell membrane with lipophilic carbocyanine dyes [316], or preferential cytosolic protein marking with amine-reactive compounds [317]. Nuclear staining dyes like Hoechst 33342 were not considered because of their reported DNA interaction and short-lived labelling [318].

Although the membrane-incorporating carbocyanine dyes, like DiI, have a proven track record of in neuron labelling their fluorescence staining can often diminish before analysis [319] and dye transfer to the nearby cells has been reported [320]–[322]. CM-DiI is a second generation carbocyanine dye which claims better retention due to the chloromethyl

group. The halogen reacts with thiol groups on membrane proteins and peptides and ensures prolonged stability and aldehyde fixability of stained cells. CellTracker Violet (BMQC) is also thiol-reactive but targets mainly the sulfhydryl groups of cytoplasmic glutathione.

The amine-reactive dyes have been reported to be superior in peak resolution and non-specific dye transfer compared to the membrane-staining dyes [323] CDCFDASE is the 2,7-dichloro derivative of CFDA SE [324] which is less susceptible to photobleaching and pH fluctuations. Both CDCFDASE and CellTrace Violet share the same mechanism for marking the cells- acetate groups allow the molecules to cross the cell membrane and are subsequently cleaved in the cytoplasm. Afterwards the succinimidyl moiety reacts with amino groups of cytosolic proteins and labels the cells for about 5-8 cell divisions [325].

A number of imaging and analytical techniques can be used to characterise the co-cultures and quantify the number and health status of the labelled cells. Microscopy techniques offer the opportunity to image the intact spheroids and reveal the spatial distribution and interaction between both cell types. However, confocal microscopy is limited by the penetration depth of short wavelength photons and can cause considerable tissue photobleaching. For example, it has been reported that confocal microscopy can only achieve 50-100 μm penetration in tissues [326]. In contrast, multiphoton microscopy uses longer wavelength photons which can penetrate deeper into the spheroids. Moreover, multiphoton microscopy focuses the energy of both photons at a single focal point limiting integral tissue exposure and photobleaching[327]. Both microscopy techniques are limited in the number of fluorophores they can analyse and spectral overlap can be a significant problem.

Flow cytometry circumvents the abovementioned obstacles by illuminating the cells with light from different lasers and detecting the emitted fluorescence in a number of separate channels. In multicolour flow cytometry experiments the cells pass sequentially in front of different lasers, the fluorophores are excited and the emitted light is

detected by a set of detectors for the laser. Afterwards they move on to the next laser, where the process is repeated without overlap between the two lasers. Notable shortcomings of flow cytometry are that it does not show the organisation and distribution of cells within the spheroid and can suffer from dissociation-related cell loss especially after drug treatment. However, flow cytometry has a larger dynamic range and is less susceptible to fluorescence interference. It also allows the use of more colours and provides superior data handling tools compared to the analysis of multiphoton images. Hence it was the preferred mode for normal brain and tumour population quantification and determination of cellular health status.

Section 4.2 Materials and methods

4.2.1 Materials:

CellTrace Violet, the chloromethyl derivative of DiI (CM-DiI)- 1,1'-dioctadecyl-3,3,3'3'-tetramethylindocarbocyanine, CellTracker Violet (BMQC- 2,3,6,7-tetrahydro-9-bromomethyl-1H,5H-quinolizino(9,1-gh)coumarin), CellTracker CMPTX and 5-(and-6)-carboxy-2',7'-dichlorofluorescein diacetate succinimidyl ester (CDCFDASE) were supplied by Invitrogen (Paisley, UK).

Annexin V-Allophycocyanin (Annexin-APC, 20X solution), propidium iodide (PI) and 7-Aminoactinomycin D (7-AAD, 50µg/mL) were purchased from Ebioscience (Hatfield, UK).

4.2.2 Cell lines and culture

UW228-3, VCR and NSC cells were cultured as described in Chapter 3

4.2.3 Cell label optimisation experiments

Cell marking optimisation and label selection was done as described in Section 2.6. Initial experiments, before the introduction of ultra-low attachment plates were performed in non-adherent flasks.

4.2.4 Co-culture formation

Co-culture spheroids were established by plating a homogenous mix of fluorescently labelled tumour and normal brain cells (200 μ L, 3500 cells/well from each type) as a single-cell suspension in ULA plates at the same time. Co-culture spheroids formed in 24h and were cultured for 7 days, exchanging with fresh media (150 μ L) on days 3 and 5.

4.2.5 Spheroid viability monitoring

Spheroid growth and metabolic activity were monitored as described in Section 2.5 with the omission of the acid phosphatase assay.

4.2.6 Multiphoton confocal microscopy

Spheroids were fixed using paraformaldehyde solution (4%) after washing twice with PBS (150 μ L). The spheroids were stored in the plates at 4°C in PBS protected from light. Imaging was done by placing the spheroids on top of a glass slide along with 20 μ L of PBS. Zeiss LSM510NLO confocal multiphoton microscope was used with a Plan-apochromat 20x/0.8 objective and 800nm excitation wavelength. Images were later processed using ImageJ by auto-adjustment of brightness and contrast, followed by creating an average intensity Z-projection.

4.2.7 Cytotoxicity screen

Labelled spheroid co-cultures were seeded in ULA plates and exposed to increasing concentrations (0.3-100 μ M) etoposide on day 3. Etoposide was replaced with fresh media on day 5 and analysed on day 7. Controls included in the screen were unstained single cultures of UW and NSC cells, unstained co-culture, single colour controls and labelled co-culture control with media and DMSO (0.2%). Six spheroids per condition were analysed on each plate. Brightfield images of the cultures were used to determine the volume of the spheroids compared to untreated controls. The percentage of each population was estimated using flow cytometry.

4.2.8 Flow-cytometry

Spheroids were washed twice with PBS (150 μ L/well), dissociated using Accutase (double concentrated, 50 μ L/well) for 30minutes at 37 °C

followed by mechanical dissociation by repeated pipetting. The resultant single cell suspensions from six wells per condition were pooled together in a microcentrifuge tube, centrifuged (300g, 5min) and resuspended in Annexin binding buffer (10 mM HEPES, 140 mM NaCl, 2.5 mM CaCl₂ pH=7.4; 50 µL). Dead and apoptotic cells were stained using 7-AAD (5 µL, 50 µg/mL) as per [328]. Early apoptotic cells were detected using Annexin V-APC (2.5 µL). After incubation for 15 minutes in the dark, further Annexin binding buffer (200 µL) was added and the cells stored on ice, protected from light were analysed within 2h. Flow cytometry experiments were done using a 14 channel MoFlo XDP cell sorter (Beckman Coulter) equipped with a three laser system (405, 488 and 630 nm). CDCFDASE and 7-AAD positive cells were detected using the blue 488 nm laser and the 529/28 and 670/30 channels respectively. CellTrace Violet positive cells were excited with the violet 405nm laser and detected with a 450/65 filter. The Annexin V-APC positive apoptotic cells were excited by the red 630 nm laser and detected in the 670/30 channel. Non-stained and single colour controls were included in each experiment. Data were analysed using the Weasel software package. Debris were identified and subsequently excluded by gating the Annexin V-APC and 7-AAD negative population on the Forward/side scatter dot plot and selecting for the particles with the lowest forward scatter values [329]. The MoFlo channel configuration (Figure 4-1) and dye emission and excitation maxima (Table 4-1) are summarised below:

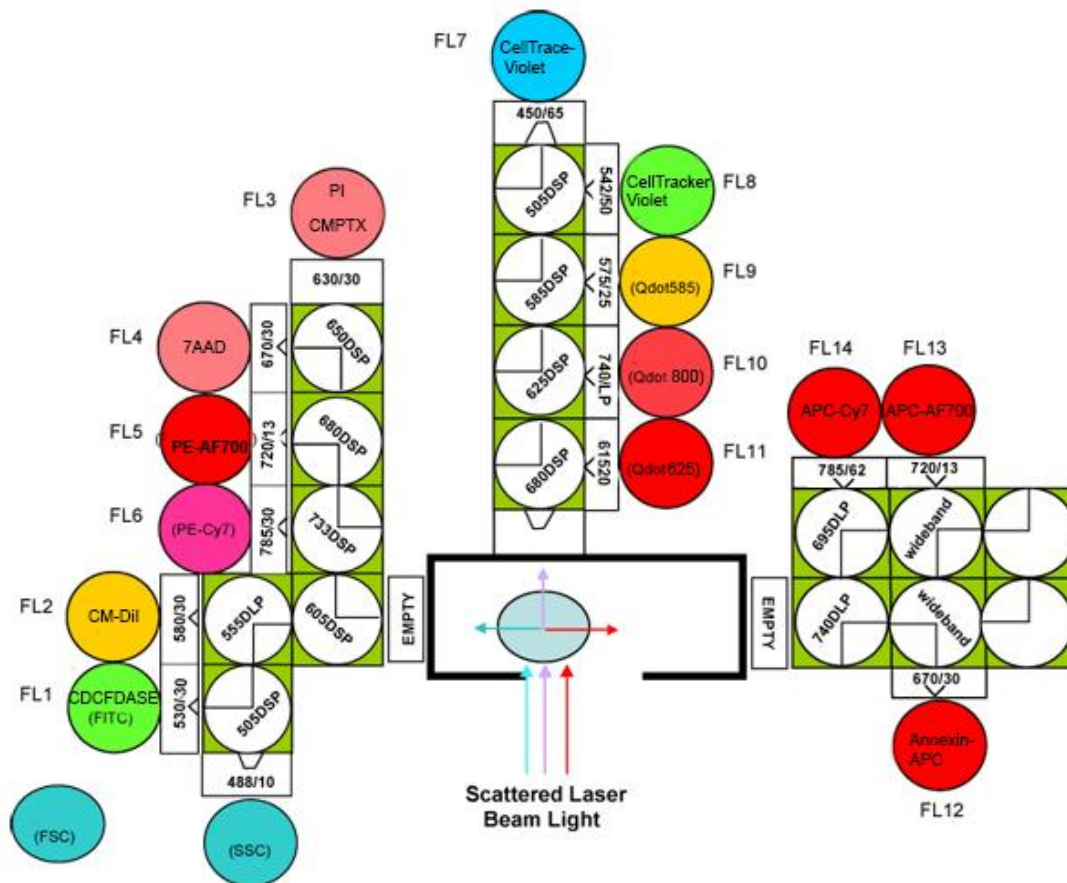


Figure 4-1. MoFlo laser and filter setup. Please note that the cells pass in front of each laser separately

Dye	Excitation	Emission	Fluorescent Channel
CellTrace Violet	405	450	FL7
CellTracker Violet	405	526	FL8
CDCFDA SE	492	517	FL1
CM-DiI	553	575	FL2
CMPTX	577	602	FL3-4
Cellular viability stains			
PI	488	647	FL3-4
7AAD	488	670	FL4
Annexin-APC	630	670	FL12

Table 4-1. Excitation and emission maxima of the fluorescent labels employed in the experiments

4.2.9 Imaging flow cytometry

Imaging flow cytometry using the Amnis Flowsight system was used to visualise the dissociated cells from the spheroid co-cultures. The following combination of lasers and detectors was employed (Table 4-2):

Dye	Function	Excitation, nm	Emission, nm
CellTrace Violet	Cell label (UW228-3)	405	Channel 7 (430-505)
CDCFDASE	Cell label (NSC)	488	Channel 2 (505-560)
7-AAD	Dead and apoptotic cells	488	Channel 5 (642-740)
Annexin-V	Early apoptotic cells	642	Channel 11 (642-740)

Table 4-2. Dye combination and detection configuration used in the Flowsight imaging flow cytometer

Non-stained and single colour controls were used to calibrate the channels and data were analysed on the AMNIS IDEAS Software.

4.2.10 Data analysis and statistics:

Raw data from volume determination, Resazurin reduction, and flow cytometry software were exported and analysed in MS Excel and GraphPad Prism 6. In label optimisation experiments, readings were normalised to the relevant unstained control (100%) and spheroid-free wells (0%). In cytotoxicity experiments, volume measurements were normalized so that untreated co-culture controls were assigned to 100% viability and media-only wells- 0% viability. Flow cytometry results for the proportion of normal brain cells and tumours were multiplied by the volume of each spheroid to estimate the surviving fraction of each cell type. Dose response curves were fitted using the four-parameter logistic equation in Prism, the top was constrained to 100% and the bottom to 5%. Results are displayed as mean \pm SD unless stated otherwise. There were n=6 replicates for each condition in each individual experiment and displayed data represent the mean of at least three independent experiments.

Section 4.3 Stain selection considerations and experiments

The cell labels included in the primary screens were CDCFDASE, CM-DiI, CellTracker Red-CMPTX, CellTracker Violet-BMQC and CellTrace Violet.

VCR and NSC cells were labelled with each stain and analysed after different number of days of culture in NSC-media in non-treated flasks.

The initial dye selection experiments were done in the early days of the project when the ultra-low attachment plates were not yet employed and the medulloblastoma working cell line was still the etoposide-resistant VC312R. After marking and culturing the spheroids they needed to be dissociated in order to be analysed by flow cytometry. The initial experiments with Trypsin required a large number of mechanical dissociation steps (pumping up and down). The procedure had to be especially harsh to dissociate the tumour tissues with Trypsin concentrations reaching 1%, while foetal neurospheres required only 0.1% of the digestive enzyme. Later experiments were performed using the marine-origin protease mixture Accutase. The process was much gentler when using Accutase, required less mechanical intervention and led to increased viability (data not shown). Nevertheless, the first experiments highlighted the importance of fluorescence signal overlap and demonstrated the toxicity of some stains.

The data for the initial experiments with CDCFDASE, CellTracker Violet and CM-DiI for VCRs and NSCs are summarised in Table 4-3 and Table 4-4.

Dye	CDCFDA SE	CDCFDA SE	CM-DiI	CTV	CTV	CTV	CTV
Dye Concentration μM	5	5	5	10	20	30	40
Dye media	HBSS	HBSS	HBSS	HBSS	HBSS	HBSS	Media
Seeded cells $\times 10^6$	0.2	1	0.5	1	1	1	1
Time of culture, days	6	4	2	2	3	3	3
Trypsin conc, %	1	1	1	1	1	1	1
Formation of spheroids	++	+++	+++	+++	+++	+++	+++
Percentage of marked cells	86	94	99	71	73	85	71

Table 4-3. Optimisation of cell staining for VCR cells labelled as monolayer and cultured as spheroid in non-treated flasks. The last row- percentage of cells brighter than control was the most important indicator of marking efficiency. The formation of spheroids was coded from none (---) to equal to control (+++).

Table 4-3 shows that the percentage of labelled tumour cells was above 85% for CDCFDASE and CM-DiI at levels as low as 5 μM . In contrast, CellTracker Violet (CTV) was not retained in the tumour population unless used at very high concentrations (30 μM), well above those recommended by the manufacturer (2.5-10 μM). The cell viability was

not affected by the marking procedure and was above 75% in all experiments.

As seen by Table 4-4 CDCFDASE was the only label retained in the foetal neurospheres with percentage of cells brighter than the unstained control surpassing 95%. CM-DiI was not as effective, being retained in only 76% of cells, while CellTracker Violet (CTV) showed toxicity towards stem cells above 5 μ M concentrations. The toxicity was seen either as inhibition of spheroid formation or the induction of delayed apoptosis and cell death. Addition of media during staining, in order to mitigate the toxic effect of CTV, was attempted but this led to a decreased marking efficiency due to a possible reaction of the dye and thiol-containing ingredients of the media.

Dye	CDCFDA SE	CM- DiI	CTV	CTV	CTV	CTV	CTV
Dye Concentration μ M	5	4	5	10	10	20	40
Dye media	PBS	PBS	PBS	PBS	media	media	media
Seeded cells $\times 10^6$	2	2	2	2	2	0.6	1
Time of culture, days	6	3	6	5	6	X	X
Trypsin conc, %	0.1	0.1	0.1	X	0.1	X	X
Formation of spheroids	+++	+++	+/-	---	+++	---	---
Percentage of marked cells	97%	76%	73%	X	60%	X	X

Table 4-4. Optimisation of cell staining for foetal neurospheres dyed as a single cell suspension and cultured as spheroids in non-treated flasks. The percentage of labelled cells and the formation of healthy spheroids were used to prioritise stains. X-indicates cell death. Spheroid formation compared to unstained control was coded from none (---) to equal to control (+++).

The results shown in the tabular data suggested that tumours stained with CM-DiI and normal cells with CDCFDASE may constitute a possible combination. However, a careful examination of the spectral properties of both dyes revealed significant spectral overlap between the stains.

Figure 4-2A shows a series of histograms plotting the distribution of fluorescence intensity of the unstained (control- blue) and stained (red) NSC cells. The unlabelled cells had a low basal fluorescence centred towards the left part of the graph. Marking the cells with CDCFDASE increased the fluorescence of the cells not only in the CDCFDASE channel but also in all channels of the blue laser (CM-DiI, PI and to a certain extent those for 7AAD) and even the CellTracker Violet channel. The CellTrace Violet channel and the AnnexinV-APC channels were the only ones not affected by the spectral spillover. The fluorescence interference could be mitigated using Weasel's software compensation algorithms. As

seen in Figure 4-2B subtraction of 38% of the CDCFDASE signal from the CM-DiI channel was needed to decrease the spillover.

The labelling of VCR cells with CM-DiI is shown in Figure 4-3. When compared to the unmarked cells- (A2) over 90% of the CM-DiI labelled cells- (B2) exhibit fluorescence brighter than the controls. Subplot C shows the histograms of labelled (red) versus unlabelled (blue) cells. The fluorescence shift in the PI and 7AAD channels excludes the use of those viability markers with CM-DiI. A similar shift in fluorescence was not seen in the other channels of interest.

NSC-CDCFDASE

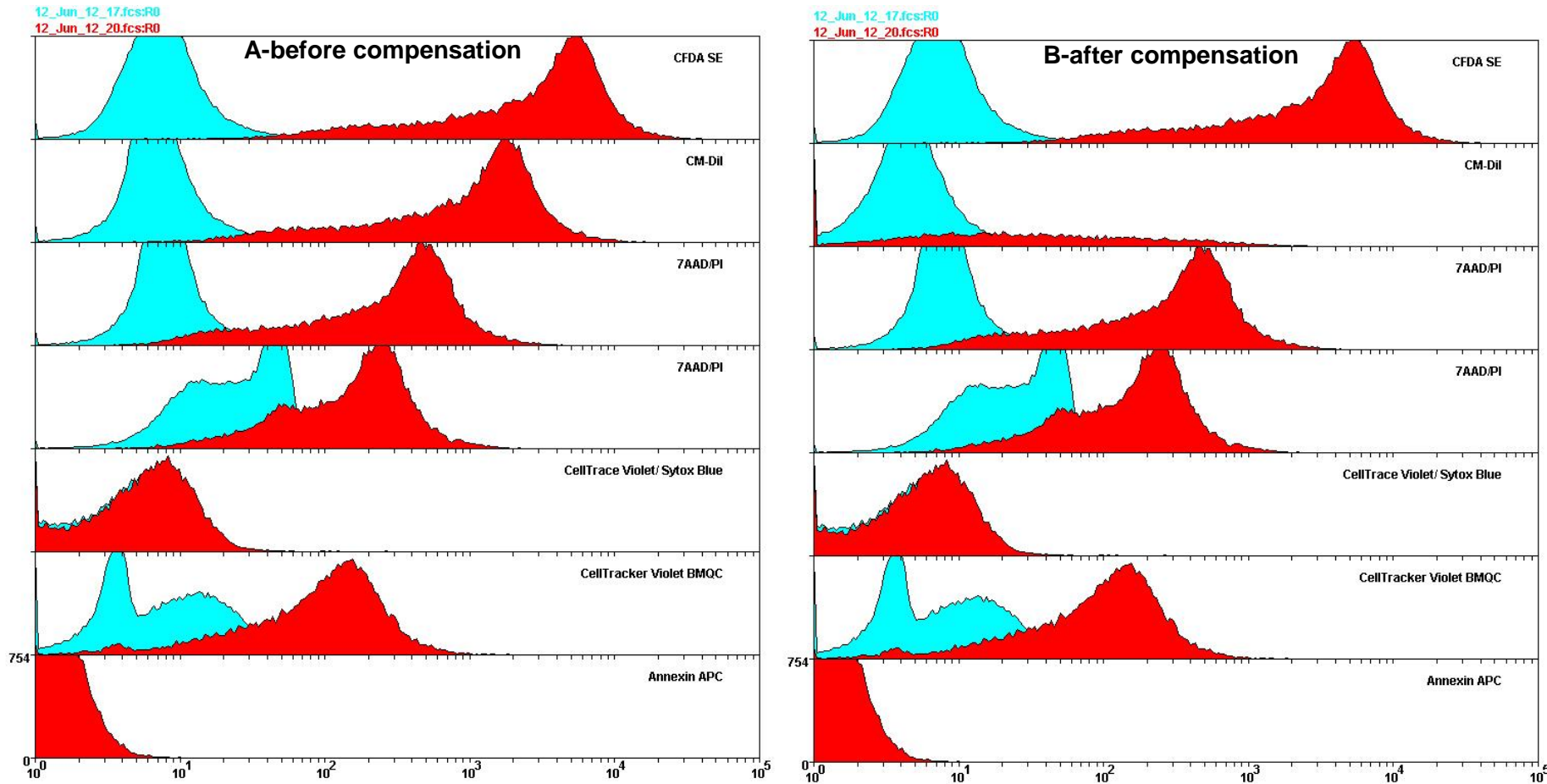


Figure 4-2. Histogram plots of control (blue) and CDCFDA SE ($5\mu\text{M}$) stained normal brain cells NSCs (red) before and after 35% software compensation in the CM-DiI channel. Fluorescent channels are named after dyes of interest that can be detected in them. A- before compensation. CDCFDA SE is spilling over in the CM-DiI, PI, and CellTracker Violet Channels. The spillover is less pronounced in the 7AAD channel and there was no channel cross-talk in the CellTrace Violet channel B-after 35% software compensation, the fluorescence in the CM-DiI channel is reduced

VCR -CM-DiI

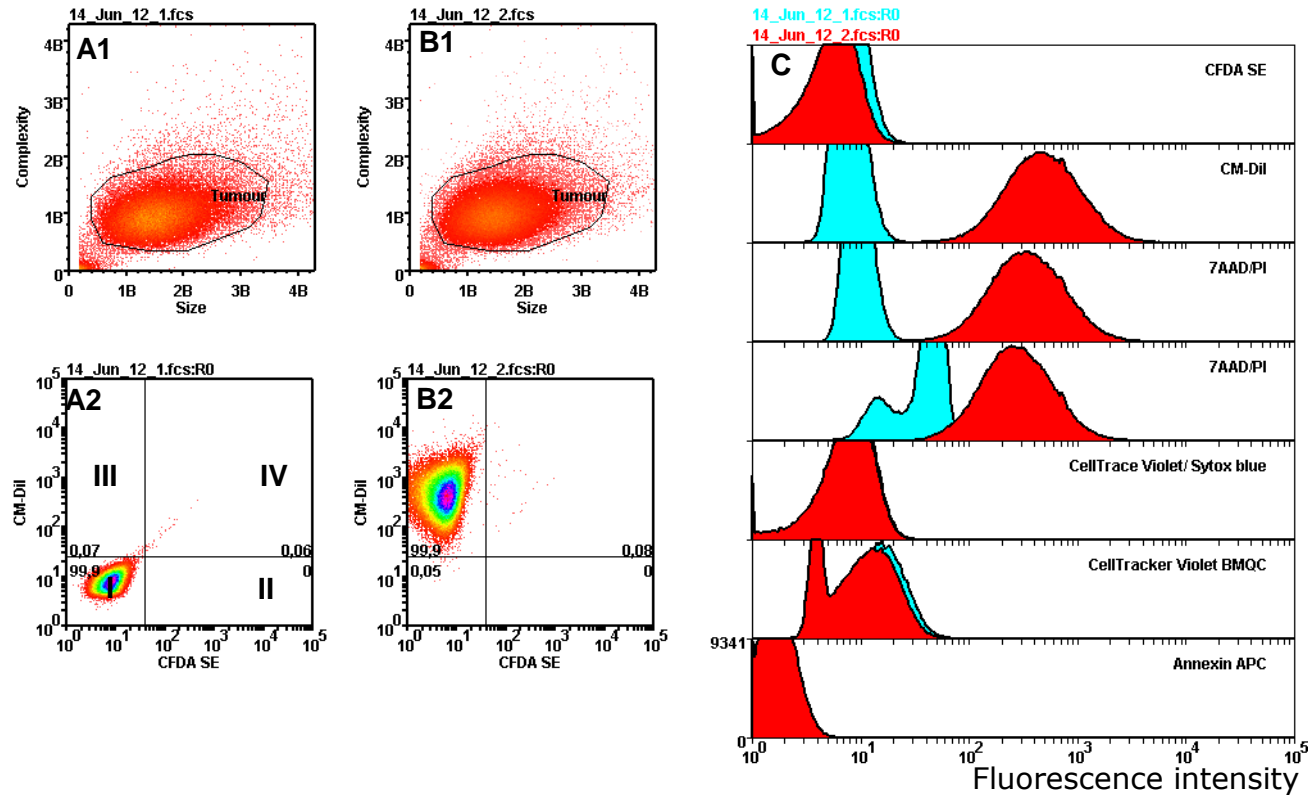


Figure 4-3 Dot plots and histograms of control and CM-DiI (5µM) dyed samples of tumour VCR cells. A1- forward and side scatter plots for control tumour cells (VCR) A2- normal autofluorescence intensity of the control cell population in the CDCFDA SE (FL1) and CM-DiI (FL2) channels and statistical markers defining four quadrants-control cells (I), CDCFDA SE (II), CM-DiI (III) and spillover (IV). B1- forward and side scatter plots for VCRs dyed with CM-DiI. B2- fluorescence of dyed VCR cells. All cells have been successfully dyed with CM-DiI and there is no spillover in the CDCFDA SE channel. C- histogram plots of control (blue) and CM-DiI dyed tumour VCR cells (red). Fluorescent channels are named after dyes of interest that can be detected in them. The CM-DiI fluorescence appears to spread over the 7AAD/PI channels and makes viability determination with these two dyes undesirable. CM-DiI does not interfere with the Sytox Blue, CellTracker Violet or the Annexin APC channels.

The immediate conclusions from these initial experiments were that CellTracker Violet (BMQC) was toxic to the normal progenitor cells, CM-DiI and CDCFDASE could not be used together and that CM-DiI had a pronounced fluorescence tailing in the red channels eliminating the options to use PI or 7-AAD. Based on these findings CMPTX was excluded from the screen due to its unfavourable fluorescence characteristics, namely being excited by green light and fluorescence in the red spectrum (Table 4-1).

The combination of dyes chose for further testing and the respective fluorescent channels are given in Table 4-5:

Component	Dye	Laser & Bandpass nm	Excitation/Emission Max nm
Cell type I	Cell Trace Violet	405 (450/50) FL7	405/450
Cell type II	CFDA SE	488(530/30) FL1	492/517
Necrotic	7AAD	488 (670/30)FL4	546/647 7AAD
	PI	488 (630/30)FL3	535/617 PI
Apoptotic	Annexin- APC	633(670/30)FL12	650/660

Table 4-5. Combination of dyes chosen for further development in labelling and analysing co-culture spheroids.

Figure 4-4 shows the labelling of VCR tumour cells with CDCFDASE and CellTrace Violet and the determination of live and dead cells using PI. The first pair of dot plots in the left panel displays the unstained control before and after the addition of PI. A very small number of dead cells are seen as a separate fraction with higher fluorescence intensity in the PI channel in the second graph of the first pair. In contrast to the unstained controls, the CDCFDASE labelled cells in the second pair of dot plots had higher fluorescence in the CDCFDASE channel. Similarly to the control graphs, upon PI addition, a population of PI-positive cells was easily distinguishable. Likewise, the third pair of dot plots illustrates the marking with CellTrace Violet. Samples without PI had no cells positive in the PI channel which indicated lack of interference. The appearance of a PI positive population shows the baseline proportion of dead cells within the population. The right panel of Figure 4-4 demonstrates the feasibility of distinguishing a mix of VCR cells marked with CDCFDASE and CellTrace

Violet. Two separate populations are visible on the first dot plot without the addition of PI. The second dot plot with PI addition illustrates the health status for each cell population separately. Although the application of 15% software compensation in the PI, channel minimized the interference between CDCFDASE and PI, it was decided that the longer emission wavelength of 7-AAD would be more advantageous as it would require little post-processing compensation.

The experiment illustrated in Figure 4-5 aimed to determine the prospects of combining CDCFDASE, CellTrace Violet and the viability markers 7-AAD and Annexin-V-APC together. The first row shows a series of unstained control samples before and after the addition of 7-AAD and Annexin-APC. Dead cells were identified as the 7-AAD positive population that appears after addition of the dye when compared to the control before dye addition. Similarly the Annexin-APC positive population after reagent addition was determined to be apoptotic. When both Annexin-APC and 7-AAD were added to the unstained control, as seen in the last dot plot of the first row, both apoptotic (7-AAD- intermediate, Annexin-high) and dead (7-AAD high, Annexin-high) could be distinguished from healthy cells (Annexin-low, 7-AAD-low). These results are in agreement with the findings of Zembruski[328] who reported that healthy cells exhibit low 7-AAD internalisation, apoptotic intermediate, while dead cells are very permeable to the dye. The second row shows the same progression of reagent addition for the CDCFDASE labelled cells. Similarly to the unstained control, cell viability could be determined using the viability stains and the 7-AAD and Annexin populations were not affected by the labelling. The same was true for the CellTrace Violet marked cells shown on the third row of the figure before and after the addition of 7-AAD and Annexin. The middle panel of the third row shows the forward and side scatter characteristics of the cells and the gate used to exclude the debris from the samples. In conclusion the use of 7-AAD and Annexin-APC to determine membrane permeability (death) and phosphatidylserine externalisation (apoptosis) was compatible with the marking procedure with CellTrace Violet and CDCFDASE. The cell labelling did not interfere with the fluorescent channels of the viability dyes and the combination was deemed successful.

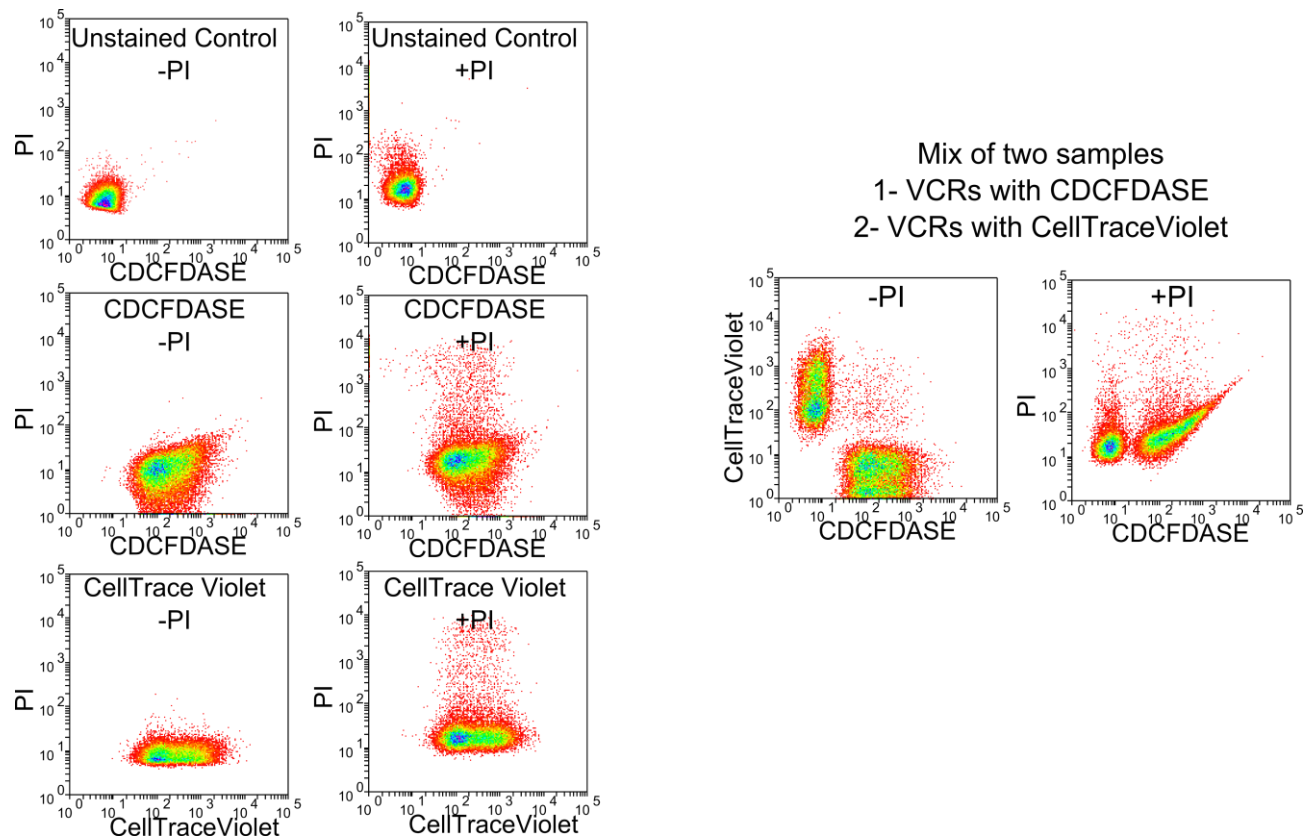


Figure 4-4. Flow cytometry dot plots of VCR cells stained with CDCFDASE or CellTrace Violet (48h after staining) and their membrane permeability status determined by propidium iodide (PI). Fluorescent intensity axes are named after the stain of interest, sample names and reagents are stated inside the dot plot squares. Top row pair of plots in the left panel shows the distribution of intrinsic cellular fluorescence of unstained VCR cells before (left) and after (right) addition of (PI). Middle row shows cells marked with CDCFDASE. The left panel (without PI) shows that there was interference between CDCFDASE and PI (diagonal tailing of the population) that required the use of 15% software compensation. The right panel shows that it was still possible to distinguish dead (PI- positive) from living cells (PI-negative) despite the spillover. Bottom panel (CellTrace Violet marked cells) shows no interference with PI. Right part of the graph illustrates the separation of a mixed sample containing VCR cells marked with CDCFDASE and CellTrace Violet

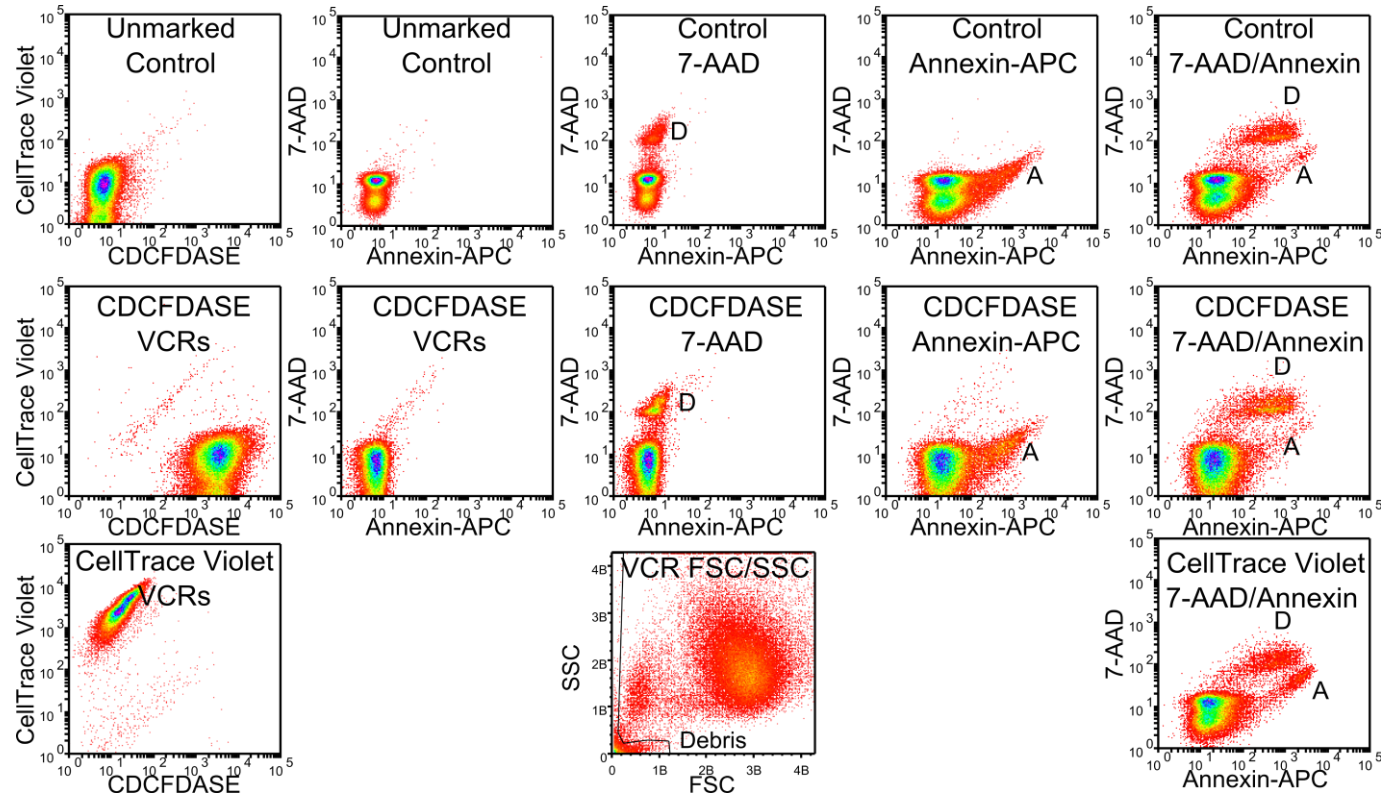


Figure 4-5. Flow cytometry dot plots showing the compatibility of cell labelling and health status determination for VCR cells (48h after marking). Top row represents the fluorescence intensity distribution of unstained control samples in the CDCFDASE, CellTrace Violet, 7-AAD and Annexin-APC channels. Sample names and the addition of 7-AAD and/or Annexin-APC are indicated within the dot plot squares. 7-AAD positive cells are identified as D-Dead, while Annexin-APC positive cells are identified as A-Apoptotic. Samples stained with CDCFDASE and CellTrace Violet exhibited fluorescence brighter than controls. Staining with CDCFDASE or CellTrace violet did not interfere with viability determination. The bottom row, middle column Forward/Side scatter (FSC/SSC) panel shows the gating strategy for the experiments- particles with low 7-AAD/Annexin-APC fluorescence and low FSC/SSC were excluded as debris as per [329].

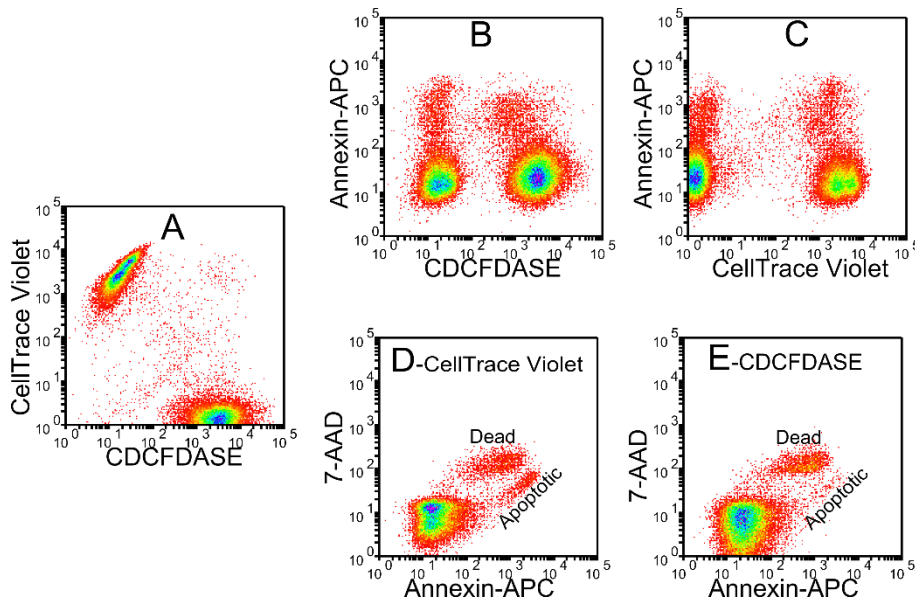


Figure 4-6. Dot plots showing the analysis of a mixture containing VCR cells marked with CDCFDASE and CellTrace Violet (48h after marking). A-fluorescence intensity dot plot of the green and violet channels. Both populations are very well separated from each other after 48h of culture and dissociation. B and C-dot plots showing fluorescence intensity in the labelling channels against Annexin-V-APC stain for apoptosis. D and E- analysis of apoptotic and dead cells for each population separately.

The principal suitability of the combination of dyes for labelling and viability was established in a proof-of-concept experiment illustrated on Figure 4-6. VCR cells were labelled with CDCFDASE and CellTrace Violet and cultured separately for 48h as spheroids in non-adherent flasks. After dissociation the two cell suspensions were mixed and analysed using flow cytometry. When a dot plot was drawn by plotting the intensity of fluorescence in the CDCFDASE and CellTrace Violet channel (Figure 4-6A), two separate populations of cells were easily distinguished. One exhibited strong fluorescence in the green (fluorescein) channel and the second one was highly fluorescent in the violet-blue (CellTrace Violet) channel. The health status of the separate populations could be determined by using a dot plot of Annexin-APC fluorescence versus the fluorescence intensity for each of the dyes (Figure 4-6B and C) or by gating each population separately (Figure 4-6D and E). By focusing on each of the two populations and drawing dot plots of Annexin vs 7-AAD fluorescence both apoptotic and dead cells could be easily distinguished. This feasibility study showed that the combination of four dyes could be employed to discern between two differently labelled populations of cells and determine their health status separately without overlap.

Section 4.4 Preliminary experiments with etoposide

After the labelling procedure was established a few exploratory experiments were performed with etoposide and the VCR cell line cultured in monolayers and as heterogeneous spheroids in non-adherent flasks. These studies aimed to establish the effects of etoposide on the tumours and whether etoposide incubation led to an increased percentage of dead and apoptotic cells. Dead and apoptotic gates were identified from unstained control samples by drawing a region around the 7-AAD intermediate, Annexin-high population for apoptotic cells and 7-AAD-high, Annexin-high population to identify dead cells. Healthy cells were defined as the ones exhibiting low Annexin and 7-AAD fluorescence. It was anticipated that dead and apoptotic cells would detach from the spheroids and the monolayers and great care was taken to preserve those fragile cells by keeping the supernatants of the monolayers and the washing fractions from the spheroid samples along with the main cell fractions. Nevertheless the percentage of dead and apoptotic cells did not appear to change with increasing concentrations of etoposide (Figure 4-7) and (Table 4-6).

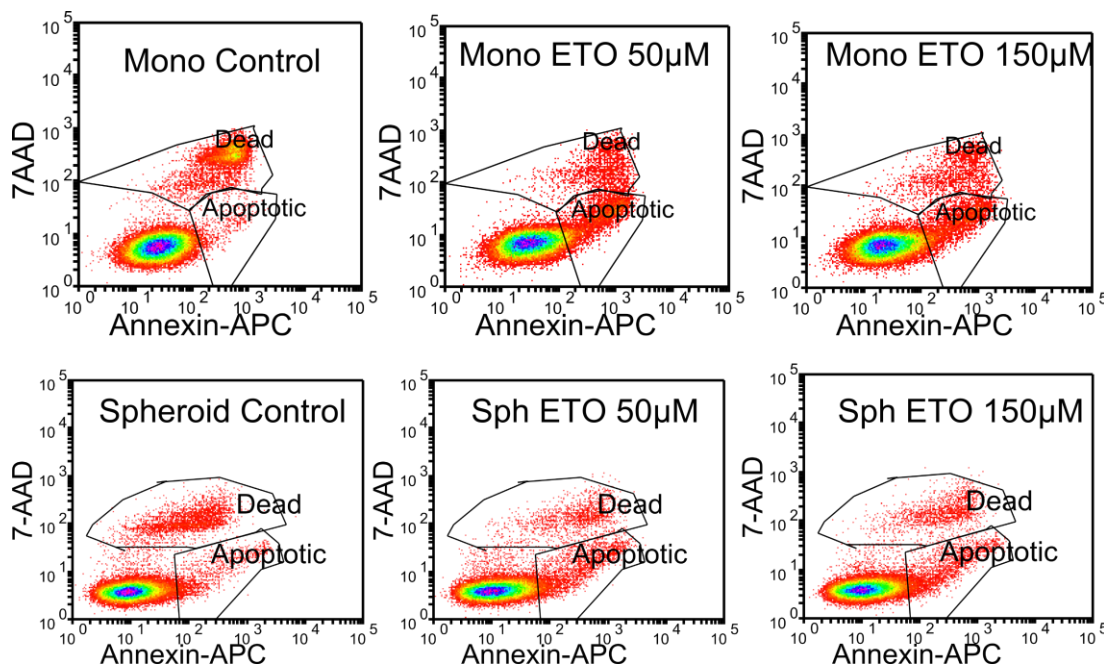


Figure 4-7 Flow cytometry analysis of monolayers and spheroids of non-stained VCR cells exposed to etoposide for 24h. Top row VCR cells exposed to etoposide as monolayers in cell culture treated flasks. Bottom row VCR spheroids exposed to etoposide in non-treated flasks. Cell viability percentages are given in Table 4-6

Sample	Cell count, cells x10 ⁴	Apoptotic %	Dead %
Monolayer Control	119	1	12
Monolayer 50 μ M	56	7	4
Monolayer 150 μ M	50	6	4
Spheroid Control	128	3	6
Spheroid 50 μ M	72	5	3
Spheroid 150 μ M	70	6	3

Table 4-6. Table summarising cell counts of VCR cells exposed to increasing concentrations of etoposide as determined by direct haemocytometer counts and percentage of dead and apoptotic cells determined via flow cytometry in Figure 4-7.

Table 4-6 shows the change in cell count and the percentage of apoptotic and dead cells after exposing the VCR cell line to increasing levels of etoposide. It is notable that despite the significant drop in number of cells with increased etoposide concentrations the percentage of dead and apoptotic cells did not appear to increase after 24h of etoposide exposure. A possible explanation of this apparent cell loss may lie in the dissociation procedure involving steps of enzymatic digestion and numerous washes. The trypsin treatment used to detach monolayer cells and the combined Accutase digestion and mechanical agitation may have led to the digestion of the fragile apoptotic and necrotic cells. The steps required to prepare the cells for analysis were likely influencing the percentage of dead and apoptotic cells and the number of living cells was emerging as a more robust analysis parameter. A complimentary interpretation of the results takes into account the relatively quick nature of apoptosis compared to the assay timing (48 with the drug and then another 48 hours in drug-free media). Apoptosis levels may remain largely unchanged for most concentrations due to the constant shedding of apoptotic cells. Moreover as the cells in the spheroid are not all in the same phase of the cell cycle they will enter and finish apoptosis at a different time thereby contributing to the small change in the percentage of apoptotic cells within the spheroids.

A few important conclusions could be made from those preliminary experiments. First, the exposure time of around 24h was not enough to

reveal the full extent of the effects of etoposide. Second, the VCR cell line showed signs of etoposide resistance which could interfere with future proof-of-concept studies and was later replaced by UW228-3. Third, the percentage of apoptotic and necrotic cells that made it to the flow cytometer may have been influenced by the dissociation procedure and therefore constituted an unreliable measurement to quantify drug effects in spheroids. Next, the number of living cells offered a more accurate representation of cytotoxic action and was prioritised. Nevertheless the elimination of excess dead and apoptotic cells from the analysis through the use of 7-AAD and Annexin-APC remained an important feature preventing noise interference in viability estimations.

To sum up, despite the fact that the experiments described above were performed in a suboptimal setting with heterogeneous spheroids produced in non-adherent flasks, the right combination of labels and viability stains was established. The pieces of the puzzle were slowly coming together and while the critical factors of dye concentration, drug exposure and time of culture remained to be optimised for UW228-3 cell as well as NSCs. The utilisation of ultra-low attachment plates greatly facilitated the process of spheroid health monitoring, culture and quantification.

Section 4.5 Marking normal brain cells and UW-228-3 with CDCFDASE and CellTrace Violet

The second phase of developing the medulloblastoma model commenced with a dye optimisation experiment. It aimed to establish the most favourable concentration to label the cells specifically without pronounced toxic effects. UW228-3 and NSC cells were marked with CDCFDASE and CellTrace Violet in concentrations ranging from 2.5 to 20 μM . Figure 4-8 shows the impact of dye concentration on the frequency distribution of cellular fluorescence in the fluorescent channels of CDCFDASE and CellTrace Violet. As seen in Figure 4-8A-B the optimal staining concentration for the tumours was 10 μM for both dyes and little was gained from increasing dye levels to 20 μM . Despite the low mean fluorescence of non-marked UW cells, dye concentrations lower than

10 μM did not shift the population's fluorescence distribution at day 7 far enough to achieve a good separation from the control. The normal brain cell population on the other hand showed a very pronounced difference in the distribution of the fluorescence signal with increasing dye concentrations. Figure 4-8C illustrates the gradual shift of the fluorescence for the whole normal cell population and clearly shows that CellTrace Violet can effectively mark the cells at levels as low as 5 μM . CDCFDASE followed a similar trend in Figure 4-8D although the shift was less pronounced when compared to CellTrace Violet. Overall, in the conditions tested, CellTrace Violet was superior in marking the cells compared to CDCFDASE because it elicited a more pronounced shift in the fluorescence of both cell types.

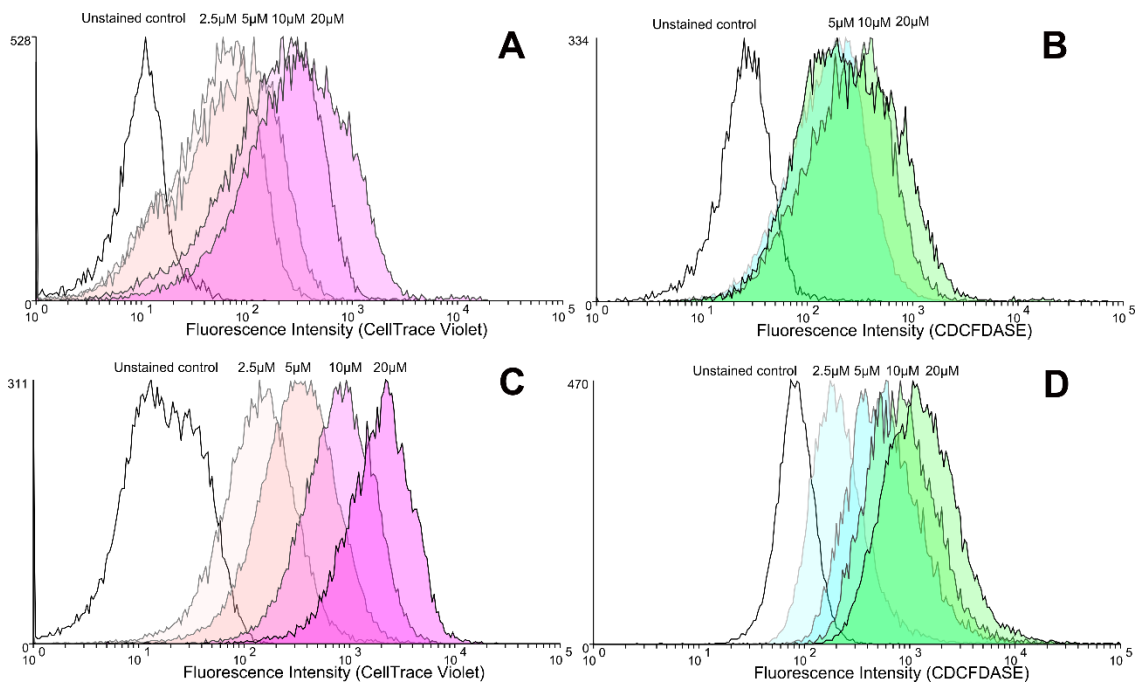


*Figure 4-8. Histograms of the frequency distributions of long-term fluorescent labelling for UW and NSC cells labelled with CellTrace Violet and CDCFDASE (Green). **A**- UW cells marked with CellTrace Violet, **B**-UW cells marked with CDCFDASE, **C**-normal cells marked with CellTrace Violet, **D**-normal cells marked with CDCFDASE*

These results were confirmed when the relative percentages of cells with fluorescence brighter than control were compared in Table 4-7. While 5 μM CellTrace Violet was enough to render over 90% of normal brain cells brighter than the unstained control, the same effect could only be achieved in tumours by using a two-times higher concentration of the

dye. Likewise, CDCFDASE levels of 5 μ M achieved effective labelling for more than 90% of normal cells but only marked 77% of the UW cell line. The data demonstrates that levels of 10 μ M were needed to stain tumour cells and 5 μ M were sufficient for normal cells for both dyes. Although these data indicated a combination of 10 μ M CellTrace Violet for the UW and 5 μ M CDCFDASE for the NSC might be advantageous, the superiority of this combination became visually apparent after comparing the dot plots in Figure 4-9.

Condition	% Positive cells	
	UW228-3	NSC
Control	2	2
CellTrace 2.5 μ M	63	74
CellTrace 5 μ M	71	94
CellTrace 10 μ M	90	99
CellTrace 20 μ M	96	100
CDCFDASE 2.5 μ M	-	50
CDCFDASE 5 μ M	77	93
CDCFDASE 10 μ M	86	98
CDCFDASE 20 μ M	85	99

Table 4-7. Marking UW-228 and NSC cells with supravital dyes CDCFDASE and CellTrace Violet. Percentage of positive cells is given compared to unstained control.

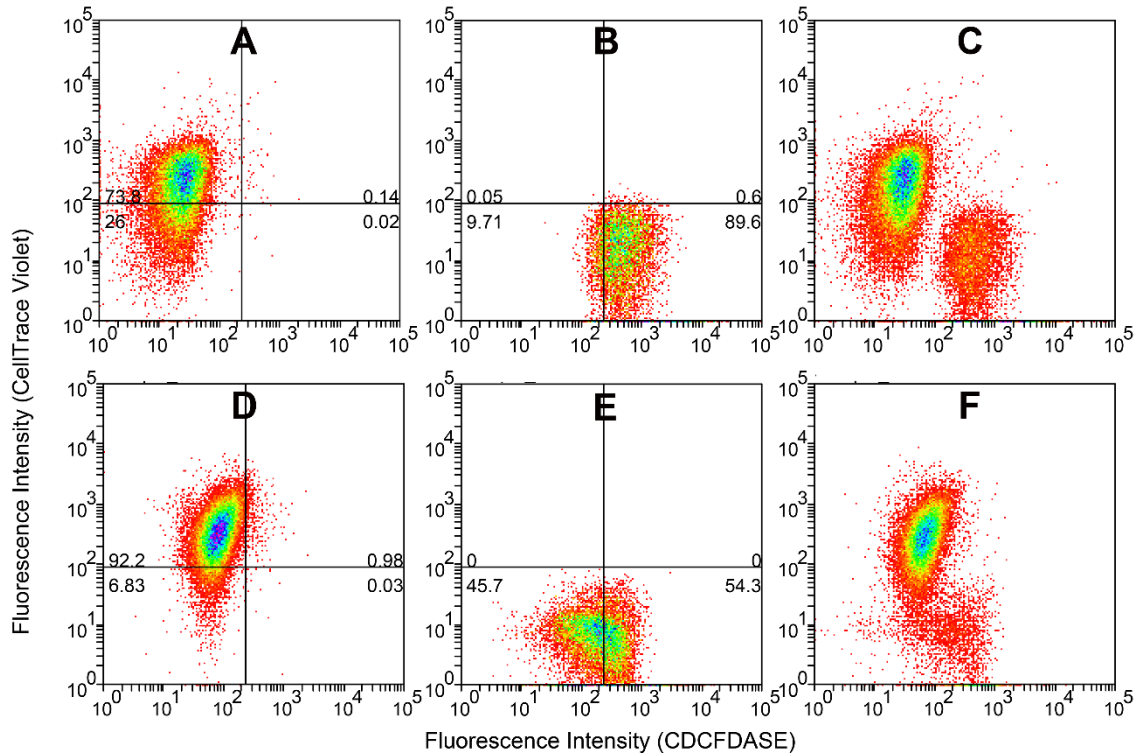


Figure 4-9. Two dimensional dot plots showing single and mixed populations of UW and NSC cells marked with both dyes. X-axis shows intensity of fluorescence in the CDCFDASE channel, Y-axis fluorescence intensity in the CellTrace Violet channel. Quadrants are defined by the autofluorescence intensity values for the unstained stem cell population which are within the lower left quadrant of the plots **A**- UW marked with 10 μ M CellTrace Violet, **B**- NSC marked with 5 μ M CDCFDASE, **C**- mix of UW-CellTrace Violet and NSC-CDCFDASE, **D**-NSC marked with 5 μ M CellTrace Violet, **E**- UW marked with 10 μ M CDCFDASE, **F**- mix of UW-CDCFDASE and NSC-CellTrace Violet

Figure 4-9 shows the results of using NSC-cells marked with Cell trace violet or CDCFDASE mixed with UW cells marked with the opposite dye. Complete and effective resolution of the two populations is only achieved by using CDCFDASE for the foetal tissue and CellTrace Violet for the tumours (Figure 4-9C). In contrast the small shift in UW cell fluorescence achieved by CDCFDASE was sufficient to distinguish them from unstained tumour cells but not enough to differentiate them from the stem cells (Figure 4-9F). This cell discrimination achieved in the former case can be explained with the higher autofluorescence of stem cells compared to tumours. CellTrace Violet achieves a more pronounced shift in fluorescence for the tumours which, combined with their intrinsically low autofluorescence in the CDCFDASE channel, leads to better separation from the stem cell population

In order to investigate the effect of marking the cells with fluorescent dyes on spheroid viability and growth, the volume and metabolic activity of stained spheroids were compared to unstained spheroids of UW and NSC cells. Figure 4-10A shows that stem cells treated with increasing concentrations of each dye yielded smaller spheroids after 7 days of culture compared to unstained controls. This effect was less pronounced for UW spheroids which were only affected at concentrations above 10 μM . Nevertheless, metabolic activity (Figure 4-10B) for all spheroids, as determined by Resazurin reduction, was above 80% when dye concentration was kept below 10 μM . Figure 4-10C shows the volume of marked spheroids made of UW or NSC cells marked with 10 μM CellTrace Violet and 5 μM CDCFDASE respectively. The results of five independent experiments showed that while stem cells produced 30% smaller spheroids than unstained controls, tumours were less affected by the marking procedure and only had 10% lower volume compared to controls.

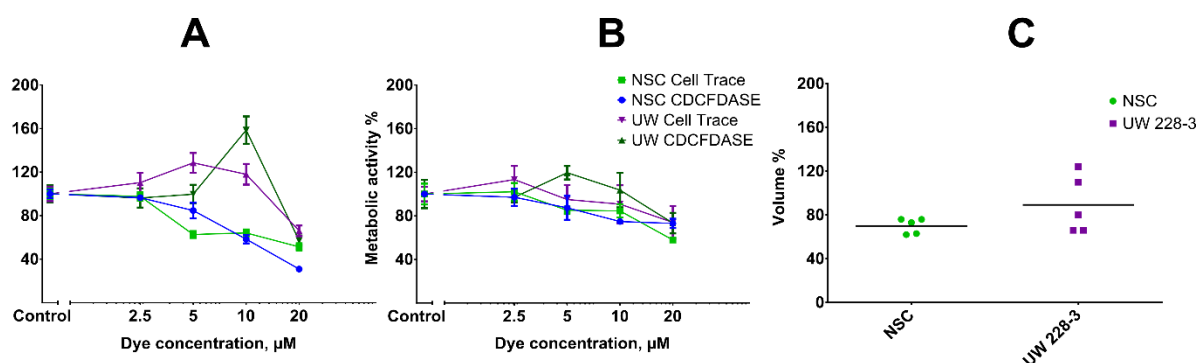


Figure 4-10. Volume and metabolic activity of spheroids marked with the supravital dyes compared to unstained controls **A**-Volume of UW and NSC spheroids marked with different levels of fluorescent dyes after 7 days of culture compared to unstained controls. **B**- Metabolic activity of the same spheroids measured as resazurin reduction compared to control. **C**- Volume of normal cell and tumour spheroids stained with 5 μM CDCFDASE and 10 μM CellTrace Violet respectively compared to unmarked controls

Section 4.6 Analysing the effects of etoposide

After the initial optimisation experiments the marked tumour and normal cells were seeded and co-cultured together mimicking the interaction between normal brain and tumour tissue (Figure 4-11). These co-cultures were allowed to grow for 3 days before they were exposed to etoposide for 48h followed by another 2 days in etoposide-free media. The right

panel in Figure 4-11 shows light microscopy images of the spheroids after 7 days of culture along with the conditions in each column.

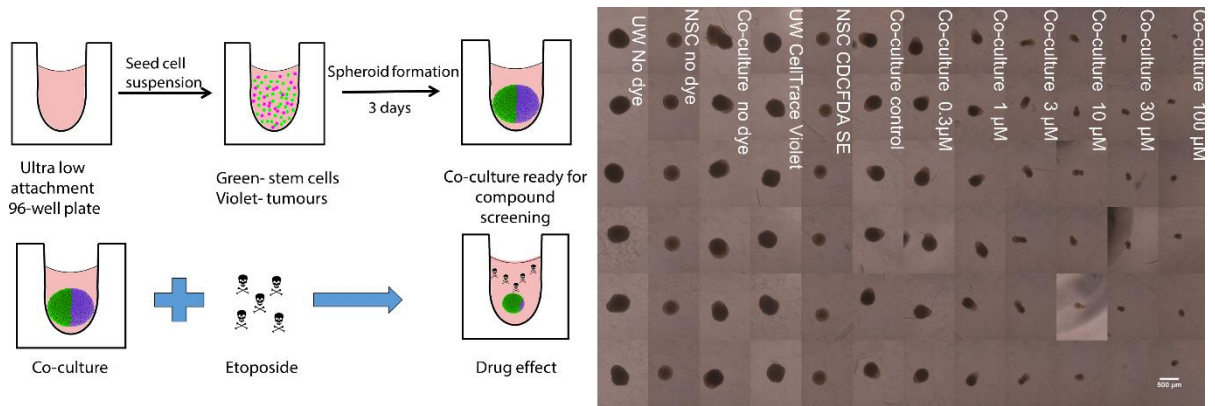


Figure 4-11. Medulloblastoma in vitro model experimental setup. Left panel- co-culture formation in overlay and etoposide exposure. Right panel- 96-well plate experiment phase contrast microscopy image after 7 days of culture along with conditions for each column.

Figure 4-12 shows the light and multiphoton microscope images of the co-cultures and the flowchart for flow cytometry gating and analysis. The multiphoton images reveal the spatial distribution of the two cell populations while flow cytometry was used to quantify the proportion of each cell type. Despite seeding the cells together in the form of a mixed single cell suspension, the cells organised themselves into polarised spheroids with discrete tumour-dominated and normal brain cell-dominated regions. As seen in the images, there were tumour cells detectable within the normal brain cell part, resembling metastases, and a fraction of double positive cells whose origin could not be identified solely on the basis of imaging. Flow cytometry after spheroid dissociation was used to quantitate the ratio of tumour and normal cells within the mixed cultures and monitor the effects of etoposide. The normal cells were well segregated from the tumours due to the bright CDCFDASE staining. The double-positive cells, which were highly fluorescent in both channels, were clearly separated from the tumour population and clustered with the normal cells. Each population was further examined for apoptosis-related phosphatidylserine externalisation using Annexin V-APC [330] and for 7-AAD uptake [328] to infer cell death.

A feasibility study similar to the one with VCR cells was undertaken in order to check the suitability of using the combination of dyes to distinguish between normal stem cells and tumours and monitor their viability at the same time. Figure 4-13 shows the viability determination for the unstained and the labelled populations of tumour and neural stem cells. The samples which did not contain AnnexinV-APC and 7-AAD (Figure 4-13A-D) did not give rise to a signal in those channels indicating the lack of interference between the cell marking and cell viability stains. Upon the addition of Annexin and 7-AAD two new populations emerged in addition to the main cell population (Figure 4-13E-H). The apoptotic cells had intermediate 7-AAD permeability and high fluorescence in the Annexin-APC channel, while the dead cells were highly fluorescent in both channels when compared to the unstained control. The percentage of apoptotic and dead cells in the untreated controls (Figure 4-13E-F) was lower than that in etoposide treated spheroids (Figure 4-13G-H). Although the percentage of apoptotic and dead cells rose with increasing concentrations of etoposide, the spike in dead and apoptotic cells could not account for the fall of healthy cell numbers. As mentioned before, dead and dying cells often detach from the spheroids and can be lost during washes or digested during the dissociation process. In this regard, it was decided that the percentage and ratios of surviving cells will be used in subsequent analyses in order to minimize the influence of the dissociation procedure on the dose-response results.

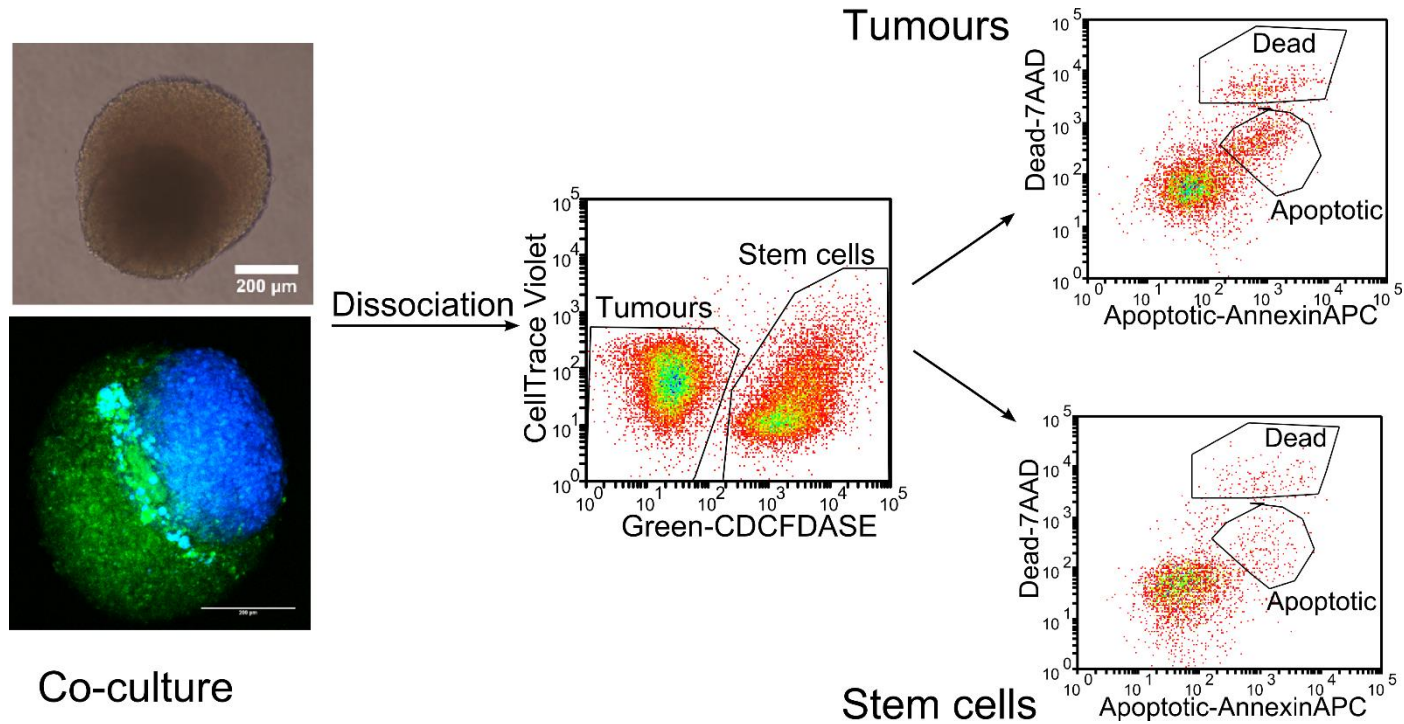


Figure 4-12. Medulloblastoma co-culture model analysis. Top left- phase contrast microscopy image of co-culture spheroid. Darker sphere is made up of UW cells while brighter cells are NSC. Bottom left multiphoton average intensity z-stack projection image of co-culture spheroids. Green cells represent NSC, blue cells -UW228-3 and Cyan-double positive cells. Scale bars 200 µm. After dissociation into single cells spheroids were analysed using flow cytometry. Middle dot plot panel shows that tumour and normal stem cell populations can be gated separately owing to their different fluorescence in both channels. Double positive cells in middle dot plot appear to cluster with stem cells. Right dot plots show tumour (top panel) and stem cells (bottom panel) assayed separately for viability using Annexin-APC for apoptotic cells and 7-AAD to mark dead cells. Note that living cells have low 7-AAD fluorescence, apoptotic medium and dead-high as described by Zemruski et al., 2012

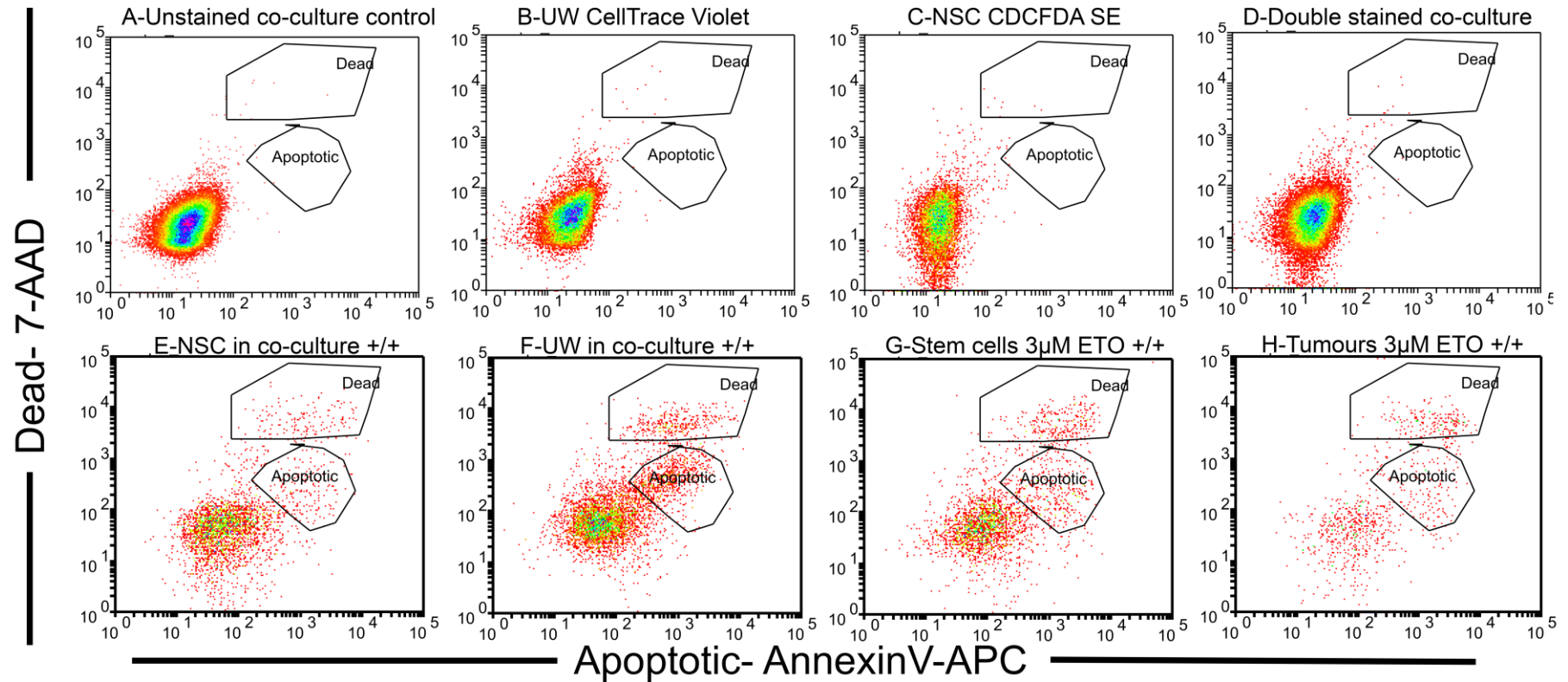


Figure 4-13 . Dot plots showing compatibility of cell labelling and determination of health status. Samples A to D did not have any added 7-AAD or Annexin-APC and were therefore negative for the stains. Samples E-F had both Annexin-APC and 7-AAD added (+/+). Note that apoptotic cells also have a slightly higher permeability for 7-AAD as well. Control and treated cultures had similar levels of apoptotic and dead cells which was attributed to the loss of fragile apoptotic and dead cells during enzymatic and mechanical dissociation of the spheroid. That is why only Annexin-APC and 7-AAD negative (healthy) cells were used in subsequent analyses.

Etoposide addition profoundly altered the ratio of tumour to normal cells in the spheroids. Although both populations started at similar numbers, increasing concentrations of etoposide primarily targeted the tumours and at 10 μM the spheroids were composed predominantly of normal cells. As seen in Figure 4-14, with increasing etoposide levels the tumour cell proportion dropped significantly and reached its lowest point at 10 μM etoposide. This is in agreement with the results from the two photon confocal microscopy shown in the bottom panel. The average intensity z-stacks show a progressive elimination of the tumour cells with only traces of these cells left at the 10 μM concentration. Nevertheless, the decrease in tumour burden was not wholly advantageous and higher etoposide concentrations elicited a shrinkage of the spheroid as a whole, indicating toxicity to the normal cells as well.

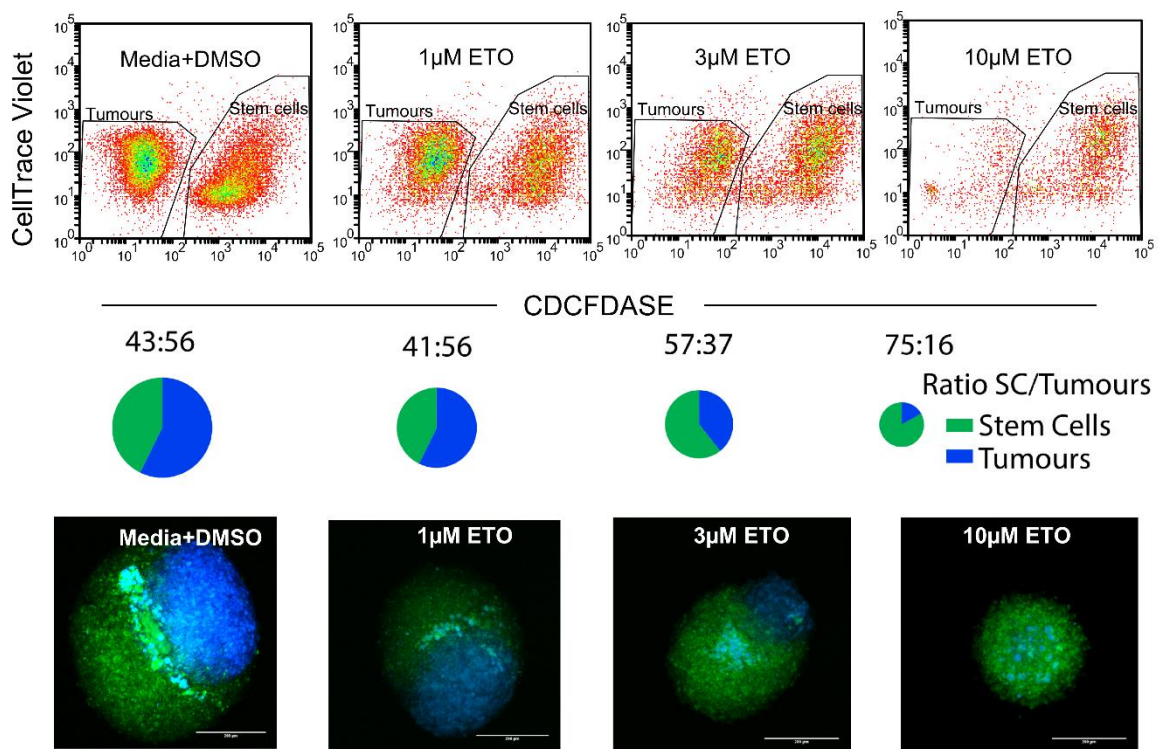


Figure 4-14 Co-cultures exposed to different levels of etoposide. Dot plots and multiphoton images. The top panel shows dot plots for the live cells in the spheroid. Top left plot represents the living cells in the controls, cultured in media and DMSO. The dot plots are marked with the relevant etoposide concentration in μM . The proportional increase of normal stem cell to tumours shown in the dot plots is represented by the pie charts of the middle row. The decrease in spheroid size is also represented by a decrease in the pie chart diameter. Increasing concentrations of etoposide gradually eliminated the tumour cells. Bottom row shows multiphoton microscope average intensity z-stacks of spheroids cultured at the above conditions. Blue cells are UW tumours, green cells are normal stem cells and scale bars are 200 μm .

A similar trend was also seen in a different experiment where the starting ratio of tumours to normal stem cells was 4:1 (Figure 4-15). The use of fluorescent beads to determine absolute cell numbers was pioneered in this experiment. The beads had distinct size and scattering characteristics and were fluorescent in all channels making them easy to distinguish from the cells. The same concentration of fluorescent beads was added to each sample and the absolute cell concentration calculated and compared to the control to express viability. Despite the starting advantage in numbers for the tumours, increasing etoposide levels affected them in a dose-dependent manner and at levels of 10 μM etoposide the tumour to normal cells ratio was reversed in favour of the normal cells. The decline in tumour viability was similarly followed by a decrease in the volume and number of cells in the spheroid as a whole. Although the normal cells were the dominating cell type in the spheroids exposed to 10 and 30 μM etoposide, the spheroid viability expressed as cell numbers compared to control was below 10%.

When the percentage of apoptotic and dead cells from Figure 4-15 was plotted against etoposide concentration the points of departure for both death and apoptosis were visualised (Figure 4-16). Significant increases in the percentage of apoptotic cells for both tumours and normal cells was seen at etoposide concentrations above 3 μM and dead cells increased at levels exceeding 30 μM . This was in stark contrast with the substantial drop in viability at etoposide concentrations below 3 μM detectable by both spheroid volume decrease and absolute cell counts and serves to further emphasize the possible underestimation of etoposide's effects by relying solely on apoptosis and cell death. This effect was most probably linked to the extensive sample preparation procedure involving multiple washing steps, mechanical and enzymatic dissociation rather than a specific biological phenomenon.

Despite the successful first experience with absolute cell counts determined with the help of fluorescent beads, later experiments highlighted the high variability in the bead addition procedure and spheroid volume was used instead of cell counts in the final analysis of the data combining all experiments to plot the dose-response curves for etoposide.

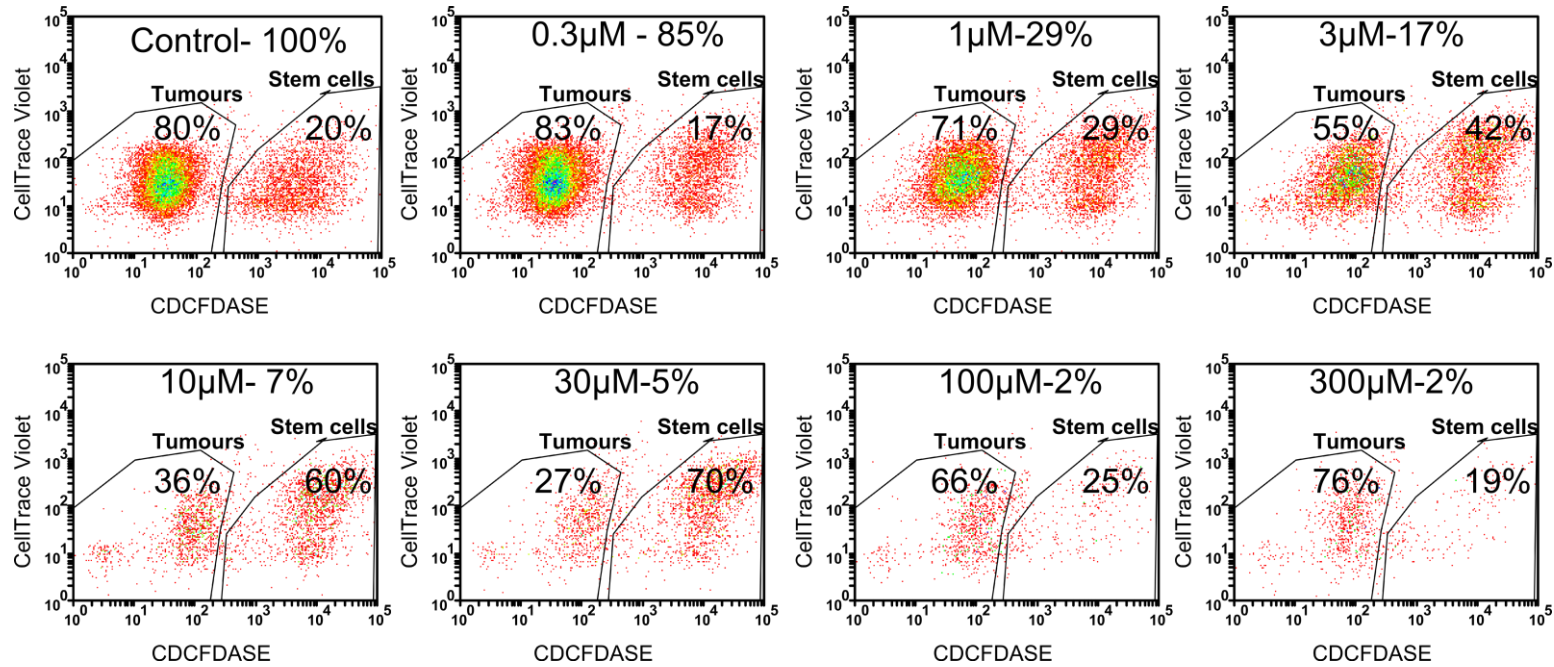


Figure 4-15. Dot plots showing the change of viability after etoposide treatment of the spheroid as a whole (top percentage next to title) and the percentages of healthy neural progenitors and UW228-3 tumour when the starting ratio is 80% tumours to 20% normal stem cells. Concentrations 3 to 30 µM were the most favourable for the neural progenitors. Even though the spheroids were composed mainly of tumour tissue at the start, at 10 µM the neural progenitor cells were almost twice as numerous as the tumours. Absolute cell numbers in this experiment were determined using BD Fluorescent microbeads which were added to each sample and the counts for the beads compared to cell counts. This procedure was highly dependent on the control samples and could not be applied to all experiments due to variation in bead counts in non-treated controls in some setups.

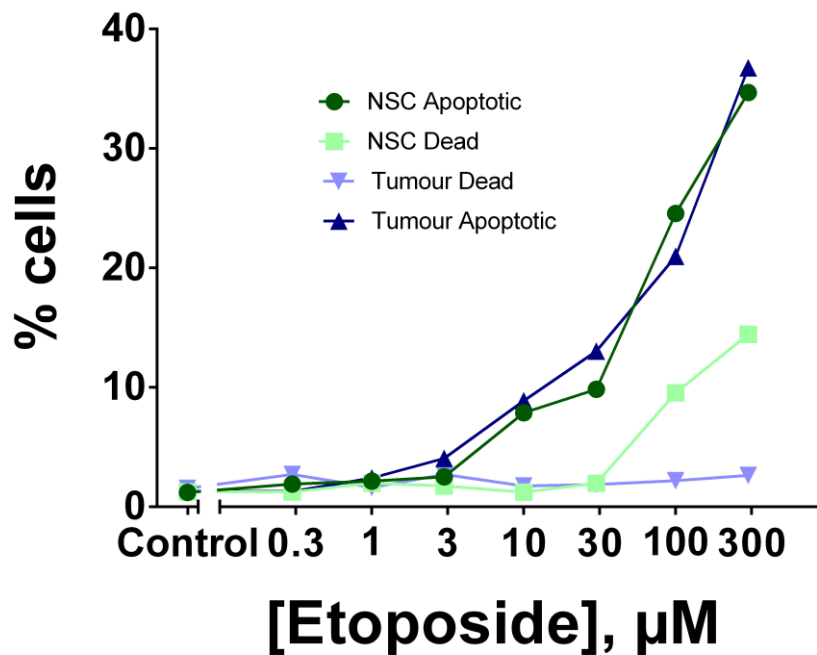


Figure 4-16 Percentage of apoptotic and dead cells in the UW228-3 tumour and neural progenitor populations after treatment with etoposide. Percentage is calculated as a fraction of the number dead or apoptotic cells from all cells of the same type.

Dose-response curves were extrapolated by using the volume of the co-culture spheroids and the proportion of progenitor cells to tumour cells determined by flow cytometry in order to fully describe the effects of etoposide on both populations. The resultant values were normalised to the initial values for progenitor cells and tumours respectively and the results plotted in Figure 4-17A. Despite the variability between the different experiments there was a clear dose-response trend in which normal cell viability was lower or equal to that of tumours below 3 μM and higher at etoposide levels between 3 and 10 μM . The most favourable etoposide concentration 10 μM when the viability of NSC (41%) was 6 times higher than tumour viability (6.5%) as shown in Figure 4-17B. This was a statistically significant difference as determined by a two-tailed t-test with Welch's correction for unequal variance ($p=0.0257$). The observed higher viability of progenitor cells at 10 μM etoposide is in agreement with the results from our previous study in separate cultures of unlabelled normal cell and tumour spheroids [331].

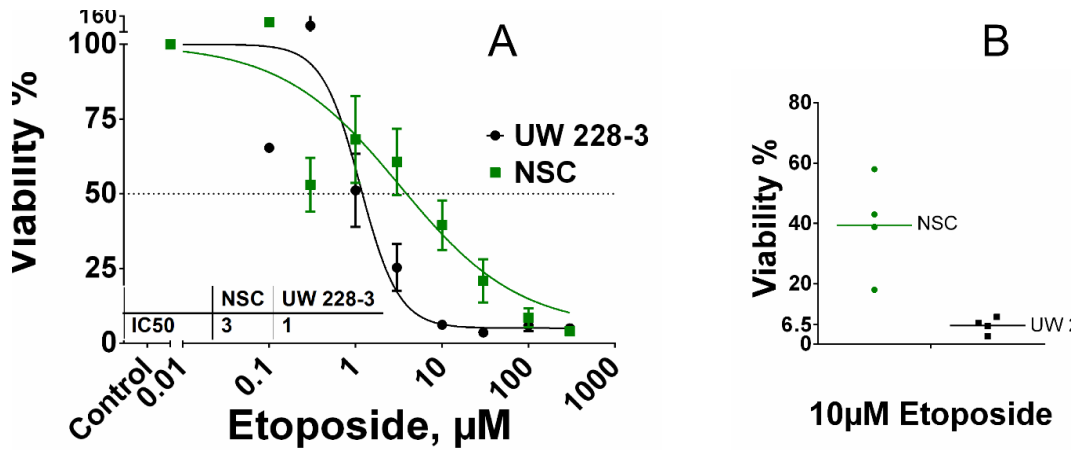


Figure 4-17 Dose-response data for co-cultures of neural stem cells and UW medulloblastoma cells exposed to etoposide. **A**-Comparison of viability for each population calculated from the total volume of the co-culture spheroid (image analysis) and the ratio between normal cells and tumours (flow cytometry). Error bars represent SEM for $n=4$ independent experiments **B**- comparison of the viability of normal cells and tumours at 10 μM etoposide, dots represent separate experiments. Note the high inter-experimental variability of the data for the normal cells and the narrow distribution for tumours. IC50 for stem cells was calculated to be 3 μM (95%CI=2-7 μM) and 1 μM (95% CI=0.8-2 μM) for UW228-3 cells.

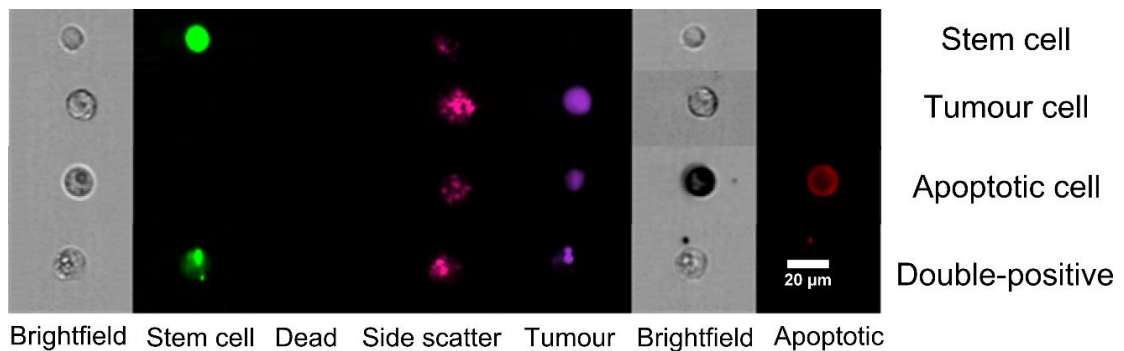


Figure 4-18 Imaging flow cytometry- representative examples of the different cell populations

In addition to the conventional flow cytometry experiments, imaging flow cytometry was employed in order to visualise and better characterise the separate populations (Figure 4-18). The normal stem cells gave a bright signal in the green channel whereas the tumours were positive for CellTrace Violet fluorescence. The membrane distribution of phosphatidylserine in apoptotic cells was also visualised. In addition the double positive cells were confirmed to be normal cells that had small particles attached to them responsible for the high-fluorescence in the violet channel.

Section 4.7 Discussion and conclusions

Through the use of CDCFDASE and CellTrace Violet in this co-culture model cellular fluorescence was maintained for 7 days. CellTrace Violet yielded a bigger shift in fluorescence compared to CDCFDASE and did not affect the medulloblastoma spheroid volume or metabolic activity. Although the final stem cell neurosphere volume was 30% lower than the unstained controls, the decreased sphere volume did not translate to reduced metabolic activity up to levels of 10 μ M of CDCFDASE and CellTrace Violet.

Remarkably, both successful dyes emerging after the labelling optimisation series rely on the same mechanism to stain the cells. Namely, they enter as acetate esters, which are then hydrolysed in the cytosol and subsequently react with cellular amines with their succinimidyl groups. This staining strategy can be used on any cell type and is substantially less toxic compared to chloro- and bromo-methyl reactive dyes that bind to cellular glutathione. Marking proteins in the cytosol would also potentially result in diminished dye exchange between adjacent cells compared to labels that bind to cellular membranes.

Spheroid co-cultures have been extensively used for invasion experiments in glioblastoma [311], [319], [332]–[334]. These studies have highlighted the importance of having a normal tissue component as well as the tumour cells. However, these experiments relied on techniques like agar overlay which produced spheroids of varying, poorly reproducible sizes. These limitations necessitated manual sorting and resulted in decrease in throughput. In most of these studies the tumour spheroids were exposed to the drug alone and only afterwards co-cultured with the normal tissue.

The tumour cells within the co-culture were organised in a main tumour mass and multiple smaller foci, thus mimicking the *in vivo* situation. Strikingly, although the tumours and progenitor cells were seeded as a mix, they organised themselves in two poles- one enriched for tumour

and one for normal tissue. Spontaneous organisation of spheroids has been reported before[335] as is probably driven by oxygen and nutrient gradients as well as cell-cell recognition mechanisms. These interactions can be linked to the 'seeds and soils' hypothesis regarding the recognition between cancer and normal cells and the spread of metastasis to specific parts of the body[336].

The combination of two dyes made it possible to assess the proportion of each cell population within the spheroid using flow cytometry after spheroid dissociation into single cells. The quantitative analysis of multiphoton images revealed the presence of double positive cells whose identity was investigated by conventional and imaging flow cytometry. The double positive cells visible in Figure 4-12 and Figure 4-14 clustered with the normal cell population in conventional flow cytometry dot plots. Moreover, the image-based flow cytometer visualised those cells as normal cells with uniform green fluorescence and small particles with bright violet/blue fluorescence attached to the outside of the cells (Figure 4-18). These flow cytometry results were confirmed in the images of intact spheroids from the multiphoton microscope. With increasing etoposide concentration the main tumour mass was almost completely eliminated but some small groups of tumour cells remained within the core of the spheroid.

The 3D co-culture model described here is made by simply mixing the NSC and UW cells in a high-throughput compatible 96-well format. No manual sorting, spheroid transfers or mixing are required and all steps could potentially be automated to increase productivity. The 96-well format allows the screening of a large number of formulations and the elucidation of dose-response relationships. Furthermore, the model includes human foetal brain tissue that shows the off-target effects of local chemotherapy on the developing brain and puts the inhibitory drug concentrations into clinical perspective. By harnessing these advantages a therapeutic range was identified for etoposide. Levels between 3 and 10 μM maximised toxicity to tumours while normal cell viability remained 6 times higher. This concentration of etoposide can be achieved in

patients by employing local intrathecal therapy [120], [121], for example.

The results from this study are supported by the work reported in Chapter 3 where both cell types were cultured separately without previous labelling [331]. Despite the slight differences in the calculated IC50s and the loss of resolution to detect the biphasic NSC response, the general viability differences remained unchanged. In agreement with the single culture studies, normal cell viability was higher compared to tumours only at levels around 10 μ M. Although the normal cell population was slightly less affected by etoposide when co-cultured with tumour cells, the interaction between normal and tumour tissue did not appear to cause enormous shifts in drug sensitivity.

The toxicity to neural progenitors shown by the model has also been reported in mice [337]. These findings are in agreement with studies that have demonstrated the damaging potential of cytotoxic drugs to progenitor cells in the subventricular zone (SVZ), dentate gyrus and the corpus callosum [338]. It should be noted, however, that the neurodevelopmental toxicity effects demonstrated by this *in vitro* model would only be replicated in patients if etoposide were to diffuse into the SVZ and dentate gyrus at high enough levels. In the context of local delivery of nanoparticles this would seem unlikely unless the nanoparticles are picked up by the CSF and etoposide is released prematurely.

As far as intrathecal administration of etoposide is concerned, leptomeningeal tumour metastases would be in direct contact with the CSF and would potentially receive the highest exposure to etoposide. In contrast progenitor cells in the SVZ are located tens of micrometres away from the wall of the lateral ventricle behind a layer of ependymal cells and a hypocellular layer [339], [340]. Neurotoxic side effects in patients have been reported for other cytotoxics like cisplatin [341], methotrexate [135], [136] and cytarabine [342] but not for intrathecal etoposide yet [119]–[121].

Nevertheless, the findings in this chapter confirm that etoposide can damage proliferating cells regardless of their origin and illustrate the failure of conventional chemotherapy to distinguish between normal and tumour cells. To this end, the next chapter describes the efforts to load biodegradable nanoparticles with etoposide in order to improve selectivity and limit off-target toxicity.

Chapter 5. Etoposide loaded Poly (glycerol adipate) nanoparticles

Section 5.1 Introduction

As seen in Chapters 3 and 4 etoposide is not very selective in its cytotoxic effects on tumour cells and adversely affects the health of normal proliferating neural progenitors. As a low Mw drug, etoposide is distributed in most cells throughout the body by diffusion. Physically entrapping the drug in a macromolecular carrier would change its distribution pattern and etoposide would reach its intracellular target (topoisomerase II) only after endocytosis and subsequent dissociation from the carrier. If tumour cells with their altered endocytosis state[192] were to take up more nanoparticles than normal brain tissue, that could be exploited to increase the selectivity of etoposide. In this regard, the ideal carrier would resemble conventional biomacromolecules in order to enhance endocytosis and exhibit rapid degradation to non-toxic products in the endosomal compartment to release the entrapped drug. It would demonstrate good loading capacity as well as sustained release of the drug to prevent premature leakage.

As was mentioned before, poly(glycerol adipate) (PGA) was selected as a promising polymer with reported biodegradability and biocompatibility as well as favourable results for the incorporation of certain drugs[179]. Meng et al demonstrated that 40% stearyl-substituted C18-PGA nanoparticles are taken up 6 times more in tumour spheroids compared to normal rat brain tissue[177]. In a parallel study Sanyogita Puri found that etoposide can be encapsulated in octanoyl-substituted C8-PGA nanoparticles in levels up to 3%[180].

This combination of selective uptake, reasonable loading capacity, biocompatibility and rapid lysosomal degradation encouraged the development of etoposide loaded PGA-based nanoparticles. This chapter aimed to reproduce and improve the previously reported etoposide

loading results for nanoparticles in order to test the delivery systems in the *in vitro* models described in Chapters 3 and 4.

Section 5.2 Chapter methods

5.2.1 Synthesis of poly(glycerol adipate) PGA:

The polymer was synthesized according to the method reported in Section 2.8.1

5.2.2 Analysis of polymer

Backbone polymers were characterised using NMR and GPC as described in Section 2.8.2.

5.2.3 Acylation of poly(glycerol adipate):

The polymers were substituted with 40% stearoyl chloride or 100% octanoyl chloride as shown in Section 2.8.3

The C18 and C8-substituted polymers were used without purification in most experiments as carried out in the historically accepted standard protocol[176]. A precipitation procedure was later tried in order to see if the removal of unconjugated acyl chloride and the respective acid would make a difference in etoposide loading. For the C18 substituted polymer this involved dissolving the polymer in acetone and precipitating with petroleum ether. The precipitation procedure for the C8-substituted polymer was done with acetone as the solvent and cold methanol as the non-solvent for the polymer. The NMR spectra given are for the purified polymers.

5.2.4 Production of nanoparticles via nanoprecipitation

Nanoparticles were produced via the nanoprecipitation method[176], [180], [343] (Section 2.9.1). A solution of PGA (2 mL, 10mg/mL) was slowly added dropwise to a buffered aqueous phase (7 mL, 10 mM HEPES) under magnetic stirring. The solution was stirred overnight and acetone was allowed to evaporate, and was then filtered through a 1 μ m sized filter. For RBITC nanoparticles the procedure described by

Meng[179] was followed where the ratio between the organic and aqueous phase was 2:7 and Tween 80 (0.1%) in HEPES(10mM, pH=7.4) was used in the aqueous phase to stabilise the nanoparticles and prevent aggregation.

Etoposide loaded nanoparticles were prepared as described by Puri [180] using the nanoprecipitation with a reconstituted matrix method. Etoposide (2 mg) and polymer (10 mg) were dissolved in acetone (1 mL). The acetone was left to evaporate by blowing a stream of dry nitrogen and left for at least 2h in the dark afterwards. The matrix was reconstituted in acetone (1 mL) and was added to distilled water (5 mL) under magnetic stirring and left overnight for the acetone to evaporate.

The loaded nanoparticles were separated from the free dye or drug via low pressure gel permeation chromatography using a SepharoseCL-4B column (2.5x25 cm, General Electric) as outlined in Section 2.9.3.

Nanoparticle radius was determined using dynamic light scattering (Section 2.9.4.) using the Viscotek 802 instrument (830 nm laser, 60 mW, 10% power). At least 10 measurements were performed on each sample with a duration of 4s per measurement.

The zeta potentials and the diameter of the nanoparticles were determined in HEPES Buffer (10mM, pH=7.4) using Laser Doppler Electrophoresis (Zetasizer NanoZS, Malvern). At least three measurements were performed on each sample.

5.2.5 Imaging the interaction of fluorescent nanoparticles and medulloblastoma cells

Confocal laser scanning microscopy (CLSM) was used to image tumour and NSC spheroids and determine nanoparticle uptake in cells in the periphery and the core of the spheroids. CLSM was performed using a Leica SP2 microscope equipped with a 405 nm (diode), 488 nm (Ar) and 543 nm (He/Ne) lasers. Images were analysed with Volocity and Leica LAS AF Light software. Background reduction in the red channel was performed on all confocal images by applying a lower threshold value of

70 units of fluorescence pixel intensity and alpha correction ($\alpha=1.1$) in Adobe Photoshop (v14).

The spheroids were grown in hanging drop culture, harvested from the bottom of the plates and pipetted onto poly-D-lysine/albumin cover slips. They were incubated on the cover slips in full culture media with or without 25% nanoparticle suspension in 10 mM HEPES for 24h in order to attach. Afterwards the attached spheroids were washed with PBS, fixed with 4% PFA for 15 minutes, dyed with 4',6-diamidino-2-phenylindole (DAPI, 1 $\mu\text{g}/\text{mL}$) for 5 minutes and washed twice with PBS. The cover slips were mounted on cavity slides with fluorescence mounting medium and sealed with clear nail polish. They were kept protected from light at 2-8 °C.

5.2.6 Etoposide-loaded nanoparticles: drug loading determination

Drug loading was determined by freeze-drying a set volume of nanoparticle suspension (1 mL) in a preweighed amber HPLC vial. The weight difference was recorded and the nanoparticles were dissolved in DCM (1 mL). Fluorescence spectrophotometry (Varian Cary Eclipse, Agilent) with excitation ($\lambda=284$ nm), emission ($\lambda=325$ nm) and slit (5 nm) was measured against freshly made standards. The standard curve for etoposide fluorescence had a hyperbolic shape due to fluorescence quenching at etoposide levels above 30 $\mu\text{g}/\text{mL}$ and a linear standard curve was fitted up to that level. For concentrations higher than 30 $\mu\text{g}/\text{mL}$ the hyperbolic equation fit from GraphPad prism was used. Quality control samples of nanoparticles spiked with known amounts of etoposide were subjected to the same treatment and used to assess the suitability of the method.

Section 5.3 Polymer synthesis and characterisation

5.3.1 Synthesis of polymer backbone

The synthesis of poly (glycerol adipate) is a polycondensation reaction that results in polymers with a broad distribution of molecular weights as seen in the GPC (Figure 5-1):

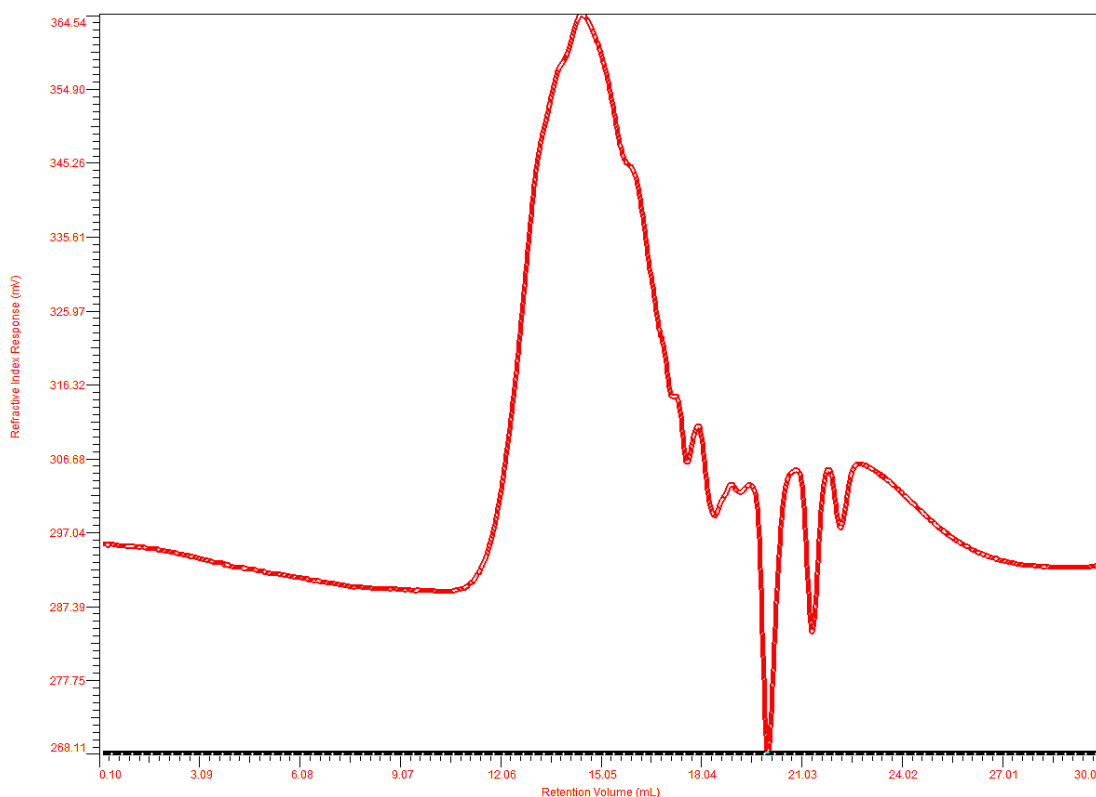


Figure 5-1. GPC chromatogram of PGA polymer synthesized in house. The average molecular weight was 12kDa and the distribution was broad as expected in polycondensation reactions GPC trace obtained from Liverpool setup

The target for the mean molecular weight of the peak was 8-12 kDa because that had been previously reported to maximise drug loading[176]. Molecular weight determinations were initially carried out at Nottingham using a Polar-Gel M column. However, these determinations seemed to give quite random molecular weights and a possible interaction between the packing material and the polymers was suspected. When the same polymer samples were analysed using the original polystyrene/divinylbenzene columns in Liverpool, employed in the inceptive work on the polymer, the molecular weight determinations were consistent with the previously reported results (Table 5-1).

Sample (name)	GMHHR-N column Polystyrene/divinylbenzene Mw(kDa)	PolarGel- M column Mw(kDa)
PGA 130106	13.6	1.4
PGA 130205	13.8	0.73
PGA 130708	22.7	11.5
PGA 130710	12	4.3
PGA 130716	18.4	12

Table 5-1. Mean molecular weight determinations for five different batches of poly (glycerol adipate) determined by GPC with two types of columns- GMHHR-N PS/DVB and PolarGel-M.

5.3.2 Substitution

Substitution reactions were performed with stearoyl (C18) and n-octanoyl (C8) chloride in order to synthesize 40%-C18 and 100%-C8 substituted polymers. The C18-derivative had previously shown promise in dexamethasone formulations[176], while the 100%C8 was the polymer that performed the best out of a selection of substituted PGA polymers in a screening study with etoposide performed by Puri[180]. The representative NMR spectra for the unsubstituted PGA, 40%-C18PGA and 100%C8-PGA are given in Figure 5-2, Figure 5-3 and Figure 5-4 respectively.

Figure 5-2 shows that despite the extensive drying procedure there was still some residual THF trapped in the polymer. The peaks at 5.1 and 5.3ppm are indicative of substitution of the secondary hydroxyl group of glycerol showing that although the enzymatic reaction is regioselective it is not completely specific.

Figure 5-3 and Figure 5-4 show the NMR spectra of the substituted polymers. The NMR spectra were used to determine the degree of substitution by exploiting the fact that the substituted part(x) of the polymer has 6 protons attached to carbons vicinal to carbonyl groups, while the non-substituted part(y) has only four.

$6x+4y=d+d'$ protons, and if $x=1$ Equation 5-1

$$y = \frac{\text{protons}_{(d+d')} - 6}{4} \quad \text{Equation 5-2}$$

$$x \% = \frac{1}{1+y} \times 100 \quad \text{Equation 5-3}$$

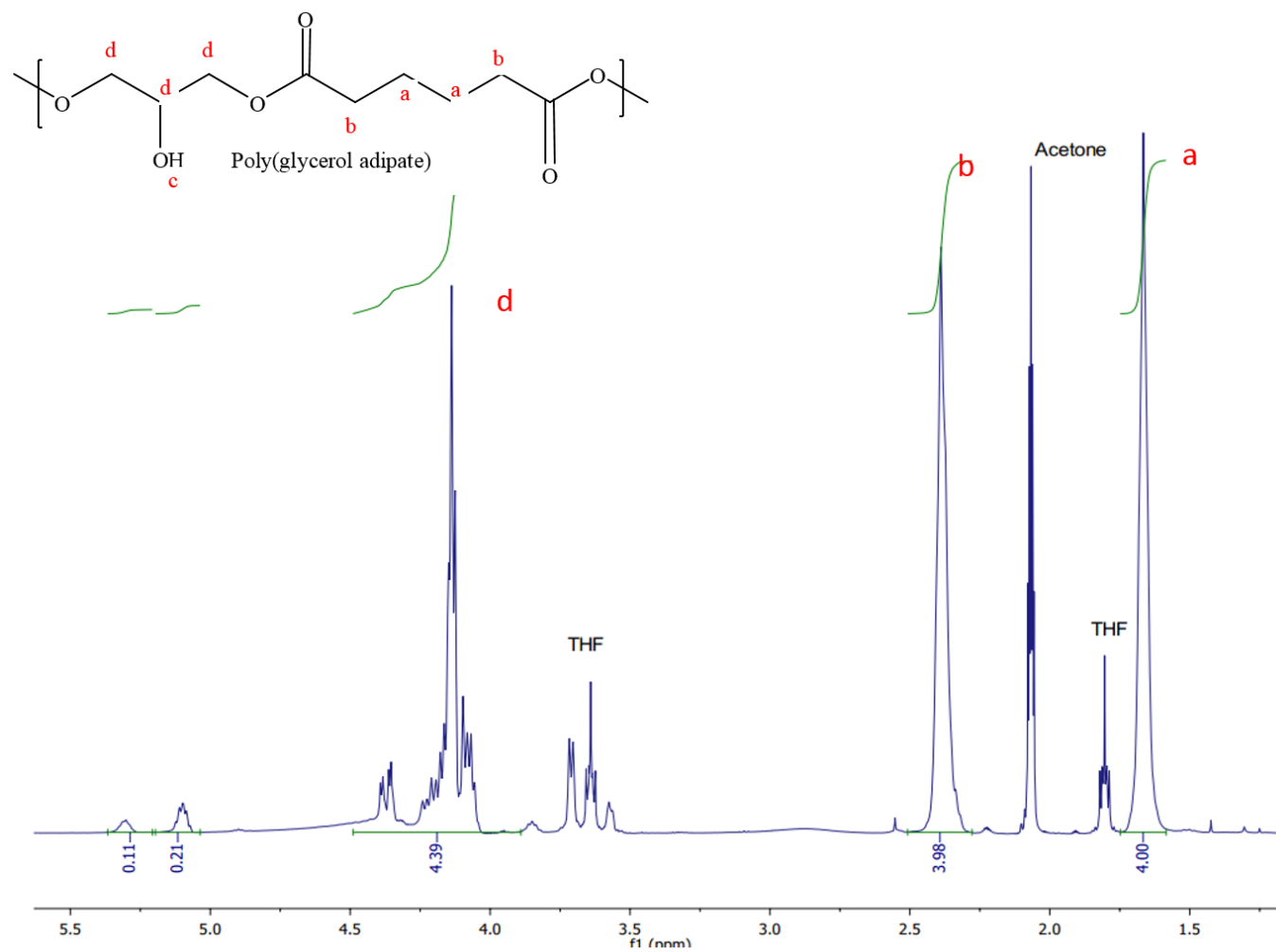


Figure 5-2. NMR spectrum for non-functionalised poly (glycerol) adipate.

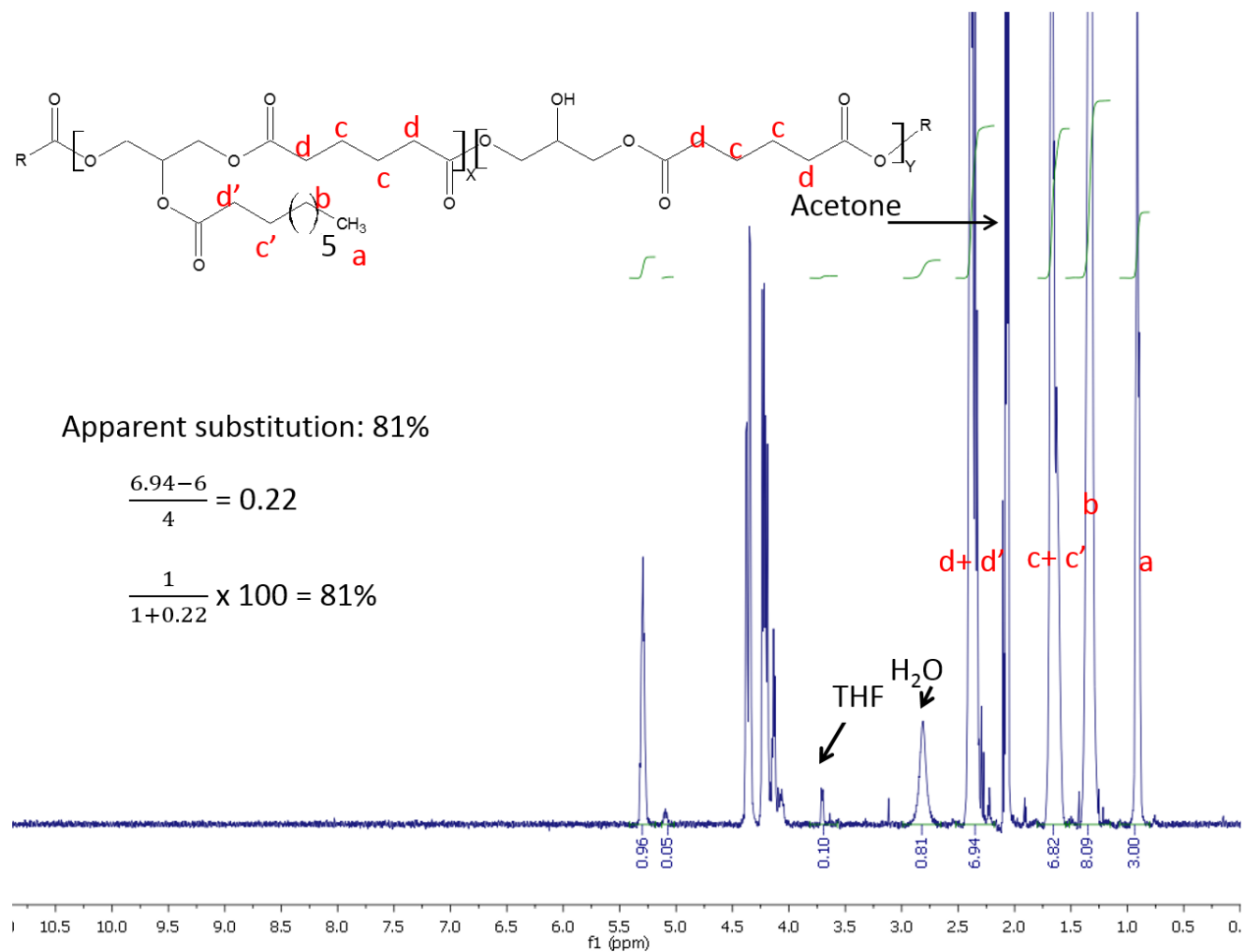


Figure 5-3 NMR spectrum for the C8 substituted PGA. Although the theoretical substitution percentage was 100% the actual substitution achieved was 81%

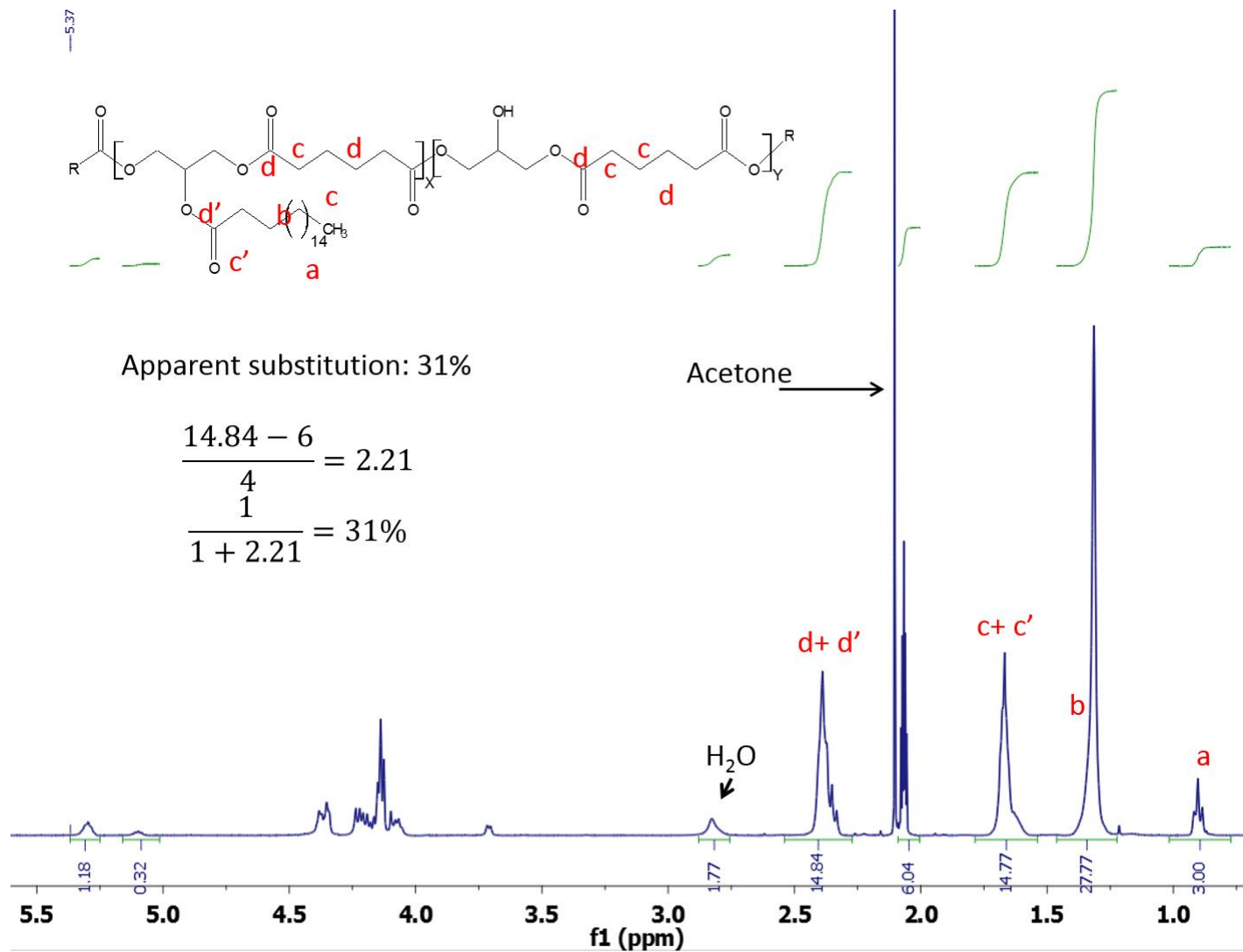


Figure 5-4. NMR spectrum for C18-substituted polymer. 31% substitution was achieved.

Section 5.4 Nanoparticle preparation and optimisation

5.4.1 RBITC loaded nanoparticles- size, zeta potential, confocal with spheroids

Upon the substitution of the pendant hydroxyl groups of the polymer backbone with stearoyl chloride the resultant new polymer was used to make Rhodamine B isothiocyanate (RBITC) loaded nanoparticles as described by Meng[179]. After separation of the free dye via low pressure gel-permeation chromatography the size and zeta potential of the nanoparticles were determined in 10 mM HEPES buffer:

Sample name	Diameter, Viscotek	Diameter, Malvern ZS	Zeta potential
RBITC NPs	250±40nm	230±50nm	-36±10mV

Table 5-2. Characterisation of RBITC-loaded fluorescent nanoparticles. Values for size and zeta potential are given with the population range

Both the Malvern ZS and the Viscotek DLS placed the size of the nanoparticles in the 230-250 nm range. The size and zeta potential of the nanoparticles were consistent with the previously reported values by Meng and Puri[179], [180]. Despite their negative charge the particles had a tendency to aggregate when freeze-dried and that is why they were stored as a colloidal suspension in 10 mM HEPES in the fridge protected from light. The nanoparticles used for uptake experiments were stored for less than 48h.

The fluorescent label RBITC was used in order to image the depth and extent of nanoparticle uptake in tumour spheroids. Imaging the distribution of nanoparticles within the intact tumour spheroids was performed using confocal laser scanning microscopy (CSLM). Even though CSLM can successfully be used to quantify the distribution of the nanoparticles the tissue was not optically transparent and both the excitation and the emission signal were scattered and dampened further into the spheroid. The physical depth limit of CSLM is around 150 µm, however there are studies which suggest that this value can be significantly improved with tissue clearing procedures[344]. The nuclear stain DAPI proved useful for locating the spheroids and focusing.

Furthermore, the cytoplasmic dye- Carboxyfluorescein diacetate succinimidyl ester (CFDA SE) was used to stain the cytoplasm of the tumour cells (Table 5-3).

Stain	Excitation	Emission	Colour
DAPI- nuclei	360	460	Blue
CFSE DA- cytoplasm	492	517	Green
RBITC- nanoparticles	554	575	Red

Table 5-3 Fluorescent dyes used in confocal imaging experiments. The tumour cells were marked with CFDA SE in monolayer, trypsinized and allowed to form spheroids in the Perfecta 3D hanging drop plates. The spheroids were harvested, allowed to attach to PDL/albumin coated cover slips and exposed to RBITC loaded nanoparticles for 24h. They were then fixed, stained with DAPI and imaged on the confocal microscope.

VCR spheroids were cultured on poly-D-lysine/albumin coated cover slips in full culture media either in the absence or presence of nanoparticles as described in the methods section. This was done to ensure the attachment of the spheroids to the cover slips in order to enhance imaging. Both the spheroids (Figure 5-5, Figure 5-7) and the monolayer of cells spreading from the spheroids on the cover slips were imaged (Figure 5-6, Figure 5-8). In the control group which was not exposed to nanoparticles no fluorescence was expected in the red channel apart from the normal levels of autofluorescence. Although red fluorescent spots could be seen in some of the control images (Figure 5-5 and Figure 5-6) these artefacts were always fluorescing in the green channel as well which indicated autofluorescence rather than nanoparticles (highlighted in Figure 5-9C and D). The diminishing fluorescence in deeper sections (Figure 5-5D) indicates the need for sectioning or tissue clarification in order to image the spheroid core. In contrast, images of spheroids exposed to RBITC (Figure 5-7 and Figure 5-8) loaded nanoparticles exhibited more intensive diffuse red fluorescence and the spots identified as nanoparticles did not fluoresce in any other channel apart from the red. The RBITC loaded nanoparticles are seen either as red fluorescent aggregates or diffuse higher levels of red fluorescence in the spheroids. The relative fluorescence intensity in the red channel was over around 2 times higher in treated spheroids (Figure 5-7) compared to the control images (Figure 5-5). This suggests that there may be free nanoparticles within the cells imaged as diffuse red fluorescence (Figure 5-9A and B).

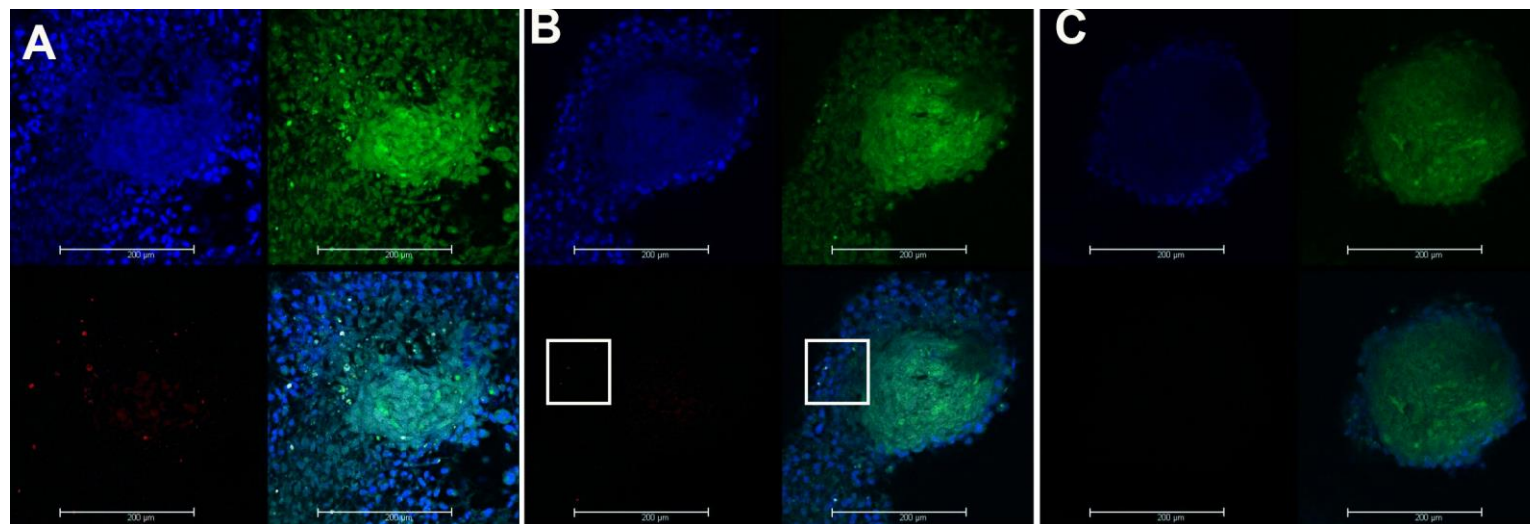


Figure 5-5 Control images(x40) of a tumour VCR spheroid attached to a coated cover slip. The blue, green and red fluorescent channels are first shown separately and then overlaid. A-Section 6 µm deep into the spheroid showing autofluorescent artefacts in both the red and the green channel. B-Section 30 µm into the spheroid displaying diminishing brightness and contrast in the blue channel. White rectangles are shown expanded in Figure 5-9D; C-Section 80 µm into the spheroid, both contrast and brightness are greatly diminished. Scale bar 200µm

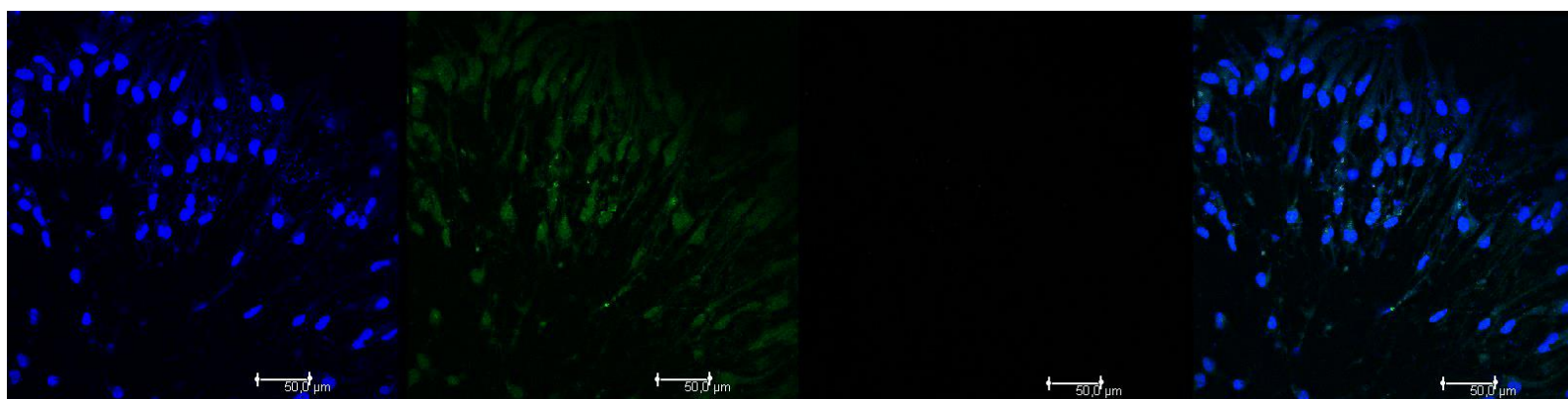


Figure 5-6 Control image(x40) of a VCR monolayer without nanoparticles showing the cells which support the spheroids' attachment to the cover slip. Scale bar 50µm.

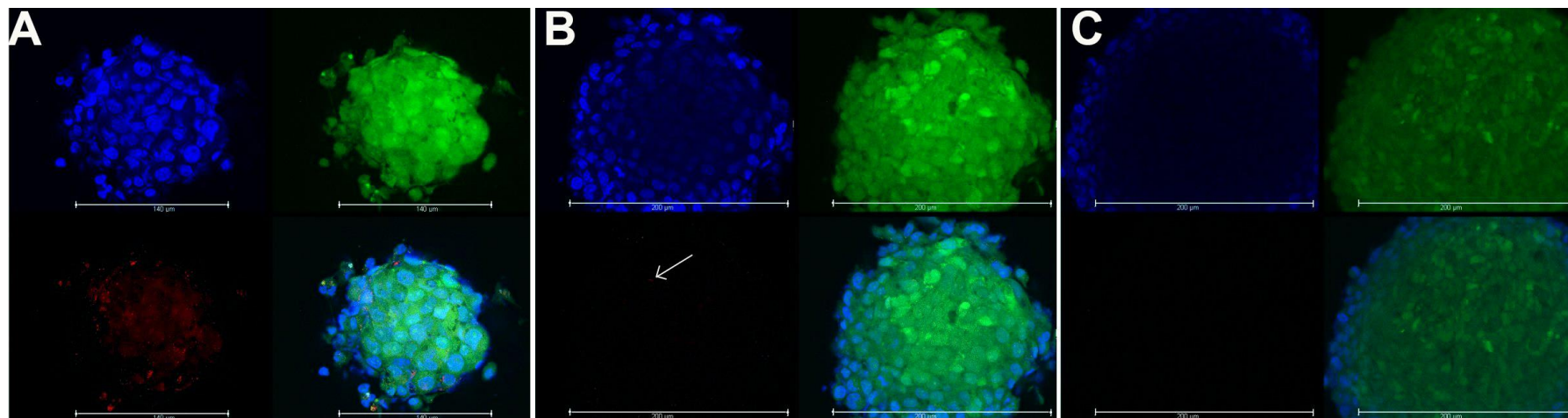


Figure 5-7. Confocal images(x40) of a VCR spheroid after 24h exposure to RBITC loaded nanoparticles. Fluorescent channels are shown separately and afterwards overlaid. A- Section 6µm into the spheroid where many fluorescent nanoparticle aggregates can be seen. B-Section 20 µm into the spheroid-most nanoparticles are in the periphery of the spheroid and very few (white arrow) were detected into the deeper layers. Expanded version shown in Figure 5-9A and B; C- Section 60µM into the spheroid, loss of contrast and brightness due to the opaque nature of the spheroids. Scale bar 200µm.

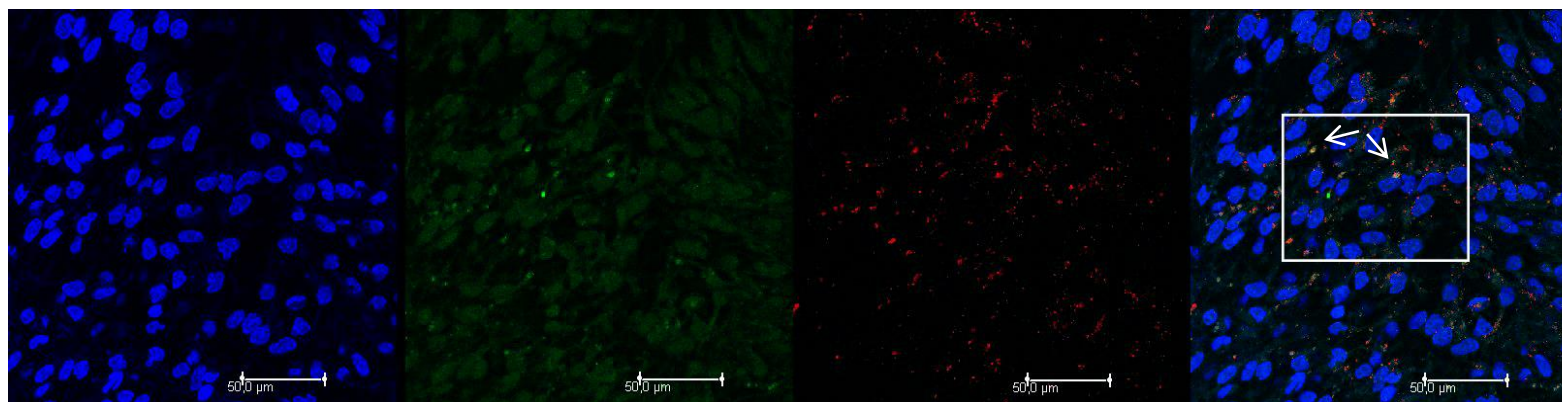


Figure 5-8 Confocal image(x63) of the monolayer of cells supporting the tumour spheroid after 24h nanoparticle exposure. Nanoparticles have accumulated into the endosomal compartments and also contribute to an increase in diffuse fluorescence when compared to the control. Artefacts (white arrows) are easily distinguished by appearing in both the green and the red channels. Highlights of the white rectangles shown in Figure 5-9C. Scale bar 50µm.

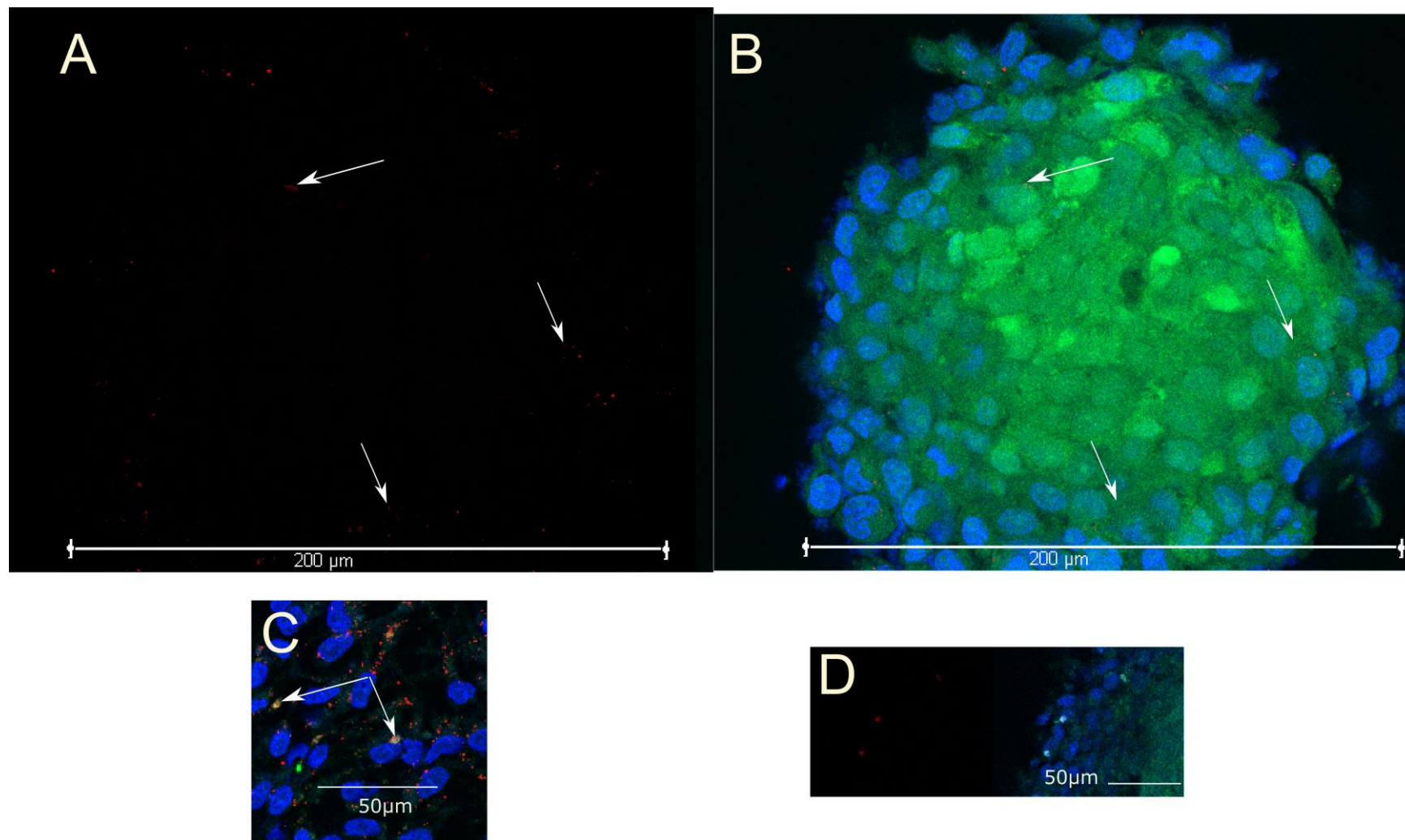


Figure 5-9. Highlights from the confocal images of nanoparticles interacting with medulloblastoma spheroids and monolayers. A (red channel) and B(overlay) of the 20μm section from Figure 5-7B, nanoparticles are fluorescent only in the red channel; C-Expansion of overlay image from the white rectangle in Figure 5-8 nanoparticles (red) can be easily distinguished from double-positive artefacts (white arrows) in VCR monolayers incubated with nanoparticles; D-Expansion of the rectangles in Figure 5-5B showing autofluorescence artefacts exhibiting fluorescence in both channels in untreated spheroid controls.

The confocal images show that the nanoparticles were taken up by the tumour cells and aggregated around the nucleus. These findings are in agreement with the studies done by Meng et al [177], [179]. The increase of diffuse red fluorescence in the images of spheroids exposed to nanoparticles may indicate that, although too small to pinpoint, the nanoparticle presence can be detected using confocal microscopy. Most nanoparticles were visible in the first cell layer of the spheroid with very little detected in the core. Despite the acceptable brightness and contrast in the spheroid sections up to 50µm in depth, the deeper sections were considerably darker and the nuclei were impossible to distinguish. This may be due to the fact that the nuclei were dyed with DAPI after the spheroids had been formed or because of the increased scattering of blue light compared to longer wavelengths. Nevertheless sectioning the spheroids or trying to increase the optical transparency of the tissues must be attempted in order to the true picture of the nanoparticle distribution and penetration depth. CSLM images can be quantitated and the diffuse fluorescence in the control and spheroids exposed to nanoparticles can be compared. However every time a new slide is inserted in the confocal microscope the difference in the distance to the objective and other optical variables could contribute a significant variation in fluorescence intensity within the same experiment. Therefore the confocal microscopy experimental setup did not have the power to quantify nanoparticle distribution within the spheroids.

5.4.2 Etoposide loaded nanoparticles- size, zeta potential, loading, stability

Etoposide loaded nanoparticles were made with the crude and purified polymers and their drug loading was measured using fluorescence spectrophotometry. To validate the suitability of the method a standard curve was constructed (Figure 5-10) and empty nanoparticles spiked with known amounts of etoposide were used as quality controls for the method (Table 5-4).

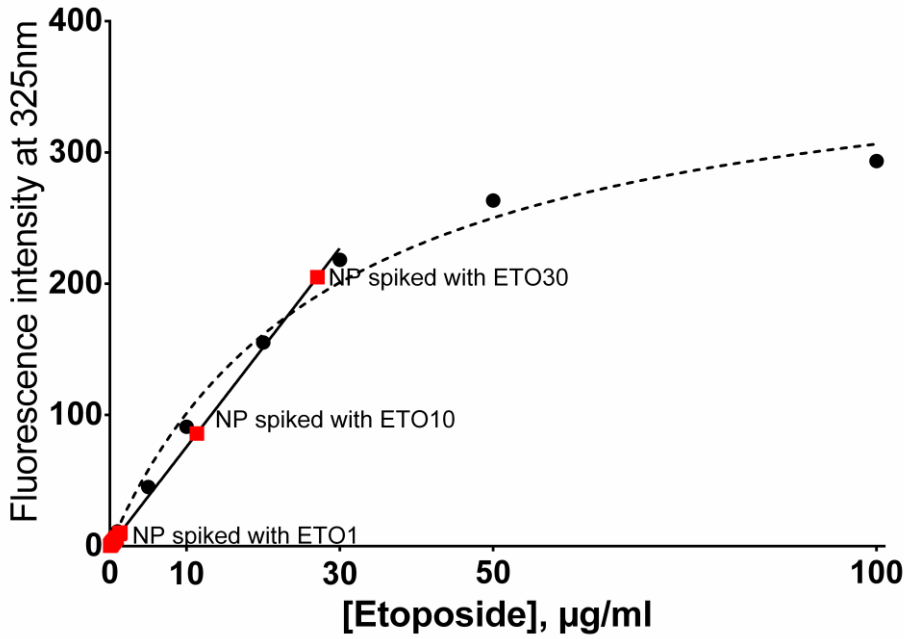


Figure 5-10. Standard curve for etoposide determination using fluorescence spectrophotometry. Fluorescence was linearly related to sample concentration up to levels of 30µg/mL etoposide (straight line). At higher concentrations fluorescence quenching due to inner filter effect absorbance was observed causing the hyperbolic shape of the standard curve at high concentrations (dashed line). Drug-loaded nanoparticle samples all clustered below the 1 µg/mL level. Empty nanoparticle samples were spiked with known amounts of etoposide and the percent of etoposide recovery was quantitated for quality control purposes Table 5-4.

Etoposide level	Recovery %
1 µg/mL	137%
10 µg/mL	113%
30 µg/mL	90%

Table 5-4. Recovery of known amount of etoposide in nanoparticle samples. These samples were prepared to test the suitability of fluorescence to be used for etoposide determination at the expected levels.

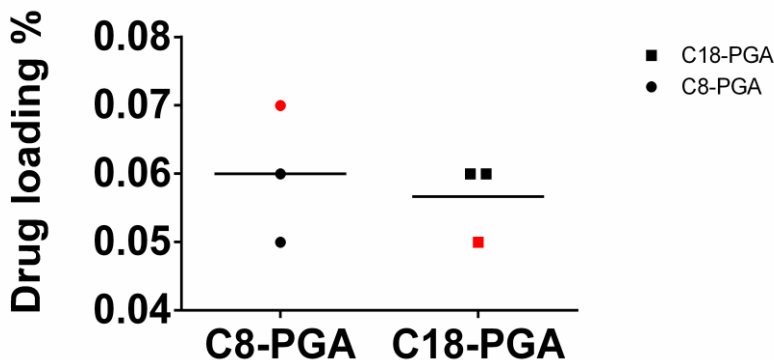


Figure 5-11. Etoposide drug loading for nanoparticles made with C8 and C18-PGA. Red dots are experiments performed with the crude polymers, while black dots represent batches made with the purified polymers. Polymer purification did not exhibit any detectable influence on loading.

As seen in Figure 5-11 the drug loading was below 1% and it did not match the 3% loading reported by Puri[180]. A comparison of nanoparticle parameters achieved in this study with the historical data from Puri is given in Table 5-5:

Parameter	Present NPs	Historical data[180]
Particle size, r, nm	132±15	126±5
Zeta potential, mV	-57±10 ³	-31±0.8 ⁴
Drug loading, %	0.06	3

Table 5-5. Comparison of etoposide-loaded nanoparticles made with the 100%C8-PGA from the present study with historical data from Puri[180].

Despite the similarities between nanoparticle size and zeta potential when compared to the results reported by Puri, the present work could not achieve the same drug loading.

Although Puri used polymers synthesized in Liverpool which had the same mean molecular weight (12 kDa) the broad Mw distribution of the polycondensation process may yield polymers with similar molecular weight but very different characteristics. It may be that the polymers synthesized in Nottingham and used in the present study differ in some way to the polymers made in Liverpool and used by Puri.

The cell culture experiments in Chapters 3 and 4 indicated that a cytotoxic level of 10 µM (6 µg/mL) etoposide would be most effective in destroying tumour tissue while preserving normal cell viability to a certain extent. A formulation with 0.06% loading would require 10mg/mL nanoparticle suspension concentrations to deliver that load. At these extremely high levels extensive aggregation, physicochemical instabilities and toxicity of the carrier may be exhibited. In contrast to that, a loading of 3% drug would require 200 µg/mL nanosuspension levels which may be achievable and have been reported to be non-toxic for PGA[176]. In order to find a solution a wide literature search into new nanoparticle production methods, polymers and etoposide analogues was undertaken. The literature search, analysis of the literature and subsequent studies are reported in the next chapter.

³ Determined in 10mM HEPES, pH=7.4

⁴ Determined in PBS

Chapter 6. Screening and evaluation of a nanoparticle library

Section 6.1 Review of etoposide and teniposide submicron delivery systems

The low drug loading results and the problems with etoposide formulation described in Chapter 5 necessitated a different approach towards formulating a successful delivery system for use in medulloblastoma and other brain tumours. Instead of focusing on a single polymer (PGA) and a single drug (etoposide), the search was expanded to include a library of polymers and etoposide analogues.

In this respect it is vital to take a closer look at podophyllotoxins and their development path up to now. Examining the tortuous path of their past is crucial for understanding the future of these mainstay anticancer drugs.

The development of the semi-synthetic drugs etoposide and teniposide is a captivating story spanning from ancient folk medicine to modern drug discovery, catalysed by a serendipitous aldehyde condensation reaction[345]. The American *Podophyllum peltatum* and the Indian *Podophyllum emodi* (or *hexandrum*) are two closely related plants which have been used in folk medicine for their emetic, purgative, anthelmintic and cholagogue effects[346]. The parent compound, podophyllotoxin, was isolated from the roots of the plants and sparked interest in the cancer field after demonstrating activity against benign genital warts[347]. Podophyllotoxin (Figure 6-1) was shown to act on the mitotic spindle similarly to colchicine[348], blocking cell division in metaphase[349].

Unacceptable gastrointestinal toxicity precluded the use of podophyllotoxin in cancer therapy and in an effort to improve its pharmacological properties around 600 derivative compounds were investigated for over 20 years by the group of Stähelin and von Wartburg in Sandoz[345]. The chemists hypothesized that the pharmacokinetics and toxicity of the lignan aglycone podophyllotoxin would be improved by

conjugating it to sugars to form glycosides in analogy with the Digitalis cardiac glycosides. The initial compounds were less toxic and more water soluble but also less active. One of the strategies to stabilise the glycosides against hydrolases was to form acetals with aldehydes. The benzaldehyde adduct of the non-purified extract (SPG) was less toxic, orally active and increased survival in leukemic mice which led to its market approval. In contrast to the tubulin interference demonstrated by the parent podophyllotoxin, the SPG mix acted via a different mechanism and prevented the cells from entering mitosis rather than blocking them during cell division. However, none of SPG's known components could be identified as responsible for its effects. An extensive search led to the discovery that a small percentage of the compound demethylepipodophyllotoxin benzylidene-glucoside (DEPBG) was the active component responsible for the anti-leukaemia action of SPG.

The most important characteristics required for the improved anticancer activity were identified as epi-configuration at C-9, free hydroxyl group at C-4' and an aldehyde-protected sugar in the glycoside. As pointed out by the leading scientists of the team[345], the cell culture studies were vital in establishing the presence of DEPBG in SPG, elucidating its new mechanism of action and understanding the structure-activity relationships of the various other aldehyde compounds in the chemical screen. Etoposide and teniposide (Figure 6-1) were taken forward based on their *in vitro* and *in vivo* potency.

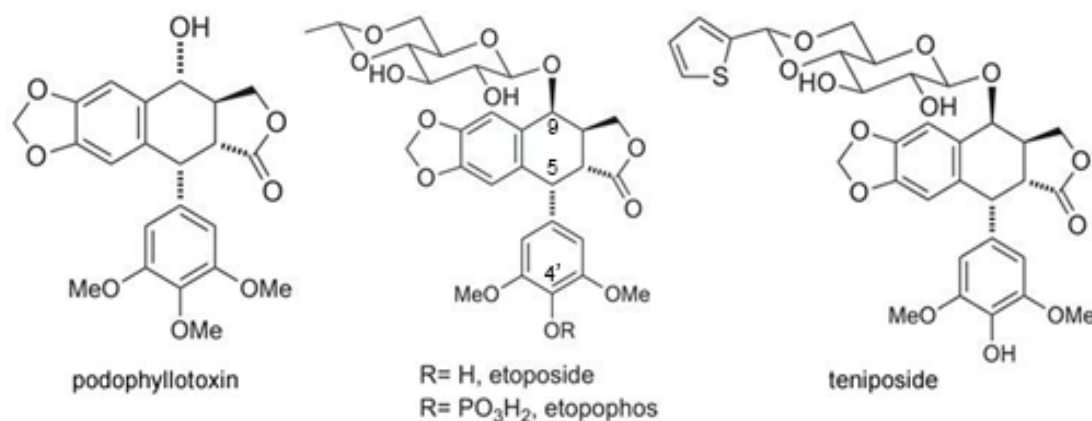


Figure 6-1. Chemical formulas of the parent drug podophyllotoxin and its semi-synthetic epipodophyllotoxin derivatives etoposide and teniposide. Notice the different conformation of the OH group at C-9 and the free phenol moiety at C-4'. Etoposide phosphate

(etopophos) is a water soluble prodrug of etoposide that is rapidly hydrolysed by phosphatases in the blood after infusion.

The clinically used etoposide, its water-soluble phosphate prodrug, and teniposide act by disrupting the mammalian topoisomerase II[350]. Topoisomerase II is responsible for unwinding knots and tangles in DNA. It relieves chain tension by introducing transient double strand breaks in the DNA and requires ATP to function[351]. Etoposide and its analogues do not inhibit the catalytic function of the enzyme but rather stabilise the normally transient covalent complex between topoisomerase II (TopoII) and DNA. This effectively poisons the enzyme turning it into a genome disruptor by introducing single and double DNA strand breaks and DNA-protein complexes. These breaks and complexes lead to chromosome aberrations, disruption of transcription and replication culminating in S/G2 blocks, apoptosis and cell death[352]. There are two forms of the TopoII enzyme in humans- α and β [353]. While α is mainly expressed in dividing cells, β is constitutively expressed in quiescent cells. The epipodophyllotoxins target both forms of the enzyme and their action towards TopoII β has been implicated in causing secondary malignancies like acute myeloid leukaemia[354]. Moreover, the lack of selectivity towards normal cells is the reason behind the dose-limiting toxicity of epipodophyllotoxins towards the bone marrow and gastro-intestinal tract[355]. Therefore, delivering TopoII inhibitors at the right place with a carrier system that offers improved selectivity can enhance their therapeutic index by increasing tumour exposure and minimizing off-target toxicity and side effects.

The importance of schedule and chemotherapy dosing is especially apparent for topoII inhibitors. Early in the development of epipodophyllotoxins it was reported that their effects are dependent on the dosing regimen[356]. Afterwards other reports and reviews have demonstrated that prolonged low-dose regimens can have a profound influence on etoposide's activity[357]–[359]. Even though this has raised hopes for the inclusion of metronomic antiangiogenic regimens in the treatment of brain tumours[122], [141], long term topoII chemotherapy has been linked to an increased risk for secondary malignancies[360]–

[362]. These side effects further stress the importance of delivering chemotherapy agents to the right cells using an appropriate formulation.

Etoposide is very slightly soluble in water (140-200µg/mL) and its octanol-water-partition coefficient is 9.94 ($\log p=1$)[363]. As seen by its chemical formula (Figure 6-1), it is a lactone and is therefore most stable at pH 5-6 and unstable in pH<3 or pH>8[363]. Due to its limited aqueous solubility, etoposide for injection is formulated with benzyl alcohol, PEG 300 and polysorbate 80 in ethanol[364]. Those excipients are not completely benign and have defined pharmacological effects. Benzyl alcohol has been implicated in anaphylactoid reactions[365], [366]. Additionally this excipient can accumulate in infants and cause the fatal "gasping syndrome"[367], [368]. Moreover, neurotoxicity of benzyl alcohol has been reported when delivered to the brain[369], [370]. The use of PEG 300 has been linked to cracking of ABS (acrylonitrile, butadiene and styrene) plastic infusion devices[371]. In addition to causing hypersensitivity reactions, polysorbate 80 in the etoposide formulation is also blamed for the leakage of phthalates from PVC infusion bags and catheters[372]-[374].

The prodrug of etoposide, etoposide phosphate, is water-soluble up to 20mg/mL and its formulation does not contain extra solvents or solubilisers. In this regard, etoposide phosphate would appear more suitable for local delivery to the brain and CSF. However, the prodrug requires phosphatase-catalysed activation to etoposide to exert its action because the free 4'-OH is crucial for topoisomerase inhibition[375]. Although the conversion to etoposide is rapidly achieved in the blood stream by plasma phosphatases, there is very limited data regarding phosphatase activity in the CSF and the conversion of phosphate prodrugs to the parent compounds in the brain. One study looking at intrathecal administration of dexamethasone phosphate found that the prodrug was hydrolysed in the CSF within 40 minutes[375]. Despite those encouraging results, additional studies are needed in order to establish whether that can be replicated for etoposide phosphate. For the purposes of nanoparticle delivery, the phosphate prodrug is less attractive because of its higher hydrophilicity and aqueous solubility

which may limit loading and increase release rates from hydrophobic-core nanoparticles.

The pharmacokinetics of the epipodophyllotoxins can reveal some crucial considerations regarding their delivery to the brain. Both etoposide and teniposide are more than 90% albumin-bound and this is thought to be the reason behind their poor penetration through the blood-brain barrier [376]. Upon intravenous and oral administration of 50-150 mg/m² etoposide or teniposide, the intratumoral concentration was found to vary for both drugs, ranging from virtually undetectable to biorelevant levels 1-2 µg/g (10-14% of plasma levels) in some brain tumours[377]–[379]. The concentrations in the bordering normal tissue were generally two times lower and CSF levels were 0.7% of the plasma concentration. Considering the demonstrated poor capacity to cross the BBB, barrier disruptions in brain tumours have been postulated to be behind the response to low dose oral etoposide therapy in medulloblastoma[202]. A useful illustration of BBB disruption in brain tumours is given in a study looking at methotrexate concentrations using microdialysis probes. The authors found 17-times higher concentrations of the drug in contrast enhancing regions compared to regions with intact blood-brain barrier[380]. Those blood-brain barrier disruptions can vary between different tumour types, between patients and also between the regions of the same tumour. Nevertheless, in the case of epipodophyllotoxins the need to maintain ten times higher plasma levels in order to achieve cytotoxic concentrations in tumours would come at the expense of severe haematological toxicity and increased risk for secondary malignancies.

In this regard, local therapy in the brain will bypass the blood brain barrier and require doses which are much lower compared to systemic treatment. For example, a feasibility study by Fleischhak[120] demonstrated that a 0.5 mg etoposide dose delivered intraventricularly maintained CSF levels >1 µg/mL for 4 hours. In contrast, even with 400 mg/m² systemic etoposide CSF levels were below 0.1 µg/mL. An important limitation was that etoposide was quickly cleared by bulk flow and penetration into the brain was minimal judging by the volume of distribution which matched that of the CSF. The rapid clearance would

necessitate frequent administration to the brain via an Ommaya reservoir or an infusion pump that would diminish patient comfort and increase risks of infectious meningitis, especially in immunocompromised patients. A possible route for improvement may be a slow-release submicron formulation of etoposide analogous to the liposomal cytarabine product Depocyte[381], [382]. It should be noted, however, that increased drug exposure of the tumour tissue would always lead to increased exposure of the normal brain as well. In the case of Depocyte this manifests as chemical arachnoiditis and requires dexamethasone pretreatment[382]. Therefore, apart from an extended release profile, an improved formulation should also display preferential uptake and toxicity in tumour cells compared to normal tissue.

In summary, epipodophyllotoxins are not specific towards cancer cells, they are poorly distributed in the brain and their action strongly depends on prolonged drug exposure. An ideal drug delivery system would be administered locally, would display an extended release profile and a certain amount of selectivity towards tumour tissue. This should warrant improved therapeutic profile with enhanced safety and efficacy.

Based on the abovementioned considerations, the cell culture results for etoposide described in Chapters 3 and 4 along with the requirements for nanoparticle delivery, acceptance criteria for etoposide loaded nanoparticles were set as:

1. Drug loading > 3%
2. Particle diameter < 300 nm
3. Drug release over 48h
4. At least 2X potentiation of toxicity *in vitro* compared to etoposide
5. Relatively non-toxic nanoparticle carrier.

An initial literature search was undertaken in order to pinpoint successful etoposide formulations in addition to important polymer characteristics and nanoparticle preparation methods. The search included the PubMed, Web of Science, Scopus and Scifinder databases using the keywords "etoposide nano*" or "etoposide formulation". Over 40 original research

articles were identified that described the preparation, purification, *in vitro* and/or *in vivo* testing of various drug delivery systems.

The results are summarised in Table 6-1 and are colour-coded using a traffic light system, based on whether the results from the study could be practically implemented in-house. Loadings above 3% and size below 300 nm received green rating. Nanoparticle purification, release, cell culture and comments were classified using an integrated approach combining reliability of methodology, possibility for reproduction and the relevance of the cell model reported. In these categories red means a rejection for further consideration, amber- proceed with caution and green-acceptance.

Screening and evaluation of a nanoparticle library

Year	Ref	Type of DDS	Method	Load ing%	Size d, nm	Clean up	Release	Cell-culture	Comments
2010	[383]	PEG-PSA microspheres	E	40	1800	C/W	Not sink	ETO not particles	improved survival in vivo
2013	[384]	Mesoporous CaCO ₃	binary solvent	39	2000	C/W	Sustained days depending on pH; Not sink	Non-toxic- HEK293T; Potentiation in gastric cancer	Not in polymer NP scope
2012 2014	[385] [386]	Dextran stearate micelles	D	30	170	D	Not sink; Burst 40% in 12h; 60% in 24h	Potentiation of tox. in cell culture. Micelles toxic as well	only IC50 given, statistical analysis not disclosed Less than one molecule stearic acid per dextran chain, 5-6ug/mL CMC, CMC higher than quoted cytotoxicity figures
2010	[387]	MePEG-PCL micelles	D	25	264	D	48% released in 24h; 60% by 48h	Higher tox in low doses same tox as etoposide after 3-10ug/mL etoposide	
2005	[388]	PEG-PCL Star micelles with PAMAM core	Solid extraction	22	17 and 60	N/A	N/A	Cytotoxicity same as etoposide	
2013	[389]	nanohybrids hydrotalcite	co-precipitation	20	60	C/W	300 minutes		Very quick release
2013	[390]	Conj. with Hyaluronic acid		17.00	32	Col/D	2% per day	4.2 times potentiation of tox	
2014	[391]	PLGA-PEG	E/ NP	12 / 7	173 / 146	C/W	11% Burst 40% 24h	In vivo- higher AUC	No cell culture studies
2013	[392]	PEG-PLGA	E	12.00	170	C/W	N/A	In vivo studies	Limited data on proportions, surfactants, loading
2011	[393]	Polyhydroxy-alkanoate NPs	E	10	200	C/W	Not sink	HeLa cells, modest effect	
2010	[394]	PLGA-MPEG; PLGA-Pluronic	E	10.00	148	C/W	26% in 12h 50% in 48h;	Cell uptake data in follow-up study; barely better than etoposide- data interpretation questionable[395]	
2011	[396]	Solid lipid NPS	NP	10.00	130 / 500	N/A	24h	N/A	Obscure journal, data very scarce, may not be genuine
2013	[397]	Albumin nanosusp.	E	8.65	190	N/A	24h	<i>In vivo</i> pK -lung, spleen	Chinese patent [398]
2013	[399]	PLGA/Pluronic F68 NPS	NP	7.70	130	C/W	60% in 6h 80% 48h	Potentiation	Glycofurol, PEG, Benzyl alcohol may have interfering effects
2010	[400]	PLGA 50:50	E	7.5	160	C/W	24h, 55%	Formulation optimization study- no cell culture	
2013	[401]	PLA	E	6.03	163	C/W	20% burst, 60% in 48h	Polymer appears as toxic as etoposide?	
2012	[402]	NP butyl-cyanoacrylate	E	6.00	160	C/W	80% 6h	Quick release	
2012	[403]	micellar formulation PEG-PCL	NP	5.32 4.5%	86	Filt	50% 48h	Loading more than theoretical; Volume in dialysis bag for release not disclosed	
2012	[404]	PEG-fatty acid micelles	E	5.00	13-479	C/ UF	Burst in 5h	No cell culture studies	

Screening and evaluation of a nanoparticle library

Year	Ref	Type of DDS	Method	Loading %	Size d, nm	Clean up	Release	Cell-culture	Comments
2014	[405]	LNC	E	3.35	110-450	C/W	N/A	Toxicity of positively charged lipids	Loading determined from supernatant
2006	[406]	LNC	E	3	370	C/W	Not sink; 30% in 24h 50% in 48,	In vivo studies - estimate tumour growth by weight gain	
	[407]								
	[408]								
	[409]								
2007	[180]	100%C8-Poly(glycerol adipate)	NP	3.00	126	Col	40% in 1 day 50% in 6	No cell culture	Can't reproduce
2007	[410]	PVP-PDLLA	E	2.00	200	C/W	20-30% in 24h 95% in 13days	No cell culture	MgCl2 salting out to increase DL%
2012	[411]	LNC	E	1.80	170	D	Release in 6h	Claimed, potentiation	Blank NPs as toxic as etoposide
2012	[412]	NP PLGA 502H	NP	1.50	150	C/W	12h - 40%, 48h- 50%	Small potentiation After 72h	
2013	[413]	PLGA	NP	1.45	105	C/W	48h; 50% in 24 <i>In vivo</i> - Tc labelling may label PLGA as well/ not specific		
2008	[414]	PLGA; PCL	NP / E	1.45	92-257				
2013	[415]	Poly(NVCL-co-MMA)	In situ Polym	0.65	20	C/W	20-40% Burst 1h	Less toxic than ETO	
2013	[416]	LNC	X Phase inversion	0.57	50		NPs toxic even w/o etoposide		
2014	[417]	LNC	E	0.30	121(50-650)	C/W	60% in 12h; Sustained for 24h	Same in cell culture and <i>in vivo</i>	
2006	[418]	LNC	E	0.10	25-100	Filt.	Sustained 60% in 48h	Potentiation of tox in cell culture	Etoposide measured from supernatant/ Filtration to clean up
2008	[419]	LNC	E	0.10	178	N/A	Sustained for 24h	Potentiation of tox in cell culture	

Table 6-1 Literature review of nanoparticle delivery systems using etoposide. Red, amber green classification is based on acceptance criteria for loading and size of submicron delivery system, quality of experimental design, probability for being reproducible, amount of data disclosed by authors and whether claims expressed in the paper match the results shown. LNC- lipid nanocapsules. Most common methods were emulsification based (E- emulsification-solvent evaporation and melt emulsification for LNC), nanoprecipitation (NP) and dialysis (D). Loading >3% is classified as green, between 1-2%- amber and below 1%-red. Size is green below 200nm, amber below 1000nm and red for microparticles. Effective nanoparticle clean-up methods were classified as green (D-dialysis, Col-gel column), amber(C/W-centrifugation and washing) and red (filtration or none)

As seen from Table 6-1 there is a considerable amount of research dealing with etoposide encapsulation in nanoparticles. While there were about 6 articles up to 2007, the number published in 2013 was over 10 and more publications are expected in 2014. Despite the large amount of data published, most of the drug delivery systems described have not been taken forward for further development.

Since the difficulties in extracting robust data from the published literature have been recognised in the preclinical and clinical settings[420]–[422], the RAG (red, amber green) coding system was employed to simplify the decision-making process in selecting reproducible reports. Emphasis was paid to articles that could be reliably used to establish a strategy for nanoparticle preparation. Some of the main considerations behind the ratings are given in the paragraphs below.

A common, but rather unhelpful, way to present nanoparticle loading data is by using encapsulation efficiency. This parameter is derived from the loaded amount of drug in the NPs divided by the starting amount of drug:

$$EE\% = \frac{\text{weight of drug in nanoparticles}}{\text{initial weight of drug}} \times 100 \quad \text{Equation 6-1}$$

$$\text{Drug loading}\% = \frac{\text{weight of drug in nanoparticles}}{\text{weight of nanoparticles}} \times 100 \quad \text{Equation 6-2}$$

Equation 6.1 shows that encapsulation efficiency is a useful measure of drug waste during the process of nanoparticle manufacture, but it does not convey any information about the amount of drug in the delivery system. Although reporting entrapment efficiency of 90%, some nanoparticle delivery systems have an actual loading of 3%[409] and 0.3%[417]. In this regard, encapsulation efficiency is a misleading way to present nanoparticle formulation data and its use without the explicit statement of drug loading can indicate selective reporting.

After preparation, the nanoparticles need to be separated from the unencapsulated drug in order to distinguish their effects from those of the free drug. This can be achieved using several methods- centrifugation and washing, size exclusion chromatography by using a gel packed column or dialysis. Centrifugation and washing is a quick and easy procedure,

however it can leave a considerable amount of surface-bound unencapsulated drug on the nanoparticles. The adsorbed drug would serve to boost reported loadings but would ultimately lead to a quick burst release. A good example of the limits of the centrifugation/washing process is the study by Gaucher et al.[410], where they used a 20% MgCl₂ solution to limit the solubility of etoposide in the aqueous phase while making the nanoparticles. Despite centrifuging and washing their particles three times, they still had 5.5% MgCl₂ in the “clean” nanoparticles. Striving for better separation some authors have opted for dialysis[385]–[387], [411], while only two of the etoposide studies report the use of a column to separate the nanoparticles from the free drug[180], [390]. Strikingly, there are a number of papers where no-clean up at all was reported or plain filtration was used for removing the unencapsulated etoposide[388], [397], [403], [418], [419]. Omitting the separation step raises considerable doubts that the reported loadings would remain as high as reported after a thorough clean-up procedure is applied.

The next step in the *in vitro* characterisation of nanosized delivery systems is the determination of drug release which aims to establish how long the drug remains associated with the carrier. The release profile can serve as a prediction tool for nanoparticle performance in cell culture and animal experiments when a biorelevant release medium is used. An important prerequisite for correctly assessing release is the experiment to be performed under sink conditions. Sink conditions approximate infinite dilution and are satisfied when the concentration of the released drug is low enough so that it does not influence the release profile. According to the EU Pharmacopoeia[423] sink conditions are achieved when the released drug is at levels 5 to 10 times below the solubility limit. As etoposide’s solubility is quite low, many of the studies reviewed did not satisfy these criteria[383], [385], [393], [408].

Determination of drug release from submicron delivery systems is a difficult task because of the small size and relatively fragile nature of some platforms like liposomes and micelles. A number of methods have

been proposed ranging from dialysis[424], centrifugal ultrafiltration[425], pressure ultrafiltration[426] and ultracentrifugation[427].

The dialysis technique is the most popular method to study drug release from submicron systems and has almost exclusively been used in the etoposide studies. The usual set up involves a small donor compartment filled with a solution containing the delivery system which is separated by a dialysis membrane from a sink acceptor compartment, containing the bulk of the release media. The release of the drug from the delivery system is compared to a control sample containing the drug in solution. Serious concerns have been raised regarding the reliability of dialysis in determining drug release. As shown by Washington[428], [429] the appearance of drug in the receiving compartment can be significantly influenced by the interaction of released drug and the surface of the colloid carrier system. The bias in results produced from release experiments using dialysis has been discussed in a number of publications[430]–[432]. Some authors have proposed solutions to the violation of sink conditions in the donor compartment by using the inverted dialysis method[433] or by extensive dilution in the dialysis tube[434]. Even with these augmentations, the influence of the surface interaction between free drug and the carrier system needs to be accounted for. That can be achieved by including an additional control of empty carrier supplemented with a solution of the drug in an amount equivalent to the one encapsulated in the delivery system. Nevertheless dialysis should be used with caution and the results interpreted carefully in nanoparticle systems showing release faster than a few days[429].

The other methods of determination of drug release involve sampling a sink compartment with the colloidal system and separating the continuous from the disperse phase. Ultracentrifugation can be used when the particles are approaching the micrometre range[384] or when there is a sufficient difference in density between the two phases[435]. However, the use of ultracentrifugation may be limited when the particle size is below 100nm, or the densities of the disperse phase and continuous phases are similar as this would lead to very long centrifugation times and may disrupt the carrier causing a premature leakage of drug[430]. This is

why many researchers have turned to centrifugal ultrafiltration which uses centrifugal force to filter a small amount of sample through a membrane with Mw cut-off of 10-300 kDa. There are a number of devices available, normally used for protein purification, which offer a small working volume (0.5 mL) and a variety of membrane sizes and materials (polyethersulfone, regenerated cellulose, cellulose esters). Additional checks for nanoparticles appearing in the filtrate[430] and non-specific drug adsorption[425] should be included when these systems are utilised. Similarly to the centrifugal filtration devices, the tangential flow filtration cells use a filter membrane to separate the dispersed from the continuous phase. However, instead of relying on centrifugation force, they utilise a tangential pressure gradient in order to minimise membrane fouling[426]. The pressure filtration units are bigger than the centrifugal ultrafiltrators, starting at 3 mL, and while their design ensures minimal membrane fouling, interaction and binding of hydrophobic drugs to the membranes still pose a problem[430]. Other more creative and elegant solutions include the utilisation of electrochemical monitoring[436], [437], microdialysis probes[438], fluorescence quenching[439] and bathochromic shift[440] methods. Since epipodophyllotoxins are electrochemically active[441] it would be feasible to determine etoposide and teniposide release from nanocarriers using electrochemical methods.

The next step after successful drug release profile characterisation is to test the nanoparticle system in an *in vitro* cell line that would be relevant for the intended use. Ideally, the carrier would not exhibit pronounced toxicity, and the drug delivery system would display superiority in either potency or selectivity when compared to the free drug. While many tumour cells are relatively easy to culture *in vitro*, finding a suitable model for normal tissue is a challenge. It can be argued that the adenovirus transformed HEK293[384] and the murine fibrosarcoma cell line L929[393] cannot be used as reliable proxies for normally behaving human tissues.

Designing a nanoparticle delivery system is often a multidisciplinary effort involving experts from different fields. That is why it is easy to imagine how some studies, interested in nanoparticle delivery, have managed to

include cell culture data with little information on the methods used to fit dose-response relationships or how they calculate and compare IC₅₀ values[385], [386], [399], [401], [411]. In their 2011 article Yadav et al[395] claim that their drug delivery system offers a three-times reduction in IC₅₀ for L1210 cells and 1.6 times for DU145 cells compared to etoposide. Surprisingly, they have not disclosed the equation used to model their dose-response data and have apparently based their IC₅₀ determination on a single measurement (Figure 1a, 5 μ M concentration). Moreover, it can be argued that the DU145 cells are resistant to etoposide and the differences in IC₅₀s may be statistically significant but are negligible in practice. A few of the carrier polymers and surfactants used in the nanoparticle delivery systems appear quite toxic[385], [386], [405] sometimes as potent as etoposide itself[401], [411]. At the very least that makes critical analysis of the *in vitro* data very difficult and brings into question the claimed effects.

Section 6.2 Nanoparticle screening strategy

Despite the heterogeneity and the patchy nature of the information collected, a few conclusions can be made from the papers discussed in Table 6-1:

1. Emulsification / solvent evaporation has higher reported drug loadings than nanoprecipitation.
2. PEGylated block copolymers(PCL-PEG, PLGA-PEG) have higher reported drug loadings
3. Micellar systems have higher reported drug loadings but some are toxic and others not much different to free etoposide[387], [388]

It is feasible to conclude that the problems of incorporating etoposide in poly (glycerol adipate) nanoparticles described in Chapter 4 are partly due to the method of nanoprecipitation and partly because of etoposide's limited affinity for the polymer. Although often being called poorly soluble etoposide has 200 μ g/mL solubility in water, logP \sim 1 and it has multiple sites suitable for H-bonds. Moreover, it is not very soluble in lipids[442] and tends to dissolve in PEG400, Tween and Cremophor EL[443], [444]. Hence a more accurate description of etoposide would be that it is a very

slightly water soluble amphiphilic molecule. With that in mind it may be possible that during nanoprecipitation with a water-miscible solvent etoposide is further solubilised in the aqueous environment and upon acetone evaporation deposits on the surface of the polymer particles or as separate crystals in the aqueous solution.

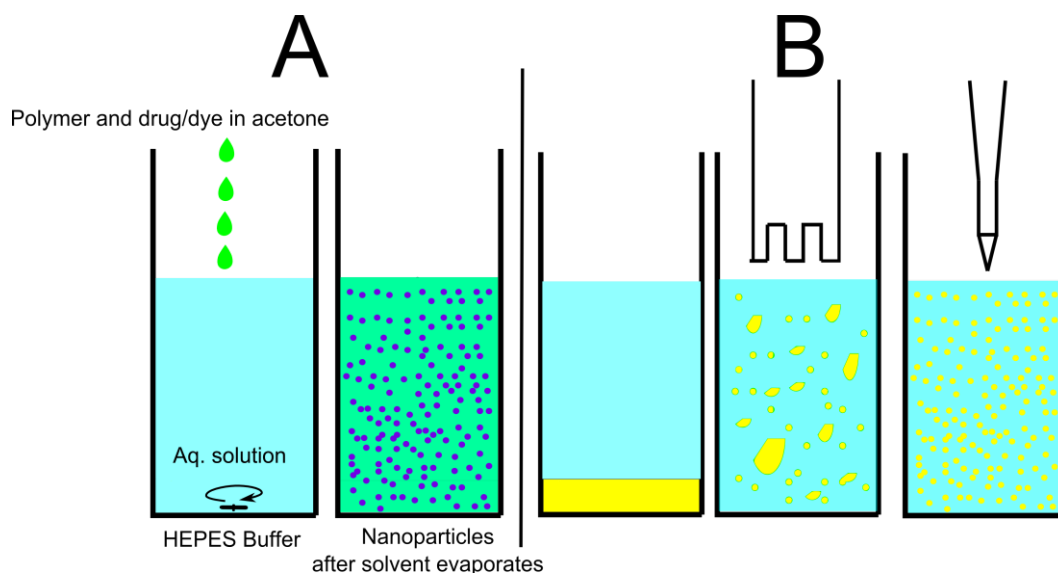


Figure 6-2. Comparison of the two most common methods for nanoparticle preparation. **A**-Nanoprecipitation: polymer and drug are dissolved in a water miscible solvent and added dropwise under stirring to the aqueous phase. **B**-Solvent-emulsification: water immiscible solvent (DCM, Benzyl alcohol or Ethyl acetate) is mixed with the aqueous phase with the help of surfactant (emulsifier) and homogenised to form a coarse emulsion with a rotor-stator homogenizer. Nanoemulsion is formed in a third step using sonication or high-pressure. The final step is solvent removal usually under reduced pressure.

The term nanoprecipitation (Figure 6-2) is often used interchangeably with the original “interfacial deposition method” described by Fessi[445]. In contrast to conventional nanoprecipitation, the Fessi method employs an additional excipient, namely an oil phase in which the drug is soluble, to make nanocapsules rather than polymer nanospheres[176], [177], [180]. Fessi et al. have relied on the solubility of the drug in the oil phase and its tendency to stay there rather than distribute in the aqueous phase. The polymer merely makes a protective film on the oil/water interface and hence the name “interfacial deposition method”. It seems that given etoposide’s solubility in water, tendency to crystallise and drop out of solution and its low solubility in lipids[442]–[444] neither the nanoprecipitation nor the interfacial deposition methods are going to be suitable.

The solvent-emulsification method (Figure 6-2) where the drug is emulsified in a solvent which is immiscible (CHCl_3 , CH_2Cl_2) or has limited miscibility with water (Ethyl acetate, Benzyl alcohol) may be a better alternative for drugs like etoposide. The limited miscibility of solvent and water will serve to keep etoposide in the organic phase and limit solubilisation in the aqueous one. The emulsification solvent-evaporation usually yields microparticles[446], [447] and the addition of water-miscible solvents like acetone or methanol[448] or surfactants like sodium cholate[449], human albumin[397], TGPS[391], Pluronic F68[394] have been suggested to achieve particle diameters below 200nm. For self-assembly PEGylated systems the issue with size appears to be less problematic although the use of Pluronic F68 in the aqueous phase was still reported[394]. In addition, most of the successful examples for nanoparticle drug delivery systems that have reached clinical trials BIND-014[449], [450], GenexolPM, and NK105[451] employ self-assembly systems with PEG and are focused on the very poorly soluble taxanes.

Etoposide's aqueous solubility (200 $\mu\text{g}/\text{mL}$) may be the reason for the low loadings reported in Chapter 4 and a more hydrophobic analogue (teniposide) could achieve higher levels of incorporation. Teniposide has aqueous solubility of 0.54 $\mu\text{g}/\text{mL}$ [452] and has been reported to be more potent compared to etoposide against medulloblastoma *in vitro*[453]. Cremophor EL in the formulation of teniposide[454] has been implicated in anaphylactic reactions and neurotoxicity[455]. In addition the formulation contains benzyl alcohol and dimethylacetamide[456] making it even less suitable for intra-CSF administration and local brain therapy[369], [370].

Compared to etoposide there is much less data on teniposide incorporation into nanoparticles and submicron delivery systems. One study looked at PLGA loaded nanoparticles and has claimed 12% loading, however the authors seem to confuse nanoprecipitation and emulsification methods and had drug degradation during the release[457]. Most other studies have looked into emulsion formulations trying to substitute Cremophor EL and organic solvents for safer alternatives[452][458].

Zhang et al. have reported 2% loading in an emulsion formulation with medium chain triglycerides, solutol HS and tocopherol polyethylene glycol 1000 succinate[459]. While the improvement shown in the *in vivo* results looks impressive, the authors have used centrifugation to clean up the emulsion and have not disclosed enough details about the release. Moreover the drug-free delivery system seems at least as toxic as teniposide to MCF-7 cells in the *in vitro* screen.

A screening plan for finding a successful nanoparticle formulation was established based on the literature search and the previous experiments. The polymers 100%C8-PGA, 40%C18-PGA and a PEGylated version of PGA were chosen from the poly(glycerol) adipate library. In order to increase the diversity of the screen four additional polymers were supplied in collaboration with Prof Cameron Alexander. Two were block copolymers of polyethylene glycol (PEG) with poly(caprolactone) and poly(decalactone). In addition two other thermoresponsive block copolymers of poly(ethyleneglycolmethacrylate) with poly(lactic acid) and poly(caprolactone) were included as well. The first phase of the screen was envisaged to compare all polymers with etoposide and teniposide using nanoprecipitation. If loadings above 3% were not achieved, then solvent-emulsification would be attempted. Finally an optimisation program with different solvents and surfactants would pinpoint the right formulation that can meet the criteria of 3% loading, lower than 300nm size and a sustained release profile.

Section 6.3 Materials and methods

6.3.1 Materials

Poly(glycerol adipate) (PGA) , 40% C18-substituted poly(glycerol adipate) (40%C18-PGA), 100% C8-substituted poly(glycerol adipate) were synthesized by the author during this PhD project. PEG-poly(glycerol adipate) (PEG-PGA) was synthesized in Prof Martin Garnett's lab. Kuldeep Bansal synthesized and characterised poly(caprolactone)-PEG(5kDa-5kDa,PCL-PEG)) and poly(decalactone)-PEG(6kDa-5kDa, PDL-PEG), while Lee Moir prepared and characterised poly(lactic acid)-co-

poly(ethyleneglycolmethacrylate) (PLA-PEGMA) and poly(caprolactone)-co-poly(ethyleneglycolmethacrylate) (PCL-PEGMA) block copolymers.

Sodium cholate, resazurin and polysorbate 80 were obtained from Acros organics (Loughborough, UK)

Teniposide was acquired from Sequioia Research Products (Pangbourne, UK)

Etoposide, tocopherol polyethylene glycol 1000 succinate, polyvinyl alcohol (88kDa) were purchased from Sigma-Aldrich (Dorset, UK)

All solvents were purchased from Sigma-Aldrich (Dorset, UK) or Fisher Scientific (Loughborough, UK)

6.3.2 Polymer characterisation

¹H-NMR spectroscopy (Bruker 400Mhz, CDCl₃), was used to calculate Mw and percent of polymerisation for PCL-PEG, PDL-PEG, PLA-PEGMA and PCL-PEGMA.

Gel permeation chromatography (GPC) was performed on a Polymer Labs GPC 50 Plus system with a refractive index detector. Separations were performed on two PL-gel Mixed-D columns. Chloroform-triethylamine 95/5 was used as the mobile phase (flow rate of 1 mL.min⁻¹). Polystyrene was used as calibration standard (160 Da–240 kDa, Polymer Labs, UK). Molecular weights and polydispersity indices were calculated using Polymer Labs Cirrus 3.0 software.

The change of absorbance of nanoparticle suspensions (PBS) in response to change of temperature was investigated using UV/VIS spectrophotometer (Beckman, DU 800). Turbidity measurements were taken at 550 nm and cycles were run from 20–90 °C at ramp rate of 1 °C.min⁻¹.

6.3.3 Nanoparticle preparation

All activities with etoposide and teniposide were performed under conditions protecting the substances from light either by using amber glassware or aluminium foil.

6.3.3.1 Nanoprecipitation

Etoposide or teniposide (1.5 mg) and polymer (10 mg) dissolved in acetone (1 mL) were mixed with water (2 mL) using a chamber mixer (Pharmacia, 50-60 Hz, 5 MPa). The aqueous (4 mL/min) and organic (2 mL/min) phases were delivered to the mixer using two peristaltic pumps (Pharmacia). Acetone was left to evaporate for 8 hours and the suspensions were filtered through a 0.45 μm syringe filter before separation of the free drug.

6.3.3.2 Solvent emulsification

Etoposide or teniposide (3 mg) and polymer (17 mg) were dissolved in dichloromethane (DCM, 1 mL) and mixed with water (4 mL) with or without the addition of different surfactants using a high-shear mixer (Ultra-Turrax, IKA T25) for 1 minute at 24000 rpm. The resultant coarse emulsion was immediately sonicated with a probe sonicator (Bandelin UW2070, 60% power, 2 minutes). The Nanoemulsion was evaporated using a rotary evaporator at 30 °C. The resultant nanoparticles were filtered through a 0.45 μm syringe filter and rapidly transferred for separation of the free drug.

6.3.4 Separation of nanoparticles and free drug

Sephadex GH25 desalting columns (PD-10, GE Healthcare) were used to separate the nanoparticles from the free drug. Briefly, the columns were washed with 10 volumes of pure water before loading with nanoparticle suspension (2.5 mL). Pure water (3.5 mL) was used to elute the nanoparticles and the columns were then washed with another 30-50 volumes of water before reuse. Either fluorescence spectrophotometry or HPLC was employed to ensure lack of etoposide/teniposide in the column eluent before nanoparticle clean up. Separation of the free drug from the nanoparticles was verified using a solution prepared in the same way as the nanoparticles but omitting the polymer. No etoposide/teniposide was detected in the fraction normally collected for the nanoparticles.

6.3.5 Size and zeta potential characterisation

The hydrodynamic radii of the nanoparticles were determined via dynamic light scattering at 90° angle using a Viscotek 802 instrument (830 nm laser, 60 mW, 10% power). At least 10 measurements were performed on each sample with a duration of 4s per measurement. While intensity measurements were used to measure particle size, mass and number distributions were examined to investigate the presence of multiple populations.

The zeta potentials of the nanoparticles were determined using Laser Doppler Electrophoresis (Zetasizer NanoZS, Malvern) in 10mM HEPES buffer. At least three measurements were performed on each sample.

6.3.6 Drug loading

Drug loading was determined by freeze-drying a set volume of nanoparticle suspension (0.5-1 mL) in a preweighed amber HPLC vial. The weight difference was recorded and the nanoparticles were dissolved in DCM:DMSO (1 mL, 50:50). Absorbance was recorded at 284 nm with a UV spectrophotometer (Varian Cary Bio 50, Agilent). Fluorescence spectrophotometry (Varian Cary Eclipse, Agilent) with excitation ($\lambda=284$ nm), emission ($\lambda=325$ nm) and slit (5 nm) was measured against freshly made standards.

6.3.7 Drug release

6.3.7.1 Kinetic solubility of teniposide in release media

Kinetic solubility of teniposide in PBS and PBS with added surfactant (1% sodium cholate or Polysorbate 80) was determined by adding teniposide (1000X stock in DMSO) to the aqueous buffers and noting the appearance of visible nanosuspension. Drug concentrations resulting in cloudy solutions were labelled as above the kinetic solubility. Levels which yielded clear solutions were kept for a 24h stability test. They were monitored for the appearance of cloudiness, crystals or decrease in absorbance of fluorescence. At the time of preparation the clear solutions were assayed for UV absorbance at 240 and 284 nm and fluorescence (Excitation 240 or 284, emission 325, slit 5). The measurements were

repeated on the next day and samples with change in signal were classified as above kinetic solubility.

Limit of quantitation (LOQ) and limit of detection (LOD) in the spectrophotometric determinations experiments were determined using the standard deviation of the y-intercept and the slope of the linear regression as per the EMEA and ICH analytical validation guidance[460].

$$LOD = 3.3 \times \frac{STDEV \text{ of } y \text{ intercept}}{Slope \text{ of linear regression}} \quad \text{Equation 6-3}$$

$$LOQ = 10 \times \frac{STDEV \text{ of } y \text{ intercept}}{Slope \text{ of linear regression}} \quad \text{Equation 6-4}$$

Release experiments were performed in release buffer containing 1% sodium cholate in PBS.

6.3.7.2 HPLC determination of teniposide

Teniposide release was determined via HPLC (HP Agilent 1050) with UV detection ($\lambda=240$ nm) using an isocratic method with a C18-reverse phase Lichrospher (250/4 mm) column at 40°C. The mobile phase was Acetonitrile (55%), aqueous phosphate buffer (45%, 50 mM, pH=7) and the flow rate was 1.2mL/min. The retention time for teniposide was 2.9 min and the area of the peak was used for concentration determination. The noise range at 2.4 to 2.5 min and 3.2 to 3.4 min and was used to determine limits of detection and quantitation as 3 and 10 times Signal/Noise respectively. Accuracy and specificity were assessed by the resolution of the teniposide peak to that of the other components of the release media. Precision was assessed by repeatability (intra-assay) and intermediate precision (inter-assay variation) using the coefficient of variation with acceptance criteria CV<15% for all samples and CV<20% for the lowest levels. The robustness of the assay was explored by determination of recovery for teniposide samples after flash freezing and thawing.

6.3.7.3 Centrifugal ultrafiltration

Centrifugal ultrafiltration devices (0.5 mL, Amicon, Vivaspin and Nanosep) with different membrane sizes (10-300 kDa) and membranes made of either polyethersulfone or regenerated cellulose were tested for their suitability in determining teniposide release from nanoparticles. Centrifugation forces ranging from 2000 to 14 000g were tested in effort to preserve nanoparticles integrity.

Non-specific binding was quantified by analysing teniposide content before and after passing standards (0.025 μ M to 30 μ M) through the devices.

Nanoparticle contamination of the filtrate was determined using dynamic light scattering. A standard curve was built from serial dilutions of a concentrated nanoparticle suspension in PBS using particle counts to determine relative nanoparticle concentration. The standard curve was used to determine the amount of nanoparticles passing through the membrane from suspensions in PBS.

6.3.7.4 Dialysis

Nanoparticle suspensions were diluted with release buffer to an equivalent sink concentration of teniposide (30 μ M) and a small volume (0.5 mL) was placed in a dialysis tube (regenerated cellulose, 12 KDa, 5mm). The tube was sealed at both ends and placed in release medium (50 mL) under constant stirring at room temperature (25 °C). Control samples of teniposide (30 μ M from 1000X DMSO stock) and empty nanoparticles supplemented with teniposide (30 μ M from the same DMSO stock) were used to determine diffusion kinetics of teniposide and account for interactions between nanoparticles and free drug in the donor compartment. Samples (1 mL) were taken at 1h, 2h, 3h, 4h, 7h, 8h, 24h, 48h and 72h. Sample volume (1 mL) was replaced with fresh media at 1,2,3,7 and 8h while full media exchange was performed at 4h, 24h and 48h. Samples were flash frozen with liquid nitrogen and stored at -20 °C until HPLC analysis. Before analysis thawing was performed at 37 °C and was followed by sonication for 1 minute.

6.3.8 Cell culture

NSC (10000 cells/well) and UW cells (5000 cells/well) were seeded in ultra-low attachment plates (200 μ L, neural stem cell media). The plates were centrifuged lightly at 100g for 3 minutes after seeding and the cells organised into one single spheroid per well within 24h.

Spheroids were photographed and sized using the settings and macro described in Chapter 3 on days 3, 5 and 7.

Freshly made nanoparticles were diluted (9:1) with PBS (10X) to form an isotonic nanosuspension. The theoretical teniposide equivalent of the initial nanoparticles suspension was estimated at 294 μ M before dilution and 265 μ M after dilution with PBS (2.4 mg/mL with approximately 8% loading). Actual concentrations were later measured spectrophotometrically and used to calculate equivalent teniposide exposure. Half-log dilutions (1 nM-30 μ M drug equivalents) of the nanosuspension were made in media in for both cell types in parallel to teniposide dilutions (1 nM-30 μ M) as well as controls with empty nanoparticles and media-only controls.

6.3.9 Data analysis

Results were analysed in Excel and Graphpad Prism version 6.0. All experiments were performed at least three times unless stated otherwise. Cumulative release was calculated from the concentrations of the samples, normalised to the highest value and plotted against time. Data were fit to first order release for comparison purposes and the 95% CIs for the time for 50% and rate constant compared after plotting. Dose-response curves were analysed as described in Chapters 3 and 4. The logIC₅₀ value determinations from the non-linear regression analysis along with the standard error of the logIC₅₀ for the nanoparticle formulations and teniposide were compared in Graphpad Prism for each cell population using a t-test with Welch's correction for unequal variance and P<0.05 was considered statistically significant.

Section 6.4 Polymer characteristics:

The chemical formulas of the polymers used in the screening programme are given in Figure 6-3

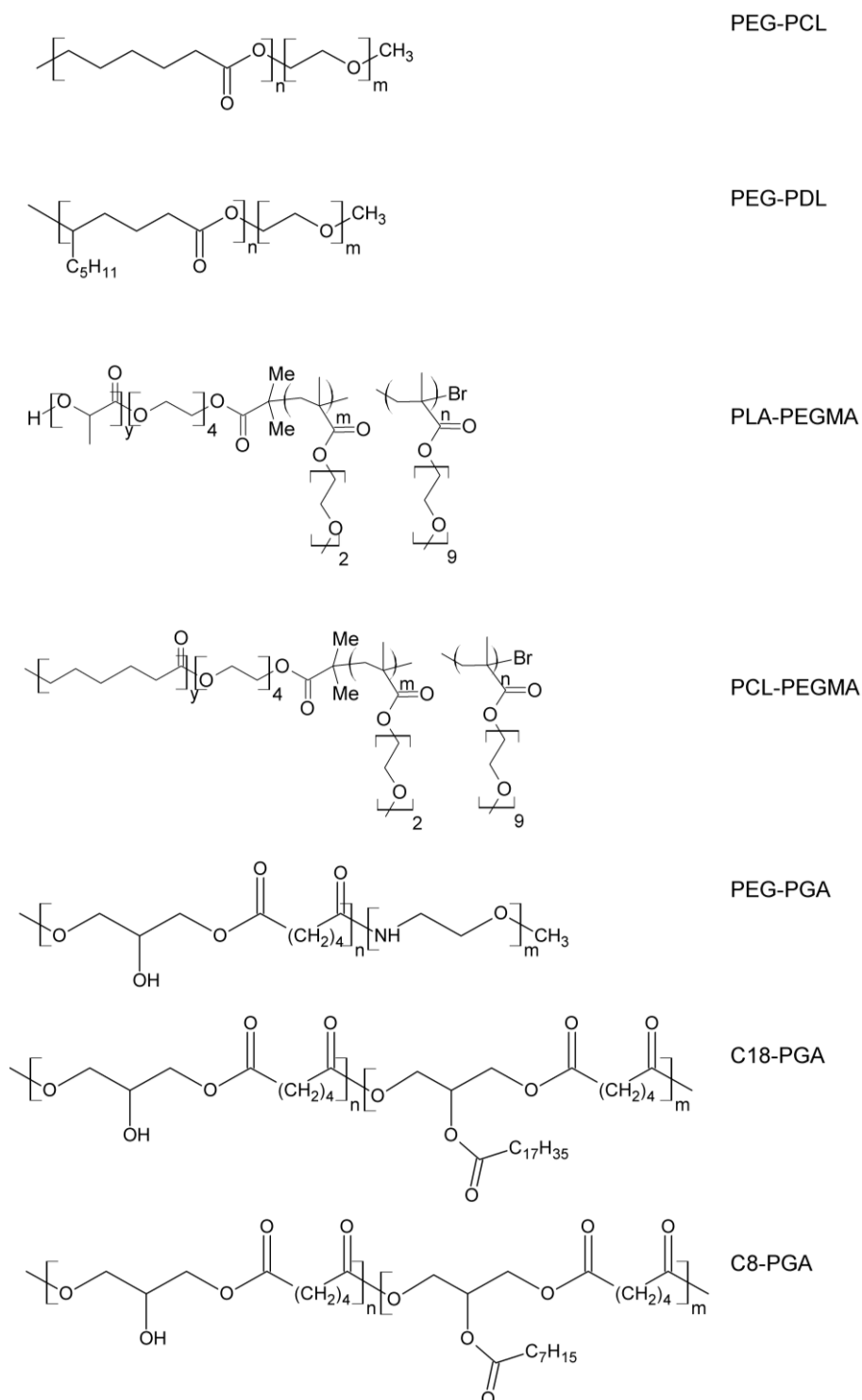


Figure 6-3. Chemical structures of polymers used in the nanoparticle screen

Poly(glycerol adipate) polymers were characterised as described in Chapter 5 using NMR and GPC. The PDL-PEG and PCL-PEG polymers were characterised by Kuldeep Bansal using NMR, GPC and Differential scanning calorimetry, while Lee Moir prepared and characterised the PLA-PEGMA and PCL-PEGMA polymers. The data is summarised in (Table 6-2):

Polymer	Mw	Core Mw	PEG(MA) Mw	Tg	Tm	LCST
			kDa		°C	
PEG-PCL	10	5	5	N/D	N/D	N/A
PEG-PDL	11	6	5	-55	55	N/A
PCL-PEGMA	27	15	12	N/D	N/D	40
PLA-PEGMA	20	12	8	N/D	N/D	48

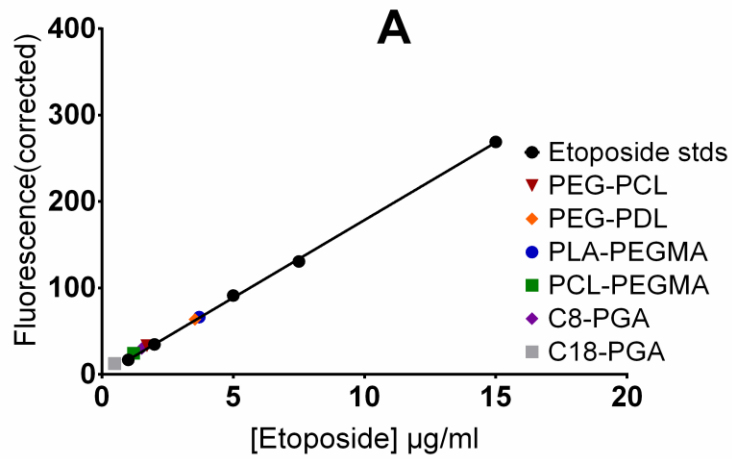
Table 6-2. Characteristics of polymers used in the screening program. Molecular weight was determined by NMR and is given in kilodaltons, kDa. Glass transition temperatures (Tg) and melting temperatures (Tm) were measure using DSC. The Lower critical solution temperature for the thermoresponsive (LCST) was only investigated in the PEGMA-based polymers.

The choice of polymers was made based on the analysis of Table 6-1 and the conclusion that block-copolymers incorporating a hydrophobic core and a hydrophilic corona have been reported to achieve higher loadings of etoposide and teniposide. Therefore block copolymers immediately available in the lab with a diverse set of chemistries were chosen in the search for formulations with higher drug loading.

Section 6.5 Drug loading results

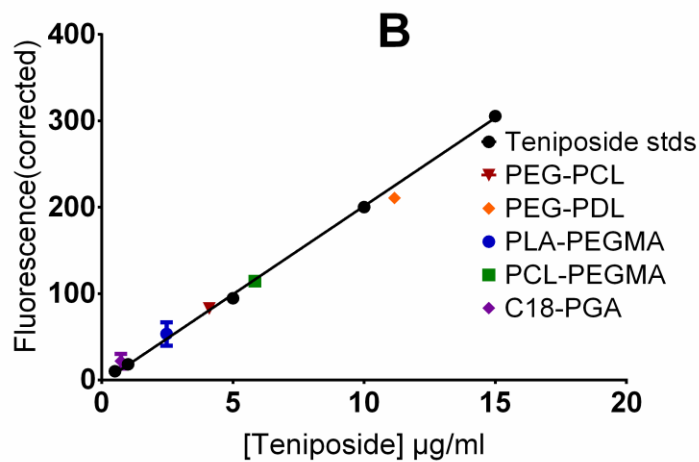
The drug content of nanoparticles was measured directly by dissolving them in DCM and DMSO (50:50). Since they were a mix of polymer and drug and in some cases surfactant, fluorescence spectrophotometry was initially chosen as the preferred method of drug loading measurement. However the absorbance of the etoposide and teniposide standards at higher concentrations was quenching the fluorescence signal and resulted in a hyperbolic shaped standard curve. To account for this "inner filter effect", fluorescence values were corrected using equation 6.3 in order to quantify nanoparticle loading as described in Lakowicz[461] (page56; Eq2.6):

$$Fl_{corrected} = Fl_{observed} \times 10^{\frac{OD_{excitation} + OD_{emission}}{2}} \quad \text{Equation 6-5}$$



$$Fl = 17.97 \times [Eto] - 1.13$$

$$r^2 = 0.9996$$



$$Fl = 20.41 \times [Teni] - 2.828$$

$$r^2 = 0.9994$$

Figure 6-4 Standard curves for teniposide and etoposide and spread of fluorescence values for encapsulated drug samples made using nanoprecipitation A-Etoposide; B-Teniposide

Figure 6-4 shows that there was a linear relationship between the corrected fluorescence values and the concentration of both drugs. The quantity of encapsulated etoposide was generally below 5 µg/mL for all formulations while teniposide levels were higher. The loading percentages

for the various formulations of etoposide and teniposide loaded nanoparticles prepared via nanoprecipitation are summarized in Figure 6-5.

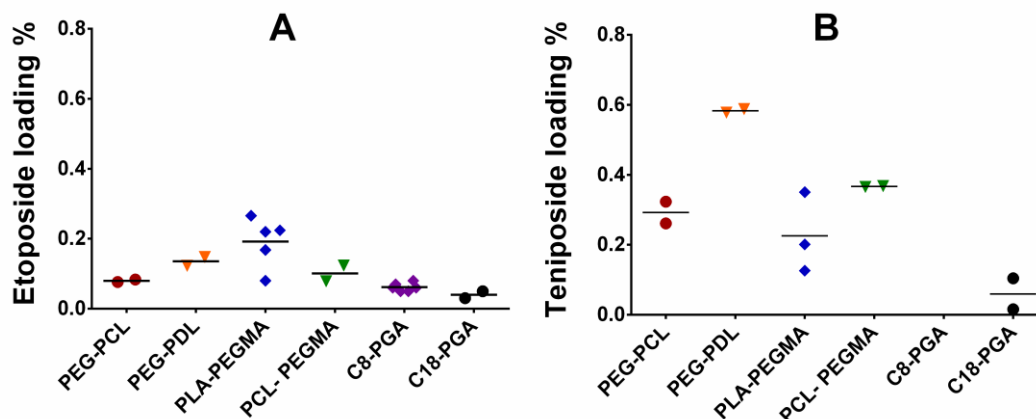


Figure 6-5 Drug loading percentages for nanoparticles made using nanoprecipitation. A- Etoposide; B-Teniposide; Dots represent separate individual experiments with at least three replicates per experiment

While etoposide loaded nanoparticles made using nanoprecipitation showed loading below 0.3%, the formulation of PEG-PDL and teniposide had nearly 0.6% w/w encapsulated drug. The PGA-based polymers showed a lower loading for etoposide compared to PLA-PEGMA. Results for C8-PGA and PEG-PGA and teniposide were not obtained due to excessive precipitation of particles $>1 \mu\text{m}$.

A screening program using solvent-emulsification was undertaken after nanoprecipitation did not achieve loadings above 1%. The initial plan was to prepare nanoemulsions without the use of surfactants and include surfactants only if there is significant phase separation and emulsion instability. However it was soon apparent that apart from PEG-PDL, PEG-PGA and to a certain extent C8-PGA all other polymers required the addition of surfactant. Despite forming relatively stable DCM/water emulsions, there was a considerable loss of nanoparticles prepared using C8-PGA without emulsifier when they were passed through a $0.45 \mu\text{m}$ filter indicating micro- instead of nanoparticle formation. The abovementioned polymers are all viscous liquids or semi-liquids and it could be hypothesized that their molecules are able to quickly assemble at the interface of the DCM droplets to form metastable emulsions. The

solid polymers PEG-PCL, PLA-PEGMA, PCL-PEGMA and C18-PGA required emulsifier in the aqueous phase to prevent phase separation. Moreover even after the use of emulsifiers the particles formed from C18-PGA would only pass through a filter with pore size above 1 μm . That is why this polymer was excluded from later screen with the solvent-emulsification method.

Several surfactants were identified based on literature reports of their effectiveness in solvent-emulsification, especially in relation to etoposide and teniposide. Polyvinyl alcohol is the most common surfactant generally employed in the solvent-emulsification method but it can be hard to remove completely[462] and has been reported to affect biocompatibility[463]. Sodium cholate is a natural bile salt emulsifier that has been employed in the production of nanoparticles already in clinical trials[449], [450]. Tocopherol polyethylene glycol 1000 succinate (TPGS) is a Vitamin E analogue used as a surfactant, solubiliser and even a drug carrier[464]. More importantly it has recently been reported to improve the drug loading and release profile from etoposide-loaded PLGA-PEG nanoparticles[391]. Pluronic F68 was also included on the basis of favourable studies reported for etoposide nanoparticles made via the solvent emulsification method[394], [399], [400], [402].

Surfactants, if used above the critical micelle concentration, may compete with the polymers for entrapping the drugs. Moreover the micelles would pass through the separation column along with the nanoparticles and artificially increase loadings. Therefore formulations of etoposide and teniposide without any polymer were prepared using the solvent-emulsification procedure with plain water as well as various surfactant solutions to identify possible contamination with drug nanoparticles and drug-loaded micelles.

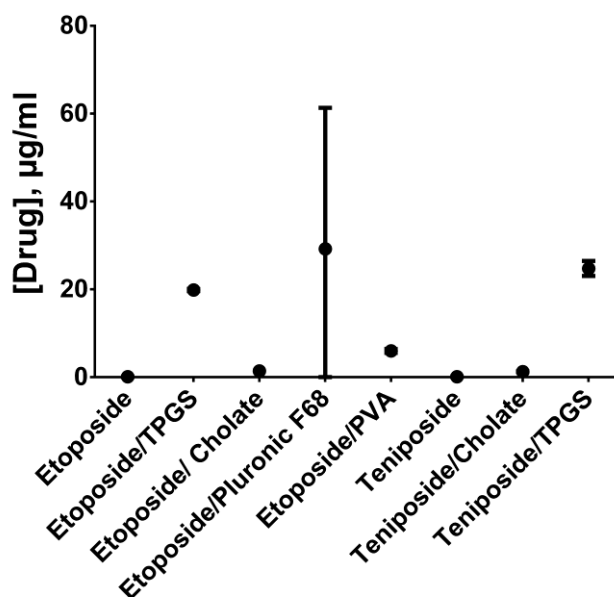


Figure 6-6 Concentration of drug passing through a Sephadex GH25 column (PD-10) after the solvent emulsification method. The drugs were dissolved in DCM without the addition of polymer. The aqueous phase contained either pure water, Sodium cholate (0.1%), TPGS(0.1%), Pluronic F68 (1%) or PVA(0.3%). Drug concentrations are determined using fluorescence spectrophotometry. None of the drug-free surfactants, with the exception of TPGS, showed a fluorescence signal. The fluorescence of drug-free TPGS was subtracted from the samples with drug to normalise signals.

Surfactant	Required emulsification concentration w/vol %	Reported critical micelle concentration w/vol%	Reference
Sodium cholate	0.1	0.2-0.4	[465]
TPGS	0.1	0.02	[466]
Pluronic F68	1	0.03	[467]
PVA	0.3	N/A	

Table 6-3 Concentrations used to form nanoemulsions and reported critical micelle concentration for the excipients used

Etoposide and Teniposide dissolved completely in the aqueous phase during the solvent-emulsification method. However, the solutions were oversaturated and within less than an hour large visible needle-like crystals of both drugs appeared. To test for the presence and possible contamination of pure drug nanoparticles, the supersaturated solutions were loaded in a PD-10 column as soon as they were prepared and the amount of etoposide and teniposide passing through quantified. As shown in Figure 6-6, there was no etoposide or teniposide contamination in the volume fractions normally collected for nanoparticles. When sodium cholate was used at levels (0.1% w/vol a value below the CMC, Table 6-3) it stabilised the oversaturated solutions but that did not result in etoposide or teniposide appearing in the nanoparticle fraction. The fluorescence signal emitted from TPGS and its absorbance in the UV range

made quantifying the amount of etoposide and teniposide less reliable. The quantities for those samples have been derived by subtracting the signal of pure TPGS. Nevertheless, direct methods using fluorescence and absorbance spectrophotometry would not be suitable to quantify TPGS containing nanoparticles without prior purification or chromatographic separation via HPLC for example. Both PVA (0.3%) and Pluronic F68 (1%) required higher concentrations than sodium cholate (0.1%) in order to emulsify the DCM/water mixture. In contrast to sodium cholate, the drug-loaded samples prepared with Pluronic F68 and PVA resulted in drugs passing through the gel column in the nanoparticle volume fraction. Additionally, sodium cholate was superior to all other emulsifiers in terms of preventing phase separation when polymers were introduced in the DCM phase. The combination of superior emulsification properties along with compatibility with drug separation procedures made sodium cholate the surfactant of choice in the next experiments.

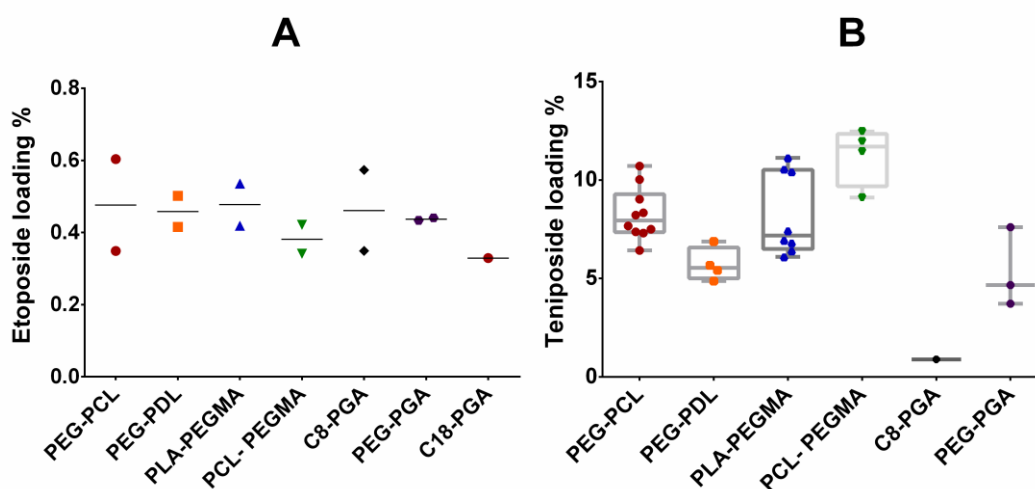


Figure 6-7 Drug loading results for nanoparticles made with the solvent-emulsification method. PEG-PDL and PEG-PGA did not require surfactant while 0.1% sodium cholate in the aqueous phase was used for all other polymers. A-etoposide B-teniposide; Dots represent separate individual experiments with three replicates in each. Notice the difference in scale between the two graphs.

Figure 6-7 shows the drug loading percentages achieved using the solvent emulsification procedure. Compared to nanoprecipitation (Figure 6-5), the process employing DCM achieved higher loadings with both drugs. While the drug loadings for etoposide were generally below 1%, the more hydrophobic and less water-soluble drug teniposide had loadings above

5% in the majority of nanoparticle formulations. In contrast to the relatively similar drug encapsulation for etoposide the formulations with teniposide differed in the amount of entrapped drug. The formulations with PEG-PDL and PEG-PGA were made without the use of surfactant. In order to compare the results for teniposide the data was tested for normal distribution. In the experiments which were repeated the most (PEG-PCL and PLA-PEGMA) the Prism's D'Agostino & Pearson omnibus normality test K2 and the Kolmogorov-Smirnov test were used. The drug loading determinations for those two formulations passed both normality tests and a one-way ANOVA analysis using Holm-Sidak's multiple comparison's correction[468] was used to check for statistical differences between the formulations. The drug loadings for PEG-PCL, PEG-PDL, PLA-PEGMA and PEG-PGA clustered together and were found to have no statistically significant differences in the percentage of encapsulated teniposide. The PCL-PEGMA formulation exhibited statistically significant higher loadings compared to all other nanoparticle formulations and the delivery system with C8-PGA had the lowest entrapment percentage.

The present studies have found much lower drug incorporation percentages for etoposide compared to the amounts reported in the literature. For example Mohanty et al.[387] have claimed an impressive loading of 60% with 68% encapsulation efficiency in the abstract of their paper for PEG-PCL micelles. A more careful examination of the manuscript reveals lower values increasing from 0.5% to 25% as more etoposide was added to the micelles. The amount of aqueous phase to form the micelles in their procedure has not been disclosed and a drug-only control to validate complete wash-out of free drug from the micelles has not been mentioned. Not surprisingly in this case, the encapsulation efficiency rose along with increasing the amounts of etoposide whereas it is more commonly found that encapsulation efficiency decreases with increasing drug concentration. The work presented here has aimed to exclude free drug contamination in the drug delivery system by employing size exclusion chromatography and validating the lack of free drug as shown in Figure 6-6. Therefore the low etoposide loadings are explained with more thorough removal of unencapsulated drug.

Particle size was investigated using dynamic light scattering (DLS) and the results are summarized in Figure 6-8 and Table 6-4. PEG-PCL formed the smallest particles which were composed of a single population with radius of around 30nm. Similarly to most other formulations the PEG-PCL particles did not significantly change in size after drug loading, as determined by ANOVA, followed by the Sidak test. On the other hand, PEG-PDL nanoparticles had a statistically significant shift in size from 56 to 88nm after loading with teniposide.

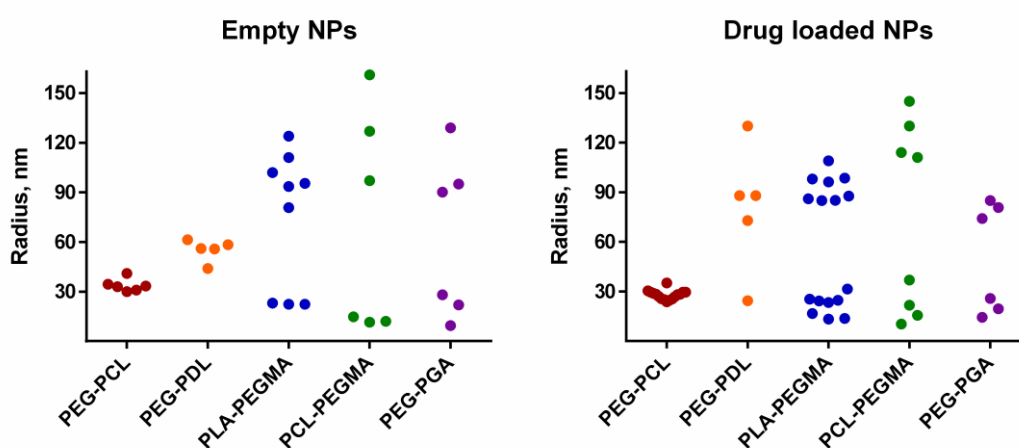


Figure 6-8. Radii of empty and teniposide-loaded nanoparticles determined by DLS. Dots represent mean peak radii for the main populations determined by DLS intensity measurements in individual independent experiments. PEG-PDL and PEG-PCL had a monomodal distribution of particle size. PLA-PEGMA, PCL-PEGMA and PEG-PGA showed two populations, a smaller population around 20nm and a larger population around 100nm.

Polymer	Empty NPs Radius, nm	Drug loaded NPs Radius, nm	Empty NPs CV%	Drug loaded NPs CV%
PEG-PCL	33	28	12	10
PEG-PDL	56	88	12	26
PLA-PEGMA	99 and 22	92 and 24	15 and 2	9 and 29
PCL-PEGMA	127 and 12	122 and 19	25 and 55	13 and 55
PEG-PGA	95 and 22	81 and 20	20 and 48	7 and 30

Table 6-4 Median sizes of empty and drug-loaded nanoparticles along with the coefficient of variation for each population.

The DLS results from Figure 6-8 suggest that the PLA-PEGMA, PCL-PEGMA and PEG-PGA nanoparticles have a bimodal distribution. Dynamic light scattering has a number of limitations when it comes to the analysis of polydisperse populations[469]. The intensity (I) of scattered light using the Rayleigh approximation is proportional to the sixth power of the

radius (r^6) which leads to overestimations in the percentage of large particles by intensity measurements. Since mass and number mathematical transformations are only accurate below 50 nm and without prior knowledge of the refractive index of the nanoparticles it was hard to elucidate what the real proportions of both populations were[268].

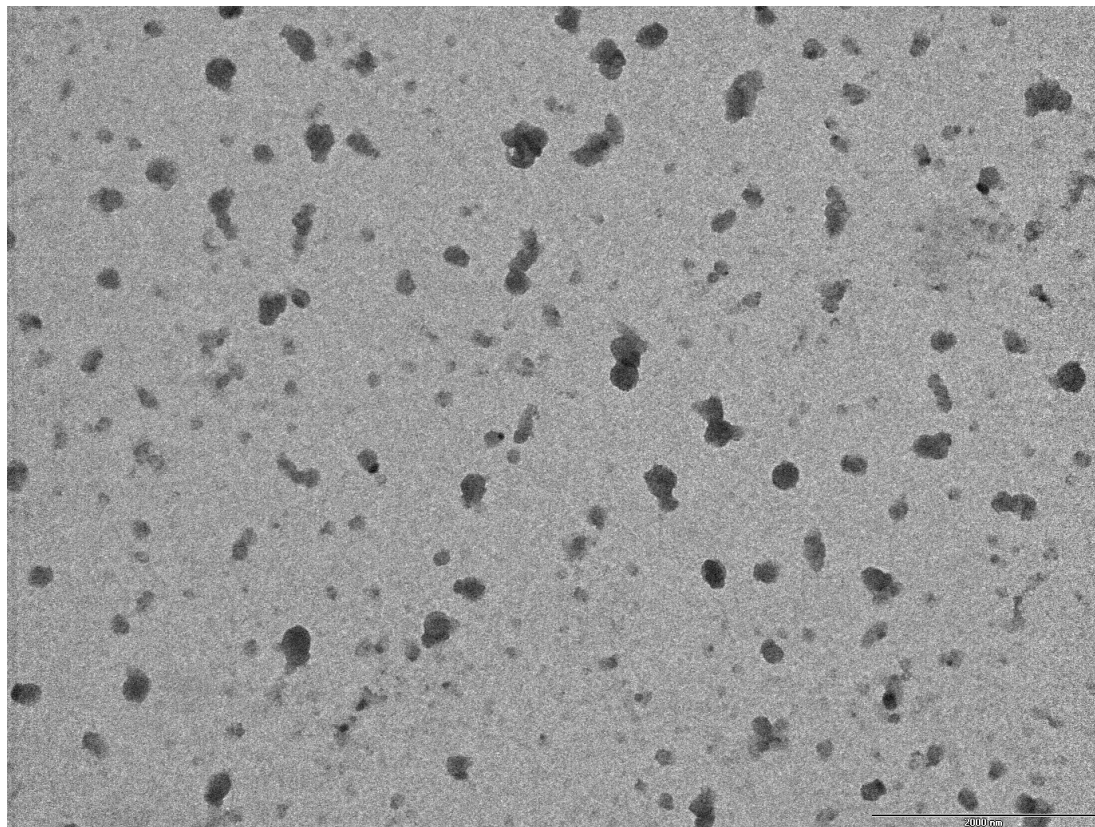


Figure 6-9 TEM image of PLA-PEGMA nanoparticles (courtesy of Lee Moir). Scale bar is 5000nm

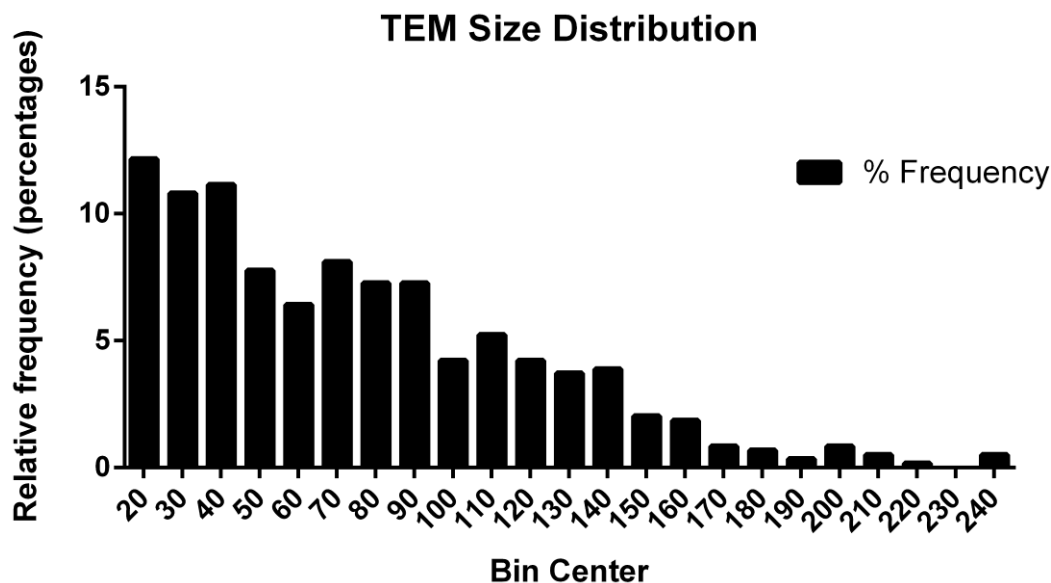


Figure 6-10. PLA-PEGMA nanoparticle size distribution after image analysis using TEM. Size is given as particle radius in nm.

Electron microscopy imaging (Figure 6-9) of the PLA-PEGMA nanoparticles revealed that there was a broad distribution of particles sizes ranging from 20 nm to 140 nm (Figure 6-10), which is probably due to the inherent limitations of the emulsification process using probe sonicators. Some aggregation was also visible but that could have been due to concentration artefacts in sample preparation. Similar pictures were seen for the teniposide loaded formulations as well (Figure 6-11).

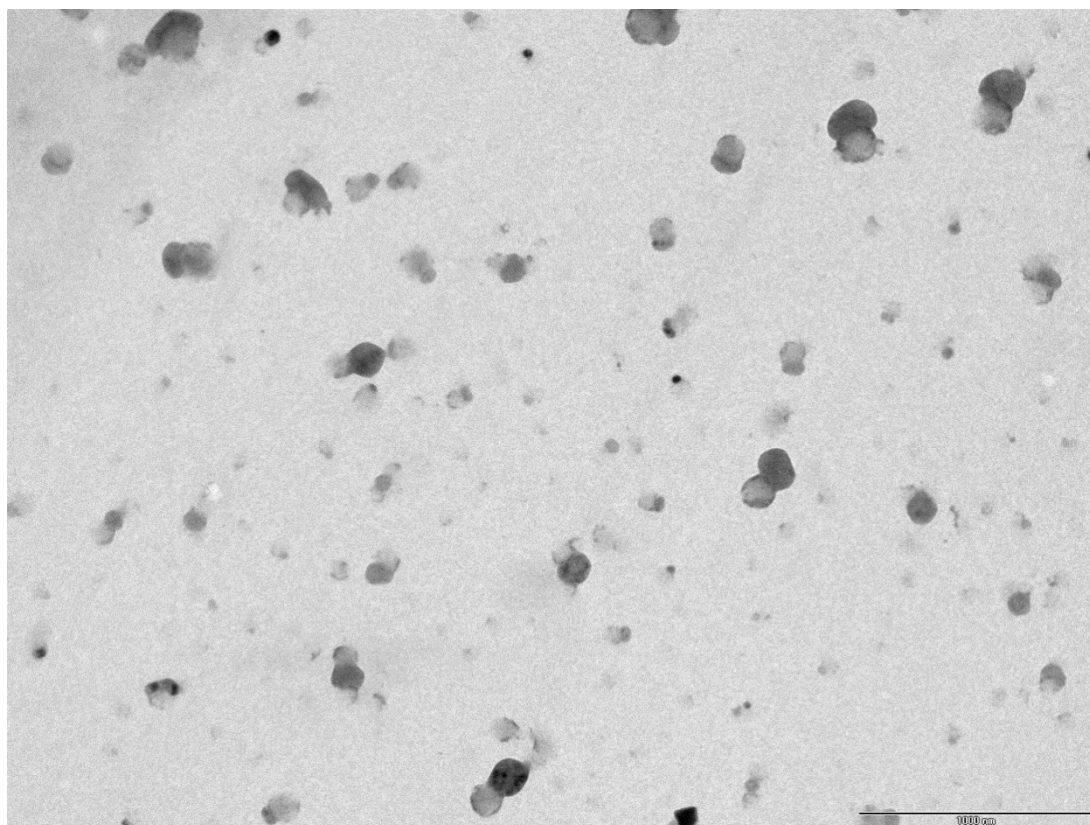


Figure 6-11 TEM pictures of teniposide-loaded PLA-PEGMA nanoparticles (courtesy of Lee Moir). Scale bar is 1000nm

The presence of small nanoparticles with radii of around 20 nm (Figure 6-11) may be considered disadvantageous for a drug delivery system aiming for sustained release. As the rate of drug release is inversely related to particle size, small nanoparticles may contribute to a significant burst release.

In this respect, the next step in characterising the nanoparticles was to determine the drug release profile in a series of experiments.

Section 6.6 Release experiments

In order to investigate the solubility of teniposide in PBS and PBS with added surfactants (1% Sodium cholate or Polysorbate 80), drug solutions were prepared in PBS from thousand-fold stock solution in DMSO (Table 6-5). The absorbance spectra of the resultant solution ($\lambda < 300\text{nm}$) and the appearance of cloudiness were used to determine the solubility of teniposide in the different media. The observed kinetic solubility would be higher than the true thermodynamic solubility as metastable oversaturated solutions are often formed[470].

Media	Kinetic solubility	Change after 24h
PBS	100 μ M	30 μ M
PBS+1% Cholate	250 μ M	None even at 200 μ M
PBS+ 1% Tween	300 μ M	Interference in UV and FI

Table 6-5. Kinetic solubility of teniposide in different release media. Solubility was determined from 1000X stocks in DMSO. Changes in solutions were monitored with UV absorbance and Fluorescence

The solubility of teniposide (Figure 6-12) was found to be 10 μ M in PBS as 30 μ M solutions left for 24h experienced a decrease in fluorescence and absorbance if left undisturbed in the dark at room temperature (25°C).

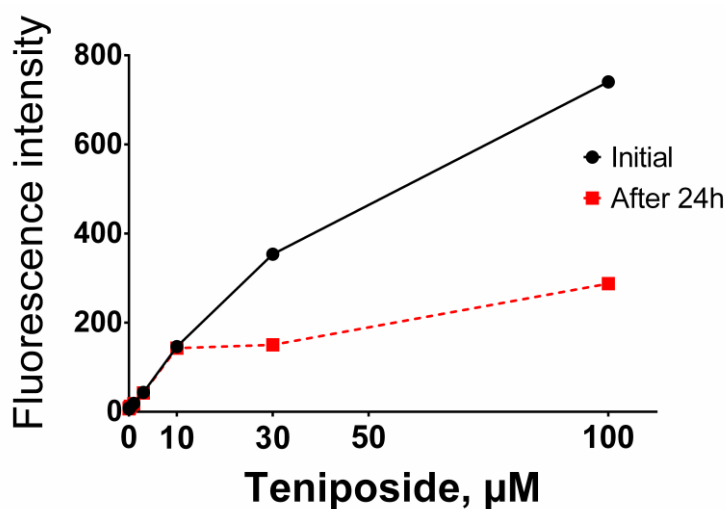


Figure 6-12 Teniposide stability in PBS immediately after dilution from DMSO stock and after 24h. Stability was quantified using fluorescence measurements. Note the hyperbolic shape of the standards due to the inner filter effect and light scattering for the 100 μ M concentration

Sodium cholate and Tween were used to solubilise teniposide and direct spectrophotometric measurements were examined for their suitability to detect the drug during the release experiments (Figure 6-13).

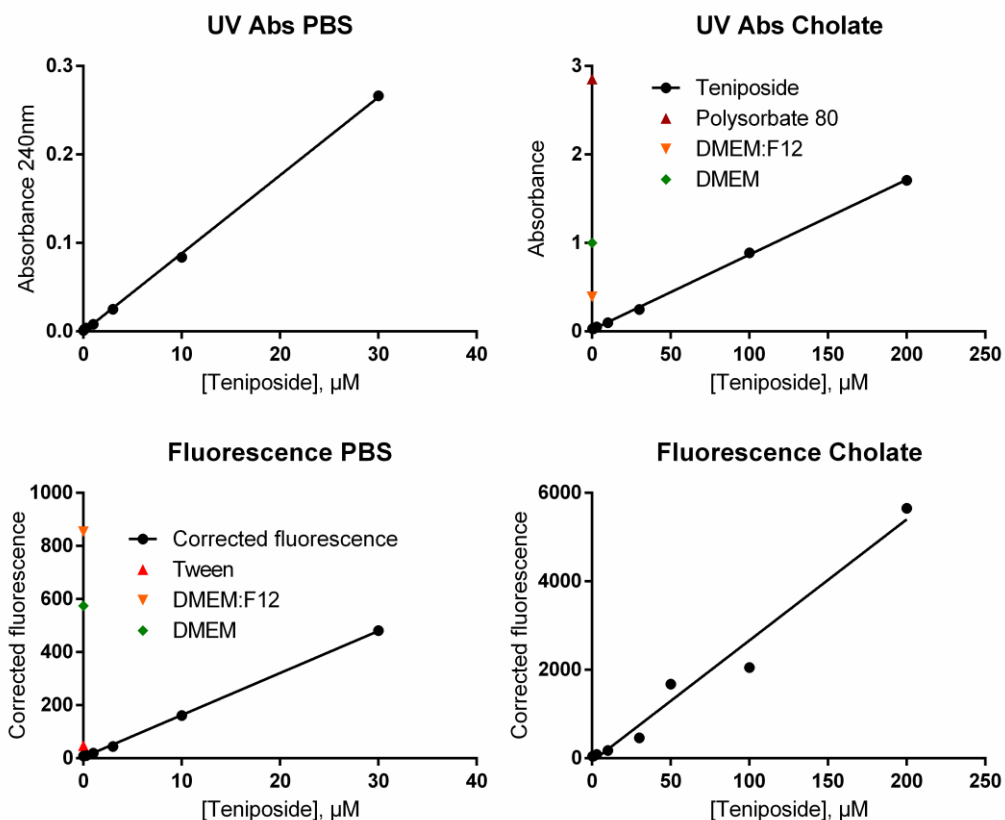


Figure 6-13 Standard curves for teniposide in PBS and PBS with 1% cholate. UV Absorbance and Fluorescence were compared for their suitability to determine Teniposide in solutions of PBS and PBS cholate. Fluorescence measurements were corrected for the inner filter effect according to Eq. 6.3 In addition the absorbance and fluorescence of Polysorbate 80, DMEM and a mixture of DMEM:F12 were assessed for applicability to be used as release media.

Parameter	UV PBS	UV Cholate	Fl. PBS	Fl. Cholate
Slope	0.0088	0.0085	15.84	27
Intercept	-6.73E-06	0.021	4.4	-72
R ²	0.9995	0.9994	0.9996	0.973
SD Intercept	0.0009	0.0076	1.46	150.9
LOQ, μM	0.3	3.0	0.3	18
LOD, μM	1.0	9.0	0.9	55

Table 6-6. Linear regression fit parameters for the standard curves from Figure 6.8. Limit of quantitation(LOQ) and limit of detection(LOD) were determined from the standard deviation of the y-intercept and the regression slope using Eq 6.4 and 6.5[460].

Sodium cholate was compatible with the determination of teniposide with both fluorescence and UV absorbance. In contrast, Polysorbate 80, and the culture media mixtures DMEM and DMEM-F12 interfered with both

types of measurement and were excluded from further screening. The linear regression parameters and the limits of quantitation and detection for the four standards curves are shown in Table 6-6. Although sodium cholate had negligible absorbance at 284 nm and was able to solubilise teniposide, the sensitivity of the spectrophotometric determinations was adversely affected. The 10 times increase in solubility was offset by a similar increase in the limit of quantitation for UV and an even larger deterioration for the fluorimetric determination. This necessitated the utilisation of HPLC in the determination of teniposide release from the nanoparticles.

The HPLC method for teniposide determination was assessed for linearity, accuracy, precision, and robustness.

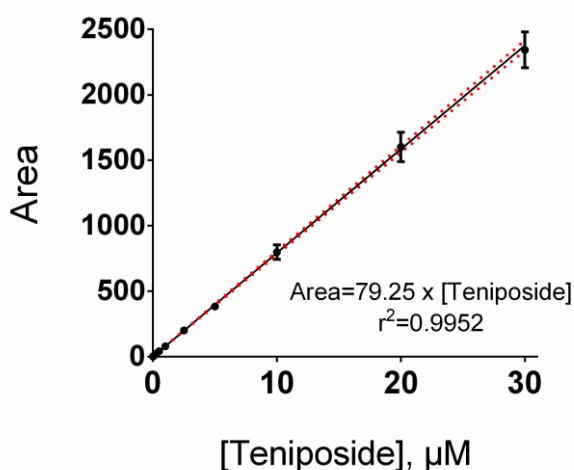


Figure 6-14. Linearity of Teniposide determination using HPLC. Red dots show the 95% confidence intervals for the linear regression

The method for teniposide determination was linear from 25 nM to 30 μM with $r^2=0.9952$ as seen in Figure 6-14. The LOD was 10 nM and the LOQ 25 nM as determined from the signal to noise levels. The representative chromatograms in Figure 6-15 show the specificity and accuracy of the method in the conditions tested. The drug peak was well resolved from the other components in the release media and it appeared as a single peak for the pure and released drug alike.

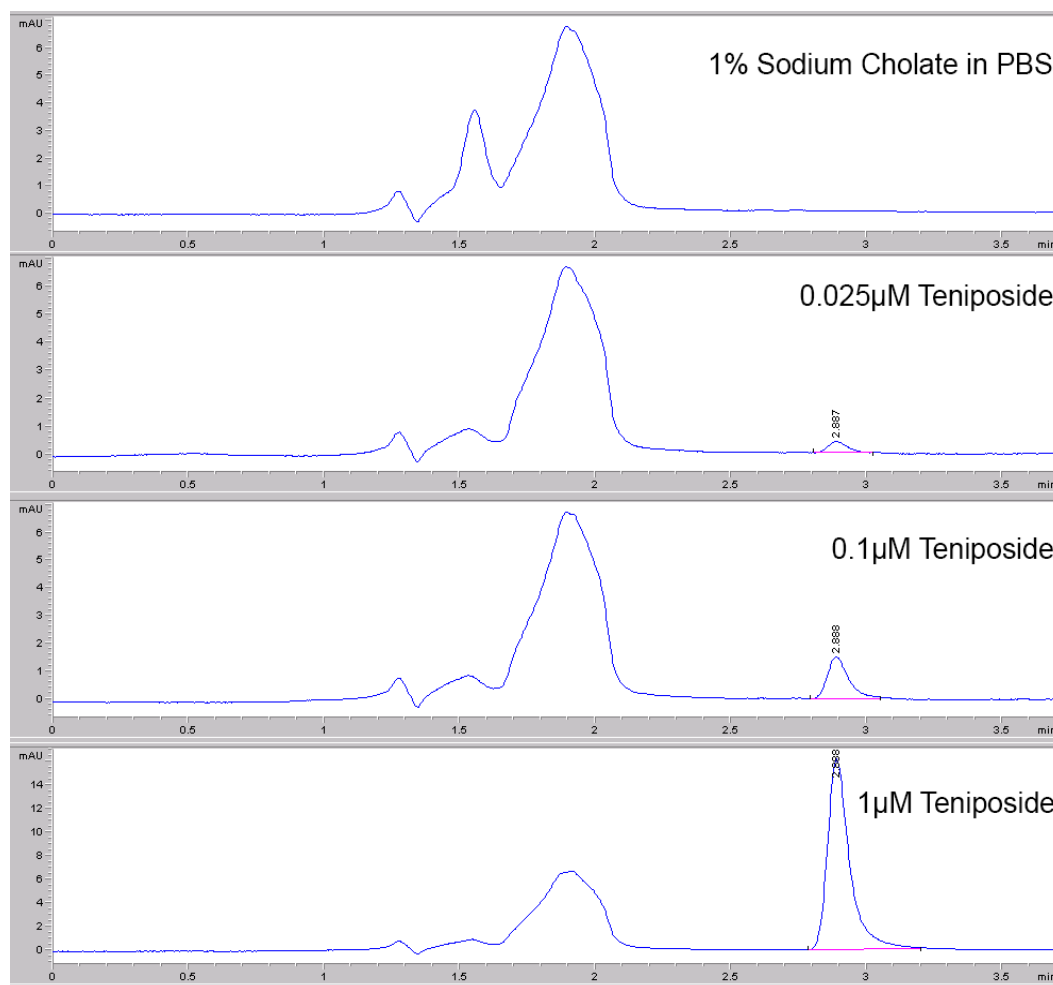


Figure 6-15 Representative chromatograms of blank release media solution and teniposide standards. Retention time of teniposide was 2.9 minutes and it appeared as a single peak well resolved from the polar sodium cholate peak at 1-2 minutes

The intra-assay variation was below 1% for all drug levels and the interexperimental repeatability was assessed using the coefficient of variation for six concentrations on six independent sets of standards on different days (Table 6-7). CV was below 15% for all tested concentrations.

[Teniposide], μM	Area	CV%
0.025	2	9
0.05	4	11
0.1	8	6
1	78	9
10	798	7
20	1601	7

Table 6-7. Inter-assay precision for 6 levels of teniposide measured in six independent experiments

The robustness of the method to measure teniposide and the stability of samples after freezing and thawing is illustrated in Figure 6-16.

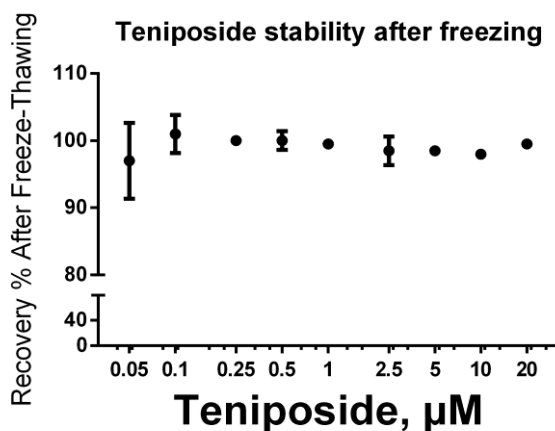


Figure 6-16 Teniposide HPLC assay robustness: Recovery of teniposide after freeze-thawing

Overall, the HPLC determination of teniposide satisfied all acceptance criteria and was suitable for the determination of teniposide in the release medium of PBS with 1% sodium cholate under the conditions of the assay.

Centrifugal ultrafiltration was compared to dialysis for its ability to measure the kinetics of teniposide release from drug loaded nanoparticles. However, the hydrophobic teniposide exhibited non-specific binding to the membrane (both polyethersulfone and regenerated cellulose) of the filtration devices and was not detectable in the filtrates. Non-specific binding was circumvented by preloading the membrane with excess of sodium cholate by passing a 10% sodium cholate solution through the devices[471]. The centrifugal device was then run twice (0.5mL each time) with the sample of interest and only the second filtrate measured. The recovery of teniposide after this procedure was 80% as illustrated in Figure 6-17. After validating that the drug can be recovered from the devices, the passage of nanoparticles was quantified using the number of counts from dynamic light scattering as a proxy for nanoparticle concentration[430] (Figure 6-18).

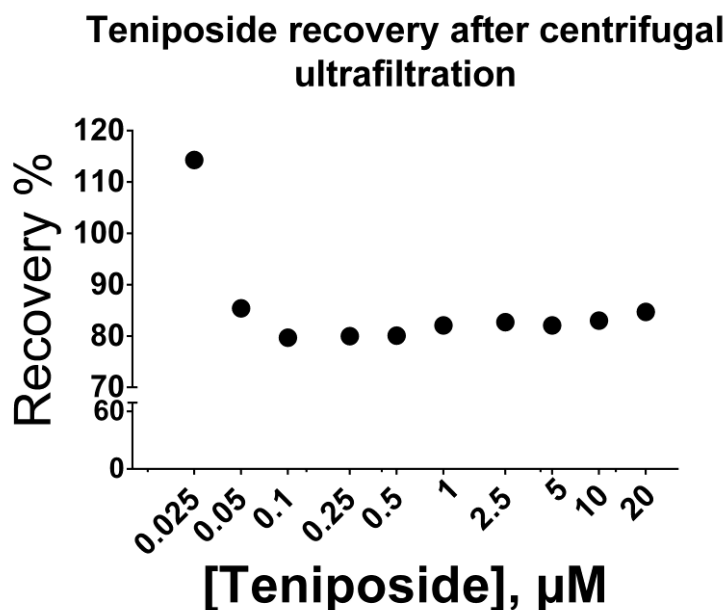


Figure 6-17 Recovery of teniposide after passage through centrifugal ultrafiltrators

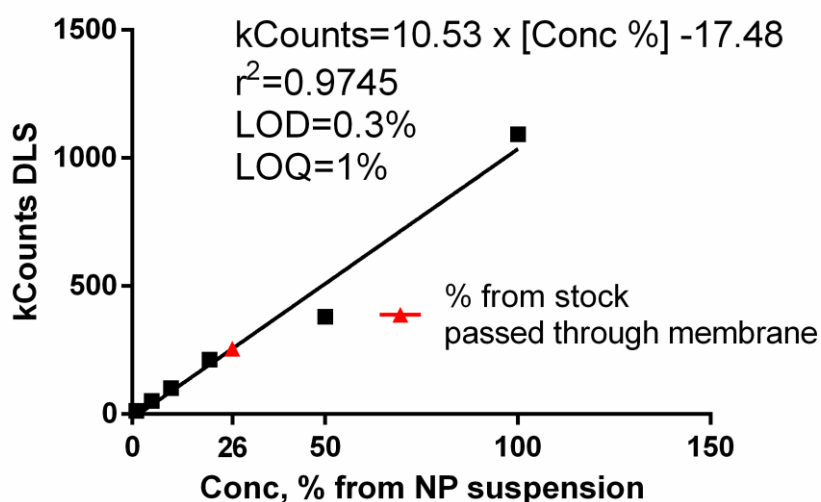


Figure 6-18 Quantitation of amount of PEG-PCL nanoparticles passing through the Nanosep 300kDa ultrafiltration device

About 25% of the PEG-PCL micelles were able to pass through the Nanosep polyethersulfone 300 kDa (35nm) membrane despite their 60nm diameter[472][473]. The same was true for the Amicon 100 kDa and Nanosep 30 kDa membranes.

In an effort to limit nanoparticle penetration in the filtrate Amicon 10 kDa membrane devices were employed for the release studies. The drug loaded nanoparticles were suspended in release media in a concentration equivalent to 20 μM in order to maintain sink conditions and samples at

different time points were filtered through the filtration devices. Although the percentage of nanoparticles passing through was easy to quantify in PBS, the presence in sub-nanometre cholate micelles in the release media resulted in a noisy background limiting assay precision.

Sample	Before filt.	After filt.	Passing	minus cholate
(name)	(kCounts)	(KCounts)	(%)	(%)
AST 13	456.5	73.8	16	2
AST 14	277.2	72.2	26	3
AST 15	291.9	121.5	42	25

Table 6-8 Presence of nanoparticles in the filtrate of nanoparticle release samples after passing through Amicon 10 KDa filtration devices. Sodium cholate gave 66, 000 Counts which limited the ability to accurately quantify the amount of nanoparticles in the filtrate. AST13-15 are PEG-PCL nanoparticle release samples from three independent batches of teniposide-loaded nanoparticles

As shown in Table 6-8, switching to a membrane with lower Mw cut-off did not completely eliminate nanoparticle contamination. Depending on whether sodium cholate counts are subtracted different percentages of NP contamination could be calculated. The samples before and after filtration were analysed for teniposide content and the results are summarised in Table 6-9.

Sample	Unfiltered	Filtrate	Recovery
(name)	(peak area)	(peak area)	(%)
AST 13	26.3	21	80
AST 14	16.2	12	74
AST 15	20.4	15.7	77

Table 6-9. Teniposide release from PEG-PCL micelles as measured by Amicon 10kDa ultrafiltration devices 1h after start of experiment.

Since the recovery of free teniposide in the filtration devices is 80% the actual release can be quantified by dividing the values in the last column in Table 6-9 by 0.8 and subtracting the % of nanoparticles passing through the membrane. The release % results using the raw DLS values and the values after subtracting the background cholate are given in Table 6-10.

Sample	% Release	% Release
	w/o background corr.	with background corr.
AST13	84	98
AST14	66.5	89.5
AST15	54.25	71.25

Table 6-10 Teniposide release from PEG-PCI micelles after correction for teniposide recovery and including the percentage of nanoparticles passing through the membrane as per Table 6.8. Incubation time was 1h in 1%-PBS cholate release media.

Despite the issues with nanoparticles passing through the filters and cholate interference, approximate values for the release from teniposide loaded PEG-PCI nanoparticles were calculated. There appears to be a significant proportion of burst release, anywhere between 50 and 90%, of teniposide upon nanoparticle dilution according to the results from centrifugal ultrafiltration.

In addition to the filtration setup, drug release experiments with dialysis, were undertaken at the same time in order to compare the results from both methods. Nanoparticle suspension samples equivalent to 30 μ M teniposide were placed in the dialysis tubes thereby maintaining sink conditions in the donor compartment as well as the acceptor one throughout the experiment. A control for the release of free teniposide was included to assay the rate of diffusion of teniposide through the membrane. The extra control containing empty nanoparticles and a solution of teniposide was employed to account for the interaction between released drug and the nanoparticles during release. As seen in Figure 6-19 the release profile of teniposide-spiked nanoparticles looks quite similar to the release profiles for the drug-loaded systems. If the process is modelled as being first-order kinetics the confidence intervals of the time for 50% release and rate constant can be compared. Figure 6-20 illustrates that although all drug loaded nanoparticle formulations exhibited slower release than the diffusion of teniposide out of the dialysis bag, the change in the release profile was due to interaction between the nanoparticles and the released drug. The release from those nanoparticles

systems was either slightly faster (PCL-PEG) or equal (PLA-PEGMA) to the profile of release of the spiked nanoparticle sample.

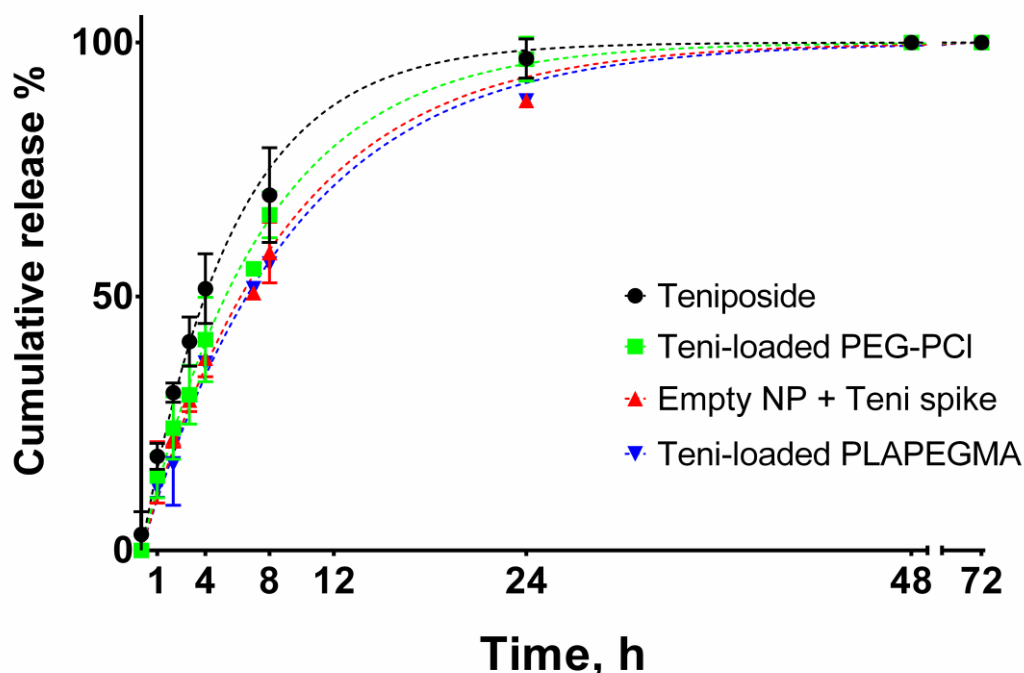


Figure 6-19 Release from teniposide-loaded nanoparticles of PEG-PCL and PLA-PEGMA as determined by dialysis experiments. Black dots- free teniposide, Green squares-Teniposide loaded PEG-PCI nanoparticles, Red triangles-Empty nanoparticle plus teniposide control; Blue triangles- PLA-PEGMA nanoparticles.

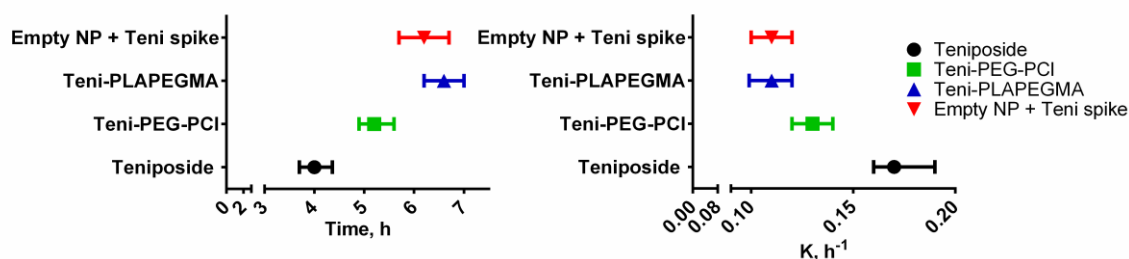


Figure 6-20 Confidence intervals for the release half-time and time constant for teniposide, PEG-PCI, PLA-PEGMA nanoparticle and spiked nanoparticles. Left panel- 95CIs for time for 50% teniposide release; Right panel-CIs of the rate constants if the process was first-order

The limitations of the dialysis method to properly resolve the release profile of nanosized systems[428], [429] have once again been confirmed. Nevertheless the similarity between the rate of release between the drug-loaded and the drug-spiked nanoparticles implies a near-complete release in the first hours of the experiment. In order to maintain detectable levels of teniposide the release media contained 1%

sodium cholate. However during the cell culture studies the nanoparticles will be suspended in serum-free media and *in vivo* they will distribute in the brain interstitium and the CSF where sodium cholate won't be present to solubilise the drug. Therefore the release profile determined here can only serve as a proxy and may significantly under- or overestimate the rate of release from the nanoparticles. The true *in vitro* benchmark would be exposing the 3D cell culture models of medulloblastoma to the nanoparticle formulations and comparing the effects.

Section 6.7 Nanoparticles in single spheroid cultures of foetal neurospheres and UW medulloblastoma

The toxicity of the empty nanoparticles was assessed in three-dimensional separate spheroid cultures of UW medulloblastoma and normal human neurospheres by using volume and metabolic activity. Figure 6-21 shows that most carrier formulations were not toxic up to concentrations of 300 µg/mL when applied for 48h followed by a 48h wash-out period. Among the polymers PEG-PDL appears to slightly lower the cell viability at high concentrations but cell health never falls below 75%. PEG-PGA on the other hand exhibited more pronounced effects as it aggregated in the media at high concentrations and formed microscopic droplets close to the spheroid surface. Both normal and tumour cells exhibited similar sensitivity towards the formulations. Moreover, nanoparticles prepared with surfactant (PLA-PEGMA, PCL-PEG, PCL-PEGMA) were equally non-toxic to those prepared without surfactant (PDL-PEG, PEG-PGA). Thus none of these factors seemed to affect adversely the toxicity of the empty nanoparticles.

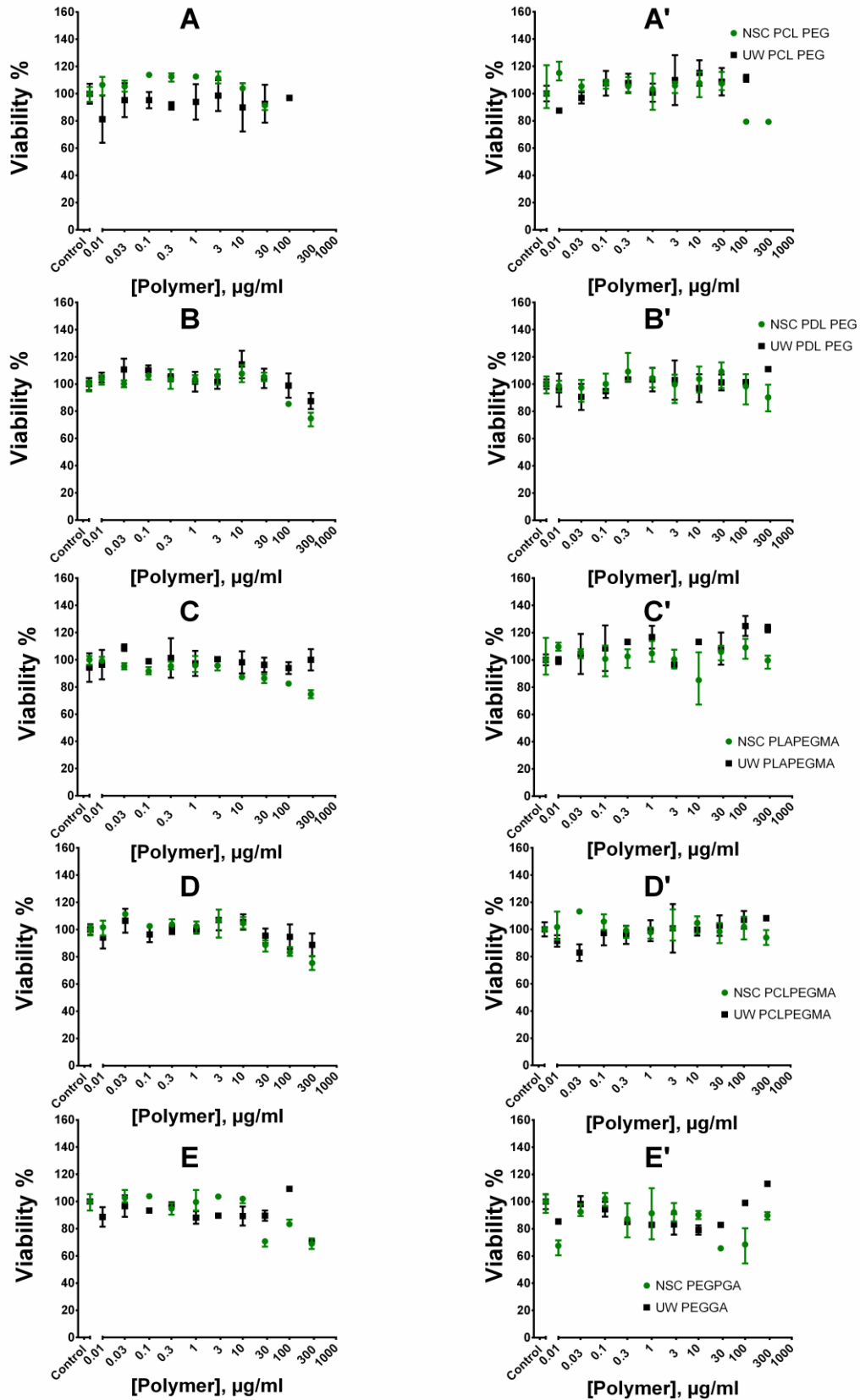


Figure 6-21 In vitro toxicity of empty nanoparticle carrier formulations. Green-normal neural stem cells; Black-UW228-3 medulloblastoma; A,A'-PCLPEG; B,B'-PDLPEG; C,C'-PLAPEGMA; D,D'-PCLPEGMA, E,E'-PEGPGA; A-E- using volume measurements. A'-E'- using metabolic activity

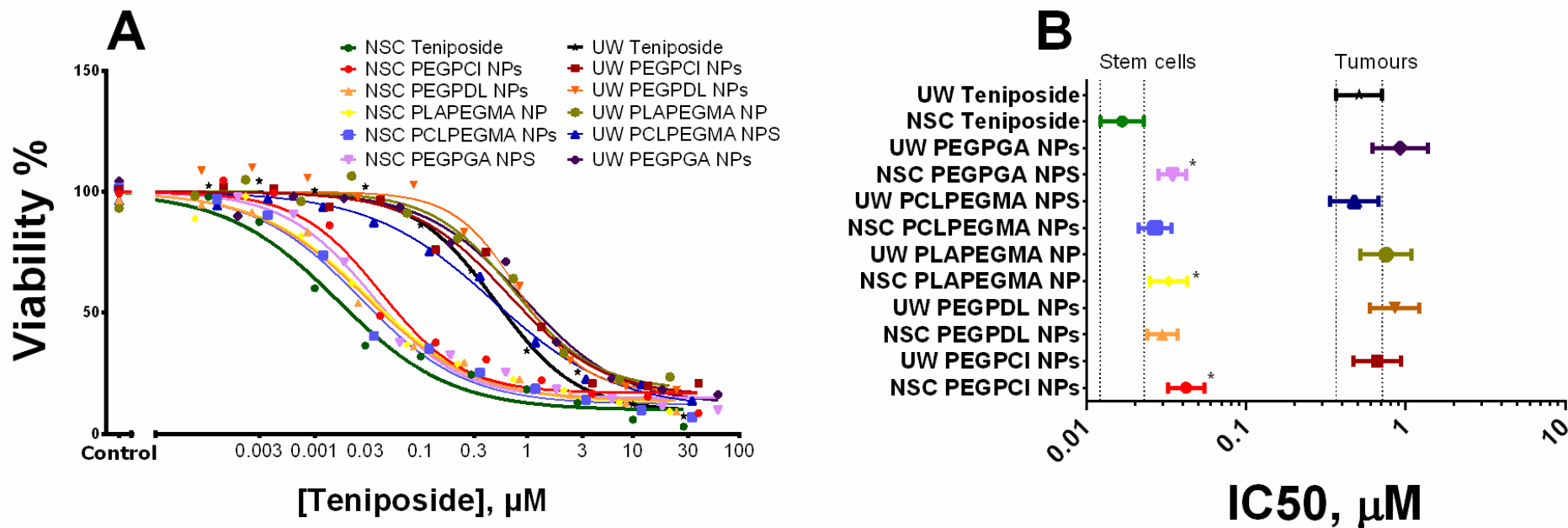


Figure 6-22. Preliminary screen of teniposide-loaded nanoparticles using spheroid Volume reduction as surrogate measure of viability. Comparison of dose-response curves with free teniposide for both neural stem cells and UW medulloblastoma cells. A- dose response curves. B- 95% CIs for the IC50 determinations.

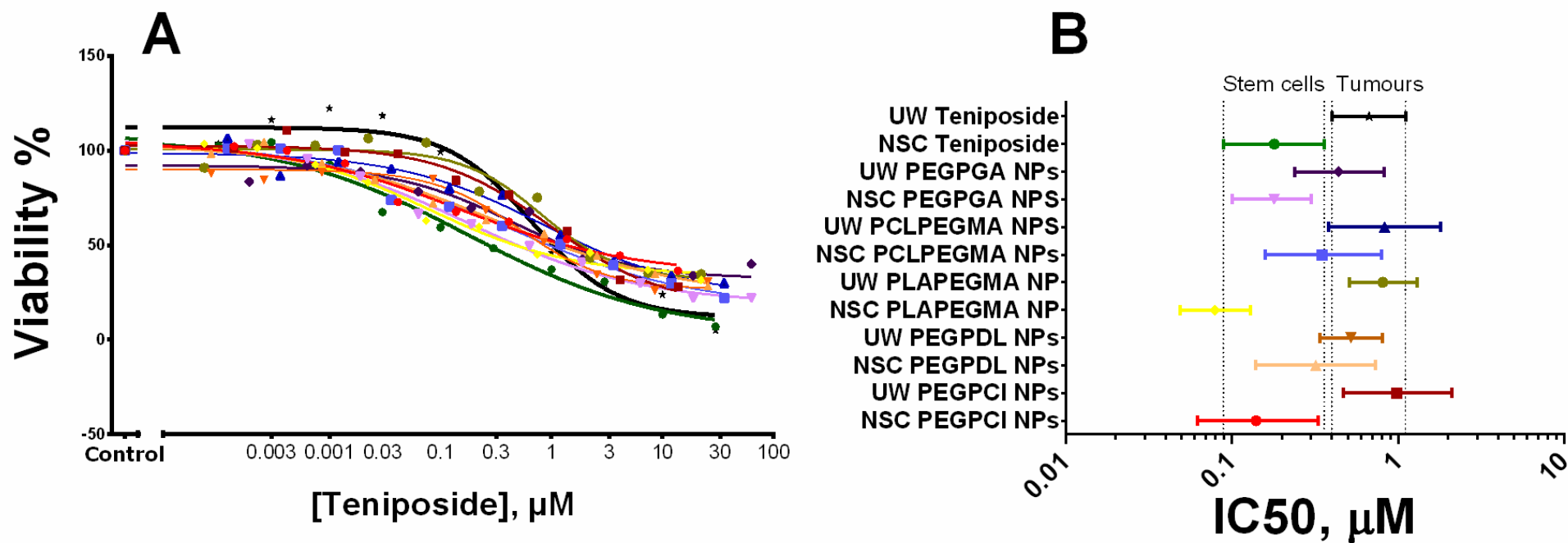


Figure 6-23. Preliminary screen of teniposide-loaded nanoparticles using resazurin reduction as surrogate measure of viability. Comparison of dose-response curves with free teniposide for both neural stem cells and UW medulloblastoma cells. A- dose response curves. B- 95% CIs for the IC50 determinations.

A preliminary screen (Figure 6-22 and Figure 6-23) with three replicates per condition was carried out initially aiming to narrow down the number of formulations for screening. Dose-response curves (Figure 6-22A and Figure 6-23A) for normal (green) and tumour cells (black) were plotted for teniposide and compared to the different nanoparticle formulations (various colours). The biphasic relationship, shown by etoposide, was much less pronounced for teniposide and a monophasic curve-fit was used for the normal cells as well. The logIC₅₀ values from the non-linear regression along with their standard errors were compared using one-way ANOVA with Sidak's test. The 95%-confidence intervals of the IC₅₀ were plotted on a log scale to visualise the shifts in IC₅₀ (Figure 6-22B and Figure 6-23B).

When spheroid volume (Figure 6-22) was used as a proxy for viability the dose response curves for each cell type were well separated. Teniposide was over 20 times more potent in decreasing the size of the neurospheres compared to the tumour tissue. In contrast, the nanoparticles appeared to be less toxic to the normal stem cells while maintaining the same activity towards the tumours. When the confidence intervals for IC₅₀s of the nanoparticles are compared to the free drug in subplot C, it is easy to see the significantly higher IC₅₀s for PEG-PCL, PLA-PEGMA and PEG-PGA for the normal cell population. The same plot for the tumours shows that the toxicity towards tumour tissue has remained at the same level as the free drug.

The dose-response relationships uncovered by metabolic activity (Figure 6-23) had a higher degree of variation and found no statistical differences between the various formulations. Although resazurin (Figure 6-23), similarly to volume (Figure 6-22), shows that the stem cell population was more sensitive to teniposide, the differences were much smaller. In illustration the dose-response curves for the nanoparticle formulations are overlapping for tumours and normal cells. This is even more apparent when the confidence intervals are compared in Figure 6-23B. The confidence intervals for resazurin reduction were much wider compared to the volume measurements and differences between the nanoparticle formulations were not observed. This has confirmed our observations in

Chapter 3 which showed that resazurin reduction is less sensitive compared to volume measurements in detecting small differences between treatments.

The first notable conclusion from this preliminary screen was that teniposide was 5-7 times more potent against the UW228-3 cells and about 10 times more potent against proliferating normal progenitor cells when compared to etoposide (Figure 3-14).

Second, as seen from the confidence intervals for the IC₅₀ determinations using volume (Figure 6-22B), most formulations were equally cytotoxic to the tumour cells. In contrast, formulations with PEG-PCL, PLA-PEGMA and PEG-PGA were less toxic to the normal cell population compared to the free drug. The combination of this finding and the low toxicity and stability of the drug-free PEG-PCL and PLA-PEGMA formulations in cell culture media led to further, more extensive screening for those two formulations.

The second phase of the cell culture screen involved six replicates per concentration and the execution of more independent experiments – two more for PLAPEGMA and four more for PEG-PCL teniposide loaded nanoparticles.

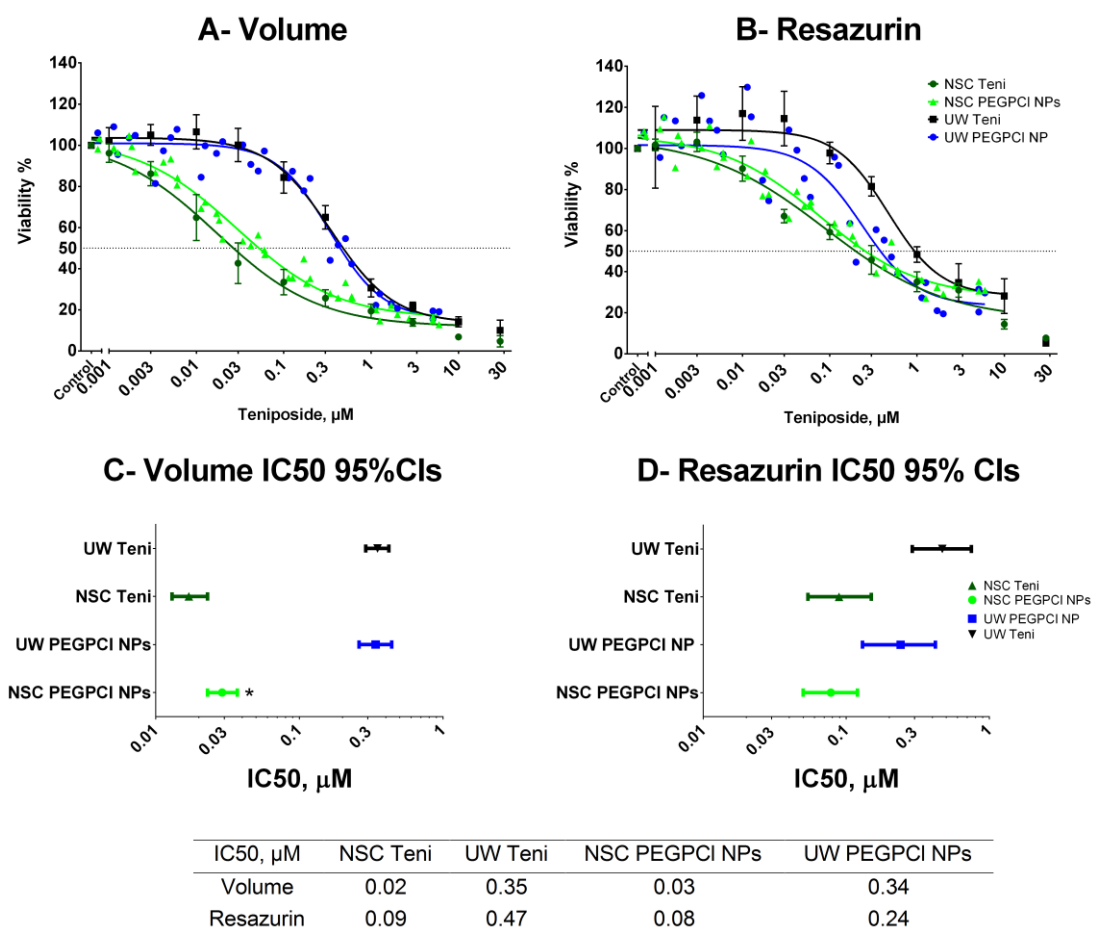


Figure 6-24 Dose-response comparison of teniposide versus teniposide-loaded PEG-PCL NPs. A-Viability determined using spheroid volume; B-Viability determined by metabolism; C-comparison of the 95% CIs for the IC50s using volume; D-comparison of the 95% CIs for the IC50s using metabolism. The table lists the mean IC50 values for neural stem cells and UW228-3 cells for free drug and PEG-PCL NPs determined using Volume and Resazurin reduction.

The teniposide-loaded PCL-PEG nanoparticles were 1.5 times less toxic to normal tissue while maintaining their toxicity towards the tumour cells. There was a statistically significant difference between the volume-derived logIC50 values for teniposide and teniposide-PCL NPs as determined by a two-tailed t-test with Welch's correction. This difference is also illustrated on Figure 6-24C where the 95% confidence intervals for both measurements do not overlap. While, for the NP-treated tumour cells, there was a visible shift towards higher activity in the resazurin dose-response curve, the 95% confidence intervals of the NPs and free drug overlapped. Consequently, the resazurin reduction assay did not yield any statistically significant differences in the t-test comparisons of logIC50s as well.

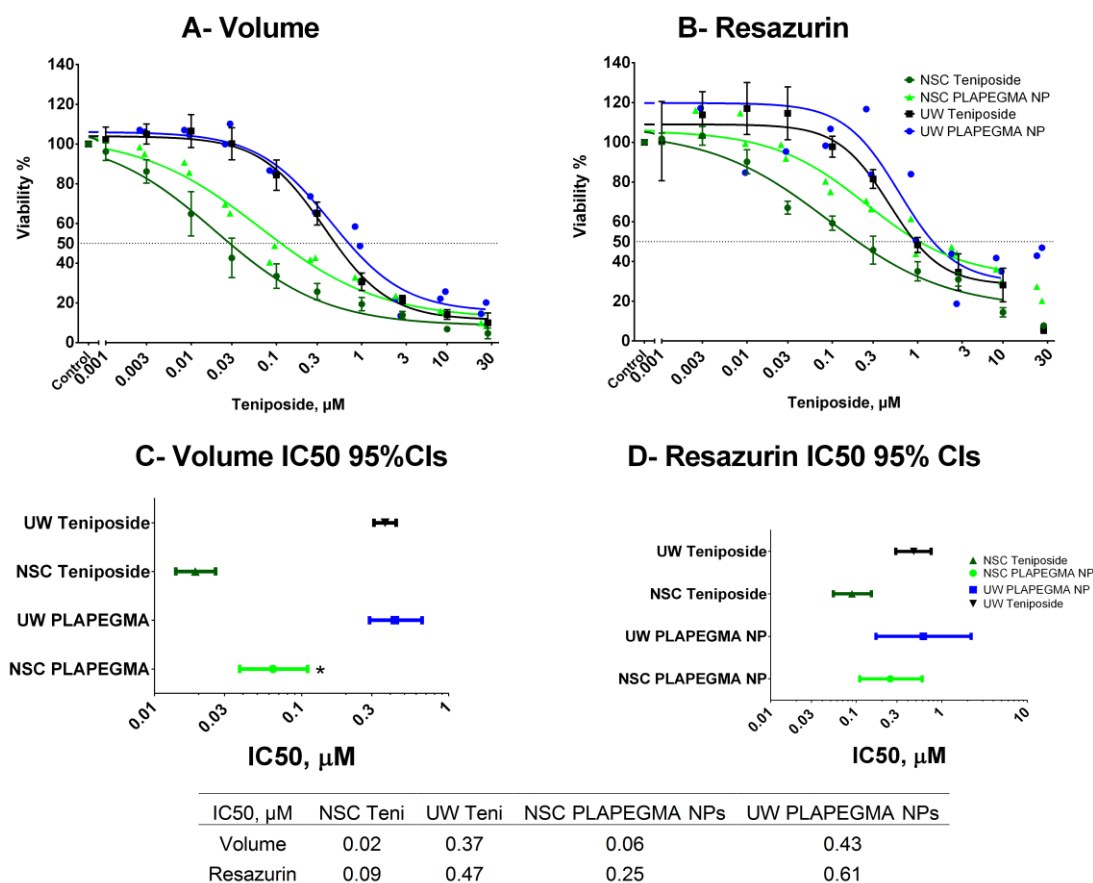


Figure 6-25 Dose-response comparison of teniposide versus teniposide-loaded PLA-PEGMA NPs. A-Viability determined using spheroid volume; B-Viability determined by metabolism; C-comparison of the 95% CIs for the IC₅₀s using volume; D-comparison of the 95% CIs for the IC₅₀s using metabolism. The table lists the mean IC₅₀ values for neural stem cells and UW228-3 cells for free drug and PEG-PLAPEGMA NPs determined using Volume and Resazurin reduction.

Similarly to the PEG-PCL micelles, the PLA-PEGMA teniposide-loaded nanoparticles were equally toxic to tumour and less toxic to normal cells. The bigger difference in IC₅₀s was offset by greater uncertainty in the calculation and wider confidence intervals (Figure 6-25C). Nevertheless the volume measurements yielded a statistically significant logIC₅₀ difference for the normal cell population.

The selective decrease in toxicity can be explained by a lower uptake of the drug loaded nanoparticles by neural stem cells compared to tumours. It could be hypothesized that true effect of the nanoparticles is obscured by the quick drug release. A system that can reliably entrap teniposide until it is endocytosed by the cells is needed to prove that relationship.

Although statistical significance was established using volume as a proxy for viability, the practical significance of this finding may be low.

Improving toxicity to the normal cell population by 1.5 or 3 times is a step in the right direction but a promising result would be at least a 10 times shift. There is a lot to be desired from the release profile and the size-distribution profile of the nanoparticles. The release studies have shown a very fast dissociation of the drug from the carrier system. That may be caused by the fraction of small 20nm nanoparticles or due to the weak interaction of polymer and drug.

In summary, nanoparticles showing improved teniposide loadings were made and their drug release and biological activity were compared to the free drug. Despite suboptimal release profile the PLAPEGMA and PEG-PCL nanoparticles showed a decrease in toxicity towards normal tissue while maintaining the same activity against tumours. This is a small step forward in the improvement of the toxicity profile of podophyllotoxins and establishment of more selective drug delivery systems for the brain.

Chapter 7. Summary, conclusions and future work

This scientific work contributes to science with the establishment of an *in vitro* model of medulloblastoma that can be used in the screening of novel treatments for the disease.

Chapter 3 has outlined the development of a battery of multiplexable, reliable and reproducible high-throughput assays for the culture of neural progenitor and medulloblastoma tumour cells in 3D. It has provided a framework for in-depth characterisation of 3D viability assays with stringent acceptance criteria and quality controls. The algorithm used to assess and compare the assays is broadly appropriate to validate various assays using different endpoints and diverse platforms. The *in vitro* models created were found fit for their intended purpose of comparing the relative safety and efficacy of local treatments for medulloblastoma.

This convenient screening method can be implemented with standard equipment and reagents and can be used for screening new agents and drug delivery systems targeting CNS tumours. It offers the opportunity to compare the effect of drugs upon the tumour and brain thereby comparing efficacy against toxicity, enhancing the bio-relevance to human tumours in clinical practice [232], [300], [474], [475]. The correlation with previously reported experimental and clinical studies [299], [301]–[304] and the practical convenience of this assay procedure suggest that it should be considered as a possible replacement for some animal testing experiments dealing with drug efficacy, particularly in brain tumour types relevant to childhood.

The co-culture model described in Chapter 4 contributes to knowledge with a universally applicable cell labelling and analysis procedure that preserves tissue heterogeneity and allows the determination of cell health for two populations cultured together. In contrast to other studies, which have employed a single cell label[305], marking both cell populations increased the fidelity of cell type determination. Similarly, employing cytoplasmic dyes instead of membrane markers[321], [476] resulted in stable marking for over 7 days with decreased dye loss or exchange between the two populations. Although other researchers have demonstrated the feasibility of differential cytotoxicity determination in

co-culture spheroids[306], [307], their cell labelling strategy was only possible for cells with differential antigen expression and was not suited for heterogeneous cell populations. The co-culture models described in this work mimic the interaction between human tumours and normal human brain tissue thus eliminating the unknowns of interspecies differences[234]. This information is extracted without sacrificing throughput and the options for complete automation. The unique combination of a universal cell marking procedure along with flow cytometry and multiphoton imaging made it possible to visualise the interaction between tumour and host tissue and to quantify the effects of cytotoxic drugs on both populations. These proof-of-concept studies suggest how a robust method for co-culture creation and analysis can be developed in a universal way to study the interaction between any two types of tissue and drugs of interest.

This work has a few important limitations. First of all, the choice of human foetal brain tissue and serum-free culture conditions with EGF and FGF supplementations encourages the enrichment for progenitor and stem cells. While that can be beneficial in studying the response of tumour stem cells, the models would have benefited from a more comprehensive characterisation of the differentiation and maturation state of the normal cells. In hindsight, growth factor withdrawal and differentiation agent supplementation could have been included in the protocol to encourage tissue maturation. In this respect, the normal tissue model created is probably a closer representation of the foetal brain and not the child's brain with its more differentiated and mature neurons and glia.

Second, as this was proof of concept work, most experiments have been performed with a single tumour cell line. While this approach is acceptable in feasibility studies, further development of this model would depend on the inclusion of primary tumour tissue and additional cell lines representing each medulloblastoma cell type[477]. Furthermore the extent to which the tumour spheroids recapitulate the biology of the parent tumour has not been characterised and would need to be included in the validation of the model.

The use of the misidentified VC312R cell line represents a valuable lesson in the importance of cell line authentication. In this respect, the UW228-3 cell line has been validated in-house to be both human and medulloblastoma[228], but STR profiling is still missing from the authentication portfolio. Nevertheless, the core of this thesis is method development, designed to be compatible with a variety of cell types.

Another limitation comes from the use of simple cytotoxicity assays to compare normal and tumour tissue. It is possible that impairment of normal tissue performance could start well before any cytotoxicity is evident. Functionality may be better captured by measuring electrophysiological impulse activity[478], neurite outgrowth[479] and differentiation[480]. However, including these in a high-throughput compatible format may require extensive additional assay development.

Moreover, in vitro models like the ones described here, generally fail to capture the full extent of drug pharmacokinetics. Postsurgical cerebral oedema and CSF flow were not included in this model and although the tumour tissue was cultured as spheroids, the interstitial pressure was not quantified and compared to in vivo data. The locally applied nanoparticles could be washed off by the CSF in the fourth ventricle and the increased interstitial pressure in tumours might potentially hinder their distribution within the tumour mass[481].

The cytotoxicity results for etoposide further stress the importance of pharmacokinetics in toxicity evaluation. Although etoposide has not shown any neurotoxicity in humans, it may be argued that this is mainly due to poor distribution within the CNS. The experimental results have demonstrated that, given the chance to reach the progenitors, etoposide will kill human neural progenitor cells. This further stresses the need for well-designed drug delivery systems to improve selectivity of chemotherapy.

When it comes to the nanoparticle experiments, only some of the initial objectives were met during the course of this work. The preliminary aim to load poly(glycerol adipate) nanoparticles with >3% etoposide was not met possibly due to problems with reproducible polymer synthesis. Nevertheless the screening of 7 polymers and two drugs with multiple

nanoparticle production methodologies yielded encouraging drug loading results for teniposide. The importance of comprehensive characterisation for drug delivery systems was emphasized when the release profile indicated very quick release and cell culture studies showed only marginal improvement in selectivity towards tumours.

The nanoparticle work contributes to science by showing a system for systematic critical review of the available literature, implementation of a broad characterisation strategy and the repeated demonstration of the limitations of dialysis to determine drug release from nanoparticle systems. The inclusion of an extra control sample with empty nanoparticles and a spike of free drug in the dialysis tube was established to be a necessary step in addition to sink conditions and free-drug control. Without these controls, most dialysis drug release experiments from nanocarriers would be meaningless. Moreover, the cell culture studies were used to complete the profile of the nanoparticles showing a 1.5-3 times less cytotoxicity towards neural progenitors compared to free teniposide.

At their current state the nanoparticle drug delivery systems developed here have met the acceptance criteria for drug loading and lack of cytotoxicity of the carrier. However, they have failed in the drug release studies and the improvement of selectivity has not been well pronounced. In this respect, the drug delivery systems as they stand should not be taken forward but need to go through further development to ensure a sustained release profile over 48h and confirm both selective tumour targeting and penetration.

Major improvements are needed in the methodologies to determine drug release from nanoparticle carriers. Dialysis has proven once again to be ill-suited for the task because of its poor time resolution and the influence of interactions between the carrier surface and the released drug on the diffusion through the dialysis bag[429]. Although centrifugal ultrafiltration has potential advantages of quick spin times and easy sample preparation, it suffers from non-specific drug binding and penetration of nanoparticles through the membrane. Similar problems would be expected for pressure ultrafiltration as the membranes have been created to keep

most of the macromolecular carriers in, but they may have a minority of larger pores allowing nanoparticle escape. Methods like centrifugation, hollow fibre ultrafiltration, entrapping the nanoparticles in gels have their own limitations of long sample preparation or drug-binding to the device or carrier. That is why alternative methods employing electrochemical monitoring[436], [437] and microdialysis probes[438], may be more reliable. The electrochemical activity of epipodophyllotoxins[441] hints at the feasibility of release determination using electrochemical detection. Furthermore, the composition of the release media with inclusion of solubilisers, solvents or surfactants creates an artificial release profile that would not necessarily match *in vivo* release. In this respect, both release media and cell culture media employed in the characterisation of nanoparticles should be as close as possible to the *in vivo* fluids composition to ensure biorelevance.

When it comes to biological selectivity improvement, a formulation that could shift the nearly 20-times higher toxicity of teniposide towards normal progenitor cells and completely abolish side effects to normal tissue would be ideal. In reality, that could only be achieved through a very selective and stable drug delivery system. Although more potent than etoposide, teniposide still requires close to micromolar concentrations to eliminate medulloblastoma cells. That necessitates high loadings which often come with the unwanted disadvantage of over-rapid release. A better approach would be to reliably encapsulate a drug (or toxin) active in the nano- or picomolar range and rely on the selectivity of the carrier system.

One aspect of drug delivery that the current *in vitro* model cannot take into account is the pharmacokinetic distribution of the nanoparticles. It could be argued that, while the drug is associated with its macromolecular carrier, it would distribute in a smaller volume and would have a longer residence time in the adjacent tissue. The nanoparticles would also be less likely to cross multiple cell layers and reach the progenitor cells in the SVZ and hypothalamus. Nanoparticles can hypothetically dislodge from their location in the tumour bed and end up in the CSF of the fourth ventricle. However, it is unlikely that they would reach the lateral ventricles and the

hypothalamus. That is because CSF flows down from the fourth ventricle to the spine and also laterally around the back of the cerebellum and then superiorly towards the cerebral hemispheres. Therefore, possible side effects can be expected mainly in the subarachnoid space and the cells of the choroid plexus, but not in the progenitor cell niches within the brain.

The future work, required to move this project forward, can be split in two streams. The first objective should focus on improving the physiological relevance and the information that the *in vitro* model can offer. The second direction would deal with improving the drug delivery system.

The physiological relevance of this *in vitro* system would be further improved by including an additional differentiation and maturation step in the culture of human neural stem cells. Establishing the proportion of early progenitors, oligodendrocytes, astrocytes and neurons in the model and determining the effects of free drug on each population would further benefit understanding of the cytotoxic mode of action and neurotoxic side effects. Moreover, multiple drugs would need to be assessed, including controls with well-established neurotoxicity (vincristine, cisplatin, or methotrexate). Establishing the dose-response relationships for these drugs in the model will serve to set relative neurotoxicity thresholds. The inclusion of multiple drugs will also allow the calculation of minimum significance ratio[482] to further validate the sensitivity of each assay. Apart from using multiple drugs, more endpoints like differentiation, migration and electrophysiological activity can be explored to compare the effects of drugs and nanoparticles. As for the tumours, the utilisation of more representative cell lines[477] and patient-derived primary tumour tissue would allow for a better recapitulation of tumour heterogeneity and can be potentially used in personalising therapy. Finally, the extent to which the tumour spheroids recapitulate the behaviour of patient tumours remains to be characterised and validated.

Regarding the nanoparticles, the employment of drugs active in the picomolar and nanomolar range would require less drug to be entrapped by the polymers. It can be argued that the required lower drug loadings could potentially result in an increase of the number of possible carriers and reduction of the premature drug release issues. A strong physical

interaction between the carrier and the drug would be needed in order to prevent rapid drug release and realize the potential benefit of nanoparticle targeting. Moreover, a more comprehensive exploration of the interaction between drugs and polymers can be modelled *in silico*[483] prior to starting lab experiments in order to pinpoint suitable chemistry and favourable interactions. Additionally, whether all medulloblastoma subtypes really have increased endocytotic activity will need to be confirmed both between and within patient-derived tumours. The question whether that potential increase in endocytosis would translate to a clinical benefit also remains unresolved.

In conclusion, the *in vitro* models described here are the first step to building a comprehensive human model for assessing local chemotherapy for medulloblastoma. Further validation with more compounds, additional characterisation and optimisation of the differentiation procedures are needed to improve the models. Although the nanoparticles produced are not currently fit for their purpose, a variety of methods to test their suitability have been established and it is only a matter of time before the optimal formulation will be created.

Supporting information

Supporting information macro S1:

```
//This macro aims to automate spheroid size measurement in three-dimensional cell culture. It
requires input and output folders with images only, processes the images, records a file with
spheroid measurements (Area, Feret max, Feret min, etc.) and writes an image with the outline/s of
the determined spheroid/s.
//The spheroid detection and size determination function to be repeated for every image is defined
below
function action(inputFolder,outputFolder,filename) {
open(inputFolder + filename);
//sets scale to predetermined values from calibration slide
run("Set Scale...", "distance=178 known=100 pixel=1 unit=µm global");
run("16-bit");
//run("Brightness/Contrast...");
run("Enhance Contrast", "saturated=0.35");
//Uses Yen thresholding algorithm
setAutoThreshold("Yen");
setOption("BlackBackground", false);
run("Convert to Mask");
//Gets the ratio between black (spheroid) and white (background) pixels. If we assume a single
spheroid, the ratio between black and white pixels would allow us to estimate the size of the
spheroid.
getHistogram(0,hist,256);
ratio = hist[255]/hist[0];
//If there are more pixels detected as spheroid(black) than background(white) then the spheroid has
not been detected due to variations in background
if (ratio>1) {
// closes the image, reopens it, subtracts the background and proceeds as normal
close();
open(inputFolder + filename);
run("16-bit");
// Subtract Background is not used in the default function because it can lead to merging of
spheroids and debris or it can remove the core of the spheroid leaving a very thin interrupted edge.
In certain cases where the edges of a spheroid are very bright removing the background can give
better results.
run("Subtract Background...", "rolling=50 light");
setAutoThreshold("Yen");
setOption("BlackBackground", false);
run("Convert to Mask");
run("Remove Outliers...", "radius=15 threshold=0 which=Dark");
getHistogram(0,hist,256);
ratio = hist[255]/hist[0];};
//The strategy here is to act differently according to spheroid size. The general pattern is to
expand and then shrink back the spheroids in order to include all cells on the edges. Then a series of
functions are used to remove noise and the Watershed function separates fused or superimposed
particles. The Analyze particles function is targeted to the specific spheroid size according to the
black/white pixel ratio.
if (ratio<0.001) {
run("Maximum...", "radius=8");
run("Fill Holes");
run("Minimum...", "radius=8");
//small spheroids require a more "gentle" function to clean up noise
run("Median...", "radius=2");
run("Maximum...", "radius=25");
run("Minimum...", "radius=25");
run("Fill Holes");
run("Watershed");
run("Analyze Particles...", "size=4000-Infinity circularity=0.20-1.00 show=[Overlay
Outlines] display exclude include summarize");};
if (ratio >=0.001 && ratio<0.01) {
run("Maximum...", "radius=8");
run("Fill Holes");
run("Minimum...", "radius=8");
//slightly bigger spheroids and a more rigorous function to remove noise
run("Remove Outliers...", "radius=10 threshold=0 which=Dark");
run("Watershed");
```

Supporting information

```
run("Analyze Particles...", "size=10000-Infinity circularity=0.20-1.00 show=[Overlay
Outlines] display exclude include summarize");};
if (ratio>=0.01 && ratio<0.2) {
run("Maximum...", "radius=8");
run("Fill Holes");
run("Minimum...", "radius=8");
run("Remove Outliers...", "radius=15 threshold=0 which=Dark");
run("Median...", "radius=4");
run("Watershed");
run("Analyze Particles...", "size=20000-Infinity circularity=0.20-1.00 show=[Overlay
Outlines] display exclude include summarize");};
if (ratio>=0.2 && ratio<1) {
//Very big spheroids generally do not need to be expanded much to fill up the edges.
run("Maximum...", "radius=3");
run("Fill Holes");
run("Minimum...", "radius=3");
//Outliers and noise are removed rigorously
run("Remove Outliers...", "radius=50 threshold=0 which=Dark");
run("Minimum...", "radius=30");
run("Maximum...", "radius=30");
run("Watershed");
run("Analyze Particles...", "size=50000-Infinity circularity=0.20-1.00 show=[Overlay
Outlines] display exclude include summarize");};
if (Overlay.size > 0) {
//Sends particles detected to the ROI manager
run("To ROI Manager");
close();
//Reopens the original image and pastes the outlines of the determined particles onto it
open(inputFolder + filename);
run("From ROI Manager");
outputPath = outputFolder + filename;
save(outputPath);
close(); }
else {
close();
};
call("java.lang.System.gc");
};
call("java.lang.System.gc");
run("Clear Results");
inputFolder = getDirectory("Choose the input folder!");
outputFolder = getDirectory("Choose the output folder!");
//Delete the next line if you want to see how the macro works on the images. However that will
reduce processing speed.
setBatchMode(true);
images = getFileList(inputFolder);
//Sets the measurements that are recorded for each spheroid
run("Set Measurements...", "area centroid shape feret's display add redirect=None decimal=1");
//That is the cycle that runs through all images
for (i=0; i<images.length; i++) {
action(inputFolder,outputFolder,images[i]);
showProgress(i, images.length);
};
//Writes in the Results and Summary windows and saves the data.
selectWindow("Results");
saveAs("Measurements", "" + outputFolder + "Results.txt");
selectWindow("Summary");
saveAs("Text", "" + outputFolder + "Summary.txt");
setBatchMode(false);
```

References

- [1] F. Ferlay J, Soerjomataram I, Ervik M, Dikshit R, Eser S, Mathers C, Rebelo M, Parkin DM, Forman D, Bray, "GLOBOCAN 2012 v1.0, Cancer Incidence and Mortality Worldwide: IARC CancerBase No. 11 [Internet]," Lyon, France, 2013.
- [2] L. Ries, M. Smith, J. Gurney, M. Linet, T. Tamra, J. Young, and G. (eds) Bunin, "Cancer Incidence and Survival among Children and Adolescents: United States SEER Program 1975-1995," 1999.
- [3] R. Peris-Bonet, C. Martínez-García, B. Lacour, S. Petrovich, B. Giner-Ripoll, A. Navajas, and E. Steliarova-Foucher, "Childhood central nervous system tumours--incidence and survival in Europe (1978-1997): report from Automated Childhood Cancer Information System project.," *Eur. J. Cancer*, vol. 42, no. 13, pp. 2064–80, Sep. 2006.
- [4] C. Stiller, *Childhood Cancer in Britain: Incidence, survival, mortality*. Oxford University Press, 2007.
- [5] R. S. Snell, *Clinical Neuroanatomy*. Lippincott Williams & Wilkins, 2010, p. 542.
- [6] R. J. Packer and D. Schiff, *Neuro-oncology*. John Wiley & Sons, 2012, p. 246.
- [7] D. Louis, H. Ohgaki, O. Wiestler, and W. (eds) Cavenee, "World Health Organization Classification of Tumours of the Central Nervous System," Lyon, France, 2007.
- [8] C. H. Chang, E. M. Housepian, and C. Herbert, "An operative staging system and a megavoltage radiotherapeutic technic for cerebellar medulloblastomas.," *Radiology*, vol. 93, no. 6, pp. 1351–9, Dec. 1969.
- [9] P. M. Zeltzer, J. M. Boyett, J. L. Finlay, A. L. Albright, L. B. Rorke, J. M. Milstein, J. C. Allen, K. R. Stevens, P. Stanley, H. Li, J. H. Wisoff, J. R. Geyer, P. McGuire-Cullen, J. A. Stehbens, S. B. Shurin, and R. J. Packer, "Metastasis stage, adjuvant treatment, and residual tumor are prognostic factors for medulloblastoma in children: conclusions from the Children's Cancer Group 921 randomized phase III study.," *J. Clin. Oncol.*, vol. 17, no. 3, pp. 832–45, Mar. 1999.
- [10] R. J. Gilbertson and D. W. Ellison, "The origins of medulloblastoma subtypes.," *Annu. Rev. Pathol.*, vol. 3, pp. 341–65, Jan. 2008.

References

- [11] D. Ellison, "Classifying the medulloblastoma: insights from morphology and molecular genetics.," *Neuropathol. Appl. Neurobiol.*, vol. 28, no. 4, pp. 257–82, Aug. 2002.
- [12] H. G. Brown, J. L. Kepner, E. J. Perlman, H. S. Friedman, D. R. Strother, P. K. Duffner, L. E. Kun, P. T. Goldthwaite, and P. C. Burger, "'Large cell/anaplastic' medulloblastomas: a Pediatric Oncology Group Study.," *J. Neuropathol. Exp. Neurol.*, vol. 59, no. 10, pp. 857–65, Oct. 2000.
- [13] M. D. Taylor, P. a Northcott, A. Korshunov, M. Remke, Y.-J. Cho, S. C. Clifford, C. G. Eberhart, D. W. Parsons, S. Rutkowski, A. Gajjar, D. W. Ellison, P. Lichter, R. J. Gilbertson, S. L. Pomeroy, M. Kool, and S. M. Pfister, "Molecular subgroups of medulloblastoma: the current consensus.," *Acta Neuropathol.*, vol. 123, no. 4, pp. 465–72, Apr. 2012.
- [14] D. W. Ellison, O. E. Onilude, J. C. Lindsey, M. E. Lusher, C. L. Weston, R. E. Taylor, A. D. Pearson, and S. C. Clifford, "beta-Catenin status predicts a favorable outcome in childhood medulloblastoma: the United Kingdom Children's Cancer Study Group Brain Tumour Committee.," *J. Clin. Oncol.*, vol. 23, no. 31, pp. 7951–7, Nov. 2005.
- [15] T. Phoenix, D. Patmore, N. Boulos, K. Wright, S. Boop, and R. Gilbertson, "Medulloblastoma subtypes specify inter-tumoral vascular heterogeneity," *Neuro. Oncol.*, vol. 16, no. 1, 2014.
- [16] P. A. Northcott, D. T. W. Jones, M. Kool, G. W. Robinson, R. J. Gilbertson, Y.-J. Cho, S. L. Pomeroy, A. Korshunov, P. Lichter, M. D. Taylor, and S. M. Pfister, "Medulloblastomics: the end of the beginning.," *Nat. Rev. Cancer*, vol. 12, no. 12, pp. 818–34, Dec. 2012.
- [17] M. Kool, D. T. W. Jones, N. Jäger, P. a Northcott, T. J. Pugh, V. Hovestadt, R. M. Piro, L. A. Esparza, S. L. Markant, M. Remke, T. Milde, F. Bourdeaut, M. Ryzhova, D. Sturm, E. Pfaff, S. Stark, S. Hutter, H. Seker-Cin, P. Johann, S. Bender, C. Schmidt, T. Rausch, D. Shih, J. Reimand, L. Sieber, A. Wittmann, L. Linke, H. Witt, U. D. Weber, M. Zapatka, R. König, R. Beroukhim, G. Bergthold, P. van Sluis, R. Volckmann, J. Koster, R. Versteeg, S. Schmidt, S. Wolf, C. Lawerenz, C. C. Bartholomae, C. von Kalle, A. Unterberg, C. Herold-Mende, S. Hofer, A. E. Kulozik, A. von Deimling, W. Scheurlen, J. Felsberg, G. Reifenberger, M. Hasselblatt, J. R. Crawford, G. a Grant, N. Jabado, A. Perry, C. Cowdrey, S. Croul, G. Zadeh, J. O. Korb, F. Doz, O. Delattre, G. D. Bader, M. G. McCabe, V. P. Collins, M. W. Kieran, Y.-J. Cho, S. L. Pomeroy, O. Witt, B. Brors, M. D. Taylor, U. Schüller, A. Korshunov, R. Eils, R. J. Wechsler-Reya, P. Lichter, and S. M. Pfister, "Genome sequencing of SHH medulloblastoma predicts genotype-related response to smoothed inhibition.," *Cancer Cell*, vol. 25, no. 3, pp. 393–405, Mar. 2014.

References

- [18] C. M. Rudin, C. L. Hann, J. Laterra, R. L. Yauch, C. a Callahan, L. Fu, T. Holcomb, J. Stinson, S. E. Gould, B. Coleman, P. M. LoRusso, D. D. Von Hoff, F. J. de Sauvage, and J. a Low, "Treatment of medulloblastoma with hedgehog pathway inhibitor GDC-0449.," *N. Engl. J. Med.*, vol. 361, no. 12, pp. 1173–8, Sep. 2009.
- [19] H. Kimura, J. M. Y. Ng, and T. Curran, "Transient inhibition of the Hedgehog pathway in young mice causes permanent defects in bone structure.," *Cancer Cell*, vol. 13, no. 3, pp. 249–60, Mar. 2008.
- [20] T. Rausch, D. T. W. Jones, M. Zapatka, A. M. Stütz, T. Zichner, J. Weischenfeldt, N. Jäger, M. Remke, D. Shih, P. a Northcott, E. Pfaff, J. Tica, Q. Wang, L. Massimi, H. Witt, S. Bender, S. Pleier, H. Cin, C. Hawkins, C. Beck, A. von Deimling, V. Hans, B. Brors, R. Eils, W. Scheurlen, J. Blake, V. Benes, A. E. Kulozik, O. Witt, D. Martin, C. Zhang, R. Porat, D. M. Merino, J. Wasserman, N. Jabado, A. Fontebasso, L. Bullinger, F. G. Rücker, K. Döhner, H. Döhner, J. Koster, J. J. Molenaar, R. Versteeg, M. Kool, U. Tabori, D. Malkin, A. Korshunov, M. D. Taylor, P. Lichter, S. M. Pfister, and J. O. Korbel, "Genome sequencing of pediatric medulloblastoma links catastrophic DNA rearrangements with TP53 mutations.," *Cell*, vol. 148, no. 1–2, pp. 59–71, Jan. 2012.
- [21] T. Pietsch, R. Schmidt, M. Remke, A. Korshunov, V. Hovestadt, D. T. W. Jones, J. Felsberg, K. Kaulich, T. Goschzik, M. Kool, P. a Northcott, K. von Hoff, A. O. von Bueren, C. Friedrich, M. Mynarek, H. Skladny, G. Fleischhack, M. D. Taylor, F. Cremer, P. Lichter, A. Faldum, G. Reifenberger, S. Rutkowski, and S. M. Pfister, "Prognostic significance of clinical, histopathological, and molecular characteristics of medulloblastomas in the prospective HIT2000 multicenter clinical trial cohort.," *Acta Neuropathol.*, vol. 128, no. 1, pp. 137–49, Jul. 2014.
- [22] D. J. H. Shih, P. a Northcott, M. Remke, A. Korshunov, V. Ramaswamy, M. Kool, B. Luu, Y. Yao, X. Wang, A. M. Dubuc, L. Garzia, J. Peacock, S. C. Mack, X. Wu, A. Rolider, a S. Morrissy, F. M. G. Cavalli, D. T. W. Jones, K. Zitterbart, C. C. Faria, U. Schüller, L. Kren, T. Kumabe, T. Tominaga, Y. Shin Ra, M. Garami, P. Hauser, J. a Chan, S. Robinson, L. Bognár, A. Klekner, A. G. Saad, L. M. Liau, S. Albrecht, A. Fontebasso, G. Cinalli, P. De Antonellis, M. Zollo, M. K. Cooper, R. C. Thompson, S. Bailey, J. C. Lindsey, C. Di Rocco, L. Massimi, E. M. C. Michiels, S. W. Scherer, J. J. Phillips, N. Gupta, X. Fan, K. M. Muraszko, R. Vibhakar, C. G. Eberhart, M. Fouladi, B. Lach, S. Jung, R. J. Wechsler-Reya, M. Fèvre-Montange, A. Jouvret, N. Jabado, I. F. Pollack, W. a Weiss, J.-Y. Lee, B.-K. Cho, S.-K. Kim, K.-C. Wang, J. R. Leonard, J. B. Rubin, C. de Torres, C. Lavarino, J. Mora, Y.-J. Cho, U. Tabori, J. M. Olson, A. Gajjar, R. J. Packer, S. Rutkowski, S. L. Pomeroy, P. J. French, N. K. Kloosterhof, J. M. Kros, E. G. Van Meir, S. C. Clifford, F. Bourdeaut, O. Delattre, F. F. Doz, C. E. Hawkins, D. Malkin, W. a Grajkowska, M. Perek-Polnik, E. Bouffet, J. T. Rutka, S. M. Pfister, and M. D.

References

- Taylor, "Cytogenetic prognostication within medulloblastoma subgroups.," *J. Clin. Oncol.*, vol. 32, no. 9, pp. 886–96, Mar. 2014.
- [23] V. Ramaswamy, M. Remke, E. Bouffet, C. C. Faria, S. Perreault, Y.-J. Cho, D. J. Shih, B. Luu, A. M. Dubuc, P. a Northcott, U. Schüller, S. Gururangan, R. McLendon, D. Bigner, M. Fouladi, K. L. Ligon, S. L. Pomeroy, S. Dunn, J. Triscott, N. Jabado, A. Fontebasso, D. T. W. Jones, M. Kool, M. a Karajannis, S. L. Gardner, D. Zagzag, S. Nunes, J. Pimentel, J. Mora, E. Lipp, A. W. Walter, M. Ryzhova, O. Zheludkova, E. Kumirova, J. Alshami, S. E. Croul, J. T. Rutka, C. Hawkins, U. Tabori, K.-E. T. Codispoti, R. J. Packer, S. M. Pfister, A. Korshunov, and M. D. Taylor, "Recurrence patterns across medulloblastoma subgroups: an integrated clinical and molecular analysis.," *Lancet Oncol.*, vol. 14, no. 12, pp. 1200–7, Nov. 2013.
- [24] J. H. Wright, "Neurocytoma or neuroblastoma, a kind of tumor not generally recognized," *J. Exp. Med.*, vol. 12, no. 4, pp. 556–61, Jul. 1910.
- [25] P. Bailey and H. Cushing, "Medulloblastoma cerebelli - A common type of midcerebellar glioma of childhood," *Arch. Neurol. Psychiatry*, vol. 14, no. 2, pp. 192–224, Aug. 1925.
- [26] H. J. G. Bloom, E. N. K. Wallace, and J. M. Henk, "The treatment and prognosis of medulloblastoma in children," *Am. J. Roentgenol.*, vol. 105, no. 1, pp. 43–62, Jan. 1969.
- [27] A. L. Albright, J. H. Wisoff, P. M. Zeltzer, J. M. Boyett, L. B. Rorke, and P. Stanley, "Effects of medulloblastoma resections on outcome in children: a report from the Children's Cancer Group.," *Neurosurgery*, vol. 38, no. 2, pp. 265–71, Feb. 1996.
- [28] P. L. Robertson, K. M. Muraszko, E. J. Holmes, R. Sposto, R. J. Packer, A. Gajjar, M. S. Dias, and J. C. Allen, "Incidence and severity of postoperative cerebellar mutism syndrome in children with medulloblastoma: a prospective study by the Children's Oncology Group.," *J. Neurosurg.*, vol. 105, no. 6 Suppl, pp. 444–51, Dec. 2006.
- [29] T. Gudrunardottir, A. Sehested, M. Juhler, and K. Schmiegelow, "Cerebellar mutism: review of the literature.," *Childs. Nerv. Syst.*, vol. 27, no. 3, pp. 355–63, Mar. 2011.
- [30] K. El-Bahy, "Telovelar approach to the fourth ventricle: operative findings and results in 16 cases.," *Acta Neurochir. (Wien).*, vol. 147, no. 2, pp. 137–42; discussion 142, Feb. 2005.
- [31] T. G. Landberg, M. L. Lindgren, E. K. Cavallin-Ståhl, G. O. Svahn-Tapper, G. Sundbärg, S. Garwicz, J. A. Lagergren, V. L. Gunnesson, A. E. Brun, and S. E. Cronqvist, "Improvements in the radiotherapy

References

- of medulloblastoma, 1946-1975.," *Cancer*, vol. 45, no. 4, pp. 670-8, Feb. 1980.
- [32] E. Paterson and R. F. Farr, "Cerebellar medulloblastoma: treatment by irradiation of the whole central nervous system.," *Acta radiol.*, vol. 39, no. 4, pp. 323-36, Apr. 1953.
- [33] K. C. De Braganca and R. J. Packer, "Treatment Options for Medulloblastoma and CNS Primitive Neuroectodermal Tumor (PNET).," *Curr. Treat. Options Neurol.*, vol. 15, no. 5, pp. 593-606, Oct. 2013.
- [34] I. Lampe and R. S. Macintyre, "Experiences in the radiation therapy of medulloblastoma of the cerebellum.," *Am. J. Roentgenol. Radium Ther. Nucl. Med.*, vol. 71, no. 4, pp. 659-68, Apr. 1954.
- [35] J. C. Probert, B. R. Parker, and H. S. Kaplan, "Growth retardation in children after megavoltage irradiation of the spine," *Cancer*, vol. 32, no. 3, pp. 634-639, Sep. 1973.
- [36] W. M. Wara, G. E. Richards, M. M. Grumbach, S. L. Kaplan, G. E. Sheline, and F. A. Conte, "Hypopituitarism after irradiation in children," *Int. J. Radiat. Oncol.*, vol. 2, no. 5-6, pp. 549-552, May 1977.
- [37] D. R. McFarland, H. Horwitz, E. L. Saenger, and G. K. Bahr, "Medulloblastoma--a review of prognosis and survival.," *Br. J. Radiol.*, vol. 42, no. 495, pp. 198-214, Mar. 1969.
- [38] J. H. Silber, J. Radcliffe, V. Peckham, G. Perilongo, P. Kishnani, M. Fridman, J. W. Goldwein, and A. T. Meadows, "Whole-brain irradiation and decline in intelligence: the influence of dose and age on IQ score.," *J. Clin. Oncol.*, vol. 10, no. 9, pp. 1390-6, Sep. 1992.
- [39] S. LeBaron, P. M. Zeltzer, L. K. Zeltzer, S. E. Scott, and A. E. Marlin, "Assessment of quality of survival in children with medulloblastoma and cerebellar astrocytoma.," *Cancer*, vol. 62, no. 6, pp. 1215-22, Sep. 1988.
- [40] E. Mostow, J. Byrne, R. Connelly, and J. Mulvihill, "Quality of life in long-term survivors of CNS tumors of childhood and adolescence," *J. Clin. Oncol.*, vol. 9, no. 4, pp. 592-599, Apr. 1991.
- [41] J. Grill, V. K. Renaux, C. Bulteau, D. Viguier, C. Levy-Piebois, C. Sainte-Rose, G. Dellatolas, M. A. Raquin, I. Jambaqué, and C. Kalifa, "Long-term intellectual outcome in children with posterior fossa tumors according to radiation doses and volumes.," *Int. J. Radiat. Oncol. Biol. Phys.*, vol. 45, no. 1, pp. 137-45, Aug. 1999.

References

- [42] B. Lannering, I. Marky, A. Lundberg, and E. Olsson, "Long-term sequelae after pediatric brain tumors: their effect on disability and quality of life.," *Med. Pediatr. Oncol.*, vol. 18, no. 4, pp. 304–10, Jan. 1990.
- [43] C. R. Kennedy and K. Leyland, "Comparison of screening instruments for disability and emotional/behavioral disorders with a generic measure of health-related quality of life in survivors of childhood brain tumors.," *Int. J. Cancer. Suppl.*, vol. 12, pp. 106–11, Jan. 1999.
- [44] R. J. Packer, T. Zhou, E. Holmes, G. Vezina, and A. Gajjar, "Survival and secondary tumors in children with medulloblastoma receiving radiotherapy and adjuvant chemotherapy: results of Children's Oncology Group trial A9961.," *Neuro. Oncol.*, vol. 15, no. 1, pp. 97–103, Jan. 2013.
- [45] T. Gudrunardottir, B. Lannering, M. Remke, M. D. Taylor, E. M. Wells, R. F. Keating, and R. J. Packer, "Treatment developments and the unfolding of the quality of life discussion in childhood medulloblastoma: a review.," *Childs. Nerv. Syst.*, vol. 30, no. 6, pp. 979–90, Jun. 2014.
- [46] K. K. Koeller and E. J. Rushing, "From the archives of the AFIP: medulloblastoma: a comprehensive review with radiologic-pathologic correlation.," *Radiographics*, vol. 23, no. 6, pp. 1613–37, 2003.
- [47] N. U. Gerber, M. Mynarek, K. von Hoff, C. Friedrich, a Resch, and S. Rutkowski, "Recent developments and current concepts in medulloblastoma.," *Cancer Treat. Rev.*, vol. 40, no. 3, pp. 356–65, Apr. 2014.
- [48] R. K. Mulhern, S. L. Palmer, T. E. Merchant, D. Wallace, M. Kocak, P. Brouwers, K. Krull, M. Chintagumpala, R. Stargatt, D. M. Ashley, V. L. Tyc, L. Kun, J. Boyett, and A. Gajjar, "Neurocognitive consequences of risk-adapted therapy for childhood medulloblastoma.," *J. Clin. Oncol.*, vol. 23, no. 24, pp. 5511–9, Aug. 2005.
- [49] I. Moxon-Emre, E. Bouffet, M. D. Taylor, N. Laperriere, N. Scantlebury, N. Law, B. J. Spiegler, D. Malkin, L. Janzen, and D. Mabbott, "Impact of craniospinal dose, boost volume, and neurologic complications on intellectual outcome in patients with medulloblastoma.," *J. Clin. Oncol.*, vol. 32, no. 17, pp. 1760–8, Jun. 2014.
- [50] D. G. Kirsch, "Conformal Radiation Therapy for Childhood CNS Tumors," *Oncologist*, vol. 9, no. 4, pp. 442–450, Jul. 2004.

References

- [51] W. R. Polkinghorn, I. J. Dunkel, M. M. Souweidane, Y. Khakoo, D. C. Lyden, S. W. Gilheeneey, O. J. Becher, A. S. Budnick, and S. L. Wolden, "Disease control and ototoxicity using intensity-modulated radiation therapy tumor-bed boost for medulloblastoma.," *Int. J. Radiat. Oncol. Biol. Phys.*, vol. 81, no. 3, pp. e15–20, Nov. 2011.
- [52] E. J. Hall and C.-S. Wu, "Radiation-induced second cancers: the impact of 3D-CRT and IMRT," *Int. J. Radiat. Oncol.*, vol. 56, no. 1, pp. 83–88, May 2003.
- [53] E. Huang, B. S. Teh, D. R. Strother, Q. G. Davis, J. K. Chiu, H. H. Lu, L. S. Carpenter, W.-Y. Mai, M. M. Chintagumpala, M. South, W. H. Grant III, E. B. Butler, and S. Y. Woo, "Intensity-modulated radiation therapy for pediatric medulloblastoma: early report on the reduction of ototoxicity," *Int. J. Radiat. Oncol.*, vol. 52, no. 3, pp. 599–605, Mar. 2002.
- [54] R. Soomal, F. Saran, and M. Brada, "In regard to Huang et al.: intensity-modulated radiation therapy for pediatric medulloblastoma: early report on the reduction of ototoxicity IJROBP 2002;52:599–605," *Int. J. Radiat. Oncol.*, vol. 55, no. 3, p. 853, Mar. 2003.
- [55] N. Jain, K. R. Krull, P. Brouwers, M. M. Chintagumpala, and S. Y. Woo, "Neuropsychological outcome following intensity-modulated radiation therapy for pediatric medulloblastoma.," *Pediatr. Blood Cancer*, vol. 51, no. 2, pp. 275–9, Aug. 2008.
- [56] N. P. Brodin, P. Munck af Rosenschöld, M. Blomstrand, A. Kiil-Berthlesen, C. Hollensen, I. R. Vogelius, B. Lannering, S. M. Bentzen, and T. Björk-Eriksson, "Hippocampal sparing radiotherapy for pediatric medulloblastoma: impact of treatment margins and treatment technique.," *Neuro. Oncol.*, vol. 16, no. 4, pp. 594–602, Apr. 2014.
- [57] W. P. Levin, H. Kooy, J. S. Loeffler, and T. F. DeLaney, "Proton beam therapy.," *Br. J. Cancer*, vol. 93, no. 8, pp. 849–54, Oct. 2005.
- [58] R. R. Wilson, "Radiological use of fast protons.," *Radiology*, vol. 47, no. 5, pp. 487–91, Nov. 1946.
- [59] C. T. Lee, S. D. Bilton, R. M. Famiglietti, B. A. Riley, A. Mahajan, E. L. Chang, M. H. Maor, S. Y. Woo, J. D. Cox, and A. R. Smith, "Treatment planning with protons for pediatric retinoblastoma, medulloblastoma, and pelvic sarcoma: how do protons compare with other conformal techniques?," *Int. J. Radiat. Oncol. Biol. Phys.*, vol. 63, no. 2, pp. 362–72, Oct. 2005.
- [60] W. H. St Clair, J. a Adams, M. Bues, B. C. Fullerton, S. La Shell, H. M. Kooy, J. S. Loeffler, and N. J. Tarbell, "Advantage of protons

References

- compared to conventional X-ray or IMRT in the treatment of a pediatric patient with medulloblastoma.," *Int. J. Radiat. Oncol. Biol. Phys.*, vol. 58, no. 3, pp. 727–34, Mar. 2004.
- [61] R. Miralbell, A. Lomax, L. Cella, and U. Schneider, "Potential reduction of the incidence of radiation-induced second cancers by using proton beams in the treatment of pediatric tumors," *Int. J. Radiat. Oncol.*, vol. 54, no. 3, pp. 824–829, Nov. 2002.
- [62] C. L. Barney, A. P. Brown, D. R. Grosshans, M. F. McAleer, J. F. de Groot, V. Puduvalli, S. L. Tucker, C. N. Crawford, M. R. Gilbert, P. D. Brown, and A. Mahajan, "Technique, outcomes, and acute toxicities in adults treated with proton beam craniospinal irradiation.," *Neuro. Oncol.*, vol. 16, no. 2, pp. 303–9, Jan. 2014.
- [63] E. W. Wells, G. Vezina, L. Kilburn, B. Rood, F. Crozier, E. Hwang, and R. Packer, "Acute brain injury may be more severe from proton beam radiation (pbr) than from conventional radiation therapy (crt) for young pediatric patients with posterior fossa tumor," in *ISPNO2014, R-008*, 2014, p. i118.
- [64] J. Gunther, M. Sato, M. Chintagumpala, E. Jo, A. Paulino, A. Adesina, L. Ketonen, J. Jones, J. Su, F. Okcu, S. Khatua, R. Dauser, W. Whitehead, J. Weinberg, and A. Mahajan, "Imaging changes in pediatric patients treated with proton beam radiation therapy compared to intensity modulated radiation therapy for intracranial ependymoma," in *RO-016 ISPNO2014*, 2014.
- [65] A. Mahajan, D. Grosshans, D. Ris, M. Chintagumpala, F. Okcu, M. F. McAleer, B. Moore, H. Stancel, C. Minard, D. Guffey, and L. Kahalley, "Neurocognitive outcomes in relationship to hippocampal and brain doses after partial brain proton radiotherapy in children," in *RO-012 ISPNO2014*, 2014.
- [66] S. L. Wolden, "Protons for craniospinal radiation: are clinical data important?," *Int. J. Radiat. Oncol. Biol. Phys.*, vol. 87, no. 2, pp. 231–2, Oct. 2013.
- [67] P. a S. Johnstone, K. P. McMullen, J. C. Buchsbaum, J. G. Douglas, and P. Helft, "Pediatric CSI: are protons the only ethical approach?," *Int. J. Radiat. Oncol. Biol. Phys.*, vol. 87, no. 2, pp. 228–30, Oct. 2013.
- [68] R. Zhang, R. M. Howell, A. Giebeler, P. J. Taddei, A. Mahajan, and W. D. Newhauser, "Comparison of risk of radiogenic second cancer following photon and proton craniospinal irradiation for a pediatric medulloblastoma patient.," *Phys. Med. Biol.*, vol. 58, no. 4, pp. 807–23, Feb. 2013.

References

- [69] W. D. Newhauser and M. Durante, "Assessing the risk of second malignancies after modern radiotherapy.," *Nat. Rev. Cancer*, vol. 11, no. 6, pp. 438–48, Jun. 2011.
- [70] T. E. Merchant, J. E. Schreiber, S. Wu, R. Lukose, X. Xiong, and A. Gajjar, "Critical Combinations of Radiation Dose and Volume Predict Intelligence Quotient and Academic Achievement Scores After Craniospinal Irradiation in Children With Medulloblastoma.," *Int. J. Radiat. Oncol. Biol. Phys.*, Aug. 2014.
- [71] A. E. Evans, R. D. Jenkin, R. Sposto, J. A. Ortega, C. B. Wilson, W. Wara, I. J. Ertel, S. Kramer, C. H. Chang, and S. L. Leikin, "The treatment of medulloblastoma. Results of a prospective randomized trial of radiation therapy with and without CCNU, vincristine, and prednisone.," *J. Neurosurg.*, vol. 72, no. 4, pp. 572–82, Apr. 1990.
- [72] D. M. Tait, H. Thornton-Jones, H. J. Bloom, J. Lemerle, and P. Morris-Jones, "Adjuvant chemotherapy for medulloblastoma: the first multi-centre control trial of the International Society of Paediatric Oncology (SIOP I).," *Eur. J. Cancer*, vol. 26, no. 4, pp. 464–9, Apr. 1990.
- [73] M. Deutsch, P. R. Thomas, J. Krischer, J. M. Boyett, L. Albright, P. Aronin, J. Langston, J. C. Allen, R. J. Packer, R. Linggood, R. Mulhern, P. Stanley, J. A. Stehbens, P. Duffner, L. Kun, L. Rorke, J. Cherlow, H. Freidman, J. L. Finlay, and T. Vietti, "Results of a prospective randomized trial comparing standard dose neuraxis irradiation (3,600 cGy/20) with reduced neuraxis irradiation (2,340 cGy/13) in patients with low-stage medulloblastoma. A Combined Children's Cancer Group-Pediatric Oncology Group," *Pediatr. Neurosurg.*, vol. 24, no. 4, pp. 167–176; discussion 176–7, Jan. 1996.
- [74] R. E. Taylor, C. C. Bailey, K. Robinson, C. L. Weston, D. Ellison, J. Ironside, H. Lucraft, R. Gilbertson, D. M. Tait, D. A. Walker, B. L. Pizer, J. Imeson, and L. S. Lashford, "Results of a randomized study of preradiation chemotherapy versus radiotherapy alone for nonmetastatic medulloblastoma: The International Society of Paediatric Oncology/United Kingdom Children's Cancer Study Group PNET-3 Study.," *J. Clin. Oncol.*, vol. 21, no. 8, pp. 1581–91, Apr. 2003.
- [75] R. J. Packer, J. Goldwein, H. S. Nicholson, L. G. Vezina, J. C. Allen, M. D. Ris, K. Muraszko, L. B. Rorke, W. M. Wara, B. H. Cohen, and J. M. Boyett, "Treatment of children with medulloblastomas with reduced-dose craniospinal radiation therapy and adjuvant chemotherapy: A Children's Cancer Group Study.," *J. Clin. Oncol.*, vol. 17, no. 7, pp. 2127–36, Jul. 1999.
- [76] B. Lannering, S. Rutkowski, F. Doz, B. Pizer, G. Gustafsson, A. Navajas, M. Massimino, R. Reddingius, M. Benesch, C. Carrie, R. Taylor, L. Gandola, T. Björk-Eriksson, J. Giralt, F. Oldenburger, T.

References

- Pietsch, D. Figarella-Branger, K. Robson, M. Forni, S. C. Clifford, M. Warmuth-Metz, K. von Hoff, A. Faldum, V. Mosseri, and R. Kortmann, "Hyperfractionated versus conventional radiotherapy followed by chemotherapy in standard-risk medulloblastoma: results from the randomized multicenter HIT-SIOP PNET 4 trial.," *J. Clin. Oncol.*, vol. 30, no. 26, pp. 3187–93, Sep. 2012.
- [77] M. D. Ris, K. Walsh, D. Wallace, F. D. Armstrong, E. Holmes, A. Gajjar, T. Zhou, and R. J. Packer, "Intellectual and academic outcome following two chemotherapy regimens and radiotherapy for average-risk medulloblastoma: COG A9961.," *Pediatr. Blood Cancer*, vol. 60, no. 8, pp. 1350–7, Aug. 2013.
- [78] R. E. Taylor, C. C. Bailey, K. J. Robinson, C. L. Weston, D. A. Walker, D. Ellison, J. Ironside, B. L. Pizer, and L. S. Lashford, "Outcome for patients with metastatic (M2-3) medulloblastoma treated with SIOP/UKCCSG PNET-3 chemotherapy.," *Eur. J. Cancer*, vol. 41, no. 5, pp. 727–34, Mar. 2005.
- [79] A. Gajjar, M. Chintagumpala, D. Ashley, S. Kellie, L. E. Kun, T. E. Merchant, S. Woo, G. Wheeler, V. Ahern, M. J. Krasin, M. Fouladi, A. Broniscer, R. Krance, G. A. Hale, C. F. Stewart, R. Dauser, R. A. Sanford, C. Fuller, C. Lau, J. M. Boyett, D. Wallace, and R. J. Gilbertson, "Risk-adapted craniospinal radiotherapy followed by high-dose chemotherapy and stem-cell rescue in children with newly diagnosed medulloblastoma (St Jude Medulloblastoma-96): long-term results from a prospective, multicentre trial.," *Lancet. Oncol.*, vol. 7, no. 10, pp. 813–20, Oct. 2006.
- [80] R. I. Jakacki, P. C. Burger, T. Zhou, E. J. Holmes, M. Kocak, A. Onar, J. Goldwein, M. Mehta, R. J. Packer, N. Tarbell, C. Fitz, G. Vezina, J. Hilden, and I. F. Pollack, "Outcome of children with metastatic medulloblastoma treated with carboplatin during craniospinal radiotherapy: a Children's Oncology Group Phase I/II study.," *J. Clin. Oncol.*, vol. 30, no. 21, pp. 2648–53, Jul. 2012.
- [81] A. O. von Bueren, K. von Hoff, T. Pietsch, N. U. Gerber, M. Warmuth-Metz, F. Deinlein, I. Zwiener, A. Faldum, G. Fleischhack, M. Benesch, J. Krauss, J. Kuehl, R. D. Kortmann, and S. Rutkowski, "Treatment of young children with localized medulloblastoma by chemotherapy alone: results of the prospective, multicenter trial HIT 2000 confirming the prognostic impact of histology.," *Neuro. Oncol.*, vol. 13, no. 6, pp. 669–79, Jun. 2011.
- [82] D. D. Shen, A. a Artru, and K. K. Adkison, "Principles and applicability of CSF sampling for the assessment of CNS drug delivery and pharmacodynamics.," *Adv. Drug Deliv. Rev.*, vol. 56, no. 12, pp. 1825–57, Oct. 2004.
- [83] J. F. Deeken and W. Löscher, "The blood-brain barrier and cancer: transporters, treatment, and Trojan horses.," *Clin. Cancer Res.*, vol. 13, no. 6, pp. 1663–74, Mar. 2007.

References

- [84] D. J. Stewart, "A critique of the role of the blood-brain barrier in the chemotherapy of human brain tumors," *J. Neurooncol.*, vol. 20, no. 2, pp. 121–139, 1994.
- [85] P. A. Stewart, K. Hayakawa, C. L. Farrell, and R. F. Del Maestro, "Quantitative study of microvessel ultrastructure in human peritumoral brain tissue. Evidence for a blood-brain barrier defect.," *J. Neurosurg.*, vol. 67, no. 5, pp. 697–705, Nov. 1987.
- [86] Y. Boucher, L. T. Baxter, and R. K. Jain, "Interstitial pressure gradients in tissue-isolated and subcutaneous tumors: implications for therapy.," *Cancer Res.*, vol. 50, no. 15, pp. 4478–84, Aug. 1990.
- [87] R. D. Zhang, J. E. Price, T. Fujimaki, C. D. Bucana, and I. J. Fidler, "Differential permeability of the blood-brain barrier in experimental brain metastases produced by human neoplasms implanted into nude mice.," *Am. J. Pathol.*, vol. 141, no. 5, pp. 1115–24, Nov. 1992.
- [88] H. W. C. Ward, "CCNU in treatment of recurrent medulloblastoma," *Br. Med. Journal*, vol. 1, no. 5908, p. 642, 1974.
- [89] H. H. Hansen, O. S. Selawry, F. M. Muggia, and M. D. Walker, "Clinical studies with 1-(2-chloroethyl)-3-cyclohexyl-1-nitrosourea (NSC 79037).," *Cancer Res.*, vol. 31, no. 3, pp. 223–7, Mar. 1971.
- [90] D. Fewer, C. B. Wilson, E. B. Boldrey, and J. K. Enot, "Phase II study of 1-(2-chloroethyl)-3-cyclohexyl-1-nitrosourea (CCNU; NSC-79037) in the treatment of brain tumors.," *Cancer Chemother. Rep.*, vol. 56, no. 3, pp. 421–7, Jun. 1972.
- [91] A. Gilman and F. S. Philips, "The Biological Actions and Therapeutic Applications of the B-Chloroethyl Amines and Sulfides.," *Science*, vol. 103, no. 2675, pp. 409–36, Apr. 1946.
- [92] J. G. MacFarland, M. C. Kirk, and D. B. Ludlum, "Mechanism of action of the nitrosoureas—IV," *Biochem. Pharmacol.*, vol. 39, no. 1, pp. 33–36, Jan. 1990.
- [93] J. R. Silber, B. A. Mueller, T. G. Ewers, and M. S. Berger, "Comparison of O6-methylguanine-DNA methyltransferase activity in brain tumors and adjacent normal brain.," *Cancer Res.*, vol. 53, no. 14, pp. 3416–20, Jul. 1993.
- [94] M. L. Meistrich, "Male gonadal toxicity.," *Pediatr. Blood Cancer*, vol. 53, no. 2, pp. 261–6, Aug. 2009.
- [95] D. M. Green, T. Kawashima, M. Stovall, W. Leisenring, C. A. Sklar, A. C. Mertens, S. S. Donaldson, J. Byrne, and L. L. Robison, "Fertility of female survivors of childhood cancer: a report from the

References

- childhood cancer survivor study.," *J. Clin. Oncol.*, vol. 27, no. 16, pp. 2677–85, Jun. 2009.
- [96] L. Hilal-Dandan, Randa; Brunton, *Goodman and Gilman Manual of Pharmacology and Therapeutics, Second Edition*. McGraw-Hill Professional, 2013.
- [97] E. H. Graul, E. Schaumlöffel, H. Hundeshagen, H. Wilmanns, and G. Simon, "Metabolism of radioactive cyclophosphamide. Animal tests and clinical studies.," *Cancer*, vol. 20, no. 5, pp. 896–9, May 1967.
- [98] S. Genka, J. Deutsch, P. L. Stahle, U. H. Shetty, V. John, C. Robinson, S. I. Rapoport, and N. H. Greig, "Brain and plasma pharmacokinetics and anticancer activities of cyclophosphamide and phosphoramidate mustard in the rat.," *Cancer Chemother. Pharmacol.*, vol. 27, no. 1, pp. 1–7, Jan. 1990.
- [99] R. J. Packer, A. Gajjar, G. Vezina, L. Rorke-Adams, P. C. Burger, P. L. Robertson, L. Bayer, D. LaFond, B. R. Donahue, M. H. Marymont, K. Muraszko, J. Langston, and R. Sposto, "Phase III Study of Craniospinal Radiation Therapy Followed by Adjuvant Chemotherapy for Newly Diagnosed Average-Risk Medulloblastoma.," *J. Clin. Oncol.*, vol. 24, no. 25, pp. 4202–4208, Sep. 2006.
- [100] W. G. Bradley, L. P. Lassman, G. W. Pearce, and J. N. Walton, "The neuromyopathy of vincristine in man," *J. Neurol. Sci.*, vol. 10, no. 2, pp. 107–131, Feb. 1970.
- [101] P. H. Hilkens and M. J. van den Bent, "Chemotherapy-induced peripheral neuropathy.," *J. Peripher. Nerv. Syst.*, vol. 2, no. 4, pp. 350–61, Jan. 1997.
- [102] S. M. El Dareer, V. M. White, F. P. Chen, L. B. Mellet, and D. L. Hill, "Distribution and metabolism of vincristine in mice, rats, dogs, and monkeys.," *Cancer Treat. Rep.*, vol. 61, no. 7, pp. 1269–77, Oct. 1977.
- [103] A. Alcaraz, C. Rey, A. Concha, and A. Medina, "Intrathecal vincristine: fatal myeloencephalopathy despite cerebrospinal fluid perfusion.," *J. Toxicol. Clin. Toxicol.*, vol. 40, no. 5, pp. 557–61, Jan. 2002.
- [104] D. X. Qin, R. Zheng, J. Tang, J. X. Li, and Y. H. Hu, "Influence of radiation on the blood-brain barrier and optimum time of chemotherapy.," *Int. J. Radiat. Oncol. Biol. Phys.*, vol. 19, no. 6, pp. 1507–10, Dec. 1990.
- [105] F. Wang, F. Zhou, G. D. Kruh, and J. M. Gallo, "Influence of blood-brain barrier efflux pumps on the distribution of vincristine in brain and brain tumors.," *Neuro. Oncol.*, vol. 12, no. 10, pp. 1043–9, Oct. 2010.

References

- [106] F. M. Boyle, S. L. Eller, and S. A. Grossman, "Penetration of intra-arterially administered vincristine in experimental brain tumor.," *Neuro. Oncol.*, vol. 6, no. 4, pp. 300–5, Oct. 2004.
- [107] D. J. Stewart, K. Lu, R. S. Benjamin, M. E. Leavens, M. Luna, H. Y. Yap, and T. L. Loo, "Concentration of vinblastine in human intracerebral tumor and other tissues.," *J. Neurooncol.*, vol. 1, no. 2, pp. 139–44, Jan. 1983.
- [108] S. J. Kellie, D. Barbaric, P. Koopmans, J. Earl, D. J. Carr, and S. S. N. de Graaf, "Cerebrospinal fluid concentrations of vincristine after bolus intravenous dosing: a surrogate marker of brain penetration.," *Cancer*, vol. 94, no. 6, pp. 1815–20, Mar. 2002.
- [109] D. J. Stewart, J. M. Molepo, R. M. Green, V. A. Montpetit, H. Hugenholtz, A. Lamothe, N. Z. Mikhael, M. D. Redmond, M. Gadia, and R. Goel, "Factors affecting platinum concentrations in human surgical tumour specimens after cisplatin.," *Br. J. Cancer*, vol. 71, no. 3, pp. 598–604, Mar. 1995.
- [110] Z. H. Siddik, "Cisplatin: mode of cytotoxic action and molecular basis of resistance.," *Oncogene*, vol. 22, no. 47, pp. 7265–79, Oct. 2003.
- [111] D. A. Walker, J. Pillow, K. D. Waters, and E. Keir, "Enhanced cisplatin ototoxicity in children with brain tumours who have received simultaneous or prior cranial irradiation.," *Med. Pediatr. Oncol.*, vol. 17, no. 1, pp. 48–52, Jan. 1989.
- [112] P. R. Brock, K. R. Knight, D. R. Freyer, K. C. M. Campbell, P. S. Steyger, B. W. Blakley, S. R. Rassekh, K. W. Chang, B. J. Fligor, K. Rajput, M. Sullivan, and E. A. Neuwelt, "Platinum-induced ototoxicity in children: a consensus review on mechanisms, predisposition, and protection, including a new International Society of Pediatric Oncology Boston ototoxicity scale.," *J. Clin. Oncol.*, vol. 30, no. 19, pp. 2408–17, Jul. 2012.
- [113] L. Gandola, M. Massimino, G. Cefalo, C. Solero, F. Spreafico, E. Pecori, D. Riva, P. Collini, E. Pignoli, F. Giangaspero, R. Luksch, S. Berretta, G. Poggi, V. Biassoni, A. Ferrari, B. Pollo, C. Favre, I. Sardi, M. Terenziani, and F. Fossati-Bellani, "Hyperfractionated accelerated radiotherapy in the Milan strategy for metastatic medulloblastoma.," *J. Clin. Oncol.*, vol. 27, no. 4, pp. 566–71, Feb. 2009.
- [114] S. Rutkowski, U. Bode, F. Deinlein, H. Ottensmeier, M. Warmuth-Metz, N. Soerensen, N. Graf, A. Emser, T. Pietsch, J. E. A. Wolff, R. D. Kortmann, and J. Kuehl, "Treatment of early childhood medulloblastoma by postoperative chemotherapy alone.," *N. Engl. J. Med.*, vol. 352, no. 10, pp. 978–86, Mar. 2005.

References

- [115] T. J. MacDonald, D. Aguilera, and R. C. Castellino, "The rationale for targeted therapies in medulloblastoma.," *Neuro. Oncol.*, vol. 16, no. 1, pp. 9–20, Jan. 2014.
- [116] S. Partap, P. A. Murphy, H. Vogel, P. D. Barnes, M. S. B. Edwards, and P. G. Fisher, "Liposomal cytarabine for central nervous system embryonal tumors in children and young adults.," *J. Neurooncol.*, vol. 103, no. 3, pp. 561–6, Jul. 2011.
- [117] P. Gaviani, E. Corsini, A. Salmaggi, E. Lamperti, A. Botturi, A. Erbetta, I. Milanese, F. Legnani, B. Pollo, and A. Silvani, "Liposomal cytarabine in neoplastic meningitis from primary brain tumors: a single institutional experience.," *Neurol. Sci.*, vol. 34, no. 12, pp. 2151–7, Dec. 2013.
- [118] M. C. Chamberlain, "Neurotoxicity of intra-CSF liposomal cytarabine (DepoCyt) administered for the treatment of leptomeningeal metastases: a retrospective case series.," *J. Neurooncol.*, vol. 109, no. 1, pp. 143–8, Aug. 2012.
- [119] A. van der Gaast, P. Sonneveld, D. R. Mans, and T. A. Splinter, "Intrathecal administration of etoposide in the treatment of malignant meningitis: feasibility and pharmacokinetic data.," *Cancer Chemother. Pharmacol.*, vol. 29, no. 4, pp. 335–7, Jan. 1992.
- [120] G. Fleischhack, S. Reif, C. Hasan, U. Jaehde, S. Hettmer, and U. Bode, "Feasibility of intraventricular administration of etoposide in patients with metastatic brain tumours," *Br. J. Cancer*, vol. 84, no. February 1998, pp. 1453–1459, 2001.
- [121] I. Slavc, E. Schuller, J. Falger, M. Günes, K. Pillwein, T. Czech, W. Dietrich, K. Rössler, K. Dieckmann, D. Prayer, and J. Hainfellner, "Feasibility of long-term intraventricular therapy with mafosfamide (n = 26) and etoposide (n = 11): experience in 26 children with disseminated malignant brain tumors.," *J. Neurooncol.*, vol. 64, no. 3, pp. 239–47, Sep. 2003.
- [122] A. Peyrl, M. Chocholous, M. W. Kieran, A. A. Azizi, C. Prucker, T. Czech, K. Dieckmann, M. Schmook, C. Haberler, U. Leiss, and I. Slavc, "Antiangiogenic Metronomic Therapy for Children With Recurrent Embryonal Brain Tumors," no. July 2011, pp. 511–517, 2012.
- [123] S. M. Blaney, M. Kocak, A. Gajjar, M. Chintagumpala, T. Merchant, M. Kieran, I. F. Pollack, S. Gururangan, R. Geyer, P. Phillips, R. E. McLendon, R. Packer, S. Goldman, A. Banerjee, R. Heideman, J. M. Boyett, and L. Kun, "Pilot study of systemic and intrathecal mafosfamide followed by conformal radiation for infants with intracranial central nervous system tumors: a pediatric brain tumor

References

- consortium study (PBTC-001).," *J. Neurooncol.*, vol. 109, no. 3, pp. 565–71, Sep. 2012.
- [124] B. L. Pierquin, "Past, present and future of interstitial radiation therapy," *Int. J. Radiat. Oncol.*, vol. 9, no. 8, pp. 1237–1242, Aug. 1983.
- [125] D. E. Spratt, Z. S. Zumsteg, P. Ghadjar, M. A. Kollmeier, X. Pei, G. Cohen, W. Polkinghorn, Y. Yamada, and M. J. Zelefsky, "Comparison of high-dose (86.4 Gy) IMRT vs combined brachytherapy plus IMRT for intermediate-risk prostate cancer.," *BJU Int.*, vol. 114, no. 3, pp. 360–7, Sep. 2014.
- [126] F. El Majdoub, T. Simon, M. Hoevels, F. Berthold, V. Sturm, and M. Maarouf, "Interstitial brachytherapy using stereotactic implanted (125)iodine seeds for recurrent medulloblastoma.," *Clin. Oncol. (R. Coll. Radiol.)*, vol. 23, no. 8, pp. 532–7, Oct. 2011.
- [127] T. A. Chan, J. D. Weingart, M. Parisi, M. A. Hughes, A. Olivi, S. Borzillary, D. Alahakone, N. A. Detorie, M. D. Wharam, and L. Kleinberg, "Treatment of recurrent glioblastoma multiforme with GliSite brachytherapy.," *Int. J. Radiat. Oncol. Biol. Phys.*, vol. 62, no. 4, pp. 1133–9, Jul. 2005.
- [128] H. Norrell, "Brain Tumor Chemotherapy With Methotrexate Given Intrathecally," *JAMA*, vol. 201, no. 1, p. 15, Jul. 1967.
- [129] A. Hindle, "Intrathecal opioids in the management of acute postoperative pain," *Contin. Educ. Anaesthesia, Crit. Care Pain*, vol. 8, no. 3, pp. 81–85, May 2008.
- [130] J. G. McGivern, "Ziconotide: a review of its pharmacology and use in the treatment of pain.," *Neuropsychiatr. Dis. Treat.*, vol. 3, no. 1, pp. 69–85, Feb. 2007.
- [131] D. Guillaume, A. Van Havenbergh, M. Vloeberghs, J. Vidal, and G. Roeste, "A clinical study of intrathecal baclofen using a programmable pump for intractable spasticity.," *Arch. Phys. Med. Rehabil.*, vol. 86, no. 11, pp. 2165–71, Nov. 2005.
- [132] S. Conroy, M. Garnett, M. Vloeberghs, R. Grundy, I. Craven, and D. Walker, "Medulloblastoma in childhood: revisiting intrathecal therapy in infants and children," *Cancer Chemother. Pharmacol.*, vol. 65, no. 6, pp. 1173–1189, 2010.
- [133] J. A. Whiteside, "Intrathecal Amethopterin in Neurological Manifestations of Leukemia," *Arch. Intern. Med.*, vol. 101, no. 2, p. 279, Feb. 1958.

References

- [134] C. M. Filley and B. K. Kleinschmidt-DeMasters, "Toxic leukoencephalopathy.," *N. Engl. J. Med.*, vol. 345, no. 6, pp. 425–32, Aug. 2001.
- [135] D. Bhojwani, N. D. Sabin, D. Pei, J. J. Yang, R. B. Khan, J. C. Panetta, K. R. Krull, H. Inaba, J. E. Rubnitz, M. L. Metzger, S. C. Howard, R. C. Ribeiro, C. Cheng, W. E. Reddick, S. Jeha, J. T. Sandlund, W. E. Evans, C.-H. Pui, and M. V Relling, "Methotrexate-induced neurotoxicity and leukoencephalopathy in childhood acute lymphoblastic leukemia.," *J. Clin. Oncol.*, vol. 32, no. 9, pp. 949–59, Mar. 2014.
- [136] a. Shuper, B. Stark, L. Kornreich, I. J. Cohen, S. Aviner, a. Steinmetz, J. Stein, Y. Goshen, and I. Yaniv, "Methotrexate Treatment Protocols and the Central Nervous System: Significant Cure With Significant Neurotoxicity.," *J. Child Neurol.*, vol. 15, no. 9, pp. 573–580, Sep. 2000.
- [137] G. P. Bodey, E. J. Freireich, R. W. Monto, and J. S. Hewlett, "Cytosine arabinoside (NSC-63878) therapy for acute leukemia in adults.," *Cancer Chemother. Rep.*, vol. 53, no. 1, pp. 59–66, Feb. 1969.
- [138] M. P. Sullivan, T. E. Moon, R. Trueworthy, T. J. Vietti, G. B. Humphrey, and D. Komp, "Combination intrathecal therapy for meningeal leukemia: two versus three drugs.," *Blood*, vol. 50, no. 3, pp. 471–9, Sep. 1977.
- [139] Y. Matloub, S. Lindemulder, P. S. Gaynon, H. Sather, M. La, E. Broxson, R. Yanofsky, R. Hutchinson, N. A. Heerema, J. Nachman, M. Blake, L. M. Wells, A. D. Sorrell, M. Masterson, J. F. Kelleher, and L. C. Stork, "Intrathecal triple therapy decreases central nervous system relapse but fails to improve event-free survival when compared with intrathecal methotrexate: results of the Children's Cancer Group (CCG) 1952 study for standard-risk acute lymphoblastic leukemia.," *Blood*, vol. 108, no. 4, pp. 1165–73, Aug. 2006.
- [140] C.-H. Pui, D. Campana, D. Pei, W. P. Bowman, J. T. Sandlund, S. C. Kaste, R. C. Ribeiro, J. E. Rubnitz, S. C. Raimondi, M. Onciu, E. Coustan-Smith, L. E. Kun, S. Jeha, C. Cheng, S. C. Howard, V. Simmons, A. Bayles, M. L. Metzger, J. M. Boyett, W. Leung, R. Handgretinger, J. R. Downing, W. E. Evans, and M. V Relling, "Treating childhood acute lymphoblastic leukemia without cranial irradiation.," *N. Engl. J. Med.*, vol. 360, no. 26, pp. 2730–41, Jun. 2009.
- [141] N. J. Robison, F. Campigotto, S. N. Chi, P. E. Manley, C. D. Turner, A. Zimmerman, C. A. Chordas, A. M. Werger, J. C. Allen, S. Goldman, J. B. Rubin, M. S. Isakoff, W. J. Pan, Z. A. Khatib, M. A. Comito, A. E. Bendel, J. B. Pietrantonio, L. Kondrat, S. M. Hubbs, D. S. Neuberg, and M. W. Kieran, "A Phase II Trial of a Multi-Agent

References

- Oral Antiangiogenic (Metronomic) Regimen in Children With Recurrent or Progressive Cancer," no. October 2013, pp. 636–642, 2014.
- [142] W. P. O'Meara, S. a Borkar, H. E. Stambuk, and S. C. Lymberis, "Leptomeningeal metastasis.," *Curr. Probl. Cancer*, vol. 31, no. 6, pp. 367–424, 2007.
- [143] W. Boogerd, "Leptomeningeal metastasis in solid tumours : I s there a role for intrathecal therapy?"
- [144] L. Marelli, R. Stigliano, C. Triantos, M. Senzolo, E. Cholongitas, N. Davies, J. Tibballs, T. Meyer, D. W. Patch, and A. K. Burroughs, "Transarterial therapy for hepatocellular carcinoma: Which technique is more effective? A systematic review of cohort and randomized studies," *Cardiovasc. Intervent. Radiol.*, vol. 30, no. 1, pp. 6–25, 2007.
- [145] G. Becker, T. Soezgen, M. Olschewski, J. Laubenberger, H. E. Blum, and H.-P. Allgaier, "Combined TACE and PEI for palliative treatment of unresectable hepatocellular carcinoma.," *World J. Gastroenterol.*, vol. 11, no. 39, pp. 6104–9, Oct. 2005.
- [146] J. B. Wolinsky, Y. L. Colson, and M. W. Grinstaff, "Local drug delivery strategies for cancer treatment: gels, nanoparticles, polymeric films, rods, and wafers.," *J. Control. Release*, vol. 159, no. 1, pp. 14–26, Apr. 2012.
- [147] B. A. Almond, A. R. Hadba, S. T. Freeman, B. J. Cuevas, A. M. York, C. J. Detrisac, and E. P. Goldberg, "Efficacy of mitoxantrone-loaded albumin microspheres for intratumoral chemotherapy of breast cancer," *J. Control. Release*, vol. 91, no. 1–2, Sp. Iss. SI, pp. 147–155, 2003.
- [148] G. M. Zentner, R. Rathi, C. Shih, J. C. McRea, M. H. Seo, H. Oh, B. G. Rhee, J. Mestecky, Z. Moldoveanu, M. Morgan, and S. Weitman, "Biodegradable block copolymers for delivery of proteins and water-insoluble drugs," *J. Control. Release*, vol. 72, no. 1–3, pp. 203–215, 2001.
- [149] B. A. Hrycushko, S. Li, B. Goins, R. A. Otto, and A. Bao, "Direct intratumoral infusion of liposome encapsulated rhenium radionuclides for cancer therapy: Effects of nonuniform intratumoral dose distribution," *Med. Phys.*, vol. 38, no. 3, pp. 1339–1347, 2011.
- [150] T. Takahashi, S. Ueda, K. Kono, and S. Majima, "Attempt at local administration of anticancer agents in form of fat emulsion," *Cancer*, vol. 38, no. 4, pp. 1507–1514, 1976.

References

- [151] A. P. Theon, J. R. Pascoe, G. P. Carlson, and D. N. Krag, "Intratumoral Chemotherapy With Cisplatin In Oily Emulsion In Horses," *J. Am. Vet. Med. Assoc.*, vol. 202, no. 2, pp. 261–267, 1993.
- [152] A. P. Theon, W. D. Wilson, K. G. Magdesian, N. Pusterla, J. R. Snyder, and L. D. Galuppo, "Long-term outcome associated with intratumoral chemotherapy with cisplatin for cutaneous tumors in equidae: 573 cases (1995-2004)," *J. Am. Vet. Med. Assoc.*, vol. 230, no. 10, pp. 1506–1513, 2007.
- [153] B. Laquente, C. Lacasa, M. M. Ginestà, O. Casanovas, A. Figueras, M. Galán, I. G. Ribas, J. R. Germà, G. Capellà, and F. Viñals, "Antiangiogenic effect of gemcitabine following metronomic administration in a pancreas cancer model.," *Mol. Cancer Ther.*, vol. 7, no. 3, pp. 638–47, Mar. 2008.
- [154] R. Colombo, L. F. Da Pozzo, A. Salonia, P. Rigatti, Z. Leib, J. Baniel, E. Caldarella, and M. Pavone-Macaluso, "Multicentric study comparing intravesical chemotherapy alone and with local microwave hyperthermia for prophylaxis of recurrence of superficial transitional cell carcinoma.," *J. Clin. Oncol.*, vol. 21, no. 23, pp. 4270–6, Dec. 2003.
- [155] A. Ojea, J. L. Nogueira, E. Solsona, N. Flores, J. M. F. Gómez, J. R. Molina, V. Chantada, J. E. Camacho, L. M. Piñeiro, R. H. Rodríguez, S. Isorna, M. Blas, J. A. Martínez-Piñeiro, and R. Madero, "A multicentre, randomised prospective trial comparing three intravesical adjuvant therapies for intermediate-risk superficial bladder cancer: low-dose bacillus Calmette-Guerin (27 mg) versus very low-dose bacillus Calmette-Guerin (13.5 mg) versus mitomycin," *Eur. Urol.*, vol. 52, no. 5, pp. 1398–406, Nov. 2007.
- [156] M. Babjuk, M. Burger, R. Zigeuner, S. F. Shariat, B. W. G. van Rhijn, E. Compérat, R. J. Sylvester, E. Kaasinen, A. Böhle, J. Palou Redorta, and M. Rouprêt, "EAU guidelines on non-muscle-invasive urothelial carcinoma of the bladder: update 2013.," *Eur. Urol.*, vol. 64, no. 4, pp. 639–53, Oct. 2013.
- [157] R. J. Tamargo, J. S. Myseros, J. I. Epstein, M. B. Yang, M. Chasin, and H. Brem, "Interstitial chemotherapy of the 9L gliosarcoma: controlled release polymers for drug delivery in the brain.," *Cancer Res.*, vol. 53, no. 2, pp. 329–33, Jan. 1993.
- [158] H. C. Lawson, P. Sampath, E. Bohan, M. C. Park, N. Hussain, A. Olivi, J. Weingart, L. Kleinberg, and H. Brem, "Interstitial chemotherapy for malignant gliomas: the Johns Hopkins experience.," *J. Neurooncol.*, vol. 83, no. 1, pp. 61–70, May 2007.
- [159] M. Westphal, D. C. Hilt, E. Bortey, P. Delavault, R. Olivares, P. C. Warnke, I. R. Whittle, J. Jaaskelainen, and Z. Ram, "A phase 3 trial

References

- of local chemotherapy with biodegradable carmustine (BCNU) wafers (Gliadel wafers) in patients with primary malignant glioma," *Neuro. Oncol.*, vol. 5, no. 2, pp. 79–88, 2003.
- [160] L. K. Fung, M. Shin, B. Tyler, H. Brem, and W. M. Saltzman, "Chemotherapeutic drugs released from polymers: distribution of 1,3-bis(2-chloroethyl)-1-nitrosourea in the rat brain.," *Pharm. Res.*, vol. 13, no. 5, pp. 671–82, May 1996.
- [161] M. G. Hart, R. Grant, R. Garside, G. Rogers, M. Somerville, and K. Stein, "Chemotherapy wafers for high grade glioma.," *Cochrane database Syst. Rev.*, no. 3, p. CD007294, Jan. 2011.
- [162] N. U. Barua, S. P. Lewis, M. Woolley, S. O'Sullivan, R. Harrison, and S. S. Gill, "Robot-guided convection-enhanced delivery of carboplatin for advanced brainstem glioma.," *Acta Neurochir. (Wien)*, vol. 155, no. 8, pp. 1459–65, Aug. 2013.
- [163] N. U. Barua, S. S. Gill, and S. Love, "Convection-enhanced drug delivery to the brain: therapeutic potential and neuropathological considerations.," *Brain Pathol.*, vol. 24, no. 2, pp. 117–27, Mar. 2014.
- [164] D. R. Groothuis, H. Benalcazar, C. V. Allen, R. M. Wise, C. Dills, C. Dobrescu, V. Rothholtz, and R. M. Levy, "Comparison of cytosine arabinoside delivery to rat brain by intravenous, intrathecal, intraventricular and intraparenchymal routes of administration.," *Brain Res.*, vol. 856, no. 1–2, pp. 281–90, Feb. 2000.
- [165] R. H. Bobo, D. W. Laske, A. Akbasak, P. F. Morrison, R. L. Dedrick, and E. H. Oldfield, "Convection-enhanced delivery of macromolecules in the brain.," *Proc. Natl. Acad. Sci. U. S. A.*, vol. 91, no. 6, pp. 2076–80, Mar. 1994.
- [166] V. Loczenski Rose, G. S. Winkler, S. Allen, S. Puri, and G. Mantovani, "Polymer siRNA conjugates synthesised by controlled radical polymerisation," *Eur. Polym. J.*, vol. 49, no. 10, pp. 2861–2883, Oct. 2013.
- [167] E. Allard, C. Passirani, and J.-P. Benoit, "Convection-enhanced delivery of nanocarriers for the treatment of brain tumors.," *Biomaterials*, vol. 30, no. 12, pp. 2302–18, Apr. 2009.
- [168] J. H. Sampson, G. Archer, C. Pedain, E. Wembacher-Schröder, M. Westphal, S. Kunwar, M. A. Vogelbaum, A. Coan, J. E. Herndon, R. Raghavan, M. L. Brady, D. A. Reardon, A. H. Friedman, H. S. Friedman, M. I. Rodríguez-Ponce, S. M. Chang, S. Mittermeyer, D. Croteau, and R. K. Puri, "Poor drug distribution as a possible explanation for the results of the PRECISE trial.," *J. Neurosurg.*, vol. 113, no. 2, pp. 301–9, Aug. 2010.

References

- [169] V. Varenika, P. Dickinson, J. Bringas, R. LeCouteur, R. Higgins, J. Park, M. Fiandaca, M. Berger, J. Sampson, and K. Bankiewicz, "Detection of infusate leakage in the brain using real-time imaging of convection-enhanced delivery.," *J. Neurosurg.*, vol. 109, no. 5, pp. 874–80, Nov. 2008.
- [170] A. B. Fleming and W. M. Saltzman, "Pharmacokinetics of the carmustine implant.," *Clin. Pharmacokinet.*, vol. 41, no. 6, pp. 403–19, Jan. 2002.
- [171] R. Saito, M. T. Krauze, C. O. Noble, M. Tamas, D. C. Drummond, D. B. Kirpotin, M. S. Berger, J. W. Park, and K. S. Bankiewicz, "Tissue affinity of the infusate affects the distribution volume during convection-enhanced delivery into rodent brains: implications for local drug delivery.," *J. Neurosci. Methods*, vol. 154, no. 1–2, pp. 225–32, Jun. 2006.
- [172] L. Vargová, A. Homola, J. Zámecník, M. Tichý, V. Benes, and E. Syková, "Diffusion parameters of the extracellular space in human gliomas.," *Glia*, vol. 42, no. 1, pp. 77–88, Apr. 2003.
- [173] E. A. Nance, G. F. Woodworth, K. A. Sailor, T.-Y. Shih, Q. Xu, G. Swaminathan, D. Xiang, C. Eberhart, and J. Hanes, "A dense poly(ethylene glycol) coating improves penetration of large polymeric nanoparticles within brain tissue.," *Sci. Transl. Med.*, vol. 4, no. 149, p. 149ra119, Aug. 2012.
- [174] L. Eikenes, M. Tari, I. Tufto, O. S. Bruland, and C. de Lange Davies, "Hyaluronidase induces a transcapillary pressure gradient and improves the distribution and uptake of liposomal doxorubicin (Caelyx) in human osteosarcoma xenografts.," *Br. J. Cancer*, vol. 93, no. 1, pp. 81–8, Jul. 2005.
- [175] T. D. McKee, P. Grandi, W. Mok, G. Alexandrakis, N. Insin, J. P. Zimmer, M. G. Bawendi, Y. Boucher, X. O. Breakefield, and R. K. Jain, "Degradation of fibrillar collagen in a human melanoma xenograft improves the efficacy of an oncolytic herpes simplex virus vector.," *Cancer Res.*, vol. 66, no. 5, pp. 2509–13, Mar. 2006.
- [176] P. Kallinteri, S. Higgins, G. A. Hutcheon, C. B. St. Pourçain, and M. C. Garnett, "Novel Functionalized Biodegradable Polymers for Nanoparticle Drug Delivery Systems," *Biomacromolecules*, vol. 6, no. 4, pp. 1885–1894, 2005.
- [177] W. Meng, "Evaluation of a nanoparticle drug delivery vehicle in medulloblastoma and organotypic brain cell cultures," University of Nottingham, 2006.
- [178] W. Meng, P. Kallinteri, D. A. Walker, T. L. Parker, and M. C. Garnett, "Evaluation of poly (glycerol-adipate) nanoparticle uptake

References

- in an in vitro 3-D brain tumor co-culture model.," *Exp. Biol. Med. (Maywood)*, vol. 232, no. 8, pp. 1100–8, Sep. 2007.
- [179] W. Meng, T. L. Parker, P. Kallinteri, D. A. Walker, S. Higgins, G. A. Hutcheon, and M. C. Garnett, "Uptake and metabolism of novel biodegradable poly (glycerol-adipate) nanoparticles in DAOY monolayer," *J. Control. Release*, vol. 116, no. 3, pp. 314–321, 2006.
- [180] S. Puri, "Novel functionalized polymers for nanoparticle formulations with anti cancer drugs," University of Nottingham, 2007.
- [181] F. Lapierre, S. D'Houtaud, and M. Wager, "Hemostatic Agents in Neurosurgery," in *Explicative Cases of Controversial Issues in Neurosurgery*, F. Signorelli, Ed. InTech, 2012.
- [182] W. Volker, H. Bärbel, and G. Sibylle, "Nanomedicine - Drivers for Development and Possible Impacts." OPOCE, 21-Jul-2008.
- [183] C. A. Lipinski, F. Lombardo, B. W. Dominy, and P. J. Feeney, "Experimental and computational approaches to estimate solubility and permeability in drug discovery and development settings.," *Adv. Drug Deliv. Rev.*, vol. 46, no. 1–3, pp. 3–26, Mar. 2001.
- [184] M. C. Garnett and P. Kallinteri, "Nanomedicines and nanotoxicology: some physiological principles.," *Occup. Med. (Lond)*, vol. 56, no. 5, pp. 307–11, Aug. 2006.
- [185] R. Duncan and M. J. Vicent, "Polymer therapeutics-prospects for 21st century: the end of the beginning.," *Adv. Drug Deliv. Rev.*, vol. 65, no. 1, pp. 60–70, Jan. 2013.
- [186] L. Illum, "Is nose-to-brain transport of drugs in man a reality?," *J. Pharm. Pharmacol.*, vol. 56, no. 1, pp. 3–17, Jan. 2004.
- [187] T. Siegal, "Which drug or drug delivery system can change clinical practice for brain tumor therapy?," *Neuro. Oncol.*, vol. 15, no. 6, pp. 656–69, Jun. 2013.
- [188] E. Garcia-Garcia, K. Andrieux, S. Gil, and P. Couvreur, "Colloidal carriers and blood-brain barrier (BBB) translocation: a way to deliver drugs to the brain?," *Int. J. Pharm.*, vol. 298, no. 2, pp. 274–92, Jul. 2005.
- [189] Y. Matsumura and H. Maeda, "A new concept for macromolecular therapeutics in cancer chemotherapy: mechanism of tumoritropic accumulation of proteins and the antitumor agent smancs.," *Cancer Res.*, vol. 46, no. 12 Pt 1, pp. 6387–92, Dec. 1986.

References

- [190] M. C. Garnett, "Targeted drug conjugates: principles and progress.," *Adv. Drug Deliv. Rev.*, vol. 53, no. 2, pp. 171–216, Dec. 2001.
- [191] J. P. Mach, S. Carrel, M. Forni, J. Ritschard, A. Donath, and P. Alberto, "Tumor localization of radiolabeled antibodies against carcinoembryonic antigen in patients with carcinoma: a critical evaluation.," *N. Engl. J. Med.*, vol. 303, no. 1, pp. 5–10, Jul. 1980.
- [192] Y. Mosesson, G. B. Mills, and Y. Yarden, "Derailed endocytosis: an emerging feature of cancer.," *Nat. Rev. Cancer*, vol. 8, no. 11, pp. 835–50, Nov. 2008.
- [193] C. de Duve, T. de Barsey, B. Poole, A. Trouet, P. Tulkens, and F. Van Hoof, "Commentary. Lysosomotropic agents.," *Biochem. Pharmacol.*, vol. 23, no. 18, pp. 2495–531, Sep. 1974.
- [194] A. Trouet, D. Deprez-de Campeneere, and C. De Duve, "Chemotherapy through lysosomes with a DNA-daunorubicin complex.," *Nat. New Biol.*, vol. 239, no. 91, pp. 110–2, Sep. 1972.
- [195] M. E. Favretto, S. Marouf, P. Ioannou, S. G. Antimisiaris, T. L. Parker, and P. Kallinteri, "Arsonoliposomes for the potential treatment of medulloblastoma.," *Pharm. Res.*, vol. 26, no. 10, pp. 2237–46, Oct. 2009.
- [196] G. Sahay, D. Y. Alakhova, and A. V Kabanov, "Endocytosis of nanomedicines," *J. Control. Release*, vol. 145, no. 3, pp. 182–195 ST – Endocytosis of nanomedicines, 2010.
- [197] G. J. Doherty and H. T. McMahon, "Mechanisms of endocytosis.," *Annu. Rev. Biochem.*, vol. 78, pp. 857–902, Jan. 2009.
- [198] H. Karpen, J. Bukowski, T. Hughes, and M. Gailani, "Association of the Hedgehog Receptor Patched with Caveolin-1," *Pediatr. Res.*, vol. 45, no. 4, Part 2 of 2, p. 54A–54A, Apr. 1999.
- [199] H. Mao, A. M. Diehl, and Y.-X. Li, "Sonic hedgehog ligand partners with caveolin-1 for intracellular transport.," *Lab. Invest.*, vol. 89, no. 3, pp. 290–300, Mar. 2009.
- [200] G. Sahay, J. O. Kim, A. V Kabanov, and T. K. Bronich, "The exploitation of differential endocytic pathways in normal and tumor cells in the selective targeting of nanoparticulate chemotherapeutic agents.," *Biomaterials*, vol. 31, no. 5, pp. 923–33, Feb. 2010.
- [201] K. Altundag, D. S. Dede, and T. Purnak, "Albumin-bound paclitaxel (ABI-007; Abraxane) in the management of basal-like breast carcinoma.," *J. Clin. Pathol.*, vol. 60, no. 8, p. 958, Aug. 2007.

References

- [202] D. M. Ashley, L. Meier, T. Kerby, F. M. Zalduondo, H. S. Friedman, A. Gajjar, L. Kun, P. K. Duffner, S. Smith, and D. Longee, "Response of recurrent medulloblastoma to low-dose oral etoposide," *J. Clin. Oncol.*, vol. 14, no. 6, pp. 1922–1927, Jun. 1996.
- [203] M. N. Needle, P. T. Molloy, J. R. Geyer, A. Herman-Liu, J. B. Belasco, J. W. Goldwein, L. Sutton, and P. C. Phillips, "Phase II study of daily oral etoposide in children with recurrent brain tumors and other solid tumors," *Med. Pediatr. Oncol.*, vol. 29, no. 1, pp. 28–32, 1997.
- [204] H. Lu, K. Searle, Y. Liu, and T. Parker, "The effect of dimensionality on growth and differentiation of neural progenitors from different regions of fetal rat brain in vitro: 3-dimensional spheroid versus 2-dimensional monolayer culture.," *Cells. Tissues. Organs*, vol. 196, no. 1, pp. 48–55, Jan. 2012.
- [205] K. H. Searle, "Medulloblastoma invasion in vitro: the role of dimensionality and regional specificity," University of Nottingham, 2004.
- [206] H. Levis, "Identification and characterisation of rat cerebellar neural stem cells and their potential use in the repair of the damaged cerebellum," University of Nottingham, 2008.
- [207] A. Rangarajan and R. A. Weinberg, "Opinion: Comparative biology of mouse versus human cells: modelling human cancer in mice.," *Nat. Rev. Cancer*, vol. 3, no. 12, pp. 952–9, Dec. 2003.
- [208] A. Rangarajan, S. J. Hong, A. Gifford, and R. A. Weinberg, "Species- and cell type-specific requirements for cellular transformation.," *Cancer Cell*, vol. 6, no. 2, pp. 171–83, Aug. 2004.
- [209] N. Shanks, R. Greek, and J. Greek, "Are animal models predictive for humans?," *Philos. Ethics. Humanit. Med.*, vol. 4, p. 2, Jan. 2009.
- [210] R. M. Sutherland, J. a McCredie, and W. R. Inch, "Growth of multicell spheroids in tissue culture as a model of nodular carcinomas.," *J. Natl. Cancer Inst.*, vol. 46, no. 1, pp. 113–20, Jan. 1971.
- [211] E. Cukierman, R. Pankov, D. R. Stevens, and K. M. Yamada, "Taking cell-matrix adhesions to the third dimension.," *Science*, vol. 294, no. 5547, pp. 1708–12, Nov. 2001.
- [212] J. E. Ekert, K. Johnson, B. Strake, J. Pardinias, S. Jarantow, R. Perkinson, and D. C. Colter, "Three-dimensional lung tumor microenvironment modulates therapeutic compound responsiveness in vitro--implication for drug development.," *PLoS One*, vol. 9, no. 3, p. e92248, Jan. 2014.

References

- [213] S. Rodríguez-Enríquez, J. C. Gallardo-Pérez, A. Avilés-Salas, A. Marín-Hernández, L. Carreño-Fuentes, V. Maldonado-Lagunas, and R. Moreno-Sánchez, "Energy metabolism transition in multi-cellular human tumor spheroids.," *J. Cell. Physiol.*, vol. 216, no. 1, pp. 189–97, Jul. 2008.
- [214] S. Carrera, P. J. de Verdier, Z. Khan, B. Zhao, A. Mahale, K. J. Bowman, M. Zainol, G. D. D. Jones, S. W. Lee, S. A. Aaronson, and S. Macip, "Protection of cells in physiological oxygen tensions against DNA damage-induced apoptosis.," *J. Biol. Chem.*, vol. 285, no. 18, pp. 13658–65, Apr. 2010.
- [215] R. Herrmann, W. Fayad, S. Schwarz, M. Berndtsson, and S. Linder, "Screening for compounds that induce apoptosis of cancer cells grown as multicellular spheroids.," *J. Biomol. Screen.*, vol. 13, no. 1, pp. 1–8, Jan. 2008.
- [216] M. Wartenberg, F. C. Ling, M. Muschen, F. Klein, H. Acker, M. Gassmann, K. Petrat, V. Putz, J. Hescheler, and H. Sauer, "Regulation of the multidrug resistance transporter P-glycoprotein in multicellular tumor spheroids by hypoxiainducible factor-1 and reactive oxygen species," *FASEB J.*, vol. 17, no. 1, p. 503+, 2003.
- [217] S. Doublier, D. C. Belisario, M. Polimeni, L. Annaratone, C. Riganti, E. Allia, D. Ghigo, A. Bosia, and A. Sapino, "HIF-1 activation induces doxorubicin resistance in MCF7 3-D spheroids via P-glycoprotein expression: a potential model of the chemoresistance of invasive micropapillary carcinoma of the breast," *BMC Cancer*, vol. 12, 2012.
- [218] Y. Sakai, S. Yamagami, and K. Nakazawa, "Comparative analysis of gene expression in rat liver tissue and monolayer- and spheroid-cultured hepatocytes.," *Cells. Tissues. Organs*, vol. 191, no. 4, pp. 281–8, Jan. 2010.
- [219] P. C. De Witt Hamer, A. A. G. Van Tilborg, P. P. Eijk, P. Sminia, D. Troost, C. J. F. Van Noorden, B. Ylstra, and S. Leenstra, "The genomic profile of human malignant glioma is altered early in primary cell culture and preserved in spheroids.," *Oncogene*, vol. 27, no. 14, pp. 2091–6, Mar. 2008.
- [220] P. F. Jacobsen, D. J. Jenkyn, and J. M. Papadimitriou, "Establishment of a human medulloblastoma cell line and its heterotransplantation into nude mice.," *J. Neuropathol. Exp. Neurol.*, vol. 44, no. 5, pp. 472–85, Sep. 1985.
- [221] J. A. Langdon, J. M. Lamont, D. K. Scott, S. Dyer, E. Prebble, N. Bown, R. G. Grundy, D. W. Ellison, and S. C. Clifford, "Combined genome-wide allelotyping and copy number analysis identify frequent genetic losses without copy number reduction in

References

- medulloblastoma.," *Genes. Chromosomes Cancer*, vol. 45, no. 1, pp. 47–60, Jan. 2006.
- [222] J. Lacroix, F. Schlund, B. Leuchs, K. Adolph, D. Sturm, S. Bender, T. Hielscher, S. M. Pfister, O. Witt, J. Rommelaere, J. R. Schlehofer, and H. Witt, "Oncolytic effects of parvovirus H-1 in medulloblastoma are associated with repression of master regulators of early neurogenesis.," *Int. J. Cancer*, vol. 134, no. 3, pp. 703–16, Feb. 2014.
- [223] F. Götschel, D. Berg, W. Gruber, C. Bender, M. Eberl, M. Friedel, J. Sonntag, E. Rüngeler, H. Hache, C. Wierling, W. Nietfeld, H. Lehrach, A. Frischauf, R. Schwartz-Albiez, F. Aberger, and U. Korf, "Synergism between Hedgehog-GLI and EGFR signaling in Hedgehog-responsive human medulloblastoma cells induces downregulation of canonical Hedgehog-target genes and stabilized expression of GLI1.," *PLoS One*, vol. 8, no. 6, p. e65403, Jan. 2013.
- [224] K. Parker and G. J. Pilkington, "Morphological, immunocytochemical and flow cytometric in vitro characterisation of a surface-adherent medulloblastoma.," *Anticancer Res.*, vol. 25, no. 6B, pp. 3855–63, Jan. .
- [225] S. C. Higgins, H. Steingrimsdottir, and G. J. Pilkington, "Human, mouse or rat? Species authentication of glioma-derived cell cultures.," *J. Neurosci. Methods*, vol. 194, no. 1, pp. 139–43, Dec. 2010.
- [226] G. E. Keles, M. S. Berger, J. Srinivasan, D. D. Kolstoe, M. S. Bobola, and J. R. Silber, "Establishment and characterization of four human medulloblastoma-derived cell lines.," *Oncol. Res.*, vol. 7, no. 10–11, pp. 493–503, Jan. 1995.
- [227] M. R. Pambid, R. Berns, H. H. Adomat, K. Hu, J. Triscott, N. Maurer, N. Zisman, V. Ramaswamy, C. E. Hawkins, M. D. Taylor, C. Dunham, E. Guns, and S. E. Dunn, "Overcoming resistance to Sonic Hedgehog inhibition by targeting p90 ribosomal S6 kinase in pediatric medulloblastoma.," *Pediatr. Blood Cancer*, vol. 61, no. 1, pp. 107–15, Jan. 2014.
- [228] R. T. Othman, I. Kimishi, T. D. Bradshaw, L. C. D. Storer, A. Korshunov, S. M. Pfister, R. G. Grundy, I. D. Kerr, and B. Coyle, "Overcoming multiple drug resistance mechanisms in medulloblastoma.," *Acta Neuropathol. Commun.*, vol. 2, no. 1, p. 57, Jan. 2014.
- [229] M. A. Lancaster, M. Renner, C.-A. Martin, D. Wenzel, L. S. Bicknell, M. E. Hurles, T. Homfray, J. M. Penninger, A. P. Jackson, and J. A. Knoblich, "Cerebral organoids model human brain development and microcephaly.," *Nature*, vol. 501, no. 7467, pp. 373–9, Sep. 2013.

References

- [230] N. Uchida, D. W. Buck, D. He, M. J. Reitsma, M. Masek, T. V Phan, A. S. Tsukamoto, F. H. Gage, and I. L. Weissman, "Direct isolation of human central nervous system stem cells," *Proc. Natl. Acad. Sci.*, vol. 97, no. 26, pp. 14720–14725, Dec. 2000.
- [231] L. S. Campos, "Neurospheres: insights into neural stem cell biology.," *J. Neurosci. Res.*, vol. 78, no. 6, pp. 761–9, Dec. 2004.
- [232] M. Moors, T. D. Rockel, J. Abel, J. E. Cline, K. Gassmann, T. Schreiber, J. Schuwald, N. Weinmann, and E. Fritsche, "Human neurospheres as three-dimensional cellular systems for developmental neurotoxicity testing.," *Environ. Health Perspect.*, vol. 117, no. 7, pp. 1131–8, Jul. 2009.
- [233] K. Hayess, C. Riebeling, R. Pirow, M. Steinfath, D. Sittner, B. Slawik, A. Luch, and A. E. M. Seiler, "The DNT-EST: a predictive embryonic stem cell-based assay for developmental neurotoxicity testing in vitro.," *Toxicology*, vol. 314, no. 1, pp. 135–47, Dec. 2013.
- [234] K. Gassmann, J. Abel, H. Bothe, T. Haarmann-Stemmann, H. F. Merk, K. N. Quasthoff, T. D. Rockel, T. Schreiber, and E. Fritsche, "Species-specific differential AhR expression protects human neural progenitor cells against developmental neurotoxicity of PAHs.," *Environ. Health Perspect.*, vol. 118, no. 11, pp. 1571–7, Nov. 2010.
- [235] M. E. Culbreth, J. A. Harrill, T. M. Freudenrich, W. R. Mundy, and T. J. Shafer, "Comparison of chemical-induced changes in proliferation and apoptosis in human and mouse neuroprogenitor cells.," *Neurotoxicology*, vol. 33, no. 6, pp. 1499–510, Dec. 2012.
- [236] L. Riggs, E. Bouffet, S. Laughlin, N. Laperriere, F. Liu, J. Skocic, N. Scantlebury, F. Wang, N. J. Schoenhoff, D. Strother, J. Hukin, C. Fryer, D. McConnell, and D. J. Mabbott, "Changes to memory structures in children treated for posterior fossa tumors.," *J. Int. Neuropsychol. Soc.*, vol. 20, no. 2, pp. 168–80, Feb. 2014.
- [237] F. Pampaloni, E. G. Reynaud, and E. H. K. Stelzer, "The third dimension bridges the gap between cell culture and live tissue.," *Nat. Rev. Mol. Cell Biol.*, vol. 8, no. 10, pp. 839–45, Oct. 2007.
- [238] S. Breslin and L. O'Driscoll, "Three-dimensional cell culture: the missing link in drug discovery.," *Drug Discov. Today*, vol. 18, no. 5–6, pp. 240–9, Mar. 2013.
- [239] H. Page, P. Flood, and E. Reynaud, "Three-dimensional tissue cultures: current trends and beyond," *Cell Tissue Res.*, vol. 352, no. 1, pp. 123–131, 2013.

References

- [240] E. Cukierman, R. Pankov, D. R. Stevens, and K. M. Yamada, "Taking cell-matrix adhesions to the third dimension.," *Science*, vol. 294, no. 5547, pp. 1708–12, Dec. 2001.
- [241] A. Astashkina, B. Mann, and D. W. Grainger, "A critical evaluation of in vitro cell culture models for high-throughput drug screening and toxicity.," *Pharmacol. Ther.*, vol. 134, no. 1, pp. 82–106, Apr. 2012.
- [242] A. Roth and T. Singer, "The application of 3D cell models to support drug safety assessment: opportunities & challenges.," *Adv. Drug Deliv. Rev.*, vol. 69–70, pp. 179–89, Apr. 2014.
- [243] F. Hirschhaeuser, H. Menne, C. Dittfeld, J. West, W. Mueller-Klieser, and L. a Kunz-Schughart, "Multicellular tumor spheroids: an underestimated tool is catching up again.," *J. Biotechnol.*, vol. 148, no. 1, pp. 3–15, Jul. 2010.
- [244] L. a Kunz-Schughart, J. P. Freyer, F. Hofstaedter, and R. Ebner, "The use of 3-D cultures for high-throughput screening: the multicellular spheroid model.," *J. Biomol. Screen.*, vol. 9, no. 4, pp. 273–85, Jun. 2004.
- [245] R. Straussman, T. Morikawa, K. Shee, M. Barzily-Rokni, Z. R. Qian, J. Du, A. Davis, M. M. Mongare, J. Gould, D. T. Frederick, Z. A. Cooper, P. B. Chapman, D. B. Solit, A. Ribas, R. S. Lo, K. T. Flaherty, S. Ogino, J. A. Wargo, and T. R. Golub, "Tumour micro-environment elicits innate resistance to RAF inhibitors through HGF secretion.," *Nature*, vol. 487, no. 7408, pp. 500–4, Jul. 2012.
- [246] M. Upreti, A. Jamshidi-Parsian, N. A. Koonce, J. S. Webber, S. K. Sharma, A. A. Asea, M. J. Mader, and R. J. Griffin, "Tumor-Endothelial Cell Three-dimensional Spheroids: New Aspects to Enhance Radiation and Drug Therapeutics.," *Transl. Oncol.*, vol. 4, no. 6, pp. 365–76, Dec. 2011.
- [247] B. C. Spink, R. W. Cole, B. H. Katz, J. F. Gierthy, L. M. Bradley, and D. C. Spink, "Inhibition of MCF-7 breast cancer cell proliferation by MCF-10A breast epithelial cells in coculture.," *Cell Biol. Int.*, vol. 30, no. 3, pp. 227–238, 2006.
- [248] M. Wartenberg, "Tumor-induced angiogenesis studied in confrontation cultures of multicellular tumor spheroids and embryoid bodies grown from pluripotent embryonic stem cells.," *FASEB J.*, vol. 15, no. 6, pp. 995–1005, Apr. 2001.
- [249] K. F. Chambers, J. F. Pearson, N. Aziz, P. O'Toole, D. Garrod, and S. H. Lang, "Stroma regulates increased epithelial lateral cell adhesion in 3D culture: a role for actin/cadherin dynamics.," *PLoS One*, vol. 6, no. 4, p. e18796, Jan. 2011.

References

- [250] E. L. Berg, Y.-C. Hsu, and J. A. Lee, "Consideration of the cellular microenvironment: physiologically relevant co-culture systems in drug discovery.," *Adv. Drug Deliv. Rev.*, vol. 69–70, pp. 190–204, Apr. 2014.
- [251] C. Zanini, E. Ercole, G. Mandili, R. Salaroli, A. Poli, C. Renna, V. Papa, G. Cenacchi, and M. Forni, "Medullospheres from DAOY, UW228 and ONS-76 cells: increased stem cell population and proteomic modifications.," *PLoS One*, vol. 8, no. 5, p. e63748, Jan. 2013.
- [252] H. D. Hemmati, I. Nakano, J. A. Lazareff, M. Masterman-Smith, D. H. Geschwind, M. Bronner-Fraser, and H. I. Kornblum, "Cancerous stem cells can arise from pediatric brain tumors," *Proc. Natl. Acad. Sci.*, vol. 100, no. 25, pp. 15178–15183, 2003.
- [253] S. J. Smith, M. Wilson, J. H. Ward, C. V. Rahman, A. C. Peet, D. C. Macarthur, F. R. A. J. Rose, R. G. Grundy, and R. Rahman, "Recapitulation of tumor heterogeneity and molecular signatures in a 3D brain cancer model with decreased sensitivity to histone deacetylase inhibition.," *PLoS One*, vol. 7, no. 12, p. e52335, Jan. 2012.
- [254] G. E. Keles, M. S. Berger, J. Srinivasan, D. D. Kolstoe, M. S. Bobola, and J. R. Silber, "Establishment and characterization of four human medulloblastoma-derived cell lines," *Oncol. Res.*, vol. 7, no. 10–11, pp. 493–503, 1995.
- [255] R. T. Othman, "ABCB1 and MGMT mediated drug resistance in medulloblastoma," University of Nottingham, 2014.
- [256] "<http://3dbiomatrix.com/protocols/>." [Online]. Available: <http://3dbiomatrix.com/protocols/>. [Accessed: 18-Jun-2012].
- [257] Y.-C. Tung, A. Y. Hsiao, S. G. Allen, Y. Torisawa, M. Ho, and S. Takayama, "High-throughput 3D spheroid culture and drug testing using a 384 hanging drop array," *Analyst*, vol. 136, no. 3, pp. 473–478, 2011.
- [258] "<http://www.microtissues.com/3dpetridish-support.htm>." .
- [259] A. P. Napolitano, D. M. Dean, A. J. Man, J. Youssef, D. N. Ho, A. P. Rago, M. P. Lech, and J. R. Morgan, "Scaffold-free three-dimensional cell culture utilizing micromolded nonadhesive hydrogels," *Biotechniques*, vol. 43, no. 4, pp. 494, 496–500, Oct. 2007.
- [260] A. Ivascu and M. Kubbies, "Rapid generation of single-tumor spheroids for high-throughput cell function and toxicity analysis.," *J. Biomol. Screen.*, vol. 11, no. 8, pp. 922–32, Dec. 2006.

References

- [261] M. Vinci, S. Gowan, F. Boxall, L. Patterson, M. Zimmermann, W. Court, C. Lomas, M. Mendiola, D. Hardisson, and S. Eccles, "Advances in establishment and analysis of three-dimensional tumor spheroid-based functional assays for target validation and drug evaluation," *BMC Biol.*, vol. 10, no. 1, pp. 1–21, 2012.
- [262] J. C. Yen, F. J. Chang, and S. Chang, "A new criterion for automatic multilevel thresholding.," *IEEE Trans. Image Process.*, vol. 4, no. 3, pp. 370–8, Jan. 1995.
- [263] C. P. Spears, "Volume doubling measurement of spherical and ellipsoidal tumors.," *Med. Pediatr. Oncol.*, vol. 12, no. 3, pp. 212–7, Jan. 1984.
- [264] J. Friedrich, C. Seidel, R. Ebner, and L. A. Kunz-Schughart, "Spheroid-based drug screen: considerations and practical approach," *Nat. Protoc.*, vol. 4, no. 3, pp. 309–324, Feb. 2009.
- [265] J. Friedrich, W. Eder, J. Castaneda, M. Doss, E. Huber, R. Ebner, and L. a Kunz-Schughart, "A reliable tool to determine cell viability in complex 3-d culture: the acid phosphatase assay.," *J. Biomol. Screen.*, vol. 12, no. 7, pp. 925–37, Oct. 2007.
- [266] A. Sukmawati, "Biodegradable microparticle for stem cell delivery and differentiation," University of Nottingham, 2013.
- [267] P. Beck, D. Scherer, and J. Kreuter, "Separation of drug-loaded nanoparticles from free drug by gel filtration.," *J. Microencapsul.*, vol. 7, no. 4, pp. 491–6.
- [268] R. Finsy, "Particle sizing by quasi-elastic light scattering," *Adv. Colloid Interface Sci.*, vol. 52, pp. 79–143, Sep. 1994.
- [269] M. Minsky, "Microscopy apparatus." U.S. Patent no. 3013467.
- [270] A. Periasamy, P. Skoglund, C. Noakes, and R. Keller, "An evaluation of two-photon excitation versus confocal and digital deconvolution fluorescence microscopy imaging in *Xenopus* morphogenesis.," *Microsc. Res. Tech.*, vol. 47, no. 3, pp. 172–81, Nov. 1999.
- [271] W. Denk, J. Strickler, and W. Webb, "Two-photon laser scanning fluorescence microscopy," *Science (80-.)*, vol. 248, no. 4951, pp. 73–76, Apr. 1990.
- [272] S. Messner, I. Agarkova, W. Moritz, and J. M. Kelm, "Multi-cell type human liver microtissues for hepatotoxicity testing.," *Arch. Toxicol.*, vol. 87, no. 1, pp. 209–13, Jan. 2013.
- [273] J. A. Green and K. M. Yamada, "Three-dimensional microenvironments modulate fibroblast signaling responses," *Adv. Drug Deliv. Rev.*, vol. 59, no. 13, pp. 1293–1298, 2007.

References

- [274] A. Monazzam, P. Razifar, O. Lindhe, R. Josephsson, B. Långström, and M. Bergström, "A new, fast and semi-automated size determination method (SASDM) for studying multicellular tumor spheroids.," *Cancer Cell Int.*, vol. 5, p. 32, Nov. 2005.
- [275] J. Xiao, Y. Zhang, J. Wang, W. Yu, W. Wang, and X. Ma, "Monitoring of cell viability and proliferation in hydrogel-encapsulated system by resazurin assay.," *Appl. Biochem. Biotechnol.*, vol. 162, no. 7, pp. 1996–2007, Nov. 2010.
- [276] J.-H. Zhang, "A Simple Statistical Parameter for Use in Evaluation and Validation of High Throughput Screening Assays," *J. Biomol. Screen.*, vol. 4, no. 2, pp. 67–73, Apr. 1999.
- [277] G. S. Sittampalam, "Design of Signal Windows in High Throughput Screening Assays for Drug Discovery," *J. Biomol. Screen.*, vol. 2, no. 3, pp. 159–169, Apr. 1997.
- [278] G. Sittampalam, N. Gal-Edd, M. Arkin, D. Auld, C. Austin, B. Bejcek, M. Glicksman, J. Inglese, V. Lemmon, Z. Li, J. McGee, O. McManus, L. Minor, A. Napper, T. Riss, J. Trask, and J. Weidner, *Assay Guidance Manual*. Bethesda (MD); Eli Lilly & Company and the National Center for Advancing Translational Sciences, 2004.
- [279] H. Motulsky and A. Christopoulos, "Fitting Models to Biological Data using Linear and Nonlinear Regression."
- [280] K. Gassmann, J. Baumann, S. Giersiefer, J. Schuwald, T. Schreiber, H. F. Merk, and E. Fritsche, "Automated neurosphere sorting and plating by the COPAS large particle sorter is a suitable method for high-throughput 3D in vitro applications.," *Toxicol. In Vitro*, vol. 26, no. 6, pp. 993–1000, Sep. 2012.
- [281] R. M. Sutherland, H. A. Eddy, B. Bareham, K. Reich, and D. Vanantwerp, "Resistance to adriamycin in multicellular spheroids.," *Int. J. Radiat. Oncol. Biol. Phys.*, vol. 5, no. 8, pp. 1225–30, Aug. 1979.
- [282] H. Mori, K. Ninomiya, M. Kino-oka, T. Shofuda, M. O. Islam, M. Yamasaki, and H. Okano, "Effect of Neurosphere Size on the Growth Rate of Human Neural Stem / Progenitor Cells," *J. Neurosci. Res.*, vol. 1691, no. 84, pp. 1682–1691, 2006.
- [283] A. S. Mikhail, S. Eetezadi, and C. Allen, "Multicellular tumor spheroids for evaluation of cytotoxicity and tumor growth inhibitory effects of nanomedicines in vitro: a comparison of docetaxel-loaded block copolymer micelles and Taxotere.," *PLoS One*, vol. 8, no. 4, p. e62630, Jan. 2013.
- [284] A. Bez, E. Corsini, D. Curti, M. Biggiogera, A. Colombo, R. F. Nicosia, S. F. Pagano, and E. A. Parati, "Neurosphere and

References

- neurosphere-forming cells: morphological and ultrastructural characterization," *Brain Res.*, vol. 993, no. 1–2, pp. 18–29, Dec. 2003.
- [285] H. Hardelauf, J.-P. Frimat, J. D. Stewart, W. Schormann, Y.-Y. Chiang, P. Lampen, J. Franzke, J. G. Hengstler, C. Cadenas, L. a Kunz-Schughart, and J. West, "Microarrays for the scalable production of metabolically relevant tumour spheroids: a tool for modulating chemosensitivity traits.," *Lab Chip*, vol. 11, no. 3, pp. 419–28, Feb. 2011.
- [286] J. Mutterer and W. Rasband, "ImageJ Macro Language Programmer 's Reference Guide v1 . 46d," pp. 1–45.
- [287] "Introduction into Macro Programming - Fiji." [Online]. Available: http://fiji.sc/wiki/index.php/Introduction_into_Macro_Programming. [Accessed: 10-Feb-2014].
- [288] S. Walenta, J. Dötsch, and W. Mueller-Klieser, "ATP concentrations in multicellular tumor spheroids assessed by single photon imaging and quantitative bioluminescence.," *Eur. J. Cell Biol.*, vol. 52, no. 2, pp. 389–93, Aug. 1990.
- [289] S. Walenta, J. Doetsch, W. Mueller-Klieser, and L. a. Kunz-Schughart, "Metabolic Imaging in Multicellular Spheroids of Oncogene-transfected Fibroblasts," *J. Histochem. Cytochem.*, vol. 48, no. 4, pp. 509–522, Apr. 2000.
- [290] M. Krzywinski and N. Altman, "Points of significance: Power and sample size," *Nat. Methods*, vol. 10, no. 12, pp. 1139–1140, Nov. 2013.
- [291] C. Sirisangtragul, "Pharmacokinetics and pharmacodynamics of intraventricularly administered etoposide," ULB Bonn, 2006.
- [292] G. K. Y. Chan, T. L. Kleinheinz, D. Peterson, and J. G. Moffat, "A simple high-content cell cycle assay reveals frequent discrepancies between cell number and ATP and MTS proliferation assays.," *PLoS One*, vol. 8, no. 5, p. e63583, Jan. 2013.
- [293] M. V Zamaraeva, R. Z. Sabirov, E. Maeno, Y. Ando-Akatsuka, S. V Bessonova, and Y. Okada, "Cells die with increased cytosolic ATP during apoptosis: a bioluminescence study with intracellular luciferase.," *Cell Death Differ.*, vol. 12, no. 11, pp. 1390–7, Nov. 2005.
- [294] M. Katayama, T. Kawaguchi, M. S. Berger, and R. O. Pieper, "DNA damaging agent-induced autophagy produces a cytoprotective adenosine triphosphate surge in malignant glioma cells.," *Cell Death Differ.*, vol. 14, no. 3, pp. 548–58, Mar. 2007.

References

- [295] X. Fu, S. Wan, Y. L. Lyu, L. F. Liu, and H. Qi, "Etoposide induces ATM-dependent mitochondrial biogenesis through AMPK activation.," *PLoS One*, vol. 3, no. 4, p. e2009, Jan. 2008.
- [296] I. D. Bowen and G. H. Lewis, "Acid phosphatase activity and cell death in mouse thymus.," *Histochemistry*, vol. 65, no. 2, pp. 173–9, Feb. 1980.
- [297] A. Christopoulos, "Assessing the distribution of parameters in models of ligand-receptor interaction: to log or not to log.," *Trends Pharmacol. Sci.*, vol. 19, no. 9, pp. 351–7, Sep. 1998.
- [298] A. Walzl, C. Unger, N. Kramer, D. Unterleuthner, M. Scherzer, M. Hengstschläger, D. Schwanzer-Pfeiffer, and H. Dolznig, "The Resazurin Reduction Assay Can Distinguish Cytotoxic from Cytostatic Compounds in Spheroid Screening Assays.," *J. Biomol. Screen.*, vol. 19, no. 7, pp. 1047–1059, Apr. 2014.
- [299] G. Toffoli, G. Corona, B. Basso, and M. Boiocchi, "Pharmacokinetic optimisation of treatment with oral etoposide.," *Clin. Pharmacokinet.*, vol. 43, no. 7, pp. 441–66, Jan. 2004.
- [300] C. L. Bregman, R. a. Buroker, R. S. Hirth, a. R. Crosswell, and S. K. Durham, "Etoposide- and BMY-40481-Induced Sensory Neuropathy in Mice," *Toxicol. Pathol.*, vol. 22, no. 5, pp. 528–535, Sep. 1994.
- [301] H. Ogasawara, K. Kiya, K. Kurisu, T. Hotta, T. Mikami, K. Sugiyama, T. Nakahara, and T. Uozumi, "Effect of intracarotid infusion of etoposide with angiotensin II-induced hypertension on the blood-brain barrier and the brain tissue.," *J. Neurooncol.*, vol. 13, no. 2, pp. 111–7, Jun. 1992.
- [302] D. Fortin, C. I. McCormick, L. G. Remsen, R. Nixon, and E. A. Neuwelt, "Unexpected neurotoxicity of etoposide phosphate administered in combination with other chemotherapeutic agents after blood-brain barrier modification to enhance delivery, using propofol for general anesthesia, in a rat model.," *Neurosurgery*, vol. 47, no. 1, pp. 199–207, Jul. 2000.
- [303] R. Faigle and H. Song, "Signaling mechanisms regulating adult neural stem cells and neurogenesis.," *Biochim. Biophys. Acta*, vol. 1830, no. 2, pp. 2435–48, Feb. 2013.
- [304] C. Zhao, W. Deng, and F. H. Gage, "Mechanisms and functional implications of adult neurogenesis.," *Cell*, vol. 132, no. 4, pp. 645–60, Feb. 2008.
- [305] A. Amann, M. Zwierzina, G. Gamerith, M. Bitsche, J. M. Huber, G. F. Vogel, M. Blumer, S. Koeck, E. J. Pechriggl, J. M. Kelm, W. Hilbe, and H. Zwierzina, "Development of an innovative 3D cell culture

References

- system to study tumour--stroma interactions in non-small cell lung cancer cells.," *PLoS One*, vol. 9, no. 3, p. e92511, Jan. 2014.
- [306] R. T. Kilani, Y. Tamimi, S. Karmali, J. Mackey, E. G. Hanel, K. K. Wong, and R. B. Moore, "Selective cytotoxicity of gemcitabine in bladder cancer cell lines.," *Anticancer. Drugs*, vol. 13, no. 6, pp. 557–66, Jul. 2002.
- [307] R. T. Kilani, Y. Tamimi, E. G. Hanel, K. K. Wong, S. Karmali, P. W. K. Lee, and R. B. Moore, "Selective reovirus killing of bladder cancer in a co-culture spheroid model," *Virus Res.*, vol. 93, no. 1, pp. 1–12, May 2003.
- [308] V. Phan-Lai, S. J. Florczyk, F. M. Kievit, K. Wang, E. Gad, M. L. Disis, and M. Zhang, "Three-dimensional scaffolds to evaluate tumor associated fibroblast-mediated suppression of breast tumor specific T cells.," *Biomacromolecules*, vol. 14, no. 5, pp. 1330–7, May 2013.
- [309] A. Y. Hsiao, Y. Torisawa, Y.-C. Tung, S. Sud, R. S. Taichman, K. J. Pienta, and S. Takayama, "Microfluidic system for formation of PC-3 prostate cancer co-culture spheroids.," *Biomaterials*, vol. 30, no. 16, pp. 3020–7, Jun. 2009.
- [310] C. Fang, I. Avis, D. Salomon, and F. Cuttitta, "Novel Phenotypic Fluorescent Three-Dimensional Platforms for High-throughput Drug Screening and Personalized Chemotherapy.," *J. Cancer*, vol. 4, no. 5, pp. 402–15, Jan. 2013.
- [311] Y. Go, S. K. Chintala, S. Mohanam, Z. Gokaslan, B. Venkaiah, R. Bjerkgvig, K. Oka, G. L. Nicolson, R. Sawaya, and J. S. Rao, "Inhibition of in vivo tumorigenicity and invasiveness of a human glioblastoma cell line transfected with antisense uPAR vectors.," *Clin. Exp. Metastasis*, vol. 15, no. 4, pp. 440–6, Jul. 1997.
- [312] R. J. Vanner, M. Remke, M. Gallo, H. J. Selvadurai, F. Coutinho, L. Lee, M. Kushida, R. Head, S. Morrissy, X. Zhu, T. Aviv, V. Voisin, I. D. Clarke, Y. Li, A. J. Mungall, R. a Moore, Y. Ma, S. J. M. Jones, M. a Marra, D. Malkin, P. a Northcott, M. Kool, S. M. Pfister, G. Bader, K. Hochedlinger, A. Korshunov, M. D. Taylor, and P. B. Dirks, "Quiescent Sox2(+) Cells Drive Hierarchical Growth and Relapse in Sonic Hedgehog Subgroup Medulloblastoma.," *Cancer Cell*, pp. 1–15, Jun. 2014.
- [313] V. K. Srivastava and J. Nalbantoglu, "Flow cytometric characterization of the DAOY medulloblastoma cell line for the cancer stem-like phenotype.," *Cytometry. A*, vol. 73, no. 10, pp. 940–8, Oct. 2008.
- [314] M. Nagato, T. Heike, T. Kato, Y. Yamanaka, M. Yoshimoto, T. Shimazaki, H. Okano, and T. Nakahata, "Prospective

References

- characterization of neural stem cells by flow cytometry analysis using a combination of surface markers," *J. Neurosci. Res.*, vol. 80, no. 4, pp. 456–466, 2005.
- [315] M. K. Carpenter, X. Cui, Z. Hu, J. Jackson, S. Sherman, and L. U. Wahlberg, "In Vitro Expansion of a Multipotent Population of Human Neural Progenitor Cells," vol. 278, pp. 265–278, 1999.
- [316] M. G. Honig and R. I. Hume, "Fluorescent carbocyanine dyes allow living neurons of identified origin to be studied in long-term cultures.," *J. Cell Biol.*, vol. 103, no. 1, pp. 171–87, Jul. 1986.
- [317] S. A. Weston and C. R. Parish, "New fluorescent dyes for lymphocyte migration studies. Analysis by flow cytometry and fluorescence microscopy.," *J. Immunol. Methods*, vol. 133, no. 1, pp. 87–97, Oct. 1990.
- [318] W. E. Samlowski, B. A. Robertson, B. K. Draper, E. Prystas, and J. R. McGregor, "Effects of supravital fluorochromes used to analyze the in vivo homing of murine lymphocytes on cellular function," *J. Immunol. Methods*, vol. 144, no. 1, pp. 101–115, Jan. 1991.
- [319] S. K. Chintala, J. Fueyo, C. Gomez-Manzano, B. Venkaiah, R. Bjerkvig, W. K. Yung, R. Sawaya, a P. Kyritsis, and J. S. Rao, "Adenovirus-mediated p16/CDKN2 gene transfer suppresses glioma invasion in vitro.," *Oncogene*, vol. 15, no. 17, pp. 2049–57, Oct. 1997.
- [320] S. Khoshyomn, P. L. Penar, W. J. McBride, and D. J. Taatjes, "Four-dimensional analysis of human brain tumor spheroid invasion into fetal rat brain aggregates using confocal scanning laser microscopy.," *J. Neurooncol.*, vol. 38, no. 1, pp. 1–10, May 1998.
- [321] S. J. Nygaard, H. K. Haugland, O. D. Laerum, M. Lund-Johansen, R. Bjerkvig, and O. B. Tysnes, "Dynamic determination of human glioma invasion in vitro.," *J. Neurosurg.*, vol. 89, no. 3, pp. 441–7, Sep. 1998.
- [322] F. Lassailly, E. Griessinger, and D. Bonnet, "Microenvironmental contaminations' induced by fluorescent lipophilic dyes used for noninvasive in vitro and in vivo cell tracking.," *Blood*, vol. 115, no. 26, pp. 5347–54, Jul. 2010.
- [323] J. Begum, W. Day, C. Henderson, S. Purewal, J. Cerveira, H. Summers, P. Rees, D. Davies, and A. Filby, "A method for evaluating the use of fluorescent dyes to track proliferation in cell lines by dye dilution.," *Cytometry. A*, vol. 83, no. 12, pp. 1085–95, Dec. 2013.

References

- [324] C. R. Parish, "Fluorescent dyes for lymphocyte migration and proliferation studies.," *Immunol. Cell Biol.*, vol. 77, no. 6, pp. 499–508, Dec. 1999.
- [325] B. J. C. Quah and C. R. Parish, "New and improved methods for measuring lymphocyte proliferation in vitro and in vivo using CFSE-like fluorescent dyes.," *J. Immunol. Methods*, vol. 379, no. 1–2, pp. 1–14, May 2012.
- [326] P. Indovina, M. Collini, G. Chirico, and M. T. Santini, "Three-dimensional cell organization leads to almost immediate HRE activity as demonstrated by molecular imaging of MG-63 spheroids using two-photon excitation microscopy.," *FEBS Lett.*, vol. 581, no. 4, pp. 719–26, Feb. 2007.
- [327] K. König, A. Uchugonova, and E. Gorjup, "Multiphoton fluorescence lifetime imaging of 3D-stem cell spheroids during differentiation.," *Microsc. Res. Tech.*, vol. 74, no. 1, pp. 9–17, Jan. 2011.
- [328] N. C. L. Zembruski, V. Stache, W. E. Haefeli, and J. Weiss, "7-Aminoactinomycin D for apoptosis staining in flow cytometry.," *Anal. Biochem.*, vol. 429, no. 1, pp. 79–81, Oct. 2012.
- [329] R. Duggan, "Ryan Duggan's three step approach to gating Annexin V data appropriately," 2012. [Online]. Available: <http://ucflow.blogspot.co.uk/2012/07/my-3-step-approach-to-gating-annexin-v.html>.
- [330] G. Koopman, C. P. Reutelingsperger, G. a Kuijten, R. M. Keehnen, S. T. Pals, and M. H. van Oers, "Annexin V for flow cytometric detection of phosphatidylserine expression on B cells undergoing apoptosis.," *Blood*, vol. 84, no. 5, pp. 1415–20, Sep. 1994.
- [331] D. P. Ivanov, T. L. Parker, D. A. Walker, C. Alexander, M. B. Ashford, P. R. Gellert, and M. C. Garnett, "Multiplexing Spheroid Volume, Resazurin and Acid Phosphatase Viability Assays for High-Throughput Screening of Tumour Spheroids and Stem Cell Neurospheres," *PLoS One*, vol. 9, no. 8, p. e103817, Aug. 2014.
- [332] A. J. Terzis, F. Thorsen, O. Heese, T. Visted, R. Bjerkvig, O. Dahl, H. Arnold, and G. Gundersen, "Proliferation, migration and invasion of human glioma cells exposed to paclitaxel (Taxol) in vitro.," *Br. J. Cancer*, vol. 75, no. 12, pp. 1744–52, Jan. 1997.
- [333] A. J. Terzis, A. Dietze, R. B. Vig, and H. A. R. N. Old, "Effects of photodynamic therapy on glioma spheroids," vol. 11, no. July 1996, pp. 196–205, 1997.
- [334] F. Thorsen, T. Visted, P. Lehtolainen, S. Ylä-Herttuala, and R. Bjerkvig, "Release of replication-deficient retroviruses from a

References

- packaging cell line: interaction with glioma tumor spheroids in vitro.," *Int. J. Cancer*, vol. 71, no. 5, pp. 874–80, May 1997.
- [335] E. Urich, C. Patsch, S. Aigner, M. Graf, R. Iacone, and P.-O. Freskgård, "Multicellular self-assembled spheroidal model of the blood brain barrier.," *Sci. Rep.*, vol. 3, p. 1500, Jan. 2013.
- [336] R. R. Langley and I. J. Fidler, "The seed and soil hypothesis revisited--the role of tumor-stroma interactions in metastasis to different organs.," *Int. J. Cancer*, vol. 128, no. 11, pp. 2527–35, Jun. 2011.
- [337] C. Nam, K. Doi, and H. Nakayama, "Etoposide induces G2/M arrest and apoptosis in neural progenitor cells via DNA damage and an ATM/p53-related pathway.," *Histol. Histopathol.*, vol. 25, no. 4, pp. 485–93, Apr. 2010.
- [338] J. Dietrich, R. Han, Y. Yang, M. Mayer-Pröschel, and M. Noble, "CNS progenitor cells and oligodendrocytes are targets of chemotherapeutic agents in vitro and in vivo.," *J. Biol.*, vol. 5, no. 7, p. 22, Jan. 2006.
- [339] A. Quiñones-Hinojosa and K. Chaichana, "The human subventricular zone: a source of new cells and a potential source of brain tumors.," *Exp. Neurol.*, vol. 205, no. 2, pp. 313–24, Jun. 2007.
- [340] N. M. Barbaro, N. Gupta, and S. Kunwar, "Unique astrocyte ribbon in adult human brain contains neural stem cells but lacks chain migration," vol. 427, no. February, pp. 740–744, 2004.
- [341] R. W. Gregg, J. M. Molepo, V. J. Monpetit, N. Z. Mikael, D. Redmond, M. Gadia, and D. J. Stewart, "Cisplatin neurotoxicity: the relationship between dosage, time, and platinum concentration in neurologic tissues, and morphologic evidence of toxicity.," *J. Clin. Oncol.*, vol. 10, no. 5, pp. 795–803, May 1992.
- [342] J. Gállego Pérez-Larraya, J. A. Palma, M. Carmona-Iragui, R. Fernández-Torrón, P. Irimia, P. Rodríguez-Otero, C. Panizo, and E. Martínez-Vila, "Neurologic complications of intrathecal liposomal cytarabine administered prophylactically to patients with non-Hodgkin lymphoma.," *J. Neurooncol.*, vol. 103, no. 3, pp. 603–9, Jul. 2011.
- [343] T. Govender, S. Stolnik, M. C. Garnett, L. Illum, and S. S. Davis, "PLGA nanoparticles prepared by nanoprecipitation: drug loading and release studies of a water soluble drug," *J. Control. Release*, vol. 57, no. 2, pp. 171–185, 1999.
- [344] H. Hama, H. Kurokawa, H. Kawano, R. Ando, T. Shimogori, H. Noda, K. Fukami, A. Sakaue-Sawano, and A. Miyawaki, "Scale: a chemical approach for fluorescence imaging and reconstruction of

References

- transparent mouse brain.," *Nat. Neurosci.*, vol. 14, no. 11, pp. 1481–8, Nov. 2011.
- [345] H. F. Stähelin and A. von Wartburg, "The chemical and biological route from podophyllotoxin glucoside to etoposide: ninth Cain memorial Award lecture.," *Cancer Res.*, vol. 51, no. 1, pp. 5–15, Jan. 1991.
- [346] T. F. Imbert, "Discovery of podophyllotoxins.," *Biochimie*, vol. 80, no. 3, pp. 207–22, Mar. 1998.
- [347] I. W. Kaplan, "Condylomata acuminata," *New Orleans Med. Surg. J.*, vol. 94, no. 388, pp. 1941–1942, 1942.
- [348] L. S. King and M. Sullivan, "The similarity of the effect of podophyllin and colchicine and their use in the treatment of condylomata acuminata.," *Sci. (washingt. DC)*, vol. 104, pp. 244–245, 1946.
- [349] M. G. Kelly and J. L. Hartwell, "The Biological Effects and the Chemical Composition of Podophyllin. A Review," *J. Natl. Cancer Inst.*, vol. 14, no. 4, pp. 967–1010, Feb. 1954.
- [350] K. R. Hande, "Etoposide: four decades of development of a topoisomerase II inhibitor," *European journal of cancer (Oxford, England : 1990)*, vol. 34, no. 10. Elsevier Science Ltd., pp. 1514–1521, 01-Sep-1998.
- [351] S. J. Froelich-Ammon and N. Osheroff, "Topoisomerase Poisons: Harnessing the Dark Side of Enzyme Mechanism," *J. Biol. Chem.*, vol. 270, no. 37, pp. 21429–21432, Sep. 1995.
- [352] J. L. Nitiss, "Targeting DNA topoisomerase II in cancer chemotherapy.," *Nat. Rev. Cancer*, vol. 9, no. 5, pp. 338–50, May 2009.
- [353] Y. Pommier, "Drugging topoisomerases: lessons and challenges.," *ACS Chem. Biol.*, vol. 8, no. 1, pp. 82–95, Jan. 2013.
- [354] M. Pendleton, R. H. Lindsey, C. a Felix, D. Grimwade, and N. Osheroff, "Topoisomerase II and leukemia.," *Ann. N. Y. Acad. Sci.*, vol. 1310, pp. 98–110, Mar. 2014.
- [355] M. L. Slevin, "The clinical pharmacology of etoposide," *Cancer*, vol. 67, no. S1, pp. 319–329, Jan. 1991.
- [356] P. Dombernowsky and N. I. Nissen, "Schedule dependency of the antileukemic activity of the podophyllotoxin-derivative VP 16-213 (NSC-141540) in L1210 leukemia.," *Acta Pathol. Microbiol. Scand. A.*, vol. 81, no. 5, pp. 715–24, Sep. 1973.

References

- [357] M. L. Slevin, P. I. Clark, S. P. Joel, S. Malik, R. J. Osborne, W. M. Gregory, D. G. Lowe, R. H. Reznek, and P. F. Wrigley, "A randomized trial to evaluate the effect of schedule on the activity of etoposide in small-cell lung cancer," *J. Clin. Oncol.*, vol. 7, no. 9, pp. 1333–1340, Sep. 1989.
- [358] P. I. Clark, M. L. Slevin, S. P. Joel, R. J. Osborne, D. I. Talbot, P. W. Johnson, R. Reznek, T. Masud, W. Gregory, and P. F. Wrigley, "A randomized trial of two etoposide schedules in small-cell lung cancer: the influence of pharmacokinetics on efficacy and toxicity.," *J. Clin. Oncol.*, vol. 12, no. 7, pp. 1427–35, Jul. 1994.
- [359] K. Hande, "The Importance of Drug Scheduling in Cancer Chemotherapy: Etoposide as an Example.," *Oncologist*, vol. 1, no. 4, pp. 234–239, Jan. 1996.
- [360] M.-C. Le Deley, G. Vassal, A. Taïbi, A. Shamsaldin, T. Leblanc, and O. Hartmann, "High cumulative rate of secondary leukemia after continuous etoposide treatment for solid tumors in children and young adults.," *Pediatr. Blood Cancer*, vol. 45, no. 1, pp. 25–31, Jul. 2005.
- [361] C. H. Pui, R. C. Ribeiro, M. L. Hancock, G. K. Rivera, W. E. Evans, S. C. Raimondi, D. R. Head, F. G. Behm, M. H. Mahmoud, and J. T. Sandlund, "Acute myeloid leukemia in children treated with epipodophyllotoxins for acute lymphoblastic leukemia.," *N. Engl. J. Med.*, vol. 325, no. 24, pp. 1682–7, Dec. 1991.
- [362] T. Kikuta, C. Shimazaki, H. Hirai, T. Sumikuma, Y. Sudo, N. Yamagata, E. Ashihara, H. Goto, T. Inaba, N. Fujita, T. Hatta, and M. Nakagawa, "[Three cases of secondary acute myeloid leukemia after long-term treatment with oral etoposide].," *Rinsho. Ketsueki.*, vol. 37, no. 11, pp. 1276–82, Nov. 1996.
- [363] J. C. Shah, J. R. Chen, and D. Chow, "Preformulation Study of Etoposide: Identification of Physicochemical Characteristics Responsible for the Low and Erratic Oral Bioavailability of Etoposide," *Pharm. Res.*, vol. 6, no. 5, pp. 408–412, 1989.
- [364] S. P. Joel, P. I. Clark, and M. L. Slevin, "Stability of the i.v. and oral formulations of etoposide in solution.," *Cancer Chemother. Pharmacol.*, vol. 37, no. 1–2, pp. 117–24, Jan. 1995.
- [365] J. A. Grant, P. A. Bilodeau, B. G. Guernsey, and F. H. Gardner, "Unsuspected benzyl alcohol hypersensitivity.," *N. Engl. J. Med.*, vol. 306, no. 2, p. 108, Jan. 1982.
- [366] J. P. Wilson, D. A. Solimando, and M. S. Edwards, "Parenteral benzyl alcohol-induced hypersensitivity reaction.," *Drug Intell. Clin. Pharm.*, vol. 20, no. 9, pp. 689–91, Sep. 1986.

References

- [367] W. Brown, N. M. Buist, H. Cory Gipson, R. Huston, and N. Kennaway, "Fatal benzyl alcohol poisoning in a neonatal intensive care unit," *Lancet*, vol. 319, no. 8283, p. 1250, May 1982.
- [368] J. Gershanik, B. Boecler, H. Ensley, S. McCloskey, and W. George, "The gasping syndrome and benzyl alcohol poisoning.," *N. Engl. J. Med.*, vol. 307, no. 22, pp. 1384–8, Nov. 1982.
- [369] J. H. Saiki, S. Thompson, F. Smith, and R. Atkinson, "Paraplegia following intrathecal chemotherapy," *Cancer*, vol. 29, no. 2, pp. 370–374, Feb. 1972.
- [370] F. H. DeLand, "Intrathecal toxicity studies with benzyl alcohol.," *Toxicol. Appl. Pharmacol.*, vol. 25, no. 2, pp. 153–6, Jun. 1973.
- [371] T. L. Schwinghammer, M. Reilly, and C. S. Rosenfeld, "Cracking of ABS plastic devices used to infuse undiluted etoposide injection.," *Am. J. Hosp. Pharm.*, vol. 45, no. 6, p. 1277, Jun. 1988.
- [372] S. D. Pearson and L. A. Trissel, "Leaching of diethylhexyl phthalate from polyvinyl chloride containers by selected drugs and formulation components.," *Am. J. Hosp. Pharm.*, vol. 50, no. 7, pp. 1405–9, Jul. 1993.
- [373] S. Bagel-Boithias, V. Sautou-Miranda, D. Bourdeaux, V. Tramier, A. Boyer, and J. Chopineau, "Leaching of diethylhexyl phthalate from multilayer tubing into etoposide infusion solutions.," *Am. J. Health. Syst. Pharm.*, vol. 62, no. 2, pp. 182–8, Jan. 2005.
- [374] B. Demoré, J. Vigneron, A. Perrin, M. A. Hoffman, and M. Hoffman, "Leaching of diethylhexyl phthalate from polyvinyl chloride bags into intravenous etoposide solution.," *J. Clin. Pharm. Ther.*, vol. 27, no. 2, pp. 139–42, Apr. 2002.
- [375] A. H. I. Witterland, C. H. W. Koks, and J. H. Beijnen, "Etoposide phosphate, the water soluble prodrug of etoposide," *Pharm. World Sci.*, vol. 18, no. 5, pp. 163–170, 1996.
- [376] J. M. Henwood and R. N. Brogden, "Etoposide: A Review of its Pharmacodynamic and Pharmacokinetic Properties, and Therapeutic Potential in Combination Chemotherapy of Cancer," *Drugs*, vol. 39, no. 3, 1990.
- [377] D. J. Stewart, M. T. Richard, H. Hugenholtz, J. M. Dennery, R. Belanger, J. Gerin-Lajoie, V. Montpetit, D. Nundy, J. Prior, and H. S. Hopkins, "Penetration of VP-16 (etoposide) into human intracerebral and extracerebral tumors.," *J. Neurooncol.*, vol. 2, no. 2, pp. 133–9, Jan. 1984.

References

- [378] M. Zucchetti, C. Rossi, R. Knerich, M. G. Donelli, G. Butti, V. Silvani, P. Gaetani, and M. D., "Original article Concentrations of VP16 and VM26 in human brain tumors," pp. 63–66, 1991.
- [379] K. Kiya, T. Uozumi, H. Ogasawara, K. Sugiyama, T. Hotta, and T. Mikami, "Cancer chemotherapy and pharmacology Penetration of etoposide into human malignant brain tumors after intravenous and oral administration," no. September 1990, pp. 339–342, 1992.
- [380] J. O. Blakeley, J. Olson, S. A. Grossman, X. He, J. Weingart, and J. G. Supko, "Effect of blood brain barrier permeability in recurrent high grade gliomas on the intratumoral pharmacokinetics of methotrexate: a microdialysis study.," *J. Neurooncol.*, vol. 91, no. 1, pp. 51–8, Jan. 2009.
- [381] A. Peyrl, R. Sauermaun, M. Chocholous, A. a Azizi, W. Jäger, M. Höferl, and I. Slavc, "Pharmacokinetics and toxicity of intrathecal liposomal cytarabine in children and adolescents following age-adapted dosing.," *Clin. Pharmacokinet.*, vol. 53, no. 2, pp. 165–73, Feb. 2014.
- [382] K. A. Jaeckle, S. Phuphanich, M. J. Bent, R. Aiken, T. Batchelor, T. Campbell, D. Fulton, M. Gilbert, D. Heros, L. Rogers, S. J. O'Day, W. Akerley, J. Allen, S. Baidas, S. Z. Gertler, H. S. Greenberg, S. LaFollette, G. Lesser, W. Mason, L. Recht, E. Wong, M. C. Chamberlain, A. Cohn, M. J. Glantz, J. C. Gutheil, B. Maria, P. Moots, P. New, C. Russell, W. Shapiro, L. Swinnen, and S. B. Howell, "Intrathecal treatment of neoplastic meningitis due to breast cancer with a slow-release formulation of cytarabine.," *Br. J. Cancer*, vol. 84, no. 2, pp. 157–63, Jan. 2001.
- [383] B. C. Tang, J. Fu, D. N. Watkins, and J. Hanes, "Enhanced efficacy of local etoposide delivery by poly(ether-anhydride) particles against small cell lung cancer in vivo.," *Biomaterials*, vol. 31, no. 2, pp. 339–44, Jan. 2010.
- [384] H. Peng, K. Li, T. Wang, J. Wang, J. Wang, R. Zhu, D. Sun, and S. Wang, "Preparation of hierarchical mesoporous CaCO₃ by a facile binary solvent approach as anticancer drug carrier for etoposide.," *Nanoscale Res. Lett.*, vol. 8, no. 1, p. 321, Jan. 2013.
- [385] J. Varshosaz, F. Hassanzadeh, H. Sadeghi, F. Firozian, and M. Mirian, "Effect of Molecular Weight and Molar Ratio of Dextran on Self-Assembly of Dextran Stearate Polymeric Micelles as Nanocarriers for Etoposide," *J. Nanomater.*, vol. 2012, pp. 1–10, 2012.
- [386] J. Varshosaz, F. Hassanzadeh, H. Sadeghi-Aliabadi, and F. Firozian, "Uptake of Etoposide in CT-26 Cells of Colorectal Cancer Using Folate Targeted Dextran Stearate Polymeric Micelles," *Biomed Res. Int.*, vol. 2014, pp. 1–11, 2014.

References

- [387] A. K. Mohanty, F. Dilnawaz, C. Mohanty, and S. K. Sahoo, "Etoposide-loaded biodegradable amphiphilic methoxy (poly ethylene glycol) and poly (epsilon caprolactone) copolymeric micelles as drug delivery vehicle for cancer therapy," *DRUG Deliv.*, vol. 17, no. 5, pp. 330–342, 2010.
- [388] F. Wang, T. K. Bronich, A. V Kabanov, R. D. Rauh, and J. Roovers, "Synthesis and evaluation of a star amphiphilic block copolymer from poly(epsilon-caprolactone) and poly(ethylene glycol) as a potential drug delivery carrier.," *Bioconjug. Chem.*, vol. 16, no. 2, pp. 397–405.
- [389] L. Qin, M. Wang, R. Zhu, S. You, P. Zhou, and S. Wang, "The in vitro sustained release profile and antitumor effect of etoposide-layered double hydroxide nanohybrids.," *Int. J. Nanomedicine*, vol. 8, pp. 2053–64, Jan. 2013.
- [390] X. Wei, T. H. Senanayake, G. Warren, and S. V Vinogradov, "Hyaluronic acid-based nanogel-drug conjugates with enhanced anticancer activity designed for the targeting of CD44-positive and drug-resistant tumors.," *Bioconjug. Chem.*, vol. 24, no. 4, pp. 658–68, Apr. 2013.
- [391] R. Saadati and S. Dadashzadeh, "Marked effects of combined TPGS and PVA emulsifiers in the fabrication of etoposide-loaded PLGA-PEG nanoparticles: In vitro and in vivo evaluation.," *Int. J. Pharm.*, vol. 464, no. 1–2, pp. 135–144, Jan. 2014.
- [392] R. Saadati, S. Dadashzadeh, Z. Abbasian, and H. Soleimanjahi, "Accelerated blood clearance of PEGylated PLGA nanoparticles following repeated injections: effects of polymer dose, PEG coating, and encapsulated anticancer drug.," *Pharm. Res.*, vol. 30, no. 4, pp. 985–95, Apr. 2013.
- [393] E. Kılıçay, M. Demirbilek, M. Türk, E. Güven, B. Hazer, and E. B. Denkbas, "Preparation and characterization of poly(3-hydroxybutyrate-co-3-hydroxyhexanoate) (PHBHHX) based nanoparticles for targeted cancer therapy.," *Eur. J. Pharm. Sci.*, vol. 44, no. 3, pp. 310–20, Oct. 2011.
- [394] K. S. Yadav, K. Chuttani, A. K. Mishra, and K. K. Sawant, "Long circulating nanoparticles of etoposide using PLGA-MPEG and PLGA-pluronic block copolymers: characterization, drug-release, blood-clearance, and biodistribution studies," *Drug Dev. Res.*, vol. 71, no. 4, pp. 228–239, Mar. 2010.
- [395] K. S. Yadav, S. Jacob, G. Sachdeva, and K. K. Sawant, "Intracellular delivery of etoposide loaded biodegradable nanoparticles: cytotoxicity and cellular uptake studies.," *J. Nanosci. Nanotechnol.*, vol. 11, no. 8, pp. 6657–67, Aug. 2011.

References

- [396] C. K. Sompur, R. C. Doijad, and G. Arjun, "A Novel Approach For Development And Characterization Of Etoposide Loaded Solid Lipid Nanoparticles," *Int. J. Pharma Bio Sci.*, vol. 2, no. 3, pp. 298–306, 2011.
- [397] Z. Wang, Z. Li, D. Zhang, L. Miao, and G. Huang, "Development of etoposide-loaded bovine serum albumin nanosuspensions for parenteral delivery.," *Drug Deliv.*, vol. 7544, pp. 1–7, Jan. 2014.
- [398] "Method for preparing etoposide nanometer suspension freeze-drying preparation," 01-Aug-2012.
- [399] M. Callewaert, S. Dukic, L. Van Gulick, M. Vittier, V. Gafa, M.-C. Andry, M. Molinari, and V. G. Roullin, "Etoposide encapsulation in surface-modified poly(lactide-co-glycolide) nanoparticles strongly enhances glioma antitumor efficiency.," *J. Biomed. Mater. Res. A*, vol. 101, no. 5, pp. 1319–27, May 2013.
- [400] K. Yadav and K. Sawant, "Formulation Optimization of Etoposide Loaded PLGA Nanoparticles by Double Factorial Design and their Evaluation," *Curr. Drug Deliv.*, vol. 7, no. 1, pp. 51–64, Jan. 2010.
- [401] R. Yadav, D. Kumar, A. Kumari, and S. K. Yadav, "Encapsulation of podophyllotoxin and etoposide in biodegradable poly-d,l-lactide nanoparticles improved their anticancer activity.," *J. Microencapsul.*, Oct. 2013.
- [402] G. Yordanov, R. Skrobanska, and A. Evangelatov, "Colloidal formulations of etoposide based on poly(butyl cyanoacrylate) nanoparticles: preparation, physicochemical properties and cytotoxicity.," *Colloids Surf. B. Biointerfaces*, vol. 101, pp. 215–22, Jan. 2013.
- [403] M. Ukawala, T. Rajyaguru, K. Chaudhari, A. S. Manjappa, S. Pimple, A. K. Babbar, R. Mathur, A. K. Mishra, and R. S. R. Murthy, "Investigation on design of stable etoposide-loaded PEG-PCL micelles: effect of molecular weight of PEG-PCL diblock copolymer on the in vitro and in vivo performance of micelles.," *Drug Deliv.*, vol. 19, no. 3, pp. 155–67, Apr. 2012.
- [404] J. Varshosaz, F. Hasanzadeh, and M. Eslamdoost, "Optimization of self-assembling properties of fatty acids grafted to methoxy poly(ethylene glycol) as nanocarriers for etoposide.," *Acta Pharm.*, vol. 62, no. 1, pp. 31–44, Mar. 2012.
- [405] Y.-C. Kuo and T.-Y. Hong, "Delivering etoposide to the brain using cationic solid lipid nanoparticles with surface 5-HT-moduline.," *Int. J. Pharm.*, Feb. 2014.
- [406] L. H. Reddy, J. S. Adhikari, B. S. R. Dwarakanath, R. K. Sharma, and R. R. Murthy, "Tumoricidal effects of etoposide incorporated

References

- into solid lipid nanoparticles after intraperitoneal administration in Dalton's lymphoma bearing mice," *AAPS J.*, vol. 8, no. 2, pp. E254–E262, Jun. 2006.
- [407] L. Harivardhan Reddy, R. K. Sharma, K. Chuttani, A. K. Mishra, and R. S. R. Murthy, "Influence of administration route on tumor uptake and biodistribution of etoposide loaded solid lipid nanoparticles in Dalton's lymphoma tumor bearing mice.," *J. Control. Release*, vol. 105, no. 3, pp. 185–98, Jul. 2005.
- [408] L. H. Reddy and R. S. R. Murthy, "Etoposide-loaded nanoparticles made from glyceride lipids: formulation, characterization, in vitro drug release, and stability evaluation.," *AAPS PharmSciTech*, vol. 6, no. 2, pp. E158–66, Jan. 2005.
- [409] L. H. Reddy, R. K. Sharma, K. Chuttani, A. K. Mishra, and R. S. R. Murthy, "Etoposide-incorporated tripalmitin nanoparticles with different surface charge: formulation, characterization, radiolabeling, and biodistribution studies.," *AAPS J.*, vol. 6, no. 3, p. e23, Jan. 2004.
- [410] G. Gaucher, M. Poreba, F. Ravenelle, and J.-C. Leroux, "Poly(N-vinyl-pyrrolidone)-block-poly(D,L-lactide) as polymeric emulsifier for the preparation of biodegradable nanoparticles.," *J. Pharm. Sci.*, vol. 96, no. 7, pp. 1763–75, Jul. 2007.
- [411] A. Khajavinia, J. Varshosaz, and A. J. Dehkordi, "Targeting etoposide to acute myelogenous leukaemia cells using nanostructured lipid carriers coated with transferrin.," *Nanotechnology*, vol. 23, no. 40, p. 405101, Oct. 2012.
- [412] S. Pimple, A. Manjappa, M. Ukawala, and R. S. R. Murthy, "PLGA nanoparticles loaded with etoposide and quercetin dihydrate individually: in vitro cell line study to ensure advantage of combination therapy," *Cancer Nanotechnol.*, vol. 3, no. 1–6, pp. 25–36, 2012.
- [413] M. Snehalatha, V. Kolachina, R. N. Saha, A. K. Babbar, N. Sharma, and R. K. Sharma, "Enhanced tumor uptake, biodistribution and pharmacokinetics of etoposide loaded nanoparticles in Dalton's lymphoma tumor bearing mice.," *J. Pharm. Bioallied Sci.*, vol. 5, no. 4, pp. 290–297, Jan. 2013.
- [414] M. Snehalatha, K. Venugopal, and R. N. Saha, "Etoposide-Loaded PLGA and PCL Nanoparticles I: Preparation and Effect of Formulation Variables," *Drug Deliv.*, vol. 15, no. 5, pp. 267–275, 2008.
- [415] S. Shah, A. Pal, R. Gude, and S. Devi, "A novel approach to prepare etoposide-loaded poly(N-vinyl caprolactam-co-methylmethacrylate) copolymeric nanoparticles and their controlled

References

- release studies," *J. Appl. Polym. Sci.*, vol. 127, no. 6, pp. 4991–4999, Mar. 2013.
- [416] B. Saliou, O. Thomas, N. Lautram, A. Clavreul, J. Hureauux, T. Urban, J.-P. Benoit, and F. Lagarce, "Development and in vitro evaluation of a novel lipid nanocapsule formulation of etoposide.," *Eur. J. Pharm. Sci.*, vol. 50, no. 2, pp. 172–80, Oct. 2013.
- [417] R. B. Athawale, D. S. Jain, K. K. Singh, and R. P. Gude, "Etoposide loaded solid lipid nanoparticles for curtailing B16F10 melanoma colonization in lung," *Biomed. Pharmacother.*, pp. 1–10, Jan. 2014.
- [418] A. Lamprecht and J.-P. Benoit, "Etoposide nanocarriers suppress glioma cell growth by intracellular drug delivery and simultaneous P-glycoprotein inhibition," *J. Control. Release*, vol. 112, no. 2, pp. 208–213, 2006.
- [419] R. R. Patlolla and V. Vobalaboina, "Folate-targeted etoposide-encapsulated lipid nanospheres.," *J. Drug Target.*, vol. 16, no. 4, pp. 269–75, May 2008.
- [420] F. Prinz, T. Schlange, and K. Asadullah, "Believe it or not: how much can we rely on published data on potential drug targets?," *Nat. Rev. Drug Discov.*, vol. 10, no. 9, p. 712, Sep. 2011.
- [421] C. G. Begley and L. M. Ellis, "Drug development: Raise standards for preclinical cancer research.," *Nature*, vol. 483, no. 7391, pp. 531–3, Mar. 2012.
- [422] J. P. A. Ioannidis, "Contradicted and initially stronger effects in highly cited clinical research.," *JAMA*, vol. 294, no. 2, pp. 218–28, Jul. 2005.
- [423] "European Pharmacopoeia 8th Edition," *Council of Europe*, 2014. [Online]. Available: <http://www.edqm.eu/en/european-pharmacopoeia-8th-edition-1563.html>. [Accessed: 31-Jul-2014].
- [424] H. Sasaki, Y. Takakura, M. Hashida, T. Kimura, and H. Sezaki, "Antitumor activity of lipophilic prodrugs of mitomycin C entrapped in liposome or O/W emulsion.," *J. Pharmacobiodyn.*, vol. 7, no. 2, pp. 120–30, Feb. 1984.
- [425] G. Dalwadi and B. Sunderland, "Comparison and validation of drug loading parameters of PEGylated nanoparticles purified by a diafiltration centrifugal device and tangential flow filtration.," *Drug Dev. Ind. Pharm.*, vol. 34, no. 12, pp. 1331–42, Dec. 2008.
- [426] B. Magenheim, M. Y. Levy, and S. Benita, "A new in vitro technique for the evaluation of drug release profile from colloidal carriers - ultrafiltration technique at low pressure," *Int. J. Pharm.*, vol. 94, pp. 115–123, 1993.

References

- [427] a. Y. Ozer and H. Talsma, "Preparation and stability of liposomes containing 5-fluorouracil," *Int. J. Pharm.*, vol. 55, no. 2–3, pp. 185–191, Oct. 1989.
- [428] C. Washington, "Evaluation of non-sink dialysis methods for the measurement of drug release from colloids: effects of drug partition," *Int. J. Pharm.*, vol. 56, no. 1, pp. 71–74, Nov. 1989.
- [429] C. Washington, "Drug release from microdisperse systems: a critical review," *Int. J. Pharm.*, vol. 58, no. 1, pp. 1–12, Jan. 1990.
- [430] S. J. Wallace, J. Li, R. L. Nation, and B. J. Boyd, "Drug release from nanomedicines: Selection of appropriate encapsulation and release methodology.," *Drug Deliv. Transl. Res.*, vol. 2, no. 4, pp. 284–292, Aug. 2012.
- [431] S. Modi and B. D. Anderson, "Determination of drug release kinetics from nanoparticles: overcoming pitfalls of the dynamic dialysis method.," *Mol. Pharm.*, vol. 10, no. 8, pp. 3076–89, Aug. 2013.
- [432] Y. Zambito, E. Pedreschi, and G. Di Colo, "Is dialysis a reliable method for studying drug release from nanoparticulate systems?-A case study.," *Int. J. Pharm.*, vol. 434, no. 1–2, pp. 28–34, Sep. 2012.
- [433] N. Chidambaram and D. J. Burgess, "A novel in vitro release method for submicron-sized dispersed systems," *AAPS PharmSci*, vol. 1, no. 3, pp. 32–40, Sep. 1999.
- [434] S. Hua, "Comparison of in vitro dialysis release methods of loperamide-encapsulated liposomal gel for topical drug delivery.," *Int. J. Nanomedicine*, vol. 9, pp. 735–44, Jan. 2014.
- [435] R. S. Pandey, S. Sahu, M. S. Sudheesh, J. Madan, M. Kumar, and V. K. Dixit, "Carbohydrate modified ultrafine ceramic nanoparticles for allergen immunotherapy.," *Int. Immunopharmacol.*, vol. 11, no. 8, pp. 925–31, Aug. 2011.
- [436] J. P. K. Tan and K. C. Tam, "Application of drug selective electrode in the drug release study of pH-responsive microgels.," *J. Control. Release*, vol. 118, no. 1, pp. 87–94, Mar. 2007.
- [437] L. Mora, K. Y. Chumbimuni-Torres, C. Clawson, L. Hernandez, L. Zhang, and J. Wang, "Real-time electrochemical monitoring of drug release from therapeutic nanoparticles.," *J. Control. Release*, vol. 140, no. 1, pp. 69–73, Nov. 2009.
- [438] C. B. Michalowski, S. S. Guterres, and T. Dalla Costa, "Microdialysis for evaluating the entrapment and release of a lipophilic drug from nanoparticles.," *J. Pharm. Biomed. Anal.*, vol. 35, no. 5, pp. 1093–100, Sep. 2004.

References

- [439] F. C. Szoka, K. Jacobson, and D. Papahadjopoulos, "The use of aqueous space markers to determine the mechanism of interaction between phospholipid vesicles and cells.," *Biochim. Biophys. Acta*, vol. 551, no. 2, pp. 295–303, Mar. 1979.
- [440] L. Illum, M. A. Khan, E. Mak, and S. S. Davis, "Evaluation of carrier capacity and release characteristics for poly(butyl 2-cyanoacrylate) nanoparticles," *Int. J. Pharm.*, vol. 30, no. 1, pp. 17–28, May 1986.
- [441] J. J. Kettenes-Van Den Bosch, J. J. M. Holthuis, and A. Bult, "Teniposide," *Anal. Profiles Drug Subst.*, vol. 19, pp. 575–600, 1990.
- [442] H. Chen, S. Shi, M. Zhao, L. Zhang, H. He, and X. Tang, "A lyophilized etoposide submicron emulsion with a high drug loading for intravenous injection: preparation, evaluation, and pharmacokinetics in rats.," *Drug Dev. Ind. Pharm.*, vol. 36, no. 12, pp. 1444–53, Dec. 2010.
- [443] Z. Wu, D. Guo, L. Deng, Y. Zhang, Q. Yang, and J. Chen, "Preparation and evaluation of a self-emulsifying drug delivery system of etoposide-phospholipid complex.," *Drug Dev. Ind. Pharm.*, vol. 37, no. 1, pp. 103–12, Jan. 2011.
- [444] J. Jain, C. Fernandes, and V. Patravale, "Formulation development of parenteral phospholipid-based microemulsion of etoposide.," *AAPS PharmSciTech*, vol. 11, no. 2, pp. 826–31, Jun. 2010.
- [445] H. Fessi, F. Puisieux, J. P. Devissaguet, N. Ammoury, and S. Benita, "Nanocapsule formation by interfacial polymer deposition following solvent displacement," *Int. J. Pharm.*, vol. 55, no. 1, pp. R1 – R4, 1989.
- [446] H.-J. Krause, A. Schwarz, and P. Rohdewald, "Polylactic acid nanoparticles, a colloidal drug delivery system for lipophilic drugs," *Int. J. Pharm.*, vol. 27, no. 2–3, pp. 145–155, Dec. 1985.
- [447] H. Jeffery, S. S. Davis, and D. T. O'Hagan, "The preparation and characterisation of poly(lactide-co-glycolide) microparticles. I: Oil-in-water emulsion solvent evaporation," *Int. J. Pharm.*, vol. 77, no. 2–3, pp. 169–175, Nov. 1991.
- [448] T. Niwa, H. Takeuchi, T. Hino, N. Kunou, and Y. Kawashima, "Preparations of biodegradable nanospheres of water-soluble and insoluble drugs with D,L-lactide/glycolide copolymer by a novel spontaneous emulsification solvent diffusion method, and the drug release behavior," *J. Control. Release*, vol. 25, no. 1–2, pp. 89–98, May 1993.
- [449] J. Hrkach, D. Von Hoff, M. Mukkaram Ali, E. Andrianova, J. Auer, T. Campbell, D. De Witt, M. Figa, M. Figueiredo, A. Horhota, S. Low,

References

- K. McDonnell, E. Peeke, B. Retnarajan, A. Sabnis, E. Schnipper, J. J. Song, Y. H. Song, J. Summa, D. Tompsett, G. Troiano, T. Van Geen Hoven, J. Wright, P. LoRusso, P. W. Kantoff, N. H. Bander, C. Sweeney, O. C. Farokhzad, R. Langer, and S. Zale, "Preclinical development and clinical translation of a PSMA-targeted docetaxel nanoparticle with a differentiated pharmacological profile.," *Sci. Transl. Med.*, vol. 4, no. 128, p. 128ra39, Apr. 2012.
- [450] G. Troiano, M. Figa, and A. Sabnis, "Drug Loaded Polymeric Nanoparticles and Methods of Making and Using Same." Google Patents, 10-Nov-2011.
- [451] D. L. Stirland, J. W. Nichols, S. Miura, and Y. H. Bae, "Mind the gap: a survey of how cancer drug carriers are susceptible to the gap between research and practice.," *J. Control. Release*, vol. 172, no. 3, pp. 1045–64, Dec. 2013.
- [452] S. He, Z. Cui, D. Mei, H. Zhang, X. Wang, W. Dai, and Q. Zhang, "A cremophor-free self-microemulsified delivery system for intravenous injection of teniposide: evaluation in vitro and in vivo.," *AAPS PharmSciTech*, vol. 13, no. 3, pp. 846–52, Sep. 2012.
- [453] F. H. Tomlinson, M. G. Lihou, and P. J. Smith, "Comparison of in vitro activity of epipodophyllotoxins with other chemotherapeutic agents in human medulloblastomas," *Br J Cancer*, vol. 64, no. 6, pp. 1051–1059, Dec. 1991.
- [454] "International Agency for Research on Cancer (IARC) monograph : Teniposide," in *IARC monographs 76*, 1996.
- [455] H. Gelderblom, J. Verweij, K. Nooter, and a Sparreboom, "Cremophor EL: the drawbacks and advantages of vehicle selection for drug formulation.," *Eur. J. Cancer*, vol. 37, no. 13, pp. 1590–8, Sep. 2001.
- [456] G. L. Kennedy and H. Sherman, "Acute and subchronic toxicity of dimethylformamide and dimethylacetamide following various routes of administration.," *Drug Chem. Toxicol.*, vol. 9, no. 2, pp. 147–70, Jan. 1986.
- [457] L. Mo, L. Hou, D. Guo, X. Xiao, P. Mao, and X. Yang, "Preparation and characterization of teniposide PLGA nanoparticles and their uptake in human glioblastoma U87MG cells.," *Int. J. Pharm.*, vol. 436, no. 1–2, pp. 815–24, Oct. 2012.
- [458] B. Lundberg, "The solubilization of lipophilic derivatives of podophyllotoxins in sub-micron sized lipid emulsions and their cytotoxic activity against cancer cells in culture," *Int. J. Pharm.*, vol. 109, no. 1, pp. 73–81, Aug. 1994.

References

- [459] Z. Zhang, L. Ma, S. Jiang, Z. Liu, J. Huang, L. Chen, H. Yu, and Y. Li, "A self-assembled nanocarrier loading teniposide improves the oral delivery and drug concentration in tumor.," *J. Control. Release*, vol. 166, no. 1, pp. 30–7, Feb. 2013.
- [460] EMEA, *ICH Topic Q2(R1) Validation of Analytical Procedures: Text and Methodology*. 1995, pp. 13–15.
- [461] J. R. Lakowicz, *Principles of Fluorescence Spectroscopy*. Springer Science & Business Media, 2007, p. 980.
- [462] P. . Scholes, A. G. . Coombes, L. Illum, S. . Davis, J. . Watts, C. Ustariz, M. Vert, and M. . Davies, "Detection and determination of surface levels of poloxamer and PVA surfactant on biodegradable nanospheres using SSIMS and XPS," *J. Control. Release*, vol. 59, no. 3, pp. 261–278, Jun. 1999.
- [463] K. Anselme, B. Flautre, P. Hardouin, M. Chanavaz, C. Ustariz, and M. Vert, "Fate of bioresorbable poly(lactic acid) microbeads implanted in artificial bone defects for cortical bone augmentation in dog mandible.," *Biomaterials*, vol. 14, no. 1, pp. 44–50, Jan. 1993.
- [464] N. Duhem, F. Danhier, V. Pourcelle, J.-M. Schumers, O. Bertrand, C. S. Leduff, S. Hoepfener, U. S. Schubert, J.-F. Gohy, J. Marchand-Brynaert, and V. Pr at, "Self-assembling doxorubicin-tocopherol succinate prodrug as a new drug delivery system: synthesis, characterization, and in vitro and in vivo anticancer activity.," *Bioconjug. Chem.*, vol. 25, no. 1, pp. 72–81, Jan. 2014.
- [465] S. Reis, C. G. Moutinho, C. Matos, B. de Castro, P. Gameiro, and J. L. F. C. Lima, "Noninvasive methods to determine the critical micelle concentration of some bile acid salts.," *Anal. Biochem.*, vol. 334, no. 1, pp. 117–26, Nov. 2004.
- [466] Z. Zhang, S. Tan, and S.-S. Feng, "Vitamin E TPGS as a molecular biomaterial for drug delivery.," *Biomaterials*, vol. 33, no. 19, pp. 4889–906, Jun. 2012.
- [467] V. D. Samith, G. Mi o, E. Ramos-Moore, and N. Arancibia-Miranda, "Effects of pluronic F68 micellization on the viability of neuronal cells in culture," *J. Appl. Polym. Sci.*, vol. 130, no. 3, pp. 2159–2164, Nov. 2013.
- [468] S. Holm, "A simple sequentially rejective multiple test procedure," *Scand. J. Stat.*, vol. 6, no. 2, pp. 65–70, 1979.
- [469] W. Anderson, D. Kozak, V. a Coleman,  . K. J mting, and M. Trau, "A comparative study of submicron particle sizing platforms: accuracy, precision and resolution analysis of polydisperse particle size distributions.," *J. Colloid Interface Sci.*, vol. 405, pp. 322–30, Sep. 2013.

References

- [470] J. Alsenz and M. Kansy, "High throughput solubility measurement in drug discovery and development.," *Adv. Drug Deliv. Rev.*, vol. 59, no. 7, pp. 546–67, Jul. 2007.
- [471] K.-J. Lee, R. Mower, T. Hollenbeck, J. Castelo, N. Johnson, P. Gordon, P. J. Sinko, K. Holme, and Y.-H. Lee, "Modulation of nonspecific binding in ultrafiltration protein binding studies.," *Pharm. Res.*, vol. 20, no. 7, pp. 1015–21, Jul. 2003.
- [472] "Selection Guide: Separation Products for Centrifugal and Tangential Flow Filtration." [Online]. Available: <http://www.pall.com/main/laboratory/literature-library-details.page?id=7046>. [Accessed: 07-Aug-2014].
- [473] K. J. Wilkinson and J. R. Lead, *Environmental Colloids and Particles: Behaviour, Separation and Characterisation*. John Wiley & Sons, 2007, p. 702.
- [474] G. Mehta, A. Y. Hsiao, M. Ingram, G. D. Luker, and S. Takayama, "Opportunities and challenges for use of tumor spheroids as models to test drug delivery and efficacy.," *J. Control. Release*, vol. 164, no. 2, pp. 192–204, Dec. 2012.
- [475] M.-G. Zurich, S. Stanzel, A. Kopp-Schneider, P. Prieto, and P. Honegger, "Evaluation of aggregating brain cell cultures for the detection of acute organ-specific toxicity.," *Toxicol. In Vitro*, vol. 27, no. 4, pp. 1416–24, Jun. 2013.
- [476] S. J. Nygaard, P. H. Pedersen, T. Mikkelsen, A. J. Terzis, O. B. Tysnes, and R. Bjerkvig, "Glioma cell invasion visualized by scanning confocal laser microscopy in an in vitro co-culture system.," *Invasion Metastasis*, vol. 15, no. 5–6, pp. 179–88, Jan. 1995.
- [477] J. Xu, A. Margol, S. Asgharzadeh, and A. Erdreich-Epstein, "Pediatric brain tumor cell lines.," *J. Cell. Biochem.*, vol. 116, no. 2, pp. 218–24, Feb. 2015.
- [478] K. Needham, T. Hyakumura, N. Gunewardene, M. Dottori, and B. A. Nayagam, "Electrophysiological properties of neurosensory progenitors derived from human embryonic stem cells.," *Stem Cell Res.*, vol. 12, no. 1, pp. 241–9, Jan. 2014.
- [479] M. Moors, J. E. Cline, J. Abel, and E. Fritsche, "ERK-dependent and -independent pathways trigger human neural progenitor cell migration.," *Toxicol. Appl. Pharmacol.*, vol. 221, no. 1, pp. 57–67, May 2007.
- [480] E. Fritsche, J. E. Cline, N.-H. Nguyen, T. S. Scanlan, and J. Abel, "Polychlorinated Biphenyls Disturb Differentiation of Normal Human Neural Progenitor Cells: Clue for Involvement of Thyroid Hormone

References

- Receptors," *Environ. Health Perspect.*, vol. 113, no. 7, pp. 871–876, Apr. 2005.
- [481] M. Vavra, "Comparative pharmacokinetics of ¹⁴C-sucrose in RG-2 rat gliomas after intravenous and convection-enhanced delivery," *Neuro. Oncol.*, vol. 6, no. 2, pp. 104–112, Apr. 2004.
- [482] B. J. Eastwood, M. W. Farnen, P. W. Iversen, T. J. Craft, J. K. Smallwood, K. E. Garbison, N. W. Delapp, and G. F. Smith, "The minimum significant ratio: a statistical parameter to characterize the reproducibility of potency estimates from concentration-response assays and estimation by replicate-experiment studies.," *J. Biomol. Screen.*, vol. 11, no. 3, pp. 253–61, Apr. 2006.
- [483] R. Mackenzie, "Computational Modelling of Polymer-Based Drug Delivery Systems," University of Nottingham, 2014.